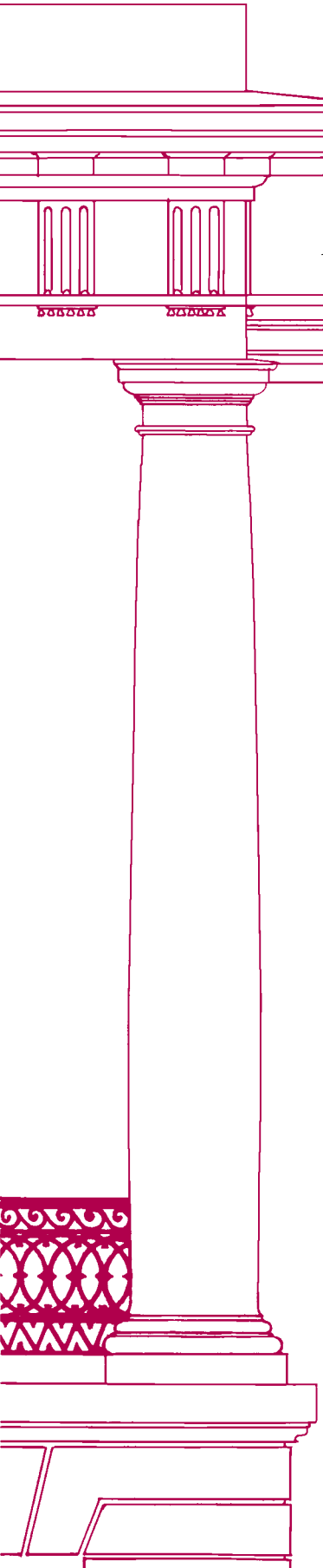

ÅBO AKADEMIS FÖRLAG – ÅBO AKADEMI UNIVERSITY PRESS

The Sottunga-Jurmo Shear Zone

Structure and Deformation History of a Crustal-Scale Ductile Shear Zone in SW Finland

Taija Torvela

ACTA ACADEMIAE ABOENSIS, SER. B

Mathematica et physica

Mathematics, science, engineering

Edited by Göran Högnäs

Vol. 67, no. 1

The Sottunga-Jurmo Shear Zone

Structure and Deformation History of a Crustal-Scale Ductile Shear Zone in SW Finland

Taija Torvela

ÅBO 2007

ÅBO AKADEMIS FÖRLAG – ÅBO AKADEMI UNIVERSITY PRESS

CIP Cataloguing in Publication

Torvela, Taija
The Sottunga-Jurmo shear zone : structure and deformation history of a crustal-scale ductile shear zone in SW Finland / Taija Torvela. - Åbo : Åbo Akademi University Press, 2007. - (Åbo Academiae Aboensis, Ser. B, Mathematica et physica, ISSN 0001-5105; vol. 67, no.1)
ISBN 978-951-765-376-3

ISSN 0001-5105
ISBN 978-951-765-376-3
ISBN 978-951-765-377-0 (digital)
Åbo Akademi University Printing House
Åbo 2007

ABSTRACT

The aim of this study is to gain a better understanding of the structure and the deformation history of a NW-SE trending regional, crustal-scale shear structure in the Åland archipelago, SW Finland, called the Sottunga-Jurmo shear zone (SJSZ). Approaches involving e.g. structural geology, geochronology, geochemistry and metamorphic petrology were utilised in order to reconstruct the overall deformation history of the study area. The study therefore describes several features of the shear zone including structures, kinematics and lithologies within the study area, the ages of the different deformation phases (ductile to brittle) within the shear zone, as well as some geothermobarometric results.

The results indicate that the SJSZ outlines a major crustal discontinuity between the extensively migmatized rocks NE of the shear zone and the unmigmatised, amphibolite facies rocks SW of the zone. The main SJSZ shows overall dextral lateral kinematics with a SW-side up vertical component and deformation partitioning into pure shear and simple shear dominated deformation styles that was intensified toward later stages of the deformation history. The deformation partitioning resulted in complex folding and refolding against the SW margin of the SJSZ, including conical and sheath folds, and in a formation of several minor strike-slip shear zones both parallel and conjugate to the main SJSZ in order to accommodate the regional transpressive stresses.

Different deformation phases within the study area were dated by SIMS (zircon U-Pb), ID-TIMS (titanite U-Pb) and $^{40}Ar/^{39}Ar$ (pseudotachylyte whole-rock) methods. The first deformation phase within the ca. 1.88 Ga rocks of the study area is dated at ca. 1.85 Ga, and the shear zone was reactivated twice within the ductile regime (at ca. 1.83 Ga and 1.79 Ga), during which the strain was successively increasingly partitioned into the main SJSZ and the minor shear zones. The age determinations suggest that the orogenic processes within the study area did not occur in a temporal continuum; instead, the metamorphic zircon rims and titanites show distinct, 10-20 Ma long breaks in deformation between phases of active deformation. The results of this study further imply slow cooling of the rocks through 600-700ºC so that at 1.79 Ga,

the temperature was still at least 600ºC. The highest recorded metamorphic pressures are 6.4-7.1 kbar.

At the late stages or soon after the last ductile phase (ca. 1.79 Ga), relatively high-T mylonites and ultramylonites were formed, witnessing extreme deformation partitioning and high strain rates. After the rocks reached lower amphibolite facies to amphibolite-greenschist facies transitional conditions (ca. 500-550ºC), they cooled rapidly, probably due to crustal uplift and exhumation. The shear zone was reactivated at least once within the semi-brittle to brittle regime between ca. 1.79 Ga and 1.58 Ga, as evidenced by cataclasites and pseudotachylytes.

In summary, the results of this study suggest that the Sottunga-Jurmo shear zone (and the South Finland shear zone) defines a major crustal discontinuity, and played a central role in accommodating the regional stresses during and after the Svecofennian orogeny.

CONTENTS

1. INTRODUCTION TO THE PALAEOPROTEROZOIC GEOLOGY OF SOUTHERN FINLAND

1.1 AN OUTLINE OF THE SVECOFENNIAN OROGENY IN FINLAND

Southern Finland is one part of the amalgam of crustal domains comprise the Fennoscandian shield. These domains cover a time span of over 2400 Ma from the Archaean to the Caledonian orogen 450-400 Ma ago (fig. 1.1). The Palaeoproterozoic Svecofennian domain, formed during the Svecofennian orogeny ca. 2.0-1.75 Ga ago (Gaál & Gorbatschev 1987) comprises large parts of Sweden, Finland and the Estonian basement as well as minor parts of Norway and Russian Karelia. The orogeny that resulted in the formation of the Palaeoproterozoic domain of Fennoscandia is sometimes in literature referred to as the Svecokarelian orogeny. This nomenclature is based on the orogenic models developed for the Fennoscandian shield in the 1960's and 1970's. However, the author prefers the nomenclature of Gaál & Gorbatschev (1987), who suggested that the term 'Karelian' be reserved to the anorogenic supracrustal rock sequences that were deposited on the Archaean craton before the formation of the Kalevian rocks (ca. 2.0 Ga). They conclude that the term 'Svecokarelian orogeny' is misleading and should be abandoned altogether, and the term Svecofennian should be used for rocks produced by the accretional orogeny that formed the bulk of the Palaeoproterozoic Fennoscandian crust between ca. 2.0-1.75 Ga. Thus, Karelian rocks are only preserved close to the suture zone between the Archaean and the Palaeoproterozoic domains and are not further discussed.

The Svecofennian orogeny is characterised by very large volumes of magmatic and volcanic rocks, mainly of intermediate to felsic composition. The 1.92-1.88 Ga volcanic and sedimentary rocks were formed within at least two separate arc complexes that subsequently collided with the Archaean craton (e.g. Nironen 1997). After the main volcanic period, the Svecofennian igneous magmatism occurred in two peaks. The first peak produced synorogenic I-type granitoids that intruded the earlier supracrustal sequences throughout the Svecofennian domain within a relatively short period ca. 1.88 Ga ago (e.g. Nironen 1997). The second, late-orogenic magmatic event ca. 1.84-1.81 Ga ago was a result of elevated heat flow, possibly due to crustal stacking (e.g. Kukkonen & Lauri 2006, Ehlers et al. 1993), which lead to formation of anatectic granites and migmatites in the present southern Finland and central Sweden. Late-orogenic ring intrusions and anorogenic rapakivi batholiths with coeval mafic dyke swarms intruded the rigid upper Svecofennian crust at ca. 1.79-1.76 Ga and 1.65-1.54 Ga, respectively (e.g. Eklund & Shebanov 2005).

The Svecofennian domain was evolved through a multi-stage arc-accretionary orogen where at least two newly formed arc complexes collided with each other and with the older Archaean craton, the main direction of thrusting being approximately towards NE (e.g.

Väisänen 2002, Nironen 1997, Gaál & Gorbatschev 1987). However, it is unclear whether the process included one prolonged orogenic period or several short-lived ones (Korja & Heikkinen 2005). It is also controversial whether or not the juvenile arcs were formed in the presence of a Palaeoproterozoic, 2.0-1.9 Ga continental crust or basement, although evidence is accumulating that 2.1-1.9 Ga material was indeed available for the ca. 1.9 Ga supracrustal rocks (e.g. Ehlers et al. 2004, Claesson et al. 1993, Welin et al. 1993). Each arc complex nevertheless exhibits distinguishable geochemical and lithological characteristics described by several authors (e.g. Rämö et al. 2001, Lahtinen & Huhma 1997) and can thus be divided into terranes (fig. 1.1). The division suggested by Korsman et al. (1997) for the Svecofennian terranes in Finland and the related abbreviations by Väisänen (2002) are used for the purposes of this study: the Primitive Arc Complex of central Finland (PAC) in the north at the suture between the Svecofennian and Archaean domains; the accretionary arc complex of central and western Finland, or Central Svecofennian Arc Complex (CSAC); and the accretionary arc complex of southern Finland, or the Southern Svecofennian Arc Complex (SSAC) in the south. The terranes extend westwards to central and south-central Sweden.

The PAC (fig. 1.1) is considered to be the oldest of the three Palaeoproterozoic terranes as defined by e.g. the 1921 $\pm$ 2 Ma rhyolites of the bimodal island arc type rocks within the PAC close to the Palaeoproterozoic-Archaean suture (Kousa et al. 1994). The volcanic rocks within the PAC commonly display positive ε_{Nd} values suggesting a very small influence of the older Archaean craton on the Palaeoproterozoic volcanism (Lahtinen & Huhma 1997). These two domains were indeed likely to have been separated from each other at the time of the volcanism within the PAC, a notion that is supported by the exposed ca. 1.96 Ga ophiolite complexes within the suture zone in Outokumpu and Jormua in eastern Finland (e.g. Kontinen 1987). The Skellefte district in northern Sweden is sometimes correlated with the PAC in Finland, although this may be disputable. As a summary, the dominant theory states that the break-up of the Archaean crust was followed by the formation of an island arc system (PAC) that was separated by an ocean that subsequently subducted under the Archaean craton (e.g. Nironen 1997). However, it is also suggested that an extensional back-arc basin structure existed instead of an ocean, with a >1.90 Ga complex intrusive and volcanic basement, on top of which the supracrustal rocks were deposited (Rutland et al. 2001).

The rocks within the CSAC further to the south and southwest (fig. 1.1) are separated from the PAC by a major, dextral strike-slip shear zone or a transform zone commonly referred to as the Ladoga-Bothnian Bay zone (LBZ). The LBZ widens and branches out towards Sweden, possibly indicating changes in the rheological properties of the lower crust (Korja & Heikkinen 2005). The dominant rocks of the CSAC comprise the supracrustal rocks of the Tampere belt, the Pirkanmaa belt and the

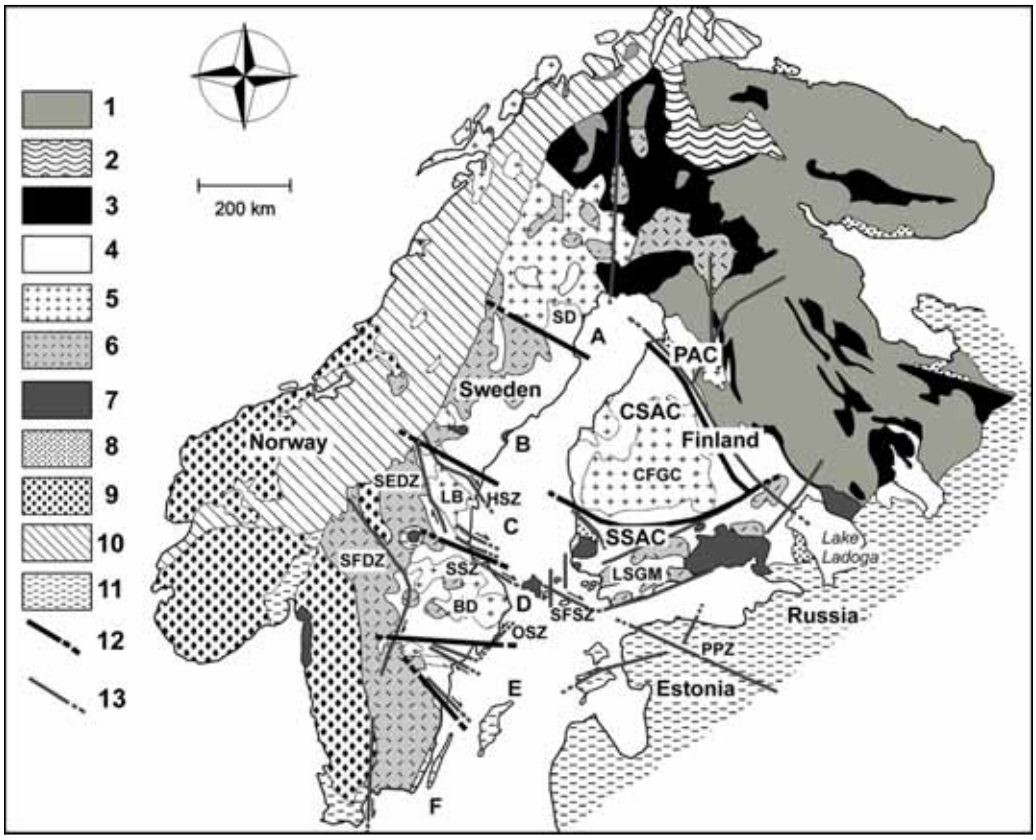

Fig. 1.1. Generalised geological map of the Fennoscandian shield. Key: **1)** Archaean rocks 3.2-2.5 Ga; **2)** Lapland granulite belt 2.2-1.9 Ga; **3)** Karelian supracrustal rocks 2.5-1.8 Ga; **4)** Svecofennian supracrustal rocks 2.0-1.85 Ga; **5)** Svecofennian pre- and synorogenic magmatic rocks 1.95-1.84 Ga; **6)** Svecofennian lateorogenic granites and migmatites; **7)** Anorogenic rapakivi granites 1.65-1.4 Ga; **8)** Sandstones, Jotnian and younger 1.5-0.57 Ga; **9)** Sveconorwegian rocks 1.25-0.9 Ga; **10)** Caledonian rocks 0.6-0.4 Ga; **11)** Phanerozoic sedimentary cover <0.57 Ga; **12)** Domain borders (Väisänen 2002, Högdahl 2000, Sjöström & Bergman 1998, Korsman et al. 1997); **13)** Major Palaeoproterozoic deformation zones of the bedrock (Soesoo et al. 2004, Högdahl 2000, Sjöström & Bergman 1998, Korsman et al. 1997, Kärki et al. 1993) **LSGM** = Late Svecofennian Granite Migmatite zone; **PAC** = Primitive Arc Complex of central Finland; **CSAC** = Central Svecofennian Arc Complex; **SSAC** = Southern Svecofennian Arc Complex; **LB** = Ljusdal batholith; **BD** = Bergslagen district; **SD** = Skellefte district; **A-F** = Palaeoproterozoic bedrock domains in Sweden; **SFSZ** =South Finland shear zone; **PPZ** = Paldiski-Pskov shear zone; **HSZ** = Hassela shear zone; **SEDZ** = Storsjön-Edsbyn deformation zone; **SSZ** = Singö shear zone; **OSZ** = Ornö shear zone; **SFDZ** = Sveconorwegian Frontal deformation zone; Modified from a map compiled from Koistinen et al. (2001) by Fredrik Strandman.

Pohjanmaa belt as well as the igneous ca. 1.88 Ga central Finland granitoid complex (CFGC; fig. 1.1). The supracrustals are dominated by evolved, continental island arc or active continental margin type volcanics, with the exception of the E-MORB type basalts of the Haveri formation (Kähkönen et al. 1989). Kähkönen et al. (1989) have dated the arc volcanic type rocks to 1905-1890 Ma, although there is isotopic evidence of an older, ca. 2.0-2.1 Ga crust underlying the present erosion surface (Lahtinen & Huhma 1997). The Skellefte district and Bothnian

Basin area in northern and north-central Sweden are often correlated with the LBZ and CSAC in Finland, based on e.g. deep seismic reflection geophysics, metallogenic similarities and crustal conductivity anomalies (e.g. Korja & Heikkinen 2005, Nironen 1997), although they may have been formed in different tectonic settings (Nironen 1997). The CSAC was stabilized soon after the main collisional stage at ca. 1.88 Ga, while the convergent orogeny continued to the south within the SSAC (e.g. Nironen et al. 2000, Ehlers et al. 1993).

The SSAC (fig. 1.1) displays different isotopic and structural characteristics compared to the CSAC (e.g. Rämö et al. 2001, Sundblad 1991), strongly implying separate histories for these terranes. The SSAC shows a more primitive arc type geochemistry and thinner crust than do the volcanic rocks and related sediments within the CSAC (e.g. Lahtinen 1996). There are MORB type volcanic rocks close to the suggested suture zone between the SSAC and CSAC that are interpreted as fragments of former oceanic crust (Peltonen 1995). A metarhyolite from SE Finland was dated by Vaasjoki & Sakko (1988) at 1906±4 Ma which is coeval with the oldest volcanism within the Tampere belt of the CSAC. It is, however, controversial whether the sampling location is actually within the SSAC or whether it in fact belongs to CSAC. Other previous age determinations from SSAC rocks conducted and published so far yield somewhat younger ages for volcanism than the age obtained for the aforementioned metarhyolite, although some age determinations have considerable analytical errors. In SSAC rocks, ages around 1.89-1.88 Ga occur frequently, and have been invariably interpreted as precollisional magmatic ages. For example, ages of 1887±14 Ma have been obtained by Patchett & Kouvo (1986), 1888±11 Ma by Vaasjoki (1994) and 1888±11 Ma by Reinikainen (2001). Väisänen et al. (2002) dated a granodiorite in Orijärvi that was interpreted to be precollisional at 1898±9 Ma, and Ehlers et al. (2004) determined the magmatic age of various igneous granitoids in Åland archipelago at ca. 1.88 Ga. Väisänen & Mänttäri (2002) dated a volcanic arc type rhyolite in Masku area at 1895±2 Ma, and a dacitic rock in the structurally overlying Kisko formation at 1878±3 Ma. Ages that are commonly interpreted as collision-related include e.g. a 1854±18 Ma age for a tonalite in Masku (Väisänen et al. 2002). The Ljusdal granitoids, or alternatively, the volcanics in the Bergslagen area in central – south-central Sweden have been referred to as being a part of the same arc complex as the SSAC (domains C and D in fig 1.1; e.g. Nironen 1997 and references therein, Bergman & Sjöström 1994 and references therein).

As evident from the discussion above, there is a trend of younging of the Palaeoproterozoic supracrustal rocks across the terranes from northeast toward southwest. The total time span of the pre- and synorogenic volcanism in these areas covers at least 60-70 Ma from the ca. 1920 Ma rocks in the north close to the Archaean suture, to the ca. 1860-1850 Ma intrusive rocks in the Uusimaa belt within the SSAC. The supracrustal sequences of all Svecofennian domains were, shortly after their formation 1.92-1.88 Ga

ago, intruded by mainly I-type granitoids and associated mafic rocks. This period of ca. 1.89-1.88 Ga plutonism that produced large volumes of magmatic rocks of was approximately coeval throughout the Svecofennian domain, largely independent of the terrane boundaries (Nironen 1997). The central Finland granitoid complex (CFGC; fig. 1.1) is considered as one of the most voluminous example of this plutonism. The magmatic rocks were subsequently deformed during the main stage of the Svecofennian orogeny (Nironen 1997). However, high-pressure metamorphism has not been recorded within the Svecofennian domain. Pressures of ca. 10 kbar, reported from localities associated with transpressional structures in central Sweden (Bergman & Sjöström 1994), are among the highest, although the authors suspected that the results might have been influenced by high Fe-contents in biotite. High-temperature low-pressure meta-morphism is instead dominant, especially within the lateorogenic, ca. 1.83 Ga granite-migmatite belt in the southern-southwestern parts of the Svecofennian domain (fig. 1.1), indicating a presence of high heat flow (Gaál & Gorbatschev 1987). The granite-migmatite zone of southern Finland is often referred to as PGMZ (potassium granite migmatite zone, Nironen 1997) or LSGM (late-Svecofennian granite-migmatite belt, Ehlers et al. 1993), the latter having been adopted by the author. The crust within the LSGM is approximately 10 km thinner than in the other parts of the Svecofennian domain.

The model of the Palaeoproterozoic crust of the Baltic shield comprising a collage of island arcs was initially suggested by Park (1985). Recent tectonic models by Korja & Heikkinen (2005), Väisänen (2002) and Nironen (1997) are briefly summarised below and in figures 1.2 and 1.3. The authors are in agreement that the initial break-up of the Archaean domain occurred ca. 2.1-2.0 Ga ago, followed by a development of a marginal rift ca. 1.96-1.95 Ga ago. The subsequent convergent tectonism resulting in lateral growth of the orogen towards the southwest has been relatively firmly established (e.g. Park 1985, Nironen 1997). There is more discrepancy regarding the number of the juvenile island arc complexes involved in the collision, as well as regarding the style and the timing of the collision of the island arcs with the Archaean craton and with each other. Only the main differences between the models are summarised here.

Both Nironen (1997) and Korja & Heikkinen (2005) conclude that the initial closure of the marginal rift south of the Archaean domain took place ca. 1.91-1.90 Ga, resulting in crustal thickening by stacking, overthrusting and subduction (fig. 1.3). Nironen (1997) suggests that three main crust-forming events took place after the break-up of the Archaean continent: (1) generation of the island arc complexes; (2) accretion of the PAC and the CSAC to the Archaean; (3) a subsequent collision of the second arc complex (the SSAC) to the first ones (fig. 1.2). According to the model by Korja & Heikkinen (2005), a gravitational collapse and a temporal break in the convergence took place at ca. 1.87-1.85 Ga, after the first collisional event where PAC and CSAC accreted to Archaean. During

the break, a new subduction zone developed south of the extending continent (CSAC), after which a second orogenic phase commenced. This model suggests that no separate island arc (SSAC) was involved in the second collisional stage. Instead, only little new supracrustal material was

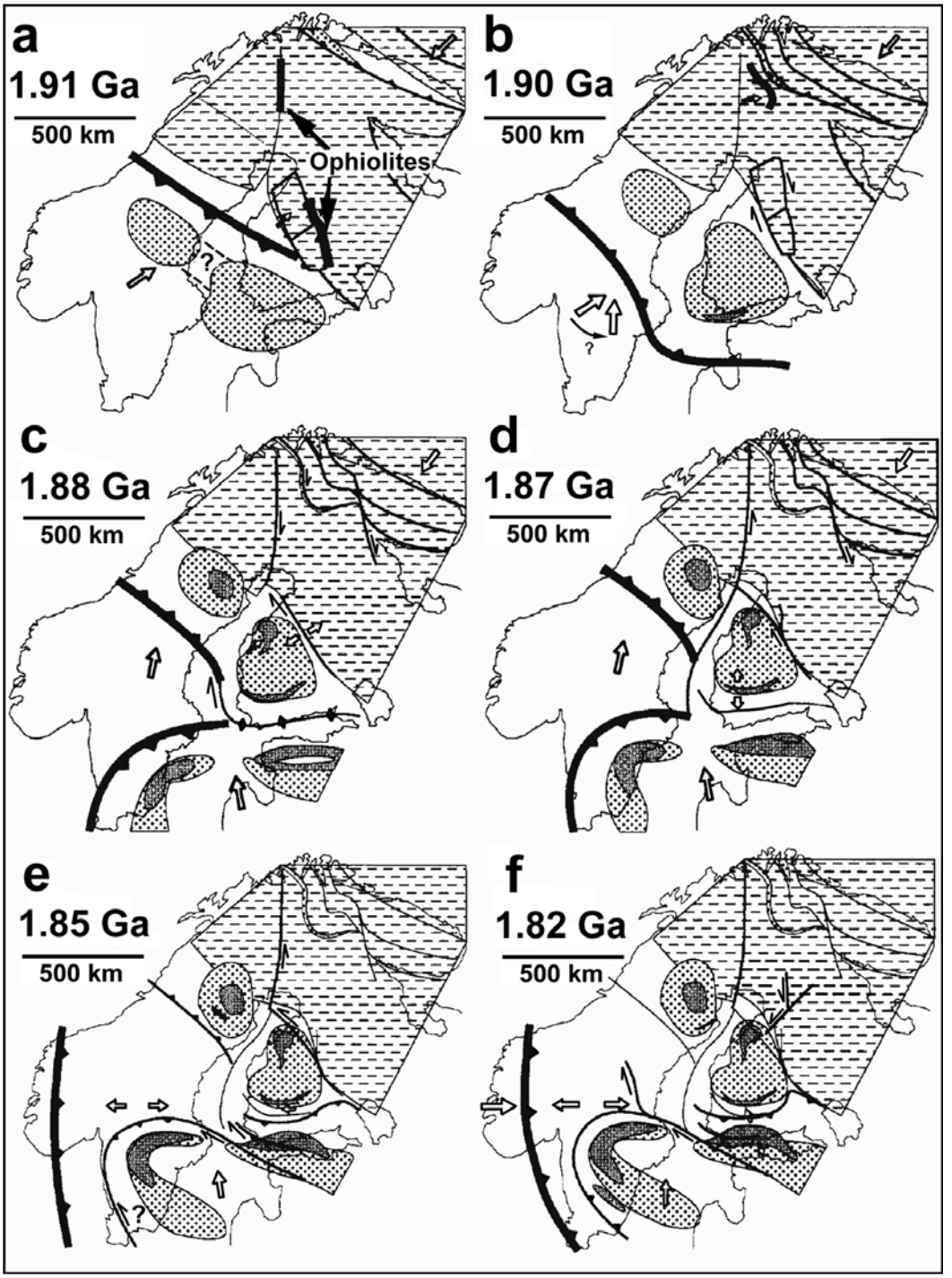

formed in the extensional basin, and the material that became stacked on top of the collapsed Svecofennian orogen consisted mainly of the extended crust (fig. 1.3). The model by Korja & Heikkinen (2005) further implies that the orogenic episode continued until ca. 1.81 Ga. Väisänen (2002) on the other hand suggests that in southern Finland, the main Svecofennian collisional stage was over by ca. 1.87-1.86 Ga, after which the SSAC continued to move northwards during postcollisional convergence. Also according to Nironen (1997), the eastern part of the Svecofennian crust was largely stabilised already by 1.87 Ga, after which the transpressional convergent deformation partitioned into ductile shear zones, while coevally a thinning of the crust in southern Svecofennian domain took place, resulting in extensive granite magmatism and migmatisation of the supracrustal rocks. Supporting results have been obtained from SW Finland, where the thrusting event continued until ca. 1875-1860 Ma, followed by crustal-scale shearing events and granulite facies migmatite-forming metamorphism (e.g. Ehlers et al. 1993, Ehlers et al. 2004, Väisänen 2002). It seems that the collision of the CSAC to the Archaean craton took place at least 10 Ma earlier than the collision between the SSAC and the CSAC, and that at least some convergence took place in southern Finland after the main Svecofennian collisional stage (Väisänen et al. 2002). It may be worth mentioning in this context that e.g. Bergman & Sjöström (1994) note a westward shift with time in both thrusting and transpressional shearing because the events recorded in Finland can systematically be observed to have happened somewhat later in Sweden; this is in accordance with the model suggested by Nironen (1997).

The origin of the LGSM within the SSAC has been disputable for years. E.g. Nironen (1997) and Ehlers et al. (1993) argue that the LSGM-zone is post-collisional, formed as a result of a crustal collapse within the southern Svecofennian domain. According to this model, the post-collisional extensional collapse would have been responsible for the thinning and partial melting of the newly formed supracrustal rocks, leading to the formation of the ca. 1.83 Ga granite-migmatite belt of southern Finland. On the other hand, a model by Korja & Heikkinen (2005) suggests that the collapse and extension preceded the formation of the migmatite belt, and that the anatexis and migmatisation were results of a second, 1.85-1.81 Ga collisional phase of the Svecofennian orogeny where an unknown continental mass to the

Fig. 1.2. Tectonic model for the Svecofennian orogeny by Nironen (1997). **a)** The collision of the 'initial island arc complex (PAC in Väisänen 2002) to the Archaean craton; **b)** subduction reversal and rotation of the plate motion direction; **c)** collision of the SSAC with CSAC in the east, development of major dextral shear zones in the east; **d)** shortening of the crust in the east, subduction continues in the west, separated by a sinistral megashear, developed from a transform fault; **e)** development of a transpressional zone in the east, a new subduction zones develops in the west causing further compression in the east; **f)** the direction of transpression shifts into an E-W direction, extensional collapse in the east. The model implies that the eastern part of the Svecofennian domain (including southern Finland) was largely stabilised at ca. 1.87 Ga, by which time the deformation had already partitioned into shear zones.

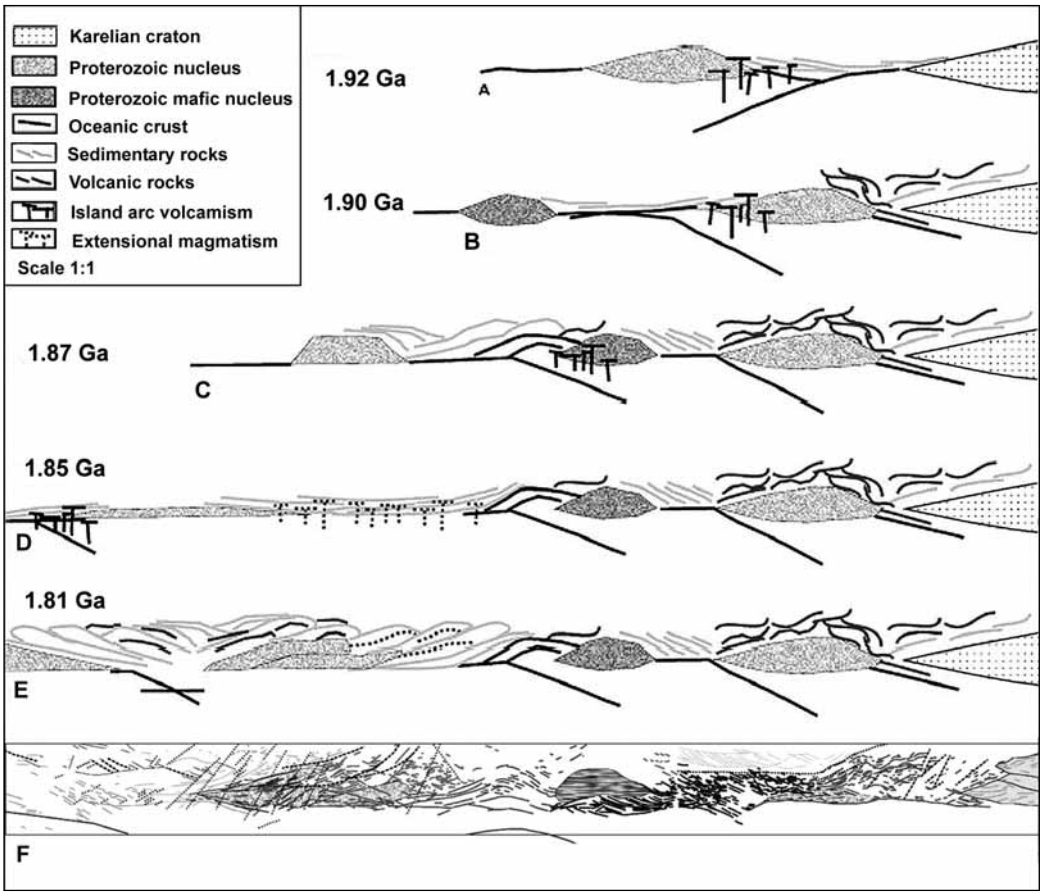

Fig. 1.3. Tectonic model for the Svecofennian orogeny by Korja & Heikkinen (2005), view toward NW. **a)** The closure of an ocean, new crust is formed in island arcs at micro-continental margins; **b)** the micro-continents collide with the Archaean Karelian craton, the location of the subduction zone shifts to in front of (south of) the micro-continent, a new island arc forms in front of the micro-continent; **c)** micro-continents continue their accretion to the Palaeoproterozoic continental nucleus; **d)** extensional collapse, a temporal break in the convergence, local crustal extension; **e)** final collision, the extended crust is stacked between another continent approaching from the south and the collapsed Svecofennian orogen; **f)** a schematic vertical section of the Svecofennides, based on the BABEL deep seismic reflection lines.

south collided with the SSAC. The high heat flow, which initiated partial melting and migmatisation, would have been achieved by stacking of hot crustal slices. According to Korja & Heikkinen (2005), this model would best explain the stacking structures visible in the deep reflection seismic BABEL-profiles. Recently, the stacking model has received support from geochemical and thermal modelling by Kukkonen & Lauri (2006). Also mafic underplating of upwelling hot asthenosphere that convectively removed the sub-continental lithospheric mantle has been suggested as a mechanism for the thinning of the crust and as a heat source for the migmatisation and anatexis (e.g. Väisänen 2002), although it is questioned by several authors (e.g. Kukkonen & Lauri 2006) whether heat production of such underplating would be sufficient for

large-scale crustal anatexis. Furthermore, the mafic sills that should have been developed as a result of underplating are absent in the deep reflection seismic BABEL-profiles (Korja & Heikkinen 2005).

1.2 SOUTHWESTERN FINLAND – A CLOSER LOOK

Southwestern Finland is here understood to comprehend the western parts of the SSAC, or the accretionary arc complex of southern Finland (fig.1.1; Väisänen 2002, Korsman et al. 1997). The SSAC can be further divided into the Häme belt comprising the northern part of the SSAC, and the Uusimaa belt in the southern SSAC (fig. 1.4; e.g. Kähkönen 1998).

The rocks within the southwestern Häme belt are characterised by metabasaltic and metaandesitic rocks, although in the southern and westernmost parts metasedimentary gneisses and migmatites (originally mainly greywackes and pelites) dominate (e.g. Kähkönen 1998). The Häme belt volcanics were deformed under amphibolite facies conditions ca. 1880 Ma ago, the metamorphic degree increasing from north to south toward the migmatite belt (Kähkönen 1998).

The Uusimaa belt, on the other hand, consists largely of rhyolitic metavolcanic rocks and a considerable percentage of sedimentary carbonates, although basic rocks are in places well represented due to the locally bimodal nature of the volcanism (Kähkönen 1998). In Nauvo – Korppoo area in the southwestern part of Uusimaa belt (fig. 1.4), mica schists and gneisses

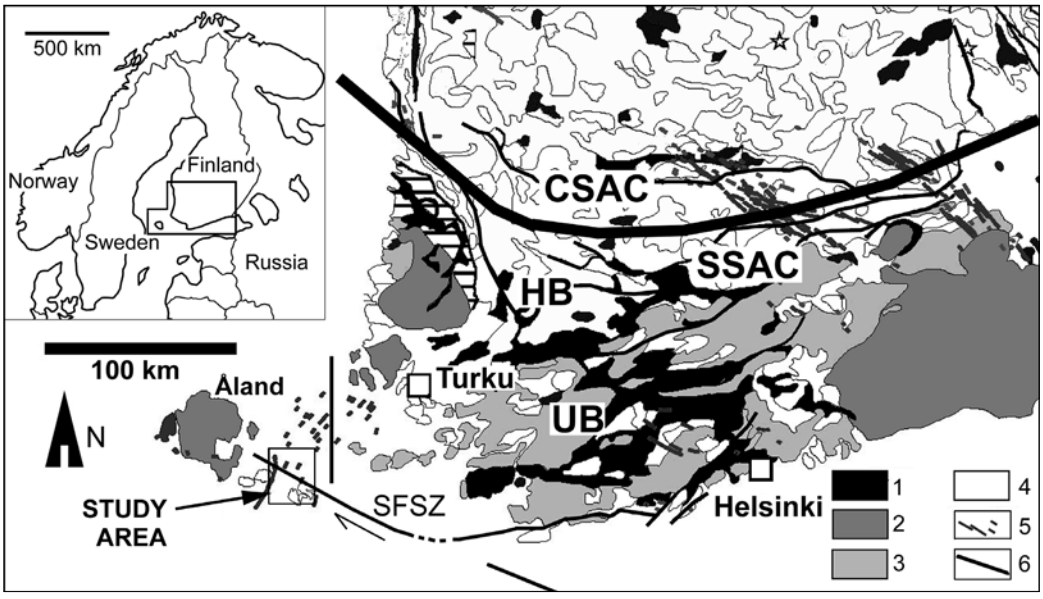

Fig. 1.4. Generalised geological map of southern Finland (modified from Korsman et al. 1997). Key: **SFSZ** = South Finland shear zone; **UB** = Uusimaa belt; **HB** = Häme belt; **CSAC** = Central Svecofennian Arc Complex; **SSAC** = South Svecofennian arc complex; **1)** Metavolcanic rocks ca. 1.92-1.88 Ga; **2)** Rapakivi granites ca. 1.6 Ga; **3)** Late-orogenic granites and migmatites of the LSGM ca. 1.85-1.80 Ga; **4)** Granitoids and/or mica schists ca. 1.89-1.88 Ga; **5)** Diabase dykes ca. 1.65-1.57 Ga; **6)** Major faults and shear zones.

formed from turbidites dominate the lithology, while basic metavolcanic rocks, including pillow lavas, are present as layers less than a kilometre thick (Kähkönen 1998). In general, the volcanic rocks within the Häme belt are more evolved than the volcanics within the Uusimaa belt (e.g. Väisänen 2002 and references therein). Väisänen (2002) interpreted this to imply that the direction of subduction is northwards under the CSAC, the Häme belt thus representing a remnant arc. Lahtinen (1996) suggested an opposite model where the subduction is directed southwards, whereby the evolved volcanic rocks of the Häme belt would represent overlying older, more primitive rocks, and the Uusimaa belt would comprise a remnant arc.

Parts of the Uusimaa belt were migmatised and metamorphosed in up to granulite facies conditions at ca. 1830-1810 Ma as a result of an elevated heat-flow in the crust (e.g. Väisänen 2002, Nironen 1997, Ehlers et al. 1993; see also discussion in chapter 1.1). This late-orogenic metamorphosis was most intense in the Turku and Karkkila areas in the western – southwestern parts of the Uusimaa belt, obliterating most of the original structures, while eastwards the structures are commonly better preserved (Kähkönen 1998). The highest recorded PT-conditions in the Turku area are from the Mynämäki and Parainen garnet-cordierite granulites, where temperatures of 800-825ºC and pressures of 6.3-6.7 kbar were obtained (Väisänen & Hölttä 1999). The belt with ca. 1.83 Ga granulite facies metamorphism and migmatisation is in this study called the Late-Svecofennian Granite Migmatite belt (LSGM; Ehlers et al. 1993; fig 1.1). The LSGM is bordered by major crustal-scale shear zones (fig. 1.1), but so far the relationship between the LSGM and the shear zones has received little attention. However, a recent study by Stålfors & Ehlers (2005) suggests that the emplacement and fractionation of LSGM granitic melts in Nagu and Hämeenlinna were shear-assisted processes, and propose a model where the vertical crustal-scale shear zones functioned as transport channels for the magmas (fig. 1.5).

In literature, the Svecofennian deformation in SW Finland is often divided into four stages D1-D4 (e.g. Levin et al. 2005, Väisänen 2002, Selonen & Ehlers 1998, Ehlers et al. 1993). The earliest deformation phase (D1) is usually considered to have preceded the intrusion of the 1.89-1.88 Ga granitoids (e.g. Korja & Heikkinen 2005, Ehlers et al. 1993). The timing for the D2 deformation phase that overprints and refolds the D1 structures along E-W trending fold axes is somewhat unclear, but occurred <1.87 Ga ago (Väisänen et al. 2002; <1.85 Ga according to Korja & Heikkinen 2005). During subsequent D3 and D4 phases much of the deformation was already partitioned into ductile crustal-scale shear zones throughout the Svecofennian domain (e.g. Kärki et al. 1993). In southern Finland, D3 occurred at ca. 1.82-1.83 Ga (coevally with the formation of the LSGM), during which the transpressional stress field rotated from an early N-S direction to a late NW-SE compression (e.g. Levin et al. 2005, Lindroos et al. 1996). D4 deformation phase in southwestern Finland is commonly referred to have taken place at ca. 1.80 Ga, although this is

a tentative age interpreted from the association of some shear zones with ca. 1.80 Ga postorogenic intrusions (e.g. Branigan 1987). Steep strike-slip shear zones in southern Finland are described by e.g. Väisänen & Hölttä (1999), who report N-S to NE-SW shear structures in Turku region where deformation initiated close to the brittle-ductile transition (during D4) and were later reactivated within the brittle regime, producing pseudotachylytes. Another example of a D4 shear structures in SW Finland is given by Lindroos et al (1996), who report a NNE-SSW striking ultramylonitic to ultracataclastic shear zone that cuts pegmatites they dated at 1807-1803 Ma (maximum ages).

According to Väisänen (2002), the uplift in southern Finland from mid-crustal levels to present level took place soon after the Svecofennian

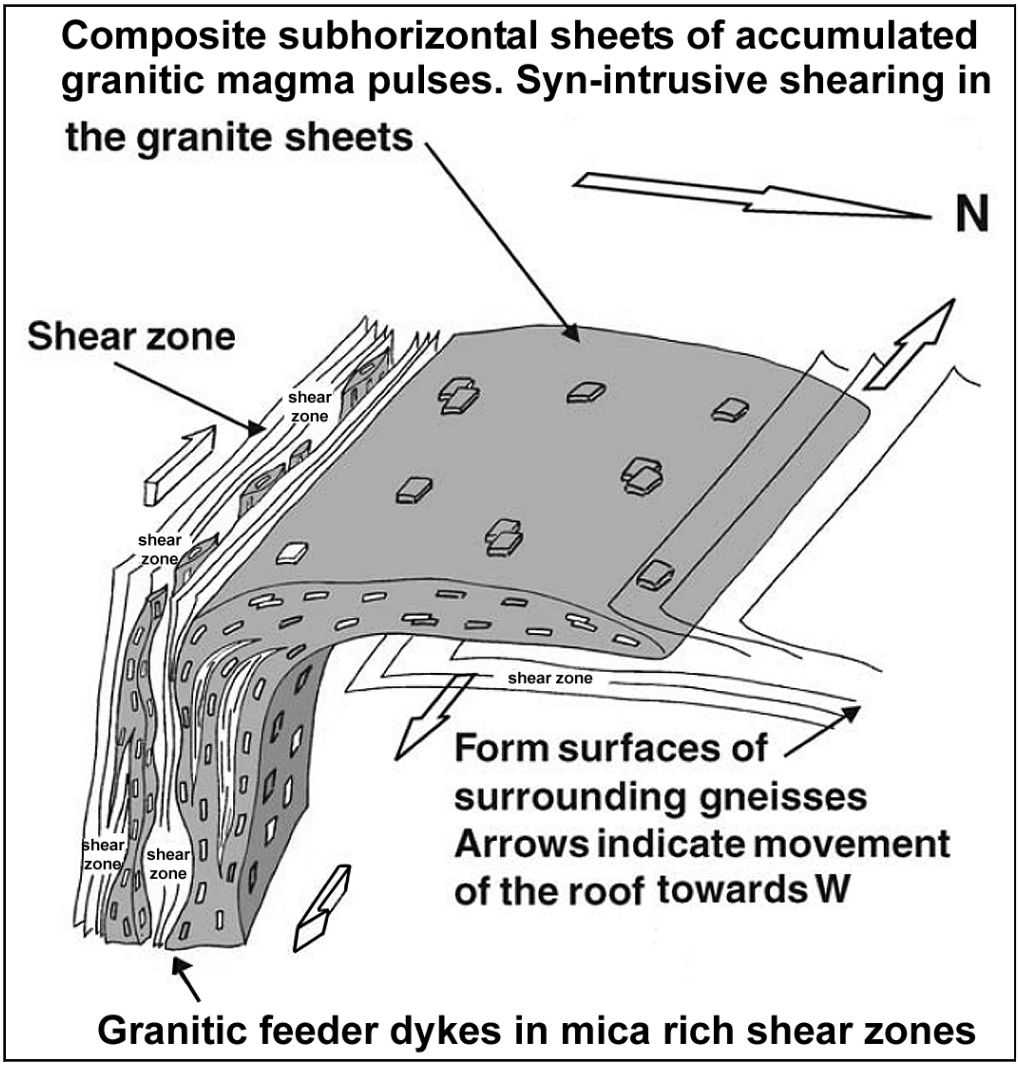

Fig. 1.5. An emplacement model for the LSGM granites by Stålfors & Ehlers (2005). The granitic melts were transported upwards long sub-vertical shear zones and subsequently emplaced as sub-horizontal metre-scale sheets.

orogeny. During the metamorphic peak in SW Finland ca. 1.83 Ga, the PT-conditions were generally around 5 kbar and 700ºC (e.g. Eklund et al. 1998), although locally PT-conditions of 6.3-6.7 kbar and 800-825ºC were obtained (Väisänen & Hölttä 1999). At 1815 Ma, the rocks of Turku area in SW Finland were still in a pressure regime of 4-5 kbar (Väisänen et al. 2000). Also Lindroos et al. (1996) note that many 1807-1803 Ma pegmatites in their study area in Kemiö, SW Finland contain sillimanite, which implies that the pegmatites were emplaced in high-T conditions. On the other hand, Welin et al. (1983) suggest that the ca. 1.79 Ga Mosshaga pluton intruded at a depth of 7 km (ca 2 kbar). If this conclusion can be considered accurate, it would indicate a rapid exhumation of the rocks from 4-5 kbar/>500ºC to 2 kbar in 15-25 million years (exhumation rate ca. 0.03-0.05 cm/a). Several authors confirm that the 1.58 Ga anorogenic rapakivi granites and associated mafic rocks were emplaced at near-surface conditions, being partly extrusive. Sederholm (1890) was the first to note the extrusive characteristics of some of the rapakivi-related rocks in Blåkobben, western Åland. Later works, e.g. Eklund et al. (1996) confirm the extrusive nature of the Blåkobben ignimbrites by textural and geochemical observations, and Shebanov and Eklund (1997) conclude that the 1.58 Ga rapakivi granites of SW Finland were emplaced under pressure conditions of 1-2 kbar.

1.3 PALAEOPROTEROZOIC SHEAR ZONES IN SWEDEN AND ESTONIA

The Palaeoproterozoic shear zones in central Sweden and Estonia are briefly described below since they display similar features to the Sottunga-Jurmo Shear Zone and may therefore have some relation to it.

1.3.1 SVECOFENNIAN SHEAR STRUCTURES IN CENTRAL SWEDEN

In Sweden, the bedrock can be divided into seven structural domains, six of which are Svecofennian, according to plate tectonic settings, dominant rock types, metamorphic features and the location of major deformation zones (fig. 1.6). Domain B is the northernmost Svecofennian domain in Sweden, consisting of Svecofennian metasedimentary and mafic volcanic rocks that are intruded by granitoids (e.g. Sjöström & Bergman 1998). Domain C is characterised by calc-alkaline granitoids, and the area is dominated by the complex Ljusdal batholith, truncated by several NW-NNW striking dextral shear zones. The domain has undergone metamorphism from amphibolite facies up to granulite (low-pressure high-temperature) conditions (Sjöström & Bergman 1998). Domain D is considered to represent a composite arc, and it makes up a major part of the Bergslagen ore district. The major rock types are very similar to those of domain C, although anatectic granites are more common, and in addition to NW-NNW striking ductile shear zones, also a set of NNE striking shear zones have been identified (Sjöström & Bergman 1998). Also, the

metamorphic grade is lower than in domain C, and indeed the tectonic boundaries of the two domains approximately coincide with metamorphic isograds. The same holds true for the boundary between domains D and E, the metamorphic grade again being higher within the supracrustal rocks of the latter (Sjöström & Bergman 1998). Domain F consists mainly of the ca. 1.80-1.70 Ga postorogenic granitoids of the TIB (Transscandinavian Igneous Belt), and domains G and H were formed during the Gothian orogeny ca. 1.75-1.55 Ga ago (Sjöström & Bergman 1998).

Especially domains C to E in fig. 1.6 are of interest for this study because they are bounded and intersected by crustal-scale, dominantly dextral, ductile shear zones with ages, tectonic characteristics and orientations similar to the western parts of the South Finland shear zone, therefore being at least apparently a part of the same shear system (see also fig. 1.1). The ductile deformation zones in domain C show ages around 1.81-1.80 Ga for the main ductile shearing, while corresponding zones in domain E are mainly 1.78-1.76 Ga old, suggesting a younging in the development of high-T deformation toward south (Sjöström & Bergman 1998 and references therein). Also, many of these zones show dextral kinematics, and most of them have been repeatedly reactivated (e.g. Högdahl 2000, Bergman & Sjöström 1994). Bergman & Sjöström (1994) also note that like in southern Finland, many of the shear structures in central and SE Sweden are dextral, transpressional with south-side up, indicating approximately N-S compression.

The ductile, dextral NW-SE striking shear zones of central Sweden are interpreted to be older than the sinistral conjugate shear zones in central Sweden that often accompany the dextral zones (Bergman & Sjöström 1994). The sinistral zones of central Sweden

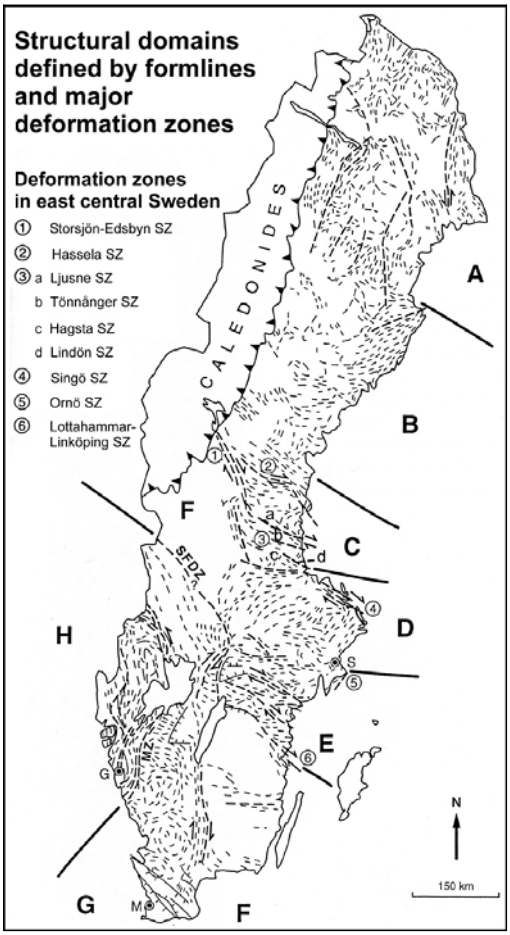

Fig. 1.6. The structural domains in Sweden according to Sjöström & Bergman (1998). Key: **A** = Archaean domain; **B** = Svecofennian supracrustals and intrusive granitoids; **C** = mainly calc-alkaline granitoids with amphibolite to granulite facies metamorphism (low-P high-T); **D** = composite island arc system with anatectic granites, mostly amphibolite facies metamorphism; **E** = supracrustal rocks, amphibolite to granulite facies metamorphism; **F** = dominantly TIB granites; **G-H** = rocks of the Gothian orogeny.

possibly developed around 1.79 Ga, indicated by a U-Pb titanite age of 1796±3 Ma from a sinistral shear zone conjugate to Hassela shear zone (Högdahl 2000). On the other hand, the high-T, dextral NW-SE striking zones of central Sweden are only marginally older: e.g. Ljusne SZ and Hagsta Gneiss zone give U-Pb titanite ages of 1789±2 Ma and 1810±2 Ma, respectively (Högdahl 2000). Later, brittle-ductile shear structures are dated at 1.80-1.76 Ga (Högdahl 2000 and references therein). As a summary, the high-T deformation zones in central Sweden (domain C) have generally formed around ca. 1.80-1.81 Ga, but some show brittle-ductile deformation around 1.80-1.76 Ga, and even later reactivation features approximately contemporaneous with ca. 1.70 Ga TIB magmatism. An interesting exception is the SEDZ, where ductile C/S mylonites still formed at ca. 1.67 Ga (Högdahl 2000). A feature not observed further eastwards is that zircons and titanites from Hassela shear zone have recorded Phanerozoic event(s) (Högdahl 2000).

Hassela shear zone shows many features similar to the western parts of the South Finland shear zone; they resemble each other structurally, geochronologically and geophysically (Högdahl 2000 and references therein). The same goes for the NW-SE striking shear zones south of the Ljusdal batholith in Bergslagen (Loftahammar-Linköping deformation zone, Åsbro-Norrköping deformation zone, Singö shear zone; fig. 1.6). It is therefore not unfeasible to suggest that the spatial and temporal coherence between the shear zones in central Sweden and SW Finland (including the SFSZ) reflect a common geological history for these shear zones.

1.3.2 SVECOFENNIAN DUCTILE SHEAR ZONES IN ESTONIA

In Estonia, several major shear structures related to the Svecofennian orogeny are recognised (fig. 1.7; Soesoo et al. 2004). The main tectonic boundary of the Estonian basement, the Paldiski-Pskov Zone (PPZ) separates the mainly granulite facies rocks SW of the PPZ and the mainly amphibolite facies rocks NE of the shear zone (Soesoo et al. 2004, All et al. 2004). The rocks to the NE of the shear zone are further divided into the Tallinn zone and the Alutaguse zone, both of which are metamorphosed in upper amphibolite facies conditions at approximately 600-700°C and 3-5 kbar (Puura et al. 2004; fig. 1.7). The Tallinn zone consists of mafic metavolcanites and metasediments, mainly in the form of amphibole gneisses, biotite-plagioclase gneisses, quartz-feldspar gneisses and mica gneisses, the rocks being extensively migmatised in many places (Soesoo et al. 2004). The Alutaguse zone is characterised by extensively migmatised Al-rich gneisses and biotite-plagioclase gneisses together with minor amphibole gneisses, amphibolites and quartz-feldspar gneisses, all of which have metamorphosed mainly in amphibolite facies conditions with some local granulite facies metamorphism (Soesoo et al. 2004). Late-orogenic microcline granites intrude both Tallinn and Alutaguse zones (All et al. 2004).

Rocks SW of the PPZ consist mainly of pyroxene- or hornblende-bearing mafic metavolcanic rocks, while metapelites and granitoid

gneisses are rare (Puura et al. 2004). The rocks are metamorphosed dominantly in granulite facies conditions (e.g. Puura et al. 2004); a study by Hölttä & Klein (1991) sets the peak PT-conditions of metamorphism for a sample from SW Estonia near a crustal-scale Middle Estonian fault zone to approximately 800°C and 6 kbar. The age of the peak metamorphism in the area is ca. 1.78 Ga (Puura et al. 2004), i.e. much later than in southern and southwestern Finland but approximately coeval with the metamorphism within domain E (Bergslagen) in Sweden.

The metavolcanic and –sedimentary rocks of northern Estonia are geochemically comparable to island arc rocks in southern Finland, whereas the granulites in SSW Estonia formed as a result of a distinct deformational event and are rather correlated with similar rocks in northern Latvia, Lithuania and Belarus (All et al. 2004, Puura et al. 2004).

The PPZ itself is a tectonic zone outlined by two crustal-scale NW-SE trending shear zones with a complex belt of granulite and upper amphibolite facies metamorphic rocks in between. The deep crustal shear zones that make up the PPZ dip toward southwest (All et al. 2004) Toward NE, there is a rapid but gradual transition from the granulites and amphibolite facies rocks of the PPZ to the mainly amphibolite facies rocks of the Alugatuse and Tallinn Zones, while the transition from the PPZ toward the SW is more obscure (All et al. 2004). Microcline granites and granite migmatite bodies that

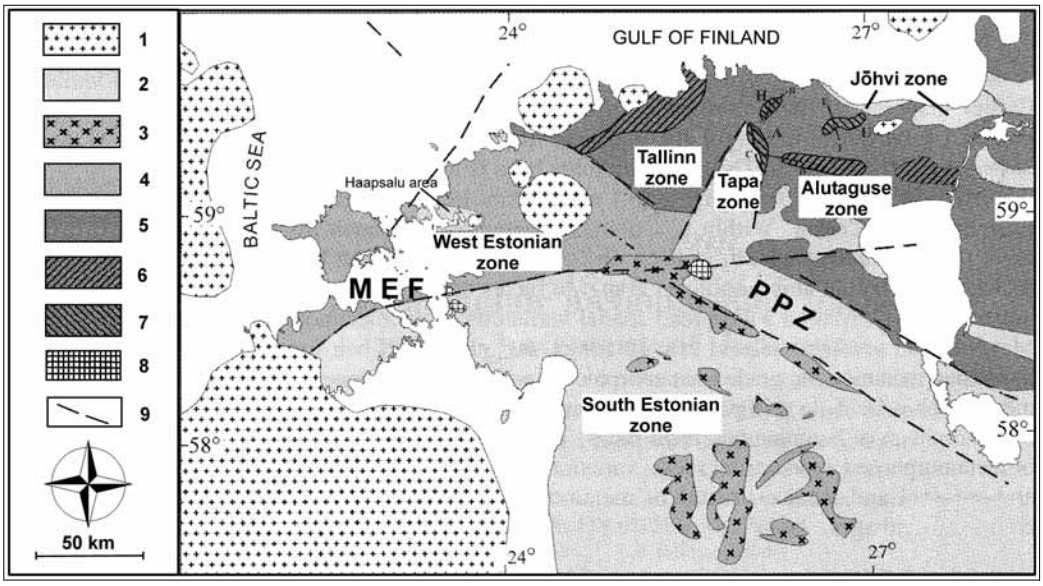

Fig. 1.7. The main features of the bedrock in Estonia (modified from Puura et al. 2004). **PPZ** = Paldiski-Pskov tectonic zone; **MEF** = Middle Estonian fault zone; **1)** anorogenic Rapakivi granites; **2)** dominantly granulite facies rocks; **3)** microcline granitoids; **4)** dominantly retrograde metamorphic facies rocks; **5)** dominantly amphibolite facies rocks; **6)** lower grade amphibolite facies rocks; **7)** higher grade amphibolite facies rocks; **8)** Taadikvere and Virtsu post-orogenic massifs; **9)** major deformation zones.

reach depths of 5-15 km and dip southwestward intrude into both the SW and the NE borders of the PPZ (All et al. 2004). The PPZ represents a deep zone of ductile deformation and has apparently not undergone brittle, cataclastic deformation, therefore interpreted to be of a late-Svecofennian origin (All et al. 2004).

The roughly W-E striking Middle Estonian fault zone MEF (also called Saaremaa tectonic zone by Soesoo et al. 2004) crosscuts the PPZ (fig. 1.7). The MEF separates the 'proper' granulite facies rocks of the South Estonian zone from the West Estonian zone which consists mainly of amphibolite facies rocks with local granulites. The structural interpretation of the MEF is that substantial uplift of the South Estonian block took place in comparison to the West Estonian block (All et al. 2004). The MEF is considered to be a post-orogenic, possibly rapakivi-related structure since it crosscuts the PPZ, displays cataclastic deformation suggestive of a near-surface deformational regime, and is intruded by post-orogenic granodiorite and quartz diorite massifs; on the other hand, both the metamorphic and intrusive rocks within the MEF have undergone intensive tectonic reworking (All et al. 2004).

The connection of the South Finland shear zone, and especially the Sottunga-Jurmo shear zone, and the ductile shear structures in Estonia remain uncertain. Soesoo et al. (2004) refer to the PPZ as Åland-Paldiski-Pskov shear zone, and Korja & Heikkinen (2005) draw an "Estonia

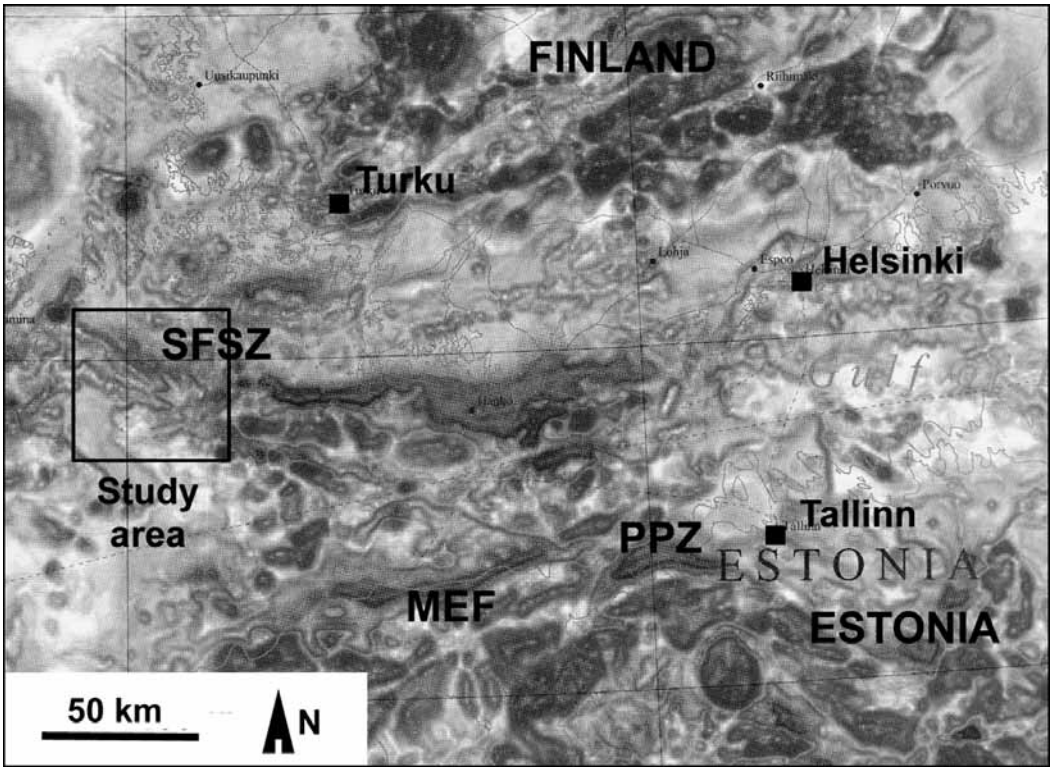

Fig. 1.8. Detail of the magnetic anomaly map of Fennoscandia (Korhonen et al. 2002).

line" from Åland to PPZ, but neither study gives any further motivation for relating the PPZ and the shear structure in Åland archipelago. However, similar structural features (both zones dip southwest, NW-SE strike) as well as the aforementioned correlation of rocks in northern Estonia and southern Finland suggest that the PPZ and the SJSZ may indeed be connected. Furthermore, the magnetic anomaly map of Fennoscandia shows a relatively continuous, linear anomaly that follows the SJSZ in Åland, continuing SE over the Baltic Sea towards and through northern Estonia (fig. 1.8; Korhonen et al. 2002). However, the rocks directly south of the SJSZ are mainly igneous granitoids metamorphosed in amphibolite facies conditions, while the rocks south of the PPZ are dominantly granulite facies mafic metavolcanites. Therefore, a simple correlation of the two structures as a single, straightforward crustal-scale strike-slip or thrust zone is likely subject to gross oversimplification.

2. SOME THEORETICAL ASPECTS OF DEFORMATION

In the following chapters, a brief summary of some of the most basic terminological aspects of deformation is given. Much of the conclusions made of the field observations within the study area are based on these basic concepts. The theoretical aspects of deformation are extensively discussed in literature, and the thorough review of the theoretical approach is considered to fall outside the scope of this study. Some important implications related to the deformation within shear zones are covered in chapter 2.2.

2.1 BASIC CONCEPTS AND TERMINOLOGY

2.1.1 STRESS

Stress (σ) is defined as the amount of force applied per an area unit. In geological systems, stress can only be defined for a limited area due to the inhomogeneous nature of the rocks and the stress fields involved (Passchier & Trouw 2005). Most rocks experience at least one stress factor at some point during their history, namely the stress due to the weight of the overlying rocks. This stress type is called the lithostatic stress, and it varies greatly, depending on the depth and the density of the overlying rocks. The lithostatic stresses are usually considered to be isotropic, in which case they also define the lithostatic pressure. The lithostatic pressure is in other words equal in all directions, and the deformation due to lithostatic pressure thus ideally leads to volume change only, without any change in the shape of the rock volume (fig. 2.1a).

Forces caused by regional, large-scale plate tectonic movements often result in stress fields that are an-isotropic, i.e. the magnitude of stress varies in different directions relative to the main direction of the force. The deformation due to such anisotropic, or deviatoric, stresses leads to changes in shape as well as to possible volume changes (fig. 2.1b).

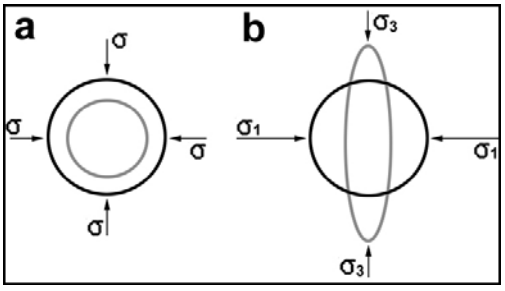

Fig. 2.1. Deformation caused by isotropic (lithostatic) and anisotropic (deviatoric) stresses. **a)** Isotropic stresses cause volume change only; **b)** anisotropic stresses cause changes in the shape of objects, with or without volume change ($\sigma_1 > \sigma_3$); see text).

Fluid pressure, i.e. the pressure of the fluids (liquid and/or gas) trapped within the intergranular spaces and as intragranular inclusions in a rock causes internal stresses in a rock. Fluid pressure is usually less than the lithostatic pressure, but in certain circumstances the fluid pressure approaches the lithostatic pressure and the rock may fracture even at great depth (Etheridge 1983). The fluid pressure as well as the amount and composition of the fluids in part affect the deformation processes and can play a significant role in determining whether the resulting deformation style is dominantly brittle or ductile, since the presence of fluids

facilitates deformation by reducing the shear strength of the rock.

All stresses can be illustrated by means of a stress ellipsoid, in which the three orthogonal symmetry axes represent the stress vectors in each direction (fig. 2.2a). The axes being vectors, the length of each is directly proportional to the principal stress value for the stress axis in question. The spatial orientation of the axes manifests the spatial orientation of the stress field. The principal stress values are usually expressed as σ_1 (largest value), σ_2 and σ_3 (smallest value). In isotropic and homogeneous stress fields, such as the lithostatic stresses, all of the three principal stress axes are of equal length ($\sigma_1 = \sigma_2 = \sigma_3$). This stress system is also called hydrostatic stress, because it corresponds to the stress state of a fluid (e.g. Park 1997). In anisotropic stress regimes, such as in e.g. areas affected by orogenic systems, $\sigma_1 \geq \sigma_2 \geq \sigma_3$. Anisotropic stresses are also called deviatoric stresses (e.g. Park 1997). If the stress field is anisotropic, it is thus possible to subdivide stress into mean stress value ($\sigma_{mean} = \sigma_1 + \sigma_2 + \sigma_3/3$), or differential stress value (usually $\sigma_{diff} = \sigma_1 - \sigma_3$, but also $\sigma_1 - \sigma_3$ or $\sigma_2 - \sigma_3$; e.g. Passchier & Trouw 2005). The stress affecting a point on a plane of a rock can be further resolved into components acting normal and parallel to the plane, i.e. the compressive component σ_n and the shear component τ (fig. 2.2b; e.g. Passchier & Trouw 2005). Determining the strain ellipsoid and resolving the regional and/or local force field into components often help in deducing the origin of many structural features observed in the field.

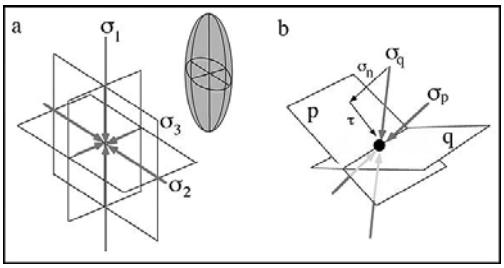

Fig. 2.2. a) The three principal stress axes and the stress ellipsoid; **b)** Illustration of the stress components. Each surface (p and q) has a different stress vector (σ_p and σ_q, respectively), and each vector (here σ_q) can be resolved into normal stress (σ_n) and shear stress (τ) components. Modified from Passchier & Trouw (2005).

The magnitude of σ_{diff} is a critical factor for rock deformation: if the σ_{diff} exceeds the yield strength of the rock, the rock will deform permanently (viscous deformation). If the failure strength of the rock is exceeded, brittle failure will occur. The compressive yield and failure strengths are higher ($\sigma_1 - \sigma_3$ positive) than the tensile yield and failure strengths ($\sigma_1 - \sigma_3$ negative) for the same rock volume; furthermore, the higher the compressive stresses (σ_n) are, the higher the shear stresses (τ) must be in order to result in failure. The yield and failure strengths of the rock depend on the lithostatic pressure, rock type, pore fluid pressure, grain size, fabric orientation etc. (e.g. Passchier & Trouw 2005). The yield strength field is small in near surface conditions, and the rocks enter the brittle failure field normally without any preceding viscous deformation, while with increasing depths (increasing temperatures and pressures), the viscous (plastic) deformation is the dominant style, and the rocks enter the brittle failure field only in very rare occasions.

2.1.2 STRAIN AND DEFORMATION

When a stress field is applied to a volume of rock, it undergoes a series of physical changes. Assuming that the rock behaves in a ductile manner, i.e. doesn't fracture, the most obvious of these physical changes are changes in shape, direction of markers and volume (distortion, rotation and dilation). Deformation is the general term usually applied for the overall changes in shape and orientation of objects in response to a stress field, while strain sensu stricto is a more restricted term that describes the change in shape only; the term deformation therefore includes both the strain as well as the rotation component (Passchier & Trouw 2005). Some authors consider the terms strain and deformation to be synonymous, but the author of this study has chosen to adopt the nomenclature suggested by Passchier & Trouw (2005). Strain rate refers to the speed, i.e. the rate of the shape change with time. Strain, and occasionally also rotation, can be observed and sometimes measured in the field. Qualitative or, in certain cases, quantitative deductions of the magnitude and direction of the (palaeo)stress field can be made based on the measurements.

Another useful concept in describing behaviour of rocks under applied stress field is that of flow. Flow differs from deformation in that it describes the movement of material in a deforming rock at a specific moment, i.e. during ongoing progressive deformation. Deformation therefore describes the overall process during which the rock volume undergoes changes by mechanism of flow from an initial to a final state (Passchier & Trouw 2005).

Similarly to stress, strain S can be expressed as an ellipsoid, where the three principal axes of the ellipsoid represent the three strain vectors ($S_1 > S_2 > S_3$). To describe the total deformation, a rotation component is added. Together these components illustrate the total deformation, i.e. the total magnitude of strain as well as the total rotation due to deformation, in relation to the reference frame. When the strain is completely non-rotational, i.e. the strain vectors are parallel to the stress axes, the deformation is said to be coaxial, or pure shear deformation. Another end-member case is when the flow is completely non-coaxial, or simple shear deformation (fig. 2.3). In nature both compressive (pure shear) and rotational (simple shear) components are almost always present, in which case the deformation is often referred to as general shear. On the other hand, the scale of observation is of essence: especially in micro- and mesoscale, partitioning into (almost) pure coaxial and non-coaxial flow can be observed.

According to the criteria, during homogeneous deformation straight and parallel lines should remain straight and parallel and any circle is deformed into an ellipse, whereas in inhomogeneous deformation lines do not remain straight and parallel and a circle is deformed into an asymmetric shape (e.g. Passchier & Trouw 2005). Deformation, as often initially observed in outcrop scale, is seldom homogeneous, and different parts of a rock therefore deform in a different style than the other parts of the same rock volume. However, it is important to realise that the homogeneity (or

lack of it) is largely dependent on the scale and the reference frame of the observation, and it is often more convenient for practical purposes to choose an observation scale within which deformation can be considered to be more or less homogeneous. On the other hand, the process of deformation partitioning often results in inhomogenities that have significant importance for the overall structural interpretation of the studied area, so it is often wise to pay some attention to

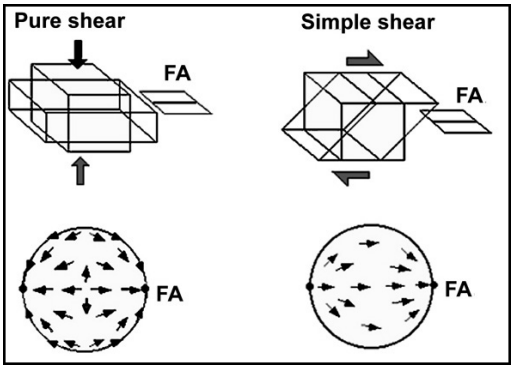

Fig. 2.3. Pure shear (coaxial) and simple shear (non-coaxial) strains are end-members cases; normally strain involves both pure shear and simple shear components. The fabric attractor (FA) is a line toward which all material lines, i.e. foliations and lineations, rotate during deformation. From Passchier & Trouw (2005).

the inhomogeneous deformation as well. Deformation partitioning refers to the localisation of strain into high strain zones that are often dominated by non-coaxial flow, while the areas between these zones often remain relatively unaffected or deform mainly by coaxial flow. This is probably in many cases due to large-scale strain softening of the rocks, which in turn is a result of differences in the rheological behaviour of the rock in different parts of a rock volume (Passchier & Trouw 2005). In the field or in thin section, deformation localisation can be observed as zones or areas with different deformation intensities and/or styles, often in the form of intensely deformed shear bands cutting through volumes of less deformed rock (or grains, in microscale). Regional shear zones are themselves a result of macro-scale deformation localisation due to extreme partitioning of flow into tabular, high strain zones required to accommodate the far-field lithospheric stresses.

2.2 DEFORMATION WITHIN SHEAR ZONES

As discussed in the previous chapter, deformation within a rock volume is seldom homogeneously distributed. Instead, the strain is localised in planar high-strain zones, i.e. shear zones, where the resulting deformation is considerably more intense than in the surrounding rocks. A shear zone thus forms when two blocks move relative to each other along such a deformation zone, the deformation within the shear zone therefore usually containing a significant rotation component of strain (fig. 2.4). Ideally, shear zones form due to a lateral-slip movement between two crustal blocks. However, the movement vectors are seldom parallel to the boundaries of a deformation zone. This will lead to oblique relative movement paths of the crustal blocks. Most shear zones are, in fact, a result of regional transpressional (or transtensional) tectonic settings, where the lateral-slip shear component is accompanied with, and sometimes dominated by, a thrusting component (or by an extensional component in case of transtension). According to the basic

model of transpressional regimes by Sanderson & Marchini (1984), a shortening component must be accommodated by an extension or stretching component, and vice versa; for example, horizontal, homogeneous constant-volume shortening must be accompanied by vertical stretching. Several adaptations of this basic model have been developed by varying the boundary conditions and the amount of volume loss during the deformation (e.g. Dewey et al. 1998; fig. 2.5). Despite all this, all the models are greatly simplified compared to natural transpressional and transtensional shear systems.

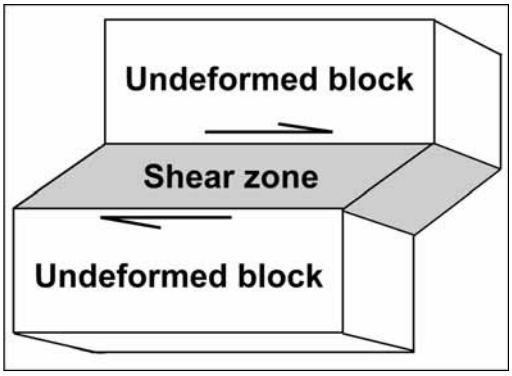

Fig. 2.4. A shear zone forms when two crustal blocks move relative to each other such that the blocks remain relatively undeformed. Shear zones can form both in subvertical or in subhorizontal positions, and the relative movement of the blocks can occur both horizontally (strike-slip movement) or vertically component (oblique-slip or thrust).

Some authors include both brittle fault zones and zones of semi-ductile to ductile flow into the definition of a shear zone (e.g. Passchier & Trouw 2005). Brittle deformation occurs at low temperatures or high strain rates, when the rock undergoes micro-fracturing, movement along the fractures and frictional grain-boundary sliding (Guermani & Pennacchioni 1998). During brittle deformation, cohesive and incohesive fault rocks such as cataclasites and pseudotachylytes form. Plastic, or ductile, deformation employs crystal-plastic processes involving dislocation glide and/or diffusive mass transfer, i.e. without fracturing on the grain scale (Passchier & Trouw 2005, Guermani & Pennacchioni 1998). Therefore, in ductile shear zones, no discrete fault planes are formed due to the nature of the deformation. Instead, there is a gradual transition between the original 'wall rock', which can be deformed or undeformed, and the shear zone. The scale of shearing can in both cases vary from microshears within individual mineral grains, to mm-to-m scale shear bands visible in an outcrop, to crustal-scale shear zones that can be hundreds of kilometres long and several kilometres wide. However, the term 'shear zone' *sensu stricto* is in the literature commonly reserved for meso-to-macro scale shear structures. Development of shear zones is of a particular significance in continental orogens, where shear zones are crucial in accommodating far-field plate tectonic stresses (e.g. Dewey et al. 1998).

The brittle deformation style is generally confined to the upper crust, while the semi-ductile to ductile behaviour becomes the dominating deformation style at depth (fig. 2.6). It is widely accepted that major brittle fault zones exposed at the surface are represented by their ductile counterparts at depth in order to be able to accommodate the total displacement of the crustal-scale rock volumes involved. The wide brittle-ductile transitional zone where both ductile and brittle mechanisms are active is

commonly considered to occur at a depth of about 10-15 km, but can vary greatly depending on factors such as bulk strain rate, geothermal gradient, grain size, fluid pressure, lithotype, orientation of the stress field and pre-existing fabrics (e.g. Passchier & Trouw 2005, Park 1997), Thus, a marble might deform ductilely at metamorphic conditions where a rheologically 'harder' rock such as sandstone would show brittle fracturing. In literature, several cases have been described where the brittle-ductile transition occurred at much higher crustal levels than 10-15 km. Wang & Ludman (2004), for example, reported ductile deformation of a metasedimentary rock in metamorphic conditions of the lower greenschist facies, within a temperature-pressure regime of 300-350ºC and 2-2.5 kbar, i.e. within a relatively shallow crustal environment. Another implication of the strong dependency of deformation behaviour on the rheology of the rock is that even small variations in the rheological properties of a superficially homogeneous rock volume can lead to contemporaneous brittle and ductile deformation of the rock, especially if the rock is within the brittle-ductile transition zone within the crust at the time of the deformation (Guermani & Pennacchioni 1998). For example, Pennacchioni & Cesare (1997) showed that ductile and brittle-ductile mylonites in their study area formed coevally due to varying water content within the rock during deformation.

Ductile deformation leads to formation of gneisses that can display any chemical composition from ultrabasic rocks to silica-saturated gneisses (e.g. Passchier & Trouw 2005). Due to the dominant deformation mechanisms in relatively high temperatures, such gneisses commonly show effects of static recrystallisation, i.e. coarsening of grain size, straightening of grain boundaries, and polygonisation (e.g. Evans et al. 2001, Kruhl 2001). These processes that result in a reduction of the internal free energy of individual grains are together called 'grain boundary area reduction' or GBAR by Passchier & Trouw (2005). Due to GBAR processes, ductile 'striped' gneisses are often medium- to coarse grained, granoblastic and do not necessarily display a strong (stretching) lineation. A mylonite is here defined as a foliated and usually lineated rock formed as a result of strong, dominantly ductile deformation, commonly containing por-

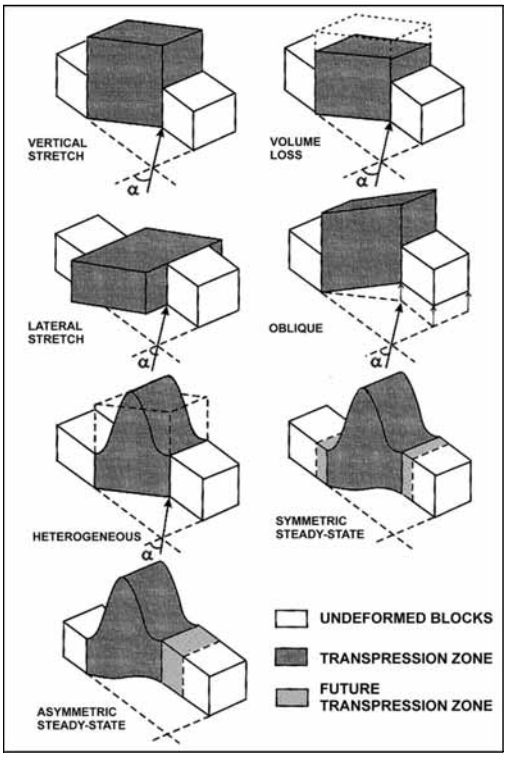

Fig. 2.5. Some examples of transpressional strain models. From Dewey et al. (1998).

phyroclasts and fabric elements with monoclinic shape symmetry (according to Passchier & Trouw 2005). The transition from striped gneisses to mylonitic texture is subtle; in fact, some authors use the term mylonite in a looser, relative sense in order to describe the textural difference between a high strain zone and the wall rock. The mylonitic rock can in this case be medium or even coarse grained, lacking a distinct porphyroclastic/monoclinic texture, but nevertheless displays stronger deformation compared to the wall rocks. In this thesis, the term mylonite is reserved for foliated rocks showing distinct porphyroclasts and fabric elements with monoclinic shape symmetry. A distinction is made between protomylonites, with relatively little (10-50%) fine-grained matrix material, 'normal' mylonites with ca. 50-90% matrix, and ultramylonites with a significant amount (> ca. 90%) of matrix.

Brittle deformation may play a role in some mylonitic rocks, commonly in isolated lenses or grains, but according to the modern definition of a mylonite, the stress-supporting network is always affected by crystal-plastic deformation mechanisms (e.g. Tullis et al. 1982). Again, there seems to be a gradual transition from mainly ductile (mylonitic) deformation to brittle fracturing. Rocks showing brittle deformation can be divided into incohesive (clast-supported) rocks such as fault gouge, and cohesive (matrix-supported) rocks such as

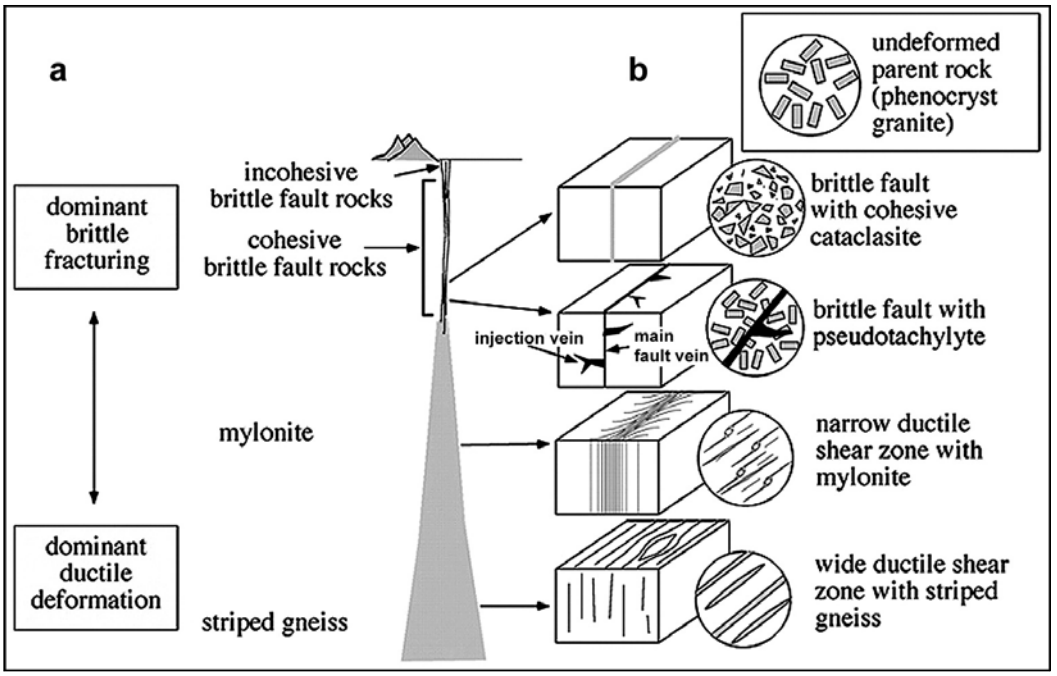

Fig. 2.6. Generalised illustration of the distribution of the fault rocks within the crust. No vertical scale is given since the brittle-ductile transition depends on factors such as rock composition, geothermal gradient and bulk strain rate (see text). **a)** In a crustal-scale deformation zone, the zone often widens downwards as the deformation style becomes increasingly ductile; **b)** a schematic presentation (not in scale) of different fault rock types and the local geometry of the shear zone in a ca. 1-m-wide block. From Passchier & Trouw (2005).

cohesive breccia and pseudotachylyte. In the area of this study, pseudotachylytes have been found in two locations (chapter 4). Pseudotachylytes are cohesive, glassy or very fine-grained fault rocks that form by frictional melting of dry protoliths as a result of very high slip rates. Pseudotachylytes are most likely to form in seismically active zones during earthquake faulting (e.g. McNulty 1995, Grocott 1981). The very high slip rates (ca. 0.1-1.0 m/s in dry rocks) due to the release of stored elastic strain energy, results in frictional melting of the wall rock (e.g. Spray 1995, Sibson 1973). Apart from earthquakes, pseudotachylytes may also form as a result of meteorite impacts, crater or caldera collapse and giant land slides (e.g. Spray et al. 1995). When associated with fossil earthquakes, the presence of pseudotachylytes is often considered to signify exhumation of rocks from the temperature/strain rate – dependent crystal-plastic deformation regime into a semi-brittle, 'transitional' deformation field with temperatures between ca. 450ºC and 300ºC, or depths of 10 to 15 km (in quartzofeldspatic rocks; McNulty 1995). The semi-brittle – ductile transition coincides approximately with the cessation of feldspar plasticity and the transition from amphibolite to greenschist facies metamorphosis. At higher levels of the crust, i.e. in the brittle (or 'seismogenic' regime), the deformation of quartzofeldspatic rocks is marked by cataclastic mechanisms and absence of quartz plasticity (McNulty 1995). Depending on strain rate, fluid pressure, operative slip system(s) and grain size, pseudotachylytes can form within both semi-brittle and brittle regimes. However, it is suggested that glassy pseudotachylytes dominate at depths above ca. 5 km, while at greater depths very fine-grained pseudotachylyte matrix is formed instead (Allen 1979).

Pseudotachylytes are from millimeters up to several centimetres thick planar structures with or without melts. When melt is present, it commonly shows inclusions of mineral or wall rock fragments (e.g. Magloughlin & Spray 1992). Pseudotachylyte melts form along planar generation surfaces (also called main fault veins) that accommodate the bulk of the slip. Generation surfaces in some cases occur as subparallel sets ('paired shears'; Grocott 1981) separated by segments of largely undeformed wall rock. Much of the melt enters the so-called injection veins, which are irregular, up to few mm or cm thick melt pockets, branching from the generation surface into the wall rock (Magloughlin & Spray 1992). The estimated melt temperatures of most pseudotachylytes vary considerably (between ca. 750-1600ºC) because they are not equilibrium melts, and the temperature of the melt is thus considered to be less dependent on the rock composition than it is on the bulk strain rate (e.g. DiToro & Pennacchioni 2004, O'Hara 2001, Lin & Shimamoto 1998).

Once a zone of weakness in form of a shear zone is established, it is commonly repeatedly activated during subsequent tectonic events. Thus, a dominantly ductile deformation can be observed to have been overprinted and/or followed by semi-ductile and, later, dominantly brittle phases (e.g. chapter 4 in this thesis). Reactivation of crustal-scale shear zones seems to

be a common phenomenon, often related to uplift and exhumation or extensional collapse of the crust during and after orogenic events (e.g. Culshaw et al. 2006, Bigi 2006, Ganne et al. 2005). However, superposition of brittle fault rocks by plastic deformation has also been recorded (Guermani & Pennacchioni 1998), although ductile overprinting can be difficult to recognise if the ductile deformation is strong. Overprinting of brittle structures by plastic deformation can occur especially within or close to the brittle-ductile transition zone in the crust if the temperature, confining pressure and water content are increased, e.g. due to (re)burial of rocks, or if the strain rate is decreased. Brittle faulting can in fact be essential for nucleating plastic shear zones in rheologically strong materials (Guermani & Pennacchioni 1998 and references therein).

3. ANALYTICAL METHODS

In the following chapters, a short description is presented of the theory and praxis of the analytical methods applied on the rocks within the area of this Ph.D. study. Furthermore, the reasons for choosing the particular method utilised during the study are explained. The most significant uncertainties and limitations of each method are also briefly reviewed. The results and interpretations of the analysis are described and discussed separately in chapter 4.

3.1 GEOTHERMOBAROMETRY

3.1.1 SOME THEORETICAL ASPECTS

When a rock is subjected to changing geological conditions, it experiences a series of chemical and physical reactions that leads to recrystallisation and/or formation of new crystals in response to the new conditions. The geological conditions mentioned above commonly refer to pressure (P) and temperature (T), or PT-conditions of metamorphism. However, other factors have significant influence on how the metamorphism is reflected in the rock, the most important of which being the original mineral composition of the rock, fluid pressure, and the addition or removal of fluids from the rock volume during the metamorphic event. Indeed, fluids facilitate metamorphic recrystallisation processes (e.g. Passchier & Trouw 2005, Spear 1995).

Metamorphism is commonly considered to be an isochemical process, i.e. the chemical composition of the rock volume does not change significantly during metamorphism, except for removal or addition of volatiles such as H_2O (e.g. Yardley 1996). If chemical changes occur, often aided by circulation of hot solutions through the rock, the process is usually referred to as metasomatism (Yardley 1996). Metamorphism takes place essentially in the solid state, but there is a gradual transition from solid-state metamorphism to complete melting of the rock (e.g. Yardley 1996). The corresponding transition in the low-PT conditions, i.e. from diagenesis to metamorphism, is also very subtle. The range of possible PT-conditions commonly included within the concept of metamorphism cover temperatures from ca. 200ºC to up to 1200ºC, the latter being the approximate melting temperature of dry basalts in middle to lower crustal pressures, and pressures from ca. 4 kbar to pressures in the order of 18 kbar in some orogenic zones (Spear 1995).

Minerals (or, rather, phases since also e.g. fluids can partake the reactions) in a rock ideally exist in a state of equilibrium, so that the chemical composition of the phases in the rock corresponds to the prevailing geological conditions such that they have the lowest possible free energy. In other words, two separate rock volumes with the same bulk composition in the same PT-conditions should have the same modal mineralogy and mineral compositions (Spear 1995). Based on the original concept of the metamorphic facies by Eskola (1915), Turner (1981) defined metamorphic facies as a ‘set of metamorphic mineral assemblages, repeatedly associated in space and time, such that there is a constant and therefore predictable relation between mineral composition and chemical

composition'. It is therefore possible to correlate the mineral chemistry of certain mineral assemblages to the PT-conditions within which the assemblage was formed, assuming that it can be argued that the minerals indeed existed in chemical equilibrium at the time of their formation or recrystallisation. Some aspects of phase relations that are important for understanding basic chemical equilibria, as well as some general concepts essential for the geothermometric calculations utilised within this study are described below.

3.1.1.1 Phase equilibrium reactions – some basic concepts

The activity (a) of a component in a phase (e.g. a mineral) can be approached as the amount of the component in a phase, e.g. the anorthite component in a plagioclase. Activity, however, is a somewhat wider concept that has influence on how the chemistry of a mineral changes in different metamorphic conditions. The activity of a component is dependent on the chemical potential of the components, as well as the prevailing temperature and the universal gas constant R (Spear 1995). Thus, the activity of a component amounts to the thermodynamically effective concentration of the component in the solution (Yardley 1996). The activity of a pure phase, e.g. pure H_2O, is $a_{H2O} = 1$, while the activity of H_2O in a solution containing H_2O and e.g. CO_2 is $a_{H2O} < 1$.

When a rock experiences metamorphism, the concentration and, therefore, the activity of a component within a mineral changes. This happens through exchange and mixing of components, commonly cations, between and within different phases in the rock. These reactions are commonly described with exchange vectors (also called substitution vectors), which express the direction and magnitude of the exchange reaction in Cartesian space (Spear 1995). Numerically expressed, the exchange vector is obtained by subtracting one mineral formula from another, and it directly describes the exchange of cations. For example, the exchange vector between orthoclase and albite components in alkali feldspar is

$$KAlSi_3O_8 \text{ (ort)} – NaAlSi_3O_8 \text{ (alb)} = K – Na$$

The resulting chemical difference, in this case K – Na between orthoclase and albite is commonly written KNa_{-1} , which simply means that if one potassium cation is added to a crystal, one sodium cation must be removed, and vice versa (Spear 1995).

By substitution reactions, the phases in a rock strive for a state of chemical equilibrium in the prevailing conditions. Phase equilibria can exist either among one phase only (homogeneous equilibria), or between two or several phases (heterogeneous equilibria). In order for a system with several phases to reach an equilibrium, certain conditions need to be met: the temperature and the pressure affecting each phase must be the same, and the free energy (Gibbs free energy) of the system must be at a minimum (Spear 1995).

Homogeneous reactions can occur by several mechanisms. In some minerals, cations mix homogeneously over individual crystallographic sites in crystals, in which case

the activity (a) of a component is simply the mole fraction (X) of a cation in a mineral (Spear 1995). For example, alkali feldspars are solid solutions of $NaAlSi_3O8$ (albite, ab) and $KalSi_3O_8$ (orthoclase, or), and the activities of the components ab and or are

$a_{ab} = X_{Na}$ and $a_{or} = X_K$;

where

$X_{Na} = Na/(Na+K)$ and

$X_K = K/(Na+K)$.

On the other hand, garnet has three 8-coordinated (distorted-cubic) sites over which the mixing of the cations can occur (general formula of garnet $(Mg,Fe,Mn,Ca)_3Al_2Si_3O_{12}$; Spear 1995). Therefore, the activities of the components pyrope (prp), almandine (alm), spessartine (sps) and grossular (grs) are, ideally,

$a_{prp} = X_{Mg}^3$, $A_{alm} = X_{Fe}^3$,

$A_{sps} = X_{Mn}^3$, and $a_{grs} = X_{Ca}^3$;

where

$X_{Mg} = Mg/(Mg+Fe+Mn+Ca)$,

$X_{Fe} = Fe/(Mg+Fe+Mn+Ca)$, etc.

However, the mixing of cations sometimes occurs on more than one crystallographic site. Garnet, for example, can also substitute cations (commonly Fe) in the 6-coordinated octahedral site in the crystal lattice that usually holds Al, in which case the formula for garnet is written:

$(Mg,Fe,Mn,Ca)_3(Al,Fe^{3+})_2Si_3O_{12}$

(Spear 1995). Accordingly, the activities of the different components are expressed as

$a_{prp} = (X_{Mg})^3(X_{Al})^2$,

$a_{grs} = (X_{Ca})^3(X_{Al})^2$,

$a_{alm} = (X_{Fe})^3(X_{Al})^2$, and

$a_{adr} = (X_{Ca})^3(X_{Fe3+})^2$

(adr = andradite $Ca_3Fe^{3+}{}_2Si_3O_{12}$)

According to Spear (1995), in the majority of garnets the cation exchange reactions occur between the four end-members pyrope, spessartine, almandine and grossular, where all the substitutions among the end-members take place in the 8-fold site, while two-site mixing (andradite) can be found in Ca-rich environments.

The activity models above assume that the cations substitute each other randomly on all sites. In some minerals, however, the exchange reactions are coupled in order to maintain local charge balance (Spear 1995). Examples of coupled substitution include the tschermak's substitution (MgSi – AlAl); the plagioclase substitution (NaSi – CaAl); and the edenite substitution (□Si – NaAl, where □ signifies an empty crystallographic site; Spear 1995). For example, in the tschermak's substitution, the substitution of Al^{3+} for Mg^{2+} creates a local charge excess of +1, which is compensated by an additional substitution reaction of an Al^{3+} atom for a Si^{4+} atom (Spear 1995).

The activity models described above are ideal and do not take into account the changes in enthalpy (H) and volume (V), i.e. it is assumed that $\Delta H_{mixing} = 0$ and $\Delta V_{mixing} = 0$ (Spear 1995). In many crystalline (solid) solutions, however, the ideal models do not describe the activity-composition relations for the phase with sufficient accuracy. Plagioclase and garnet, for example, are non-ideal solutions, and corrections ('calibrations') to the activity-composition

relations need to be made (Spear 1995). The reproduction of the mathematical expressions for the several suggested corrections is not considered to be necessary for the purposes of this study. The calibrations used for the individual geothermobarometric calculations within this study are briefly discussed in the following chapter (3.2.2).

Heterogeneous phase relations are even more complicated than homogeneous phase relations since the reactions occur among two or several different phases in a rock. Heterogeneous phase relations are often expressed and studied with petrogenetic grids, which outline the P-T-X stability fields of mineral assemblages and the reactions relating those assemblages (Spear 1995). In other words, for each bulk rock composition, it is theoretically possible to construct a petrogenetic grid that describes the mineral reactions that take place in changing PT-conditions. Apart from petrogenetic grids, tertiary AKF, AKM and AFM phase diagrams are useful when visualizing changes in mineralogy in different PT-conditions and chemical systems. Pelitic rocks constitute the most extensively studied metamorphic system, and petrogenetic grids have been produced for various bulk compositions of metapelites, commonly CKNASH, KFMASH, and their subsystems (Spear 1995). Also metamorphic reactions in intermediate to mafic rocks have been relatively well established; indeed, the original concept of metamorphic facies by Eskola (1915) is based on a study of basic rocks. However, basalts are chemically more complex than pelites, and consist of relatively few minerals that in some cases (especially amphibole) display a wide range of compositions (Spear 1995). Calc-silicate rocks make a third important group whose metamorphism has been studied rather extensively, starting with Bowen (1940).

3.1.1.2 Basic concepts of geothermobarometric calculations

Calculation of the temperature and pressure of equilibration on the basis of mineral chemistry is referred to as geothermometry and geobarometry, respectively, or collectively as geothermobarometry. The most useful pressure indicators are, obviously, those mineral reactions that take place at nearly the same pressure over a wide range of temperatures, while the opposite holds true for temperature indicators (e.g. Yardley 1996). Expressed using the terms of thermodynamics, the Gibbs free energy of a mineral or a mineral assemblage varies with changing pressure, depending on the molar volume (V) of the mineral. On the other hand, the variation of Gibbs free energy with temperature is dependent on entropy (S) and enthalpy (H). Therefore, reactions with a large ΔS and ΔH but a small ΔV are the most useful geothermometers, while reactions with a large ΔV and small ΔS and ΔH make the best geobarometers (e.g. Yardley 1996, Spear 1995). Some reaction types consistently show either of these tendencies. Especially cation exchange reactions typically show very small changes in molar volumes, while e.g. net transfer reactions usually have a relatively large ΔV. However, most reactions that are sensitive to pressure are also somewhat dependent on

temperature, which means that there are more good geothermometers than there are good geobarometers (Yardley 1996).

Cation exchange reactions are heterogeneous reactions that can be written to show only the exchange components. For example, the popular garnet-biotite Fe-Mg exchange thermometer is based on the reaction

$Fe_3Al_2Si_3O_{12} + KMg_3AlSi_3O_{10}(OH)_2 = Mg_3Al_2Si_3O_{12} + KFe_3AlSi_3O_{10}(OH)_2$

(almandine + phlogopite = pyrope + annite)

which by subtracting like components reduces to

$FeMg_{-1}^{Grt} = FeMg_{-1}^{Bt}$.

This simply means that for each Fe cation that is removed from biotite and added to garnet, a Mg cation must be removed from garnet and added to biotite, and vice versa. Examples of other exchange thermometers include the garnet-cordierite thermometer, the biotite-tourmaline thermometer (both Fe-Mg exchange thermometers), and the garnet-ilmenite thermometer (Fe-Mn exchange thermometer; Spear 1995). Besides cation exchange thermometers, solvus thermometers are widely used. Solvus geothermometers are based on the distribution of an element between immiscible phases, for example the distribution of Ca and Mg between coexisting clinopyroxene and orthopyroxene (the so-called two-pyroxene geothermometer; e.g. Spear 1995).

Net transfer reactions refer to reactions that cause production and consumption of phases, which results in large $\Delta V_{reaction}$ (Spear 1995). Many net transfer equilibria can be at least theoretically used as a geobarometer, but the most widely used net transfer reaction is probably the so-called GASP reaction (garnet-aluminosilicate-silica-plagioclase)

$3CaAl_2Si_2O_8 = Ca_3Al_2Si_3O_{12} + 2Al_2SiO_5 + SiO_2$

(anorthite = grossular + kyanite + quartz)

which describes the upper pressure stability of anorthite. The active components in this reaction are plagioclase and garnet because quartz and aluminosilicate can be considered to be very nearly pure phases and their activities, therefore, are 1 (Spear 1995). The GASP geobarometer is generally suitable for a wide variety of rock types (Spear 1995). For the reasons described in chapter 3.2.2, the GASP geobarometer could not, however, be employed for the rocks within the study area. Instead, the newly calibrated GBPQ (garnet-biotite-plagioclase-quartz) geobarometer which is based on a similar net transfer reaction to GASP was utilised (Wu et al. 2004).

In order to be able to perform geothermobarometric calculations, it is necessary to involve the concepts of equilibrium constant (K or K_{eq}) and distribution coefficient (K_D). The mathematical derivation of the equilibrium constant and the distribution coefficient can be considered to be basic thermodynamics and is thoroughly described in literature (e.g. Spear 1995). The reproduction of the derivations here is not considered to be a priority, and only a brief summary is presented below. In short, the K_{eq} is an expression of the ratios of the activities of the phases involved

in an equilibrium reaction, and is directly dependent on the pressure and temperature conditions of the reaction. K_{eq} is therefore essential in calculation the phase equilibria (e.g. Spear 1995). Taking a simple example, for a homogeneous reaction

$$xA + yB = zC + wD,$$

the K_{eq} is:

$$K_{eq} = (a_C^z * a_D^w) / (a_A^x * a_B^y) .$$

The K_{eq} and the pressure and temperature of the equilibrium reaction are related through the Gibbs free energy (G):

$$G = U + PV - TS,$$

where U = the internal energy of the phase. This is related to the equilibrium constant through the equation for the change in the Gibbs free energy according to

$$\Delta G = -RT\ln K_{eq} ,$$

where R = the universal gas constant.

The distribution coefficient K_D, on the other hand, describes the partitioning of elements between phases. For example, the K_D for the Fe-Mg exchange reaction between garnet (Grt) and biotite (Bt) is

$$K_D = (X_{Mg}^{Grt} * X_{Fe}^{Bt}) / (X_{Fe}^{Grt} * X_{Mg}^{Bt}) = (Mg/Fe)^{Grt} / (Mg/Fe)^{Bt} .$$

The basic principle of performing geothermobarometric calculations is relatively straightforward. The values of the variables ΔH, ΔS, ΔV for many mineral reactions have been determined experimentally or are known from thermodynamic tables (Spear 1995). The equilibrium constant is calculated based on the compositions of minerals coexisting in equilibrium, measured by e.g. a electron microprobe. The result plots as a line on a PT-diagram, which means that the sample must have equilibrated at some PT-conditions along this line (e.g. Spear 1995). Consequently, if two such lines can be determined, the intersection of those lines gives the PT-conditions of equilibration for the mineral assemblage. For example, the garnet-biotite Mg-Fe exchange thermometer ideally plots as steep lines, their position depending on the distribution coefficient (fig. 3.1a). If another line from e.g. a GASP geobarometer (fig. 3.1b) can be added to the same plot, the exact PT-conditions for the equilibration of the system is obtained. In practice, however, the calculations are complicated by the non-ideality of several common solutions; for example, the Ca-Mg solid solutions (e.g. garnet) as well as plagioclase solutions are nonideal, so corrections to the activity-component relations are required (Spear 1995). There are several such activity models for different phases presented in literature, often together with a new calibration for the thermometer or barometer in question, and the reproduction of even the most common ones is outside the scope of this study. In chapter 3.2.2, however, the activity models and calibrations chosen for the geothermometers and geobarometers utilised within this study are briefly presented.

3.2.1.3 Role of fluids in metamorphism

When analysing phase relations in metamorphic rocks, the presence of an aqueous phase must usually be considered - fluid pressure directly

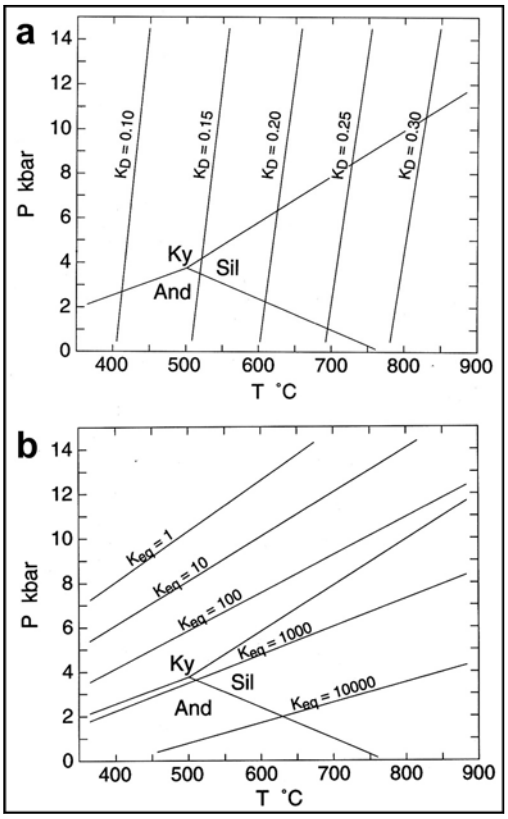

Fig. 3.1. a) P-T diagram with lines of constant K_D for the garnet-biotite thermometer. **b)** P-T diagram with values of K_{eq} for the GASP geobarometer. From Spear (1993).

affects the deformation mechanisms acting within the rock volume; both crystalline and pore fluids partake in many metamorphic reactions; and fluid pressure influences the temperature where both dehydration and melting reactions occur. In addition, large amounts of circulating fluids can change the bulk rock geochemistry or the redox state of the rock, and very large volumes of fluid can transport heat in the crust (Spear 1995). Pure H_2O is usually assumed to be present in the rock during metamorphism, while in reality the presence or quality of fluids cannot often be exhaustively confirmed (Spear 1995). In contrast to metapelites and metabasites where the bulk of the fluid usually consists of H_2O, calc-silicate rocks typically produce CO_2 as well as H_2O. The analysis of the phase equilibria in calc-silicates therefore requires that the presence of CO_2-H_2O fluids be taken into account (Spear 1995).

Due to the strong solvent properties of H_2O under crustal PT-conditions, metamorphic fluids seldom consist of pure H_2O or CO_2-H_2O, but often also contain other components such as CH_4, SO_2, N_2, H_2, H_2SiO_4 and H_2S as well as various salts such as NaCl, KCl and $CaCl_2$ (Bodnar 2003, Diamond 2003). For example, SiO_2 is soluble in H_2O in elevated temperature-pressure conditions, making dissolution of quartz possible far below the melt point of the mineral (e.g. Spear 1995). Since most metamorphic (prograde) reactions are devolatilisation reactions, fluids in most cases escape from the rock during metamorphism, a process that enables reprecipitation of quartz into veins a distance away from the source rock; quartz veins are indeed very common in all types of metamorphic rocks. The escape of metamorphic fluids is focused into channels such as rock fractures, and on a larger scale, into faults and shear zones (e.g. Spear 1995).

3.1.1.4 The importance of petrography in geothermobarometry

All geothermometers and geobarometers are based on the assumption that the studied phases (re)crystallised in a chemical equilibrium with each other in the prevailing pressure and temperature conditions. However, this condition is not always met

in the entire sample or parts of it, due to e.g. incomplete reactions between minerals or the preservation of porphyroclasts of previously formed minerals in the rock (Yardley 1996). Therefore, it is critical to make sure that the minerals used for geothermobarometric calculations have at least with some degree of certainty been equilibrated. This is best done by a meticulous microscopy of each sample. Microtextures give invaluable evidence of equilibrium, or lack of it, consequently also helping in choosing appropriate points for microprobe analysis. Microscopy should therefore always constitute an integral part of any geothermobarometric study. Zoning and other textures important for geothermobarometry are well described in e.g. Yardley (1996) and Spear (1995), and a brief summary is given below.

Many metamorphic equilibrium reactions are continuous and, therefore, by definition incomplete. Incomplete reactions resulting from disequilibrium, however, produce so-called disequilibrium textures, many of which can be studied in thin section with a polarizing transmitted-light microscope (Yardley 1996). Chemical zoning of minerals is probably one of the most common of these and can form by various mechanisms. When a solid solution mineral such as plagioclase grows, the core of the mineral usually cannot equilibrate with the surrounding rock as it is shielded by later growth zones. The core of the grain is, therefore, in disequilibrium with the surrounding minerals that formed later during (re)crystallisation of the rock. This type of zoning is called growth zoning and in metamorphic rocks typically occurs during progressive metamorphism (porphyroblasts; fig. 3.2a; Yardley 1996). On the other hand, a pre-existing mineral grain can recrystallise in equilibrium with its surroundings such that the chemical reactions only affect the grain rims (no grain growth), leaving the core of the crystal in disequilibrium with the surrounding minerals. In metamorphic rocks, this type of zoning often develops during retrograde reactions and is referred to as retrograde zoning (fig. 3.2b; Yardley 1996). As a third example, if the reactions within the rock volume involve an exchange reaction only, i.e. without any net transfer reactions, the equilibrium reaction may only occur at the contact between the minerals involved in the reaction (e.g. between biotite and garnet), leaving the rest of the involved mineral grains in disequilibrium with its surroundings (fig. 3.3c). This type of localised zoning requires that the diffusion of the elements within the rock volume is very limited. In some minerals (e.g. plagioclase, hornblende) the chemical differences between zones, regardless of the way they formed, is often accompanied by colour differences, readily observable under the microscope, while in other minerals (e.g garnet) the zones can only be distinguished by chemical analysis of a series of points across the grain (Yardley 1996).

Selecting the points for analysis should also be done carefully, bearing the implications of the petrographic observations in mind. Depending on the scope of the study, the cores of the grains within the sample can be analysed, in which case it should be established that the cores of the various grains can be assumed to have existed in equilibrium with each other at the time of their formation (fig. 3.3). On the other hand, if grain

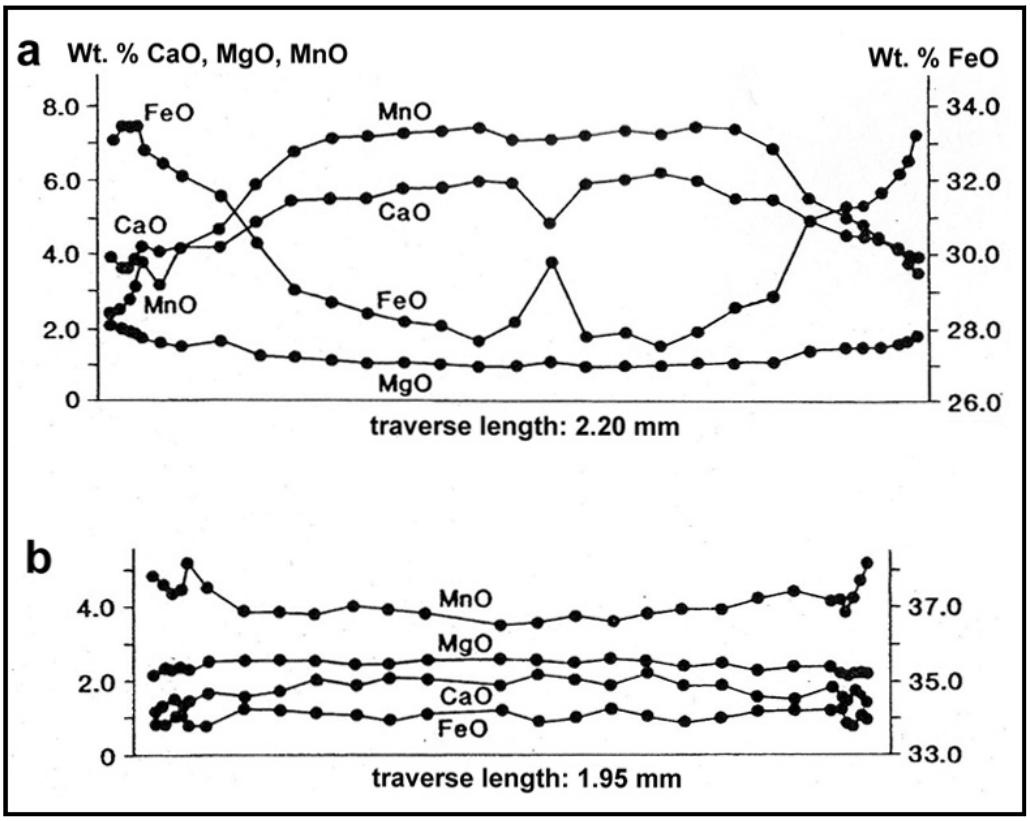

Fig. 3.2. The variation of composition across typical metamorphic garnets (from Yardley 1996). Spots represent individual analysis points. **a)** Typical lower amphibolite facies garnet from a pelitic schist, with a 'bell-shaped' profile where the core is enriched in Mn and Ca, while the rim is enriched in Fe and Mg. The anomalous points in the core occur at the edge of an inclusion. **b)** A typical profile for a high-grade garnet. Diffusion has destroyed any primary zoning, the fluctuations at the edges being a result of retrograde effects, i.e. due to limited diffusion at the crystal edge during cooling.

rims are analysed, the contact zone of two minerals that reacted with each other may be preferable since the diffusion of elements was most effective there, although as mentioned above, the reaction type(s) also has influence on the selection of the analysis points. Especially when net transfer reactions have been operating in the system, caution should be exercised since a straightforward analysis of core compositions of individual rains can give altogether wrong and misleading results (points G_1 and B_3 in fig. 3.3f; Spear 1995).

In summary, mineral reactions are very complicated, but the recognition of them is nevertheless critical in order to be able to produce high-quality geothermobarometric results.

3.1.2 GEOTHERMOBAROMETERS APPLIED IN THE STUDY

The rocks within the study area are not strictly pelitic in composition (chapter 4.4). However, the system CKNASH represents the bulk

composition of quartzo-feldspathic gneisses relatively well, and can be thus considered as a subset of pelitic bulk compositions (Spear 1995). The geothermometric methods employed for the purposes of this study are equally suitable for pelitic as well as other rock types, while the GPBQ method described below requires a pelitic bulk composition.

Within this study, two exchange geothermometers and a net transfer geobarometer were utilised. Due to the geochemical and, hence, the mineralogical composition of the rocks, the number of geothermobarometers that could be applied was rather small. Al_2SiO_5 polymorphs, for example, are completely absent throughout the area, and the popular GASP-geobarometre could consequently not be employed. The recently calibrated garnet-biotite-plagioclase-quartz geo-barometer (GBPQ) by Wu et.al. (2004) could be applied with some certainty, but due to the rarity of garnet-bearing rocks the number of suitable samples was small. The garnet-biotite Fe-Mg exchange geothermometer was combined with the GBPQ geobarometer. An attempt to determine the temperature conditions of the mylonitic deformation in comparison to that of the gneissose deformation with the

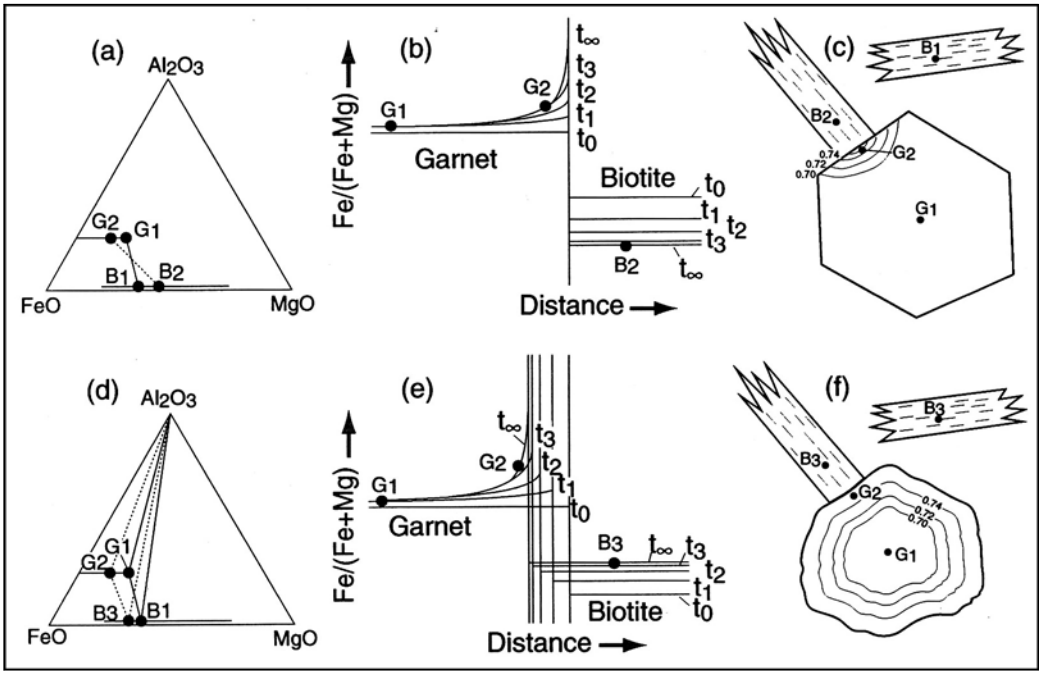

Fig. 3.3. A schematic presentation of evolution of garnet and biotite compositions trough Fe-Mg exchange reaction only between garnet and biotite (top row: a-c), versus compositional changes when both Fe-Mg exchange reaction and net transfer reaction are involved (bottom row: d-f). Solid lines in the AFM diagrams (**a** and **d**) show peak metamorphic compositions, the dotted lines sow conditions due to retrogression. **b** and **e** are schematic zoning profiles from garnet into biotite and the evolution of the garnet and biotite compositions with time: T_0 is the metamorphic peak, t_1-t_3 represent progressively later times, t_∞ is the final zoning profile. In b (exchange reactions only) garnet is not consumed, and Fe/Mg in biotite *decreases* with retrogression, whereas in e (exchange and net transfer reactions) the garnet is consumed and Fe/Mg in biotite *increases*. In **c** and **f**, possible analytical points are marked. From Spear (1993).

amphibole-plagioclase thermometer was also made

The amphibole-plagioclase thermometer was calibrated by Holland & Blundy (1994) based on the equilibria

$NaCa_2Mg_5AlSi_7O_{22}(OH)_2 + 4SiO2 = Ca_2Mg_5Si_8O_{22}(OH)_2 + NaAlSi_3O_8$

(the edenite-tremolite thermometer)

$NaCa_2Mg_5AlSi_7O_{22}(OH)_2 + NaAlSi_3O_8 = Na(CaNa)Mg_5Si_8O_{22}(OH)_2 + CaAl_2Si_2O_8$

(the edenite-richterite thermometer)

These two end-member reactions are based on the edenite exchange vector $(NaAl)(\square Si)_{-1}$ (Holland & Blundy 1994). The edenite-tremolite thermometer requires silica saturated parageneses, while the edenite-richterite thermometer can also be applied to silica-undersaturated rocks. The presence of free quartz combined with the overall mineralogy in all analysed samples indicates that the rocks were formed in a silica-saturated environment. The two thermometers should therefore give approximately similar results when applied to a single set of geochemical data derived from the analysed samples. On the other hand, using the intersection of the two thermometers as an indication of the barometry of the sample should be avoided (see chapter 4.6; Holland & Blundy 1994). The Hbl-Plg thermometer can be applied to rocks with a broad range of bulk composition, and it performs well within a temperature range of 400-1000ºC and a pressure range of 1-15 kbar, the uncertainty of the thermometer being ±35-40ºC (Holland & Blundy 1994). The calculations within this study were performed with the HbPl 1.2 software, developed by Tim Holland and Jon Blundy.

The Mg-Fe exchange geothermometers are widely used. The probably most popular of these is the garnet-biotite geothermometer, and it is also applied within this study. The thermometer is based on the reaction between garnet and biotite:

$Fe_3Al_2Si_3O_{12} + KMg_3AlSi_3O_{10}(OH)_2 = Mg_3Al_2Si_3O_{12} + KFe_3AlSi_3O_{10}(OH)_2$

(almandine + phlogopite = pyrope + annite)

Numerous calibrations have been presented for the Gt-Bt exchange thermometer. The early calibrations treat both minerals as ideal solid solutions (e.g. Ferry & Spear 1978). However, both garnet and biotite show nonideal behaviour, and the more modern calibrations of the thermometer have taken this into account (e.g. Bhattacharya et al. 1992, Kaneko & Miyano 2004). In addition, the possible presence of Fe^{3+} in both minerals affects the calculations, which further complicates the calibration of the thermometer, especially since the detection of the cation remains a difficult task even with many modern analytical methods. Some recent calibrations of the Gt-Bt geothermometer present alternative formulae for systems with or without Fe^{3+} (Kaneko & Miyano 2004). The calibration of Bhattacharya et al. (1992) was used because of the relatively low uncertainty of the calibration (± 50ºC).

The GBPQ barometer, like many geobarometers, is based on net transfer reaction since such reactions often result in large volume changes. The GBPQ net transfer equilibrium

reactions from higher to lower pressure are:

$Mg_3Al_2Si_3O_{12} + 2Ca_3Al_2Si_3O_{12} + 3K(Mg_2Al)(Si_2Al_2)O_{10}(OH)_2 + 6SiO_2 = 6CaAl_2Si_2O_8 + 3KMg_3(AlSi_3)O_{10}(OH)_2$

(pyrope + grossular + eastonite + quartz =anorthite + phlogopite)

and

$Fe_3Al_2Si_3O_{12} + 2Ca_3Al_2Si_3O_{12} + 3K(Fe_2Al)(Si_2Al_2)O_{10}(OH)_2 + 6SiO_2 = 6CaAl_2Si_2O_8 + 3KFe_3(AlSi_3)O_{10}(OH)_2$

(almandine + grossular + sidero-phyllite + quartz = anorthite + annite)

When using the geobarometer, corrections to the activity-composition relations are required because garnet, biotite and plagioclase are non-ideal solutions. On the other hand, quartz can be assumed to be a pure phase, its activity therefore being $a_{qtz} = 1$. Taking this into account, the barometer is calibrated to pelitic geo-chemistries when the activities of the relevant end-members are a_{Gros} >3%, a_{An} >17% and a_{Al} in biotite > 3% (Wu et al. 2004). If these conditions are not met the barometer should be applied with caution. The uncertainty of the GBPQ geobarometer when applied to rocks with sufficient mineral activities is $\pm$ 1.2 kbar, and it can be considered applicable within a P-T range of at least 1.0-11.4 kbar and 515-878ºC (Wu et al. 2004). To perform the calculations, the formulae and polynomial expressions presented in Wu et al. (2004) were copied into Microsoft Excel as macros, which in turn were utilised to produce plots representing the results of the barometric calculations (chapter 4.6).

Polished thin sections were prepared from the rock samples selected for analysis. The samples were coated with carbon and analysed at the electron microprobe laboratory at the Department of Earth Sciences at Uppsala University and at the mineralogical laboratory at the Geological Survey of Finland in Espoo as a joint project with Hans Annersten and Bo Johansson, respectively. The laboratory in Uppsala uses a Cameca SX-50 equipped with three wavelength dispersive spectrometers and a backscattered electron detector. Geological Survey of Finland uses a Cameca SX100 instrument with an accelerating voltage of 15 kV. Probe current and beam diameter used were 20 nA and 5 micrometers respectively. Analytical results were corrected using the PAP on-line correction programme (Pouchou & Pichoir 1986).

3.2 GEOCHRONOLOGY

Isotopic age determination techniques that are based on radioactive decay of certain isotopes within minerals are very commonly utilised. The parent/daughter isotope ratios that form during this process can be measured and used to determine the age of the rock sample. For the age determination by radiometric methods to be reliable, certain conditions have to be met. First of all, the rate of decay of the studied parent isotope must be known. The half-lives of the isotopes suited for age determination purposes of rock samples vary greatly, but can generally be estimated with satisfying accuracy (e.g. Geyh & Schleicher 1990). Also, the principle of uniformitarianism is applied, i.e. it is assumed that the decay constants of isotopes within Earth's crust have

remained unchanged for the past 4.6 Ga (Dickin 1997). The second condition is that the system in which the radioactive decay takes place must be closed so that the system neither loses nor gains parent or daughter isotopes during the process (e.g. Faure 1986). Thirdly, it must be possible to estimate a realistic value for the initial amount of the daughter isotopes in the rock (Faure 1986). Finally, the analytical method utilised must be accurate enough and suitable for the rock or mineral to be dated (Faure 1986).

The conditions listed above are, however, not always met, and some assumptions are generally necessary. While the decay rates for most isotopes can today be calculated with acceptable accuracy and the modern analysis techniques produce data that can be considered reliable, two important uncertainty factors remain. Firstly, the initial amount of the daughter isotope in the sample cannot always be estimated with sufficient reliability. However, the initial amount of the daughter isotope can be assumed to be zero in many isotope systems or the amount can be determined by means of e.g. the isochron method (Geyh & Schleicher 1990). The second important source of uncertainty is that systems do not always remain closed but can gain or lose either parent or daughter isotopes, thus altering the ratio of the isotopes. A system can be opened due to e.g. alteration or deformation. For example, U-Pb systems rarely remain closed due to the mobility of the isotopes (Dickin 1997). However, in this case the U and Pb parent and daughter isotopes show coherent chemical behaviour and reliable age determination is therefore possible even from disturbed systems (Dickin 1997). U-Pb age determination techniques are among the most widely utilised for dating magmatic and metamorphic rocks.

Within this study, three separate analytical methods were applied to selected samples. Whole-rock $^{39}Ar/^{40}Ar$ method was used in dating the pseudotachylytes. The U-Pb SIMS method was utilised for zircons, while ID-TIMS U-Pb method was applied to selected titanites. The principles as well as some of the more important uncertainties of the methods are outlined below.

The $^{40}Ar/^{39}Ar$ (or Ar-Ar) method was first detailed by Merrihue & Turner (1966). Since those days, the method has been improved significantly and despite the complicated analytical procedure, it is considered to be well suited especially for very small or valuable samples (Geyh & Schleicher 1990). The method is based on the decay of potassium isotopes into isotopes of argon. ^{40}K in potassium-bearing minerals such as alkali feldspar decays naturally to stable radiogenic ^{40}Ar by means of electron capture and positron emission (Faure 1986). It is generally assumed that (magmatic) rock systems are outgassed of Ar at the time of their formation, the initial amount of ^{40}Ar in a rock therefore being effectively zero (Dickin 1997). ^{39}K, on the other hand, can be artificially converted to ^{39}Ar by irradiation of ^{39}K with fast neutrons (Dickin 1997). The ^{39}Ar isotope that is produced by this neutron capture – proton emission reaction is unstable, but since the half-life of the isotope is 269 years it can be considered stable during the time the analysis procedure requires (Faure 1986). After the

irradiation, the isotopic compositions of the sample(s) together with a sufficient number of standards are analysed with a mass spectrometer or a laser probe (Dickin 1997). Once the $^{40}Ar/^{39}Ar$ ratios are known from both the samples and the standards, the ages of the samples can be calculated (Dickin 1997). Corrections need to be made, described by e.g. Dickin (1997), for interfering Ar-isotopes derived from neutron reactions from Ca as well as other K-isotopes than ^{39}K. In this study, $^{40}Ar/^{39}Ar$ method was chosen for dating the pseudotachyly tes for two obvious reasons. Firstly, pseudo-tachylytes form by frictional melting of their protoliths, which in this case are granodioritic where alkali feldspar is a key constituent. It can therefore be expected that the pseudotachyly tes contain sufficient amounts of potassium for Ar-Ar dating. Secondly, the grain-size and volume of the pseudotachylyte material is so small that the separation of any mineral fraction possibly present and suitable for other dating techniques is impossible.

There are several widely utilised age determination methods that are based on the decay of uranium (and thorium) to stable lead isotopes (e.g. Faure 1986). The long half-lives of the isotopes allow dating of a very wide range of ages from Earth's very first known rocks to ages less than 1 Ma (Geyh & Schleicher 1990). Minerals that contain U, Th and Pb and, hence, their isotopes are common in all igneous and metamorphic rocks. Zircon is generally suitable due to its wide distribution in crustal rocks and therefore widely used, although even sphene and monazite are common and routinely used for U-Pb dating (Geyh & Schleicher 1990). Age determination from whole-rock samples is also possible, although not as common as mineral dating (Geyh & Schleicher 1990). Within this project, zircons and titanites were dated with U-Pb methods.

Uranium (and thorium) decay naturally into the lead isotopes ^{208}Pb, ^{207}Pb, ^{206}Pb and ^{204}Pb through complex decay chains (e.g. Dickin 1997). Of the lead isotopes, only ^{204}Pb is non-radiogenic and can therefore be used as a stable reference isotope, while the other isotopes have a radiogenic and a non-radiogenic ('common') component (Geyh & Schleicher 1990). Concentration of each isotope is analysed, either separately from each crystal or from a whole rock sample. With modern accurate techniques such as ion microprobes, analysing parts of a single crystal has become a common procedure. In the U-Pb (zircon) dating method, the ratios of $^{206}Pb/^{238}U$ and $^{207}Pb/^{235}U$ (most commonly) are measured, and since the decay constant of the uranium isotopes are known, the time *t* since the closure of the isotopic system can be calculated (Dickin 1997). Systems that have remained closed give concordant values of *t*, defining a so-called concordia curve when plotted graphically (fig. 3.4; Wetherill 1956). A small amount of initial, or 'common' lead is often present in zircons. The concentrations of the initial lead isotopes ^{206}Pb and ^{207}Pb can be estimated by measuring the amount of the non-radiogenic ^{204}Pb in the sample and comparing it to the measured concentration of the other lead isotopes (Dickin 1997).

As discussed above, many U-bearing systems are disturbed due to

the high mobility of the isotopes. Especially lead loss is a frequently encountered phenomenon when dealing with U-Pb systems, since Pb fits relatively poorly into zircon lattice and is therefore easily mobilised (Dickin 1997). For example, evidence from various studies suggest that unaltered zircon lattices lose no or very little lead, while altered zircons, especially those whose alteration has been aided by metamictisation, are very prone to lead loss (Dickin 1997 and references therein). A single zircon crystal often has both unaltered and altered domains, which can have important implications for the geological interpretation of the data. As a result of lead loss, the data does not plot on the concordia curve. However, the U-Pb methods by nature are based on the decay of two uranium isotopes, each with different half-lives independent of each other (Geyh & Schleicher 1990). Consequently, two independent radiometric 'clocks' exist in the system. Disturbances affect both decay systems in a similar manner, which can be utilised to get age data even from altered systems (Geyh & Schleicher 1990). In practice this means that, when plotted in a $^{206}Pb/^{238}U$ and $^{207}Pb/^{235}U$ diagram, the obtained data often define a linear trend, termed discordia (fig. 3.4; Dickin 1997). The upper (older) intersect point of the discordia and the concordia curves has been found to ideally represent the time of the formation of the studied mineral. The lower (younger) intercept age is sometimes interpreted to mark the time of the event that caused the lead loss from the system, although the latter interpretation should only be

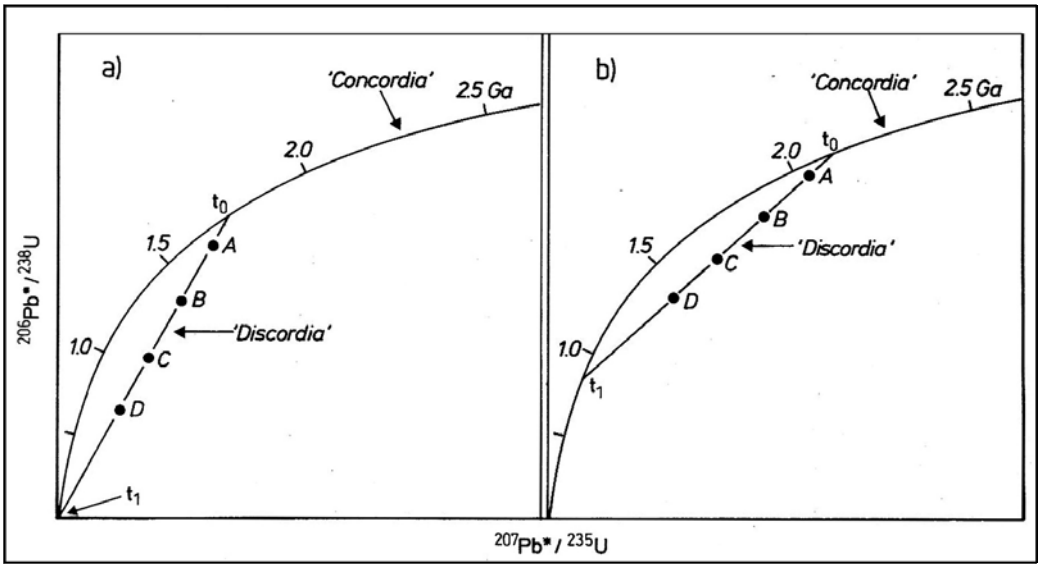

Fig. 3.4. U-Pb concordia and discordia curves and the principle of U/Pb evolution. Points that have the same (=concordant) 206Pb/238U and 207Pb/235U ages define the concordia curve. In an undisturbed sample formed at time t_0, the U/Pb isotopic ratios change with time along this curve. **a)** If there is a loss of lead at time t_1, the isotopic ratios of the sample plot along a line between t_1 and t_0. **b)** With time, both points t_1 and t_0 shift along the concordia curve, but the plot of the sample points remains linear, forming a straight line called the discordia. The discordia intersects the concordia at t_0 (primary age). From Geyh & Schleicher (1990).

considered reasonable if it's supported by other geological evidence (Dickin 1997 and references therein).

3.2.1 U-PB SIMS AND U-PB ID-TIMS – ANALYTICAL PROCEDURES

During this project, one major goal was to determine the ages of different deformation phases within the study area. There is an abundance of zircons and titanites of different generations in many samples collected from the study area. Therefore, a combination of U-Pb age determination techniques for zircons and titanites was chosen.

The selected rock samples were grinded and minerals separated at the Åbo Akademi University and the Geological Survey of Finland. The zircon SIMS and titanite ID-TIMS age determinations were realised as a joint project with the Geological Survey of Finland (Irmeli Mänttäri). The description of the U-Pb analytical procedures in this chapter is therefore partly based on the text by I. Mänttäri, also published in Torvela et al. (accepted).

SIMS is an abbreviation of 'Secondary Ion Mass Spectrometry'. In SIMS analysis, the U and Pb isotopes are measured *in situ* from selected mineral grains with an ion microprobe. The grains are bombarded with a small (diameter in the order of 10-30 µm) beam of high-energy light ions such as O^{2-} to yield a secondary beam of Pb ions, which are analysed in a double mass spectrometer (Dickin 1997).

For SIMS-dating, the chosen zircons were mounted in epoxy, polished and coated with gold. The SIMS analyses were made using the Nordic Cameca IMS 1270 at the Swedish Museum of Natural History, Stockholm, Sweden. The spot-diameter for the 10nA primary O_2^- ion beam was ca. 25 µm and oxygen flooding in the sample chamber was used to increase the production of Pb^+ ions. Three counting blocks, each including four cycles of the Zr, Pb, Th, and U species of interest were measured from each spot. The mass resolution ($M/\Delta M$) was 5400 (10%). The raw data were calibrated against a zircon standard (91500; Wiedenbeck et al. 1995) and corrected for modern common lead (T=0; Stacey & Kramers 1975). For the detailed analytical procedure see Whitehouse et al. (1999) and Whitehouse and Kamber (2005).

Titanite reacts and recrystallises readily during metamorphism, and U–Pb titanite ages are therefore likely to yield the age of metamorphic crystallisation (Frost et al. 2001). Titanites were separated from selected samples and analysed with the ID-TIMS method (isotope dilution - thermal ionisation mass spectrometer). In this method, in order to determine the unknown quantity of an element with a known isotope ratio (analysed with e.g. a mass spectrometer) in the sample, the element is 'spiked' by adding a known quantity of the same element with a know isotope ratio in the sample (Geyh & Schleicher 1990). If the original sample is solid, it needs to be digested in acid either prior to or after adding the spike. The new isotopic ratio of the

obtained homogeneous mixture is measured with a mass spectrometer. Based on the measurement, it is possible to calculate the amount of the element in the original sample and subsequently obtain an age for the sample from the data (Geyh & Schleicher 1990). The procedure is time-consuming but has several qualities due to which it is generally considered to be very accurate: i) there is minimal interference from other elements since they are removed chemically, ii) the method has high sensitivity even for sub-microgram sample amounts, and iii) more than two natural isotopes of an element can be measured at the same time (Dickin 1997, Geyh & Schleicher 1990). In addition to the possible (geological) disturbances in the analysed material and the possible inaccuracies in the used measurement technique(s), the sources for error of the method are: i) the isotopic compositions of the sample and the spike must be accurately known, iii) the proportions of the sample and the spike must be as close to equal as possible in order to avoid magnification errors, and iii) the sample and the spike must form a homogeneous mixture (e.g. Faure 1986).

For multi-grain ID-TIMS U-Pb dating, the selected titanite grains were air-abraded (Krogh 1982). The decomposition of titanites and extraction of U and Pb follows mainly the procedure described by Krogh (1973). ^{235}U-^{208}Pb-spiked and unspiked isotopic ratios were measured using a VG Sector 54 thermal ionization multicollector mass spectrometer. The measured lead isotopic ratios were normalized to the accepted ratios of SRM 981 standard (fractionation 0.15±0.05% / a.m.u). The U-Pb age calculations were done using PbDat-program (Ludwig 1991).

For both SIMS and ID-TIMS, plotting of the U-Pb isotopic data, fitting of the discordia lines and calculating the intercept and concordia ages were performed using Isoplot/Ex 3 program (Ludwig 2003). The error ellipses in the concordia diagrams are 2σ. All errors in age calculations are 2σ and decay constant errors are ignored.

3.2.2 ^{40}AR/^{39}AR METHOD – ANALYTICAL PROCEDURE

The ^{40}Ar/^{39}Ar analyses were carried out in cooperation with the Department of Geology at Lund University (Laurence Page and Tobias Hermansson), also published in Torvela et al. (accepted). Therefore, the description below of the analysis procedure for the Ar-Ar method is in part taken from an original text by Hermansson and Page.

The technique used for Ar-Ar dating is that of step heating, where the progressive heating of the sample with a laser results in stepwise outgassing of the argon isotopes from the sample (e.g. Dickin 1997). After each heating step, the obtained argon gas is cleaned and Ar isotopic ratios are measured with a mass spectrometer. The apparent age that can be calculated from the ^{40}Ar/^{39}Ar ratio is then plotted against the fraction of ^{39}Ar released (e.g. Dickin 1997). The stepwise heating of the

sample continues until the degassing curve ideally forms a plateau, which gives the Ar-Ar age for the sample. The measured isotope ratios are also often presented as a isochron diagram, where chosen isotope ratios are plotted against each other. Isochron plots are especially useful if it becomes necessary to determine whether the system contains any inherited argon, in which case the measured ratios do not define a straight line (Dickin 1997). A common problem with the Ar-Ar method is the ^{39}Ar recoil, i.e. a process of small-scale redistribution of argon, probably due to the irradiation (Dickin 1997). ^{39}Ar recoil can cause diffusion and depletion of Ar from a crystal surface down to a mean depth of 0.08 μm, which in worst cases leads to severe deflection of the plateau curve (Dickin 1997 and references therein). The problems caused by recoil can be reduced by using whole-rock samples, where the individual grains are in close contact with each other and therefore minimising the loss of Ar from the sample, or if powdered or very fine-grained rock samples are used, by encapsulating the sample in a small glass ampoules which trap the recoil products that can be used to correct the measured values (Dickin 1997).

As discussed above, the ^{39}Ar recoil is a potential problem when analysing very fine-grained or glassy whole-rock samples such as pseudotachylytes. Another problem, specific for pseudotachylytes, is the possible 'extra' argon (inherited or excess) originating form the parent rock and hosted by the microscopic clasts that are often present in a pseudotachylyte (Vincenzo et al. 2004). This means that a pseudotachylyte-forming event does not (completely) reset the argon signature within the clasts. According to Vincenzo et al. (2004), quartz and probably also plagioclase should be considered as a possible contaminant sources since their argon signatures do not appear to reset readily during the short time the melt remains unsolified, while the isotope signature of alkali feldspar seems to be somewhat more easily reset. In a whole-rock analysis, where individual clasts cannot be excluded, the obtained ages can therefore represent a composite age intermediate of the melt and the clasts. To reduce this problem, pseudotachylitic material situated in the injection veins instead of material within the generation surface should be favoured since the injection veins generally contain fewer clasts (Vincenzo et al. 2004). On the other hand, some authors have concluded that the high temperatures commonly generated during the pseudotachylyte-forming event combined with the generally relatively low pressures of formation should be enough to degas any inherited argon (Cosca et al. 2005). Despite the problems, the Ar-Ar method has been successfully employed to dating pseudotachylytes (e.g. Davidson et al. 2003, Cosca et al. 2005), although an integrated approach involving both chemical and textural analysis at the microscale together with step-heating methods should probably be favoured, at least if the pseudotachylyte can be deduced to have formed at relatively low

temperatures and/or relatively high pressures (Vincenzo et al. 2004).

Within this study, several pseudotachylyte veins were sampled with a hand drill. Melt pockets situated within injection veins were favoured whenever possible. Two samples were selected for $^{40}Ar/^{39}Ar$ analysis. For comparison, one sample was included from Torsholma, situated within a N-W striking fault zone ca. 40 km NNE of the area of this study (chapter 4.5.2). Several mm-scale pieces were sawed from the selected pseudotachylyte samples in order to separate the pseudotachylyte from the wall rock. The obtained small pseudotachylyte whole-rock samples were irradiated together with the TCR sanidine standard (28.34 Ma recalculated by Renne et al. 1998), for 35 hours at the NRG-Petten HFR RODEO facility in the Netherlands. J-Values were calculated with a precision of better than 0.25%. The samples were analysed with $^{40}Ar/^{39}Ar$ Micromass 5400 mass spectrometer with a Faraday detector and an electron multiplier. The analysis equipment include a metal extraction line, which contains two SAES C50-ST101 Zr-Al getters and a cold finger cooled to ca –155°C by a Polycold P100 cryogenic refrigeration unit. Individual fragments of pseudotachylyte were loaded into a copper planchette that consists of several 3 mm holes. Samples were step-heated using a defocused 50W CO_2 laser. Sample clean-up time that made use of the two hot Zr-Al SAES getters and a cold finger with a Polycold refrigeration unit was five minutes. The entire analytical process is automated and runs with Macintosh software modified specifically for the laboratory at the University of Lund and developed originally at the Berkeley Geochronology Center by Al Deino. Time zero regressions were fitted to data collected from 10 scans over the mass range of 40 to 36. Peak heights and backgrounds were corrected for mass discrimination, isotopic decay and interfering nucleogenic Ca-, K-, and Cl-derived isotopes. Isotopic production values for the cadmium lined position in the Petten reactor are $^{36}Ar/^{37}Ar(Ca)$ = 0.000270, $^{39}Ar/^{37}Ar(Ca)$ = 0.000699, and $^{40}Ar/^{39}Ar(K)$ = 0.00183. ^{40}Ar blanks were calculated before every new sample and after every three sample steps. Blank values were subtracted for all incremental steps from the sample signal.

4. THE SOTTUNGA-JURMO SHEAR ZONE

During the Ph.D. project, a relatively wide range of geological research methods was used to achieve an overall picture of the structures and the deformation history of the Sottunga-Jurmo shear zone (SJSZ) as well as of the temporal and spatial relationships of the shear zone to the Svecofennian orogeny. In the following chapters, the results of these investigations are presented. The general description of the SJSZ is followed by chapters portraying the observations within the study area including lithotypes and deformation styles, mineralogy, structures and microstructures, general geochemical features of the studied rocks, results from the geochronological analyses and, finally, results from the geothermobarometric study. The combination of several different methods in interpreting the overall geological features and deformation history of the shear zone has contributed to what the author believes to be a sound scientific ground, where the results from different analyses and observations support each other. The downside of utilising multiple methods, combined with the relatively large geographical size of the study area, is that no single part of this study can be considered to be exhaustive and much detailed work remains to be done.

4.1 INTRODUCTION TO THE STUDY AREA

As discussed in chapter 1, the Palaeoproterozoic crust in southern Finland was stabilised 1.85-1.80 Ga ago, after the main accretional phase of the Svecofennian orogeny. As the active thrusting ceased, the regional NNW – SSE compression (e.g. Ehlers 1976) partitioned into several transpressional, ductile crustal-scale shear zones throughout the Svecofennian domain (e.g. Väisänen 2002, Kärki et al. 1993, Ehlers & Lindroos 1990). Some of these shear zones follow crustal unconformities that have been interpreted as terrane boundaries (e.g. 'Pori shear zone', Hassela shear zone, Singö shear zone; fig. 1.1; e.g. Högdahl 2000, Sjöström & Bergman 1998, Gaál & Gorbatschev 1987). For example, the major dextral shear structure trending from close to the city of Pori (fig. 4.1) east – southeastwards, here called the 'Pori shear zone', was recognized by Gáal & Gorbatschev (1987) to be approximately following the terrane boundary between the Häme belt and the Uusimaa belt of the SSAC (chapter 1).

A more than a kilometre wide shear zone system extends in a NW-SE direction through the Åland and Turku archipelagos. According to Ehlers et al. (2004), the structure continues towards and along the southern coast of Finland, curving gradually towards northeast so that the entire structure is more than 200 km long (fig. 4.1). They proposed the name South Finland Shear Zone (SFSZ) for this major shear structure. Other interpretations and terminology exist: Soesoo et al. (2004) suggest that the NW-SE trending major shear structure in northern Estonia

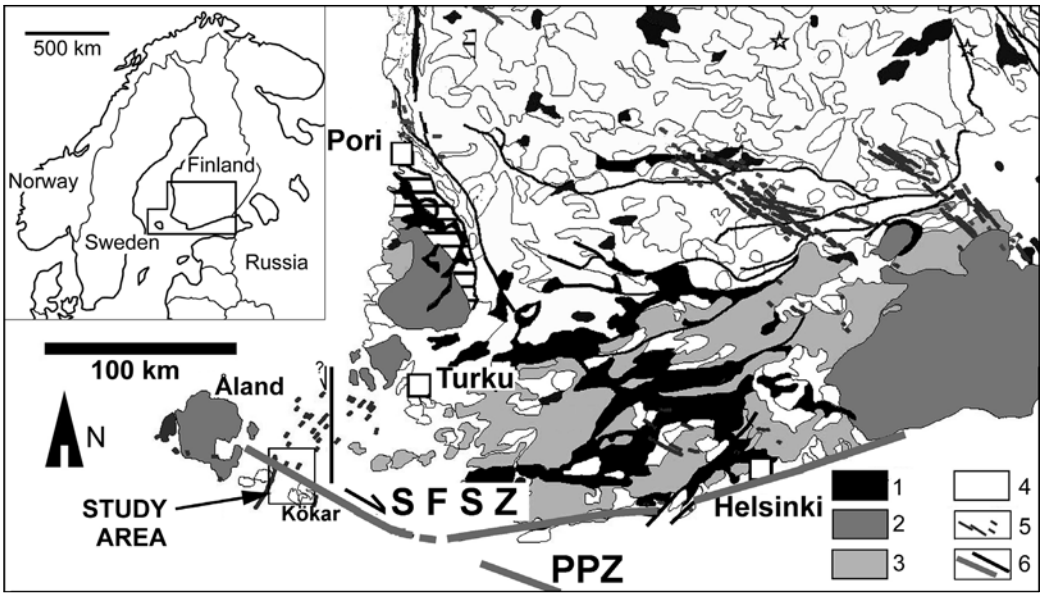

Fig. 4.1. Generalised geological map of southern Finland (modified from Korsman et al. 1997). Key: **SFSZ** = South Finland shear zone, PPZ = Paldiski-Pskov Zone, **1)** Metavolcanic rocks ca. 1.92-1.88 Ga, **2)** Granitoids and/or mica schists/gneisses ca. 1.89-1.88 Ga, migmatites of the LSGM ca. 1.85-1.81 Ga, **3)** Late-orogenic granites and migmatites of the LSGM ca. 1.85-1.81 Ga, **4)** Rapakivi granites ca. 1.6 Ga, **5)** Diabase dykes ca. 1.65-1.57 Ga, **6)** Major faults and shear zones.

(Paldiski-Pskov Zone; chapter 1.3.2) is a direct continuation of the shear zone in Åland, calling the whole structure the Åland-Paldiski-Pskov Shear Zone. Both of these aforementioned works assume a regional shear zone as a single, continuous structure, a notion that may or may not be correct and that remains an open question until more data is collected. In this work, however, the term South Finland Shear Zone is applied for the regional shear structure because it is more widely used in literature, despite its implications of the structure of the entire shear zone. On the other hand, the area of this study comprises only a minor part of the regional structure. Hence, the westernmost part of the regional shear zone within which the study area is located is referred to as Sottunga-Jurmo Shear Zone (SJSZ; figs. 4.2 and 4.3, appendix 1). By introducing this name for the NW-SE striking shear zone in the Åland and Turku archipelagos, the author wishes to avoid confusion by making a distinction between the regional shear structure and the area of this study. On the other hand, the author does not at this point wish to make assumptions of the continuation of the regional shear structure eastwards and/or southeastwards, and the term SJSZ avoids any such implications.

Ehlers & Ehlers (1977), Branigan (1987) and Hubbard & Branigan (1987) were among the first to recognise the existence of large, NW-SE and N-S as well as NE-SW shear structures in the Åland archipelago. Branigan (1987) and Hubbard & Branigan (1987) described the NW-SE trending shear structure that was later given the name South Finland Shear Zone (SFSZ; Ehlers et al.

2004), as a late-orogenic sinistral structure, belonging to a conjugate set of shears that also produced dextral, NE-SW trending zones (fig. 4.4). However, their interpretation of shear kinematics was based on local structural mapping in Seglinge area as well as on the NW-SE direction of the stress field at the time of the shearing (e.g. Ehlers 1976) which was thought to produce deformation with a simple-shear dominated flow according to theoretical calculations based on the Mohr-Coulomb criterion of fracture, producing Riedel-type shears (Riedel 1929). However, the model predicts that the main sinistral shear zone run in an approximately E-W direction, which the authors were not able to confirm during their field studies. Today, ductile shear behaviour of rocks in convergent systems is better understood, while the Riedel shears are recognised to form dominantly within a brittle regime where they are considered to be useful kinematic indicators (e.g. Chester & Logan 1987, Rutter 1986). The current interpretation of the ductile SJSZ is that it is a dextral structure, formed under a trans-pressive environment resulting from the regional stress field of the Svecofennian orogeny (e.g. Ehlers et al. 2004, Ehlers et al. 1993, Ehlers & Lindroos 1990). The kinematic interpretation is based on the deflection of the large-scale foliations

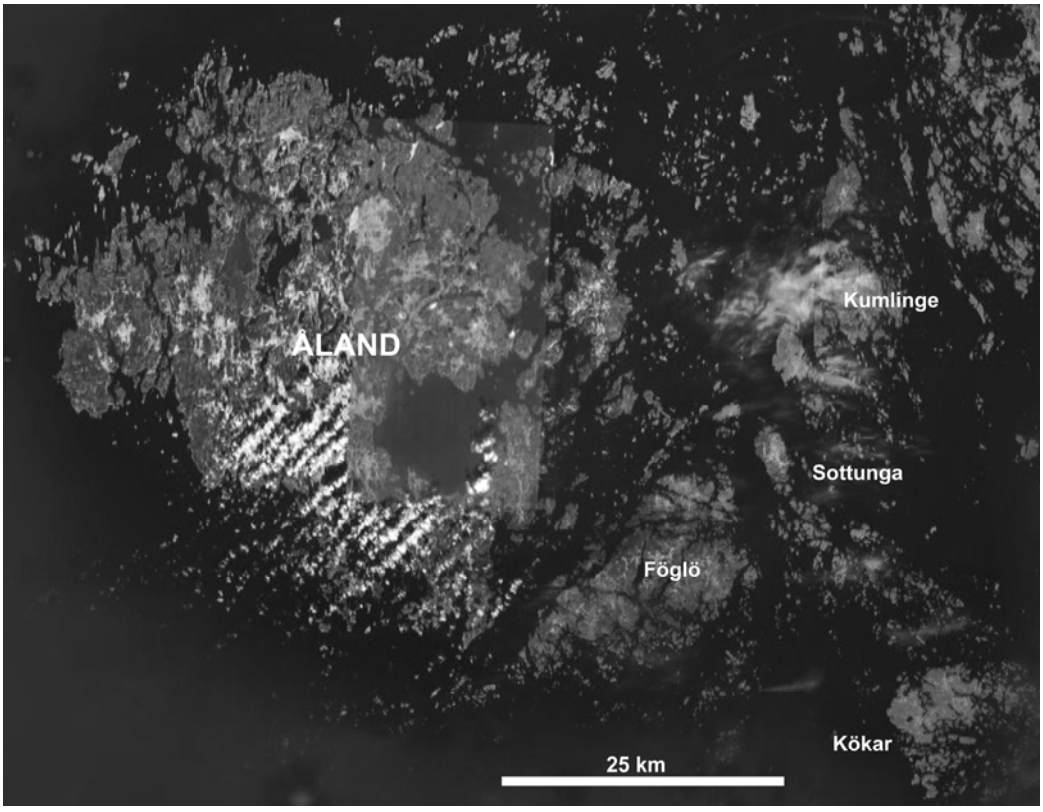

Fig. 4.2. Satellite image of the Åland archipelago (modified from image provided by Google Earth). The SJSZ is clearly observable as a linear, approximately NW-SE directed fault structure continuing from NE Kökar to N of the Åland main island.

south of the shear zone, a map of which was compiled by Ehlers & Lindroos (1990; fig. 4.3), as well as on field observations.

The rocks within the SJSZ are dominantly felsic, gneissose granitoids with steeply dipping, NW-SE striking foliations (appendix 1). Locally, mafic lenses have intruded the granitoids. South of the shear zone, the rock types are very similar but less deformed and show steep foliations striking mainly E-W. To the north of the SJSZ, the structurally overturned, sub-horizontal, extensively migmatised supracrustal rocks of the Late-Svecofennian Granite-Migmatite Zone (LSGM; Ehlers et al. 1993) are exposed. The SJSZ thus runs roughly along the contact between the granitoids to the south and the LGSM to the north.

Within the shear zone, the steeply dipping foliations anastomose around less deformed lenses but has an overall strike of ca. 120º. The foliation along the southern margin of the dextral ductile shear zone is folded along fold axes plunging gently southeastwards. The mineral and stretching lineations within the gneissose foliation, both within the shear zone and south of it, also plunge gently to steeply eastwards, probably relating to a relative upward movement of the SW side (chapter 4.2.2). The transition from SJSZ rocks towards NE into the LSGM is not exposed within the study area.

As will be demonstrated in the following chapters, the SJSZ has been repeatedly reactivated, starting with periods of regional, ductile dextral shearing that produced striped gneisses. The ductile deformation is locally followed, in places possibly overprinted, by higher strain-rate, ductile to semi-ductile deformation producing mylonite zones of variable widths. The latest stage of activity along the shear zone is recorded by brittle deformation structures (pseudotachylytes and cataclasites).

Previous works have been successful in giving an overall time frame for the deformation within the SJSZ (e.g. Ehlers et al. 2004, Suominen 1991). The ages frequently encountered within these studies cluster in three distinctive groups of ca. 1.88 Ga, 1.83 Ga and 1.79-1.80 Ga. The first of ca. 1.88 Ga have been interpreted to represent the approximate intrusive ages of the rocks in the area (Ehlers et al. 2004). The 1.83 Ga age, recorded from late-orogenic granitic intrusions within and close to the SJSZ (Suominen 1991), is coeval with the migmatites and anatectic granites of the migmatite zone of southern Finland (see also chapter 1.2). The third age group of ca. 1.79 Ga is common in the rocks close to the study area and also elsewhere in SW Finland (e.g. Suominen 1991). Suominen (1991) concluded that this age represents a postorogenic regional metamorphic event, the cause and nature of which was however not speculated.

4.2 FIELD OBSERVATIONS

The area of this study comprises the parish of Sottunga as well as large parts of the parish of Kökar in the Åland archipelago in SW Finland (figs. 4.2 and 4.3). The area was chosen because the SJSZ crosses approximately through the middle of the area and is well exposed along the shores of the hundreds of small islands and skerries. It is possible to

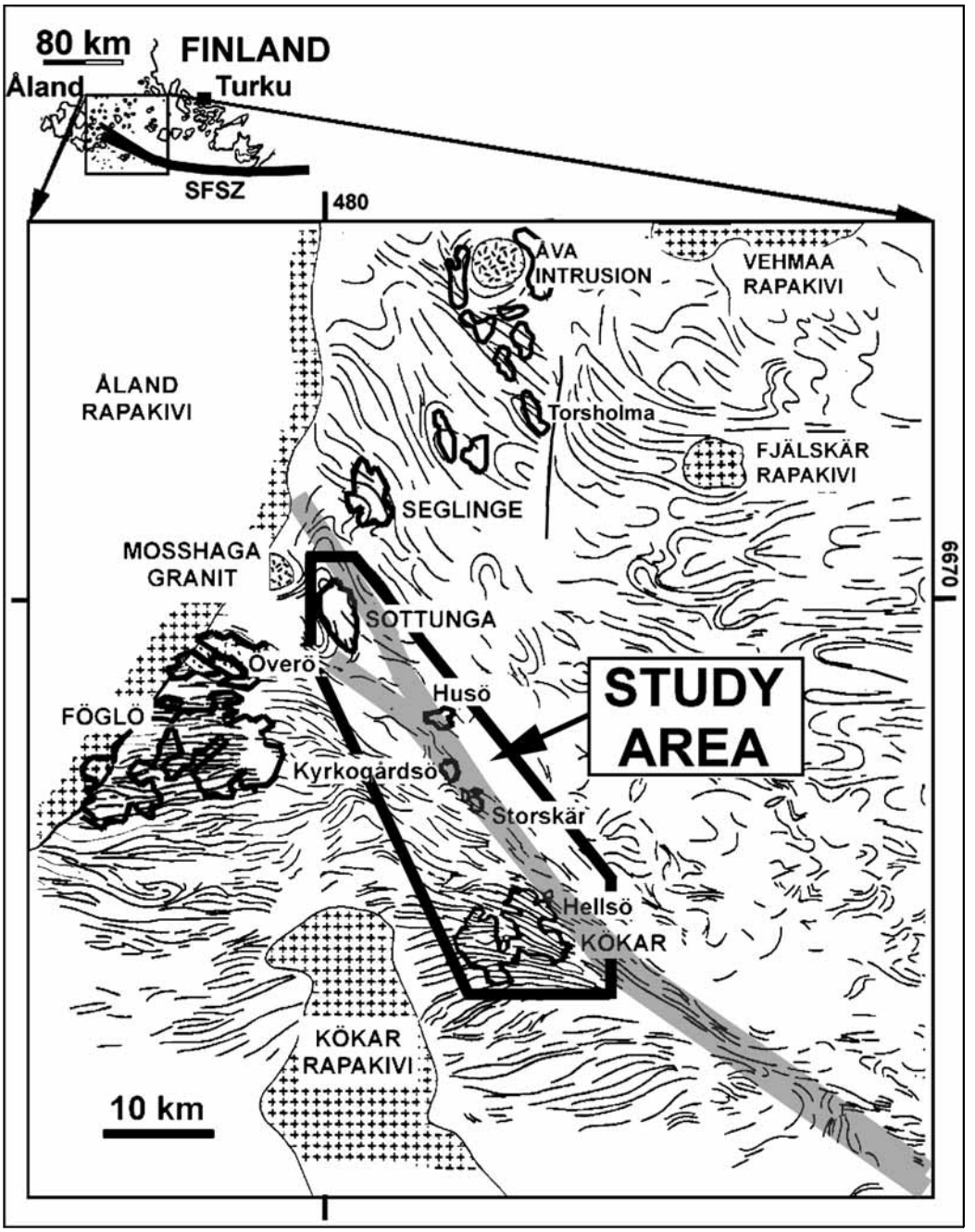

Fig. 4.3. Foliation map of Åland archipelago (modified from Ehlers & Lindroos 1990). The SJSZ is marked with grey, and the most important islands are outlined. To the NW, the SJSZ is cut by the anorogenic Åland rapakivi granite massif. The overturned, migmatised, mostly supracrustal rocks and anatectic granites lie to the NW or the SFSZ, while to the SW the bedrock is dominated by non-migmatised, intrusive granitoids and associated mafic lenses with steeply dipping foliations. The overall dextral kinematics of the large-scale shearing is clearly visible as the foliations SW of the shear zone are drawn into the zone.

follow the change in the deformation style and the orientation of the deformation fabrics from southern and western Kökar, south of the main shear zone, northwards into the zone of the highest strain. In the NW, the exposed shear zone terminates against the anorogenic, ca. 1.58 Ga Åland rapakivi batholith and the late-orogenic, 1.79 Ga Mosshaga pluton, although it is highly likely that a continuation of the shear zone exists in south-central Sweden. From the SE parts of the study area, the shear zone continues toward the Turku archipelago (Jurmo).

4.2.1 ROCK TYPES: DEFORMATION STYLES AND MINERALOGY

In the field, the rocks within the SJSZ can be superficially divided into different categories based on their overall deformation styles and mineralogy (tab. 4.1). The different deformation styles are represented by three major categories: the ductilely deformed gneisses belonging to the earliest shearing phases (fig. 4.5a); the protomylonites, mylonites and ultramylonites, mainly belonging to a younger ductile deformation phase (Fig. 4.5b-c); and the rare

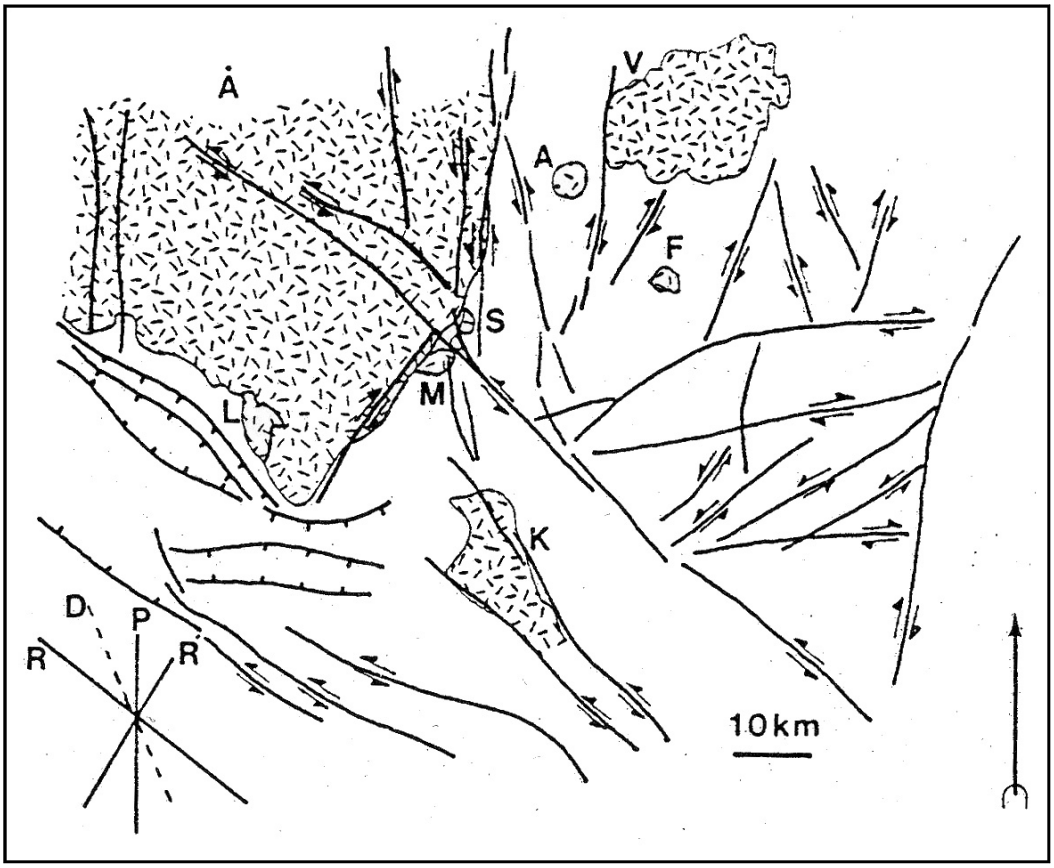

Fig. 4.4. A lineament map by Branigan (1987). Key: **Stippled areas** = post-orogenic granites. Early post-orogenic granites: **A** = Åva, **S** = Seglinge, **M** = Mosshaga, **L** = Lemland. Rapakivi granites: **Å** = Åland, **V** = Vehmaa, **K** = Kökar, **F** = Fjällskär. The orientation diagram refers to the now outdated interpretation of the distribution of the major "Riedel" shear sets (see text).

pseudotachylytes and cataclasites, representing the last (brittle) tectonic activities along the zone (fig. 4.5d). The internal fabrics of the three different deformation types are more closely described in chapter 4.3, while an overall description is given below.

The ductile, striped gneisses dominate the lithology (fig. 4.6). They are medium-grained, intensely deformed rocks that usually are relatively granoblastic, although augen gneiss –like varieties exist, especially within the main shear zone where the deformation intensity and strain rate were greatest. Locally, mylonite zones of variable width exist, both along and crosscutting the gneissose foliation. The mylonite zones that follow the gneissose foliation are generally wide, up to 30-40 meters across. The mylonites that cut the gneisses are much narrower, less than 10 cm across, distinctly marking a late ductile to semi-ductile deformation phase within the shear zone. Brittle pseudotachylytes formed during the last observed kinematic events along the shear zone have been found in two locations.

The striped gneisses form zones of differing compositions, easily recognisable in the field (fig. 4.5a, tab. 4.1). The widths of the individual compositional zones vary from less than one meter to several tens of metres. The gneisses are here divided into three types: ‘alkali feldspar gneisses’ with a granitic to granodioritic composition; ‘amphibole gneisses’ or ‘tonalitic gneisses’ with a quartzdioritic to tonalitic composition; and the less common mafic lenses with gabbroic to dioritic compositions that often display a less gneissose character, being brecciated or in some cases only weakly foliated. The alkali-feldspar rich granitic and granodioritic gneisses seem to be somewhat dominant over the tonalitic varieties although no statistical study has been made.

The alkali feldspar gneisses typically consist of quartz, plagioclase, potassium feldspar, biotite ± minor amphibole and accessories such as epidote group minerals, titanite, apatite , zircon and occasional garnet and rutile. The same minerals are present in the tonalitic gneisses with the exception of alkali feldspar and biotite that are often absent, hornblende amphibole being a dominant mineral instead. Also titanite is more abundant in the tonalitic gneisses than in the granodioritic varieties. The biotite in all rocks, when present, is typically dark greenish brown and the hornblendes are of the dark brownish green to dark green variety. On the other hand, in the rare garnet-bearing gneiss layers hornblende, epidote and titanite are essentially absent and the biotite is commonly red-brown in colour, indicating a high Ti-content of the mineral.

The mafic lenses are dominantly composed of amphibole (hornblende), plagioclase and mica (dominantly biotite) with some accessory opaques. In W Kökar, the lenses are more massive and commonly relatively unaltered, while within the shear zone, the lenses frequently display brecciation and extensive mineral alteration – however, chloritisation has not been significant, implying that the temperatures were still relatively high when the alteration occurred.

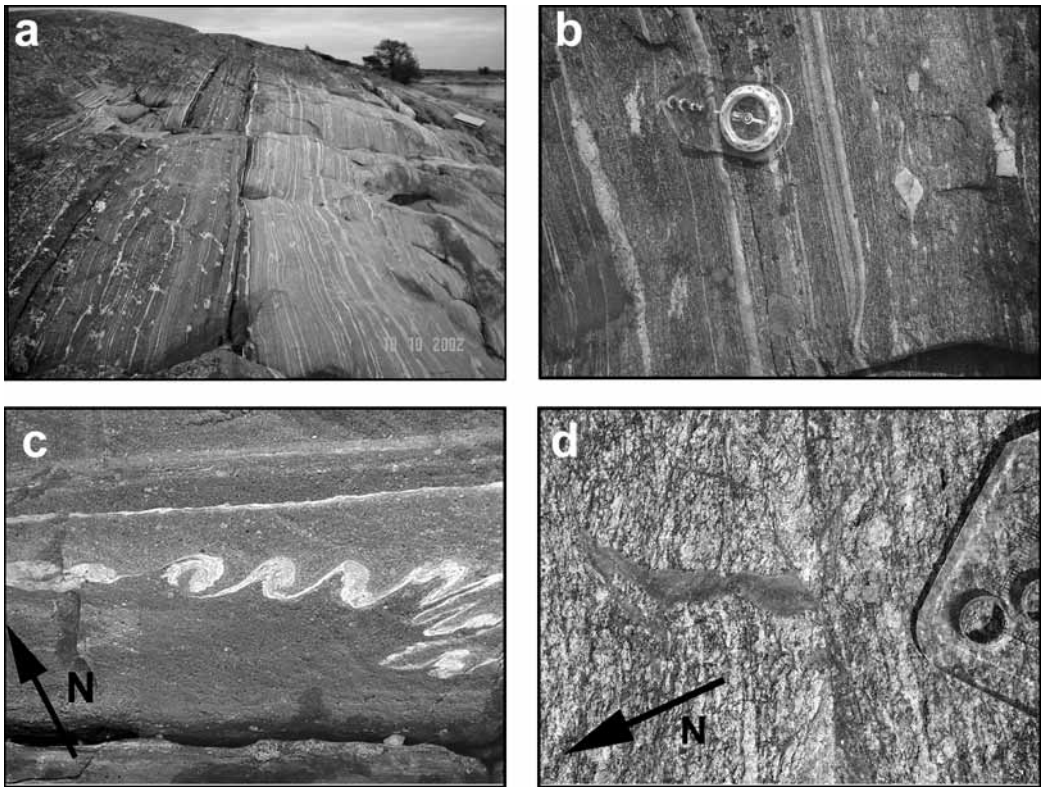

Fig. 4.5. Different rock types commonly observed within the study area. The length of the compass ca. 15 cm. **a)** Ductilely deformed, medium-grained gneisses. To the left of the picture, a layer of amphibolite-rich tonalite gneiss runs parallel to the granodioritic gneiss on both sides. The tonalitic layer is slightly boudinaged. Storskär, Kyrkogårdsö area, view toward SE. **b)** Alkali feldspar-rich mylonite with σ-porphyroclasts, Skattskär, Kyrkogårdsö area. **c)** Alkali feldspar-rich ultramylonite with δ-porphyroclasts, Kyrkogårdsö, width of the photo ca. 7 cm. **d)** Pseudotachylyte with a granodioritic gneiss protolith, Hellsö, Kökar, width of the photo ca. 12 cm.

In addition to the rock types mentioned above, there are occasional, rare, intensely deformed and altered, relatively thin (up to 1 m) layers of calc-silicate rocks along the gneissose foliation that are probably of supracrustal origin. There are different types of layers, but they are commonly composed of garnet, plagioclase (extensively sericitised), epidote, calcite/dolomite and quartz in different proportions so that some layers are quartz-rich and garnet poor, or vice versa; in some layers, diopside occurs associated with garnet and calcite/dolomite.

The gneisses are locally cut or overprinted by mylonites and ultramylonites (fig. 4.6). A distinction is made between protomylonites with 10-50% matrix, 'normal' mylonites with ca. 50-90% matrix and ultramylonites with >90% matrix. The mylonites are usually quite coarse-grained, falling into the category of protomylonites or mylonites, although the ultramylonitic varieties are locally common, especially within the widest mylonite zones. The different mylonite types are locally present as narrow, mostly as cm-scale bands but occasionally as up to 30-40 m wide zones where the relatively

granoblastic wall rock gneisses grade into increasingly mylonitic rocks (Fig. 4.5 b and c, respectively). As mentioned above, the widest mylonite zones commonly follow the strike of the gneissose foliation, while the narrow zones sometimes, but not always, cut the ductile gneisses. The ultramylonites are here tentatively interpreted to be somewhat younger than the coarser-grained mylonites, formed due to increasing partitioning of strain into narrower zones as the rocks were exhumed to less ductile regimes; on the other hand, they may also have been formed coevally with the coarser varieties due to rheological differences between different rock compositions, fluid channelling, and/or as a result of strain partitioning due to strain softening along certain zones of weakness (e.g. Passchier & Trouw 2005, White et al. 1980).

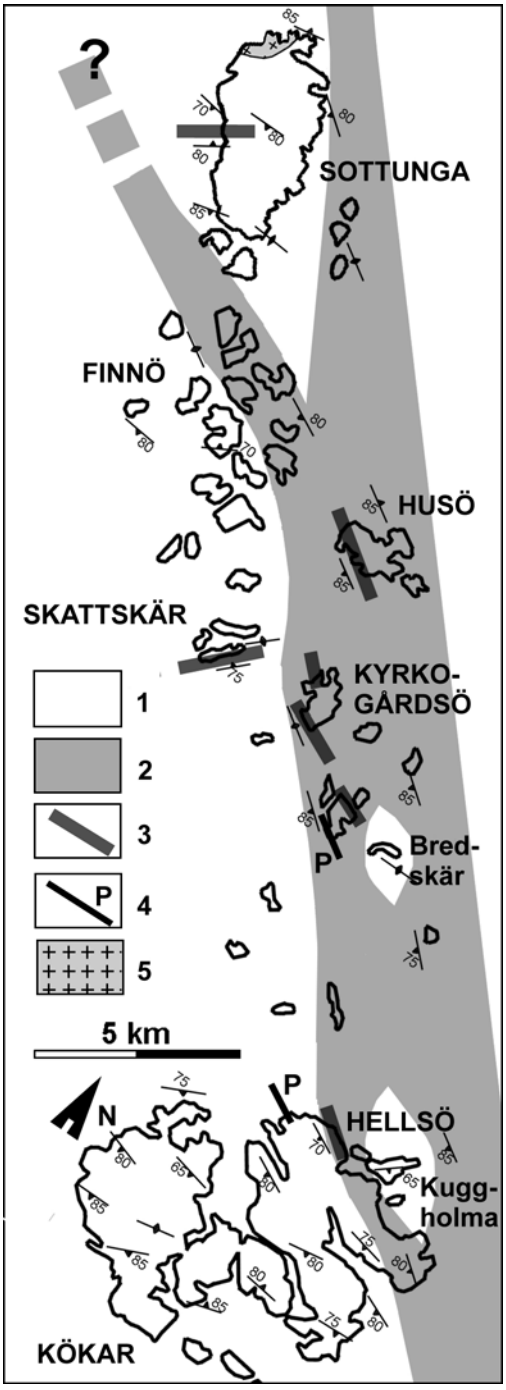

The mylonites were formed from the coarser gneissose rocks, consequently containing rounded porphyroclasts of plagioclase, accompanied by either alkali feldspar or amphibole depending on the protolith mineralogy. In contrast to the gneisses, the different mineralogies in the mylonites are not always readily observable in the field. Compared to the gneisses the retrograde reactions seem more intense in the ultramylonites, resulting in abundant

Fig. 4.6. The study area and the location of the most prominent mylonite zones, as well as the location of the found pseudotachylytes. Also the most notable lenses (the Kuggholma lens NE of Kökar, the Bredskär lens E of Kyrkogårdsö and, possibly, the whole island of Sottunga) within the anastomosing shear zone are marked; the foliation within these lenses is clearly oblique with respect to the main shear zone foliation. Most of the smaller islets and skerries have been omitted for clarity. **1)** Medium-grained, granitic to tonalitic gneisses with local dioritic and gabbroic lenses; **2)** Main shear zone; **3)** Prominent mylonite zones; **4)** Pseudotachylytes; **5)** Mosshaga post-orogenic granite.

small epidote grains in the fine-grained biotite-rich matrix, and the amphibole-rich mylonites often also contain significant amounts of titanite. The ultramylonite matrixes therefore commonly show a partly greenschist facies mineral assemblage with abundant brown mica + epidote + some chlorite ± titanite, while the porphyroclast rims are not always altered accordingly. It is consequently somewhat unclear whether the greenschist facies assemblage of the matrix formed during mylonitisation or after it due to subsequent retrograde processes.

Pseudotachylytes have been found in two locations within the study area (fig. 4.5d and 4.6). They commonly form a paired set of tabular surfaces (generation surfaces) where the bulk of the melts were probably formed. The paired sets of pseudotachylytes comprise of two, sometimes three (sub)parallel melt generation surfaces, running approximately along the strike of the gneissose foliation and separated by up to over a meter of largely unfractured gneissose rock. The generation surfaces are thought to have accommodated the bulk of the strike-slip component of the brittle deformation. Between the generation surfaces, injection veins and sets of conjugate cracks and surfaces cut the gneissose foliation. The conjugate surfaces seem to have played an important role in the transportation of the relatively small volumes of melt formed during the deformation: the melts have sometimes been deposited along the generation surfaces, but much of the melt was injected into the wall rock along the conjugate surfaces, 'freezing' as separate pockets and veins (fig. 4.5d). In two locations, the pseudotachylyte generation surfaces have been found to cut pegmatite dykes that were intruded into the ductile gneisses. The pseudotachylytes, where observed, have apparently formed from granodioritic protoliths.

4.2.2 STRUCTURES

The structures as well as the rock types S and SW of the SJSZ have some fundamental differences compared to the rocks N and NE of the zone, emphasising the character of the shear zone as a major geological discontinuity. Results from the field studies indicate that the present structure of the SJSZ is closely related to the structural development of the crust at the SW margin of the shear zone, as will be described in following chapters. All structural observations are expressed following the right hand-rule.

4.2.2.1 Structures in the gneisses

The rocks north and northeast of the shear zone belong to the late-Svecofennian Granite-Migmatite zone (LGSM; Ehlers et al. 1993). The LGSM rocks define very different structural, lithological and meta-morphic trends compared to the rocks south and southwest of the shear zone: the LGSM consists of structurally overturned, supracrustal rocks metamorphosed and magma-tised in high-T low-P conditions, intruded by flat-lying sheets of granites and tonalites (e.g. Ehlers et al. 2004, Stålfors & Ehlers 2005). The relationship between the LGSM and the SJSZ (and SFSZ) remains uncertain, although an obvious spatial connection can be observed as the SFSZ closely corresponds to the

Table 4.1. Summary of the different rock types within the study area. Abbreviations: qtz = quartz; plg = plagioclase; kfs = potassium feldspar; bt = biotite; mu = muscovite; hbl = hornblende; epi = epidote; chl = chlorite; ti = titanite; ap = apatite; gt = garnet; rut = rutile; opq = opaques; cpx = clinopyroxene; ol = olivine; di = diopside.

Rock type	**K-feldspar gneisses**	**Tonalitic gneisses**	**Mafic lenses**	**Ca-rich layers**	**(Proto)mylo-nite**	**Ultramylonite**	**Pseudo-tachylyte**
Occurrence	Dominating	Very common	Locally common	Rare	Locally common	Locally occurring	Rare
Mineralogy	Qtz, plg, kfs, bt ± mu ± hbl; acc. epi, ap, chl (rare), ti (rare), rut (rare), gt (rare)	Plg, hbl, qtz ± ti (common) ± bt ± kfs (rare); acc. epi, ap, rut, chl (rare), gt (rare)	Hbl, plg, bt, opq, rarely cpx, ol	Qtz, calc ± gt ± epi ± plg ± mu ± di (rare)	Depending on the mineralogy of the original rock; either hbl-plg rich or kfs-plg rich	Depending on the mineralogy of the original rock; either hbl-plg rich or kfs-plg rich	Plg microlites sometimes discernible in the microscope
Texture	Medium grained, equigranular, occasionally porphyritic	Medium grained, equigranular, rarely porphyritic	Medium to coarse grained, mostly equigranular	Fine to coarse grained, mostly equigranular	Porphyroclasts in fine-grained mica-rich matrix (10- ca. 90%)	Porphyroclasts in fine grained to aphanitic matrix (> ca. 90%)	Glassy to ophitic
Deformation regime and style(s)	Ductile;	Ductile;	Ductile (commonly only little deformed but extensively altered)	Ductile?, extensive metasomatic alteration	Ductile;	Ductile to semi-ductile;	Semi-brittle to brittle

southern margin of the LSGM. The migmatisation is however relatively limited within the shear zone itself and completely absent S of the SJSZ. Stålfors & Ehlers (2005) suggest that the emplacement and fractionation of LSGM granitic melts in Nagu and Hämeenlinna were shear-assisted processes, and propose a model where the vertical crustal-scale shear zones functioned as transport channels for the magmas (fig. 1.5). In any case, the SJSZ represents a major crustal boundary between the up to granulite facies LGSM rocks and the amphibolite facies granitoid gneisses to the south. Within the area of this study, however, the migmatised rocks of the LGSM or their outcrops are absent, although limited minor migmatisation has been observed within the SJSZ (fig. 4.7). It is interesting to note in this context that the major ductile shear zones in central Sweden separate domains C and D as well as domains D and E (fig. 1.6), the domain D being dominantly of lower metamorphic grade than both domains C and E (Sjöström & Bergman 1998, see also chapter 1.3.2). Furthermore, the major shear structure cutting through Estonia (the Paldiski-Pskov Zone PPZ) also separates a dominantly granulite facies terrain and an amphibolite facies terrain, the granulites being located south and southwest of the PPZ while the amphibolite facies rocks lie to N-NE of the PPZ (Soesoo et al. 2004; see also chapter 1.3.2). In geophysical maps, all the aforementioned regional shear structures are clearly visible. For example, the magnetic anomaly map (Korhonen et al. 2002) shows the SJSZ, as well as the larger crustal structure(s) to which it is related (fig. 4.8).

Fig. 4.7. Locally within the shear zone, small-scale migmatitic melts have formed, possibly as a result of locally higher amounts of fluids which would have lowered the melt point of the rock. Length of the compass ca. 15 cm. A granite-granodiorite gneiss, Storskär, Kyrkogårdsö.

South and southwest of the SJSZ, the amphibolite facies rocks are dominantly gneissose granitoids; medium-grained plutonic rocks with some local mafic, less deformed lenses of up to several hundred metres across. Mafic dykes within the granitoids are common, and many of the dykes deformed in a more incompetent manner than the granites, forming mullion-like structures (e.g. Talbot & Sokoutis 1992). No migmatisation of these rocks have been observed. In general terms, the dominantly E-W to ENE-WSW striking, steep gneissose foliations dip mainly towards north, but also southwards dipping foliations occur (appendix 1). The foliation pattern could thus be interpreted to reflect large-scale, isoclinal, upright folds; there are some observations in the field of fold axes dipping gently towards E-ENE or towards W-WSW (fig. 4.9). These folds are referred to

as *F_1-folds*, and the foliations that make up the F_1 folds are called *S_1 foliations*. The F_1 folds refold into open *F_2 folds* with fold axes dipping relatively steeply toward E-ENE (fig. 4.9). The F_1 and F_2 folds are only exposed in southern and western Kökar.

In general terms, as the shear zone is approached, the F_2 folds get tighter and eventually refold into *F_3 folds* against the SW margin of the main SJSZ. The large-scale F_3 fold variety is here referred to as *margin folds*. In the SE part of the study area (Kökar), the margin folds are open, flatly lying, and show dominantly SE trending, gently plunging fold axes and strong mineral and stretching lineations plunging gently toward SE (fig. 4.9). The strong lineation patterns are here interpreted to indicate flow along the axes of the margin folds toward NW. On the other hand, in the central and NW parts of the study area (Kyrkogårdsö-Skattskär to Sottunga), the open margin folds dominantly have steeply toward S-SSE plunging fold axes (fig. 4.9). The F_3 folds get tighter in the immediate vicinity of the main shear zone, until within the shear zone, the folds disappear or become tight to isoclinal. The last ductile deformation phase did apparently not result in any large-scale refolding of earlier folds; instead, the deformation was at this stage mostly partitioned into steeply dipping, local and regional high-strain zones, although some tightening of the F_3 folds probably took place. Besides the main shear zone, the strike-slip component of the large-scale (D_3-D_4,) deformation was accommodated by shear zones conjugate to the main SJSZ, as the NE-SW striking limbs of the F_3 margin folds are often marked by zones of more intense, sometimes mylonitic deformation (e.g. Skattskär; figs. 4.5

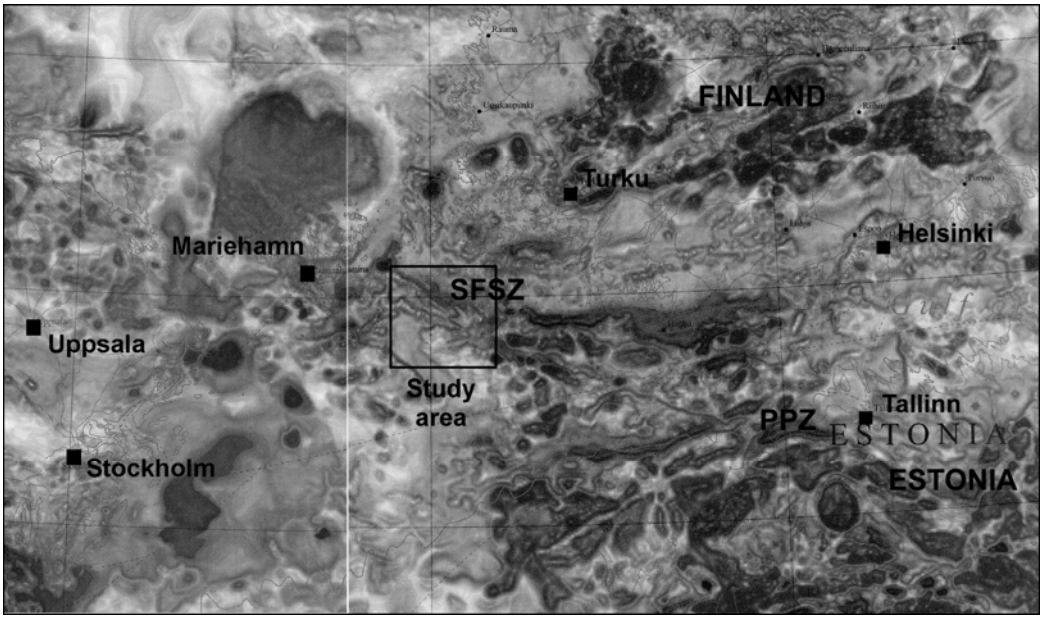

Fig. 4.8. Magnetic anomaly map of southern Finland, northern Estonia and eastern central Sweden. The regional shear structures of the South Finland shear zone and the Paldiski-Pskov shear structure (Estonia) are clearly visible. Modified from Korhonen et al. 2002.

and 4.6). The main shear zone and the conjugate, ca. NE-SW striking high-strain zones would thus have formed as a response to the simple shear component of the regional strain, principally during the D_3 and D_4 deformation phases.

Within the shear zone, the invariably steeply dipping foliations define the overall direction of the zone to ca. 120º (fig. 4.9, appendix 1). The lenses around which the foliation anastomoses usually consist of mafic rocks (amphibolite to gabbro-diorite) that is only weakly deformed, although even lenses composed of a more felsic material together with more mafic layers and inclusions occur (fig. 4.10). In the latter case, the lenses are considerably more deformed than the mafic lenses, but the deformation intensity is still visibly lower than within the main zone. Also, the direction of the foliation varies within the mixed felsic-mafic lenses, and complex folding patterns are common due to the differing competences and rheological properties of the rocks (fig. 4.10). Toward NW, the main shear zone seems to widen and finally divide itself, creating a lens with less intense deformation and a local stress minimum (Sottunga area) where the post-orogenic Mosshaga pluton and associated granite dykes could intrude (figs. 4.3 and 4.6).

The lineations within the zone of most intensive shearing are in many places relatively difficult to observe, possibly due to intensive static recovery in high-T conditions (chapter 4.3). However, the general trend of the mineral and stretching lineations is toward SE along the strike of the shear zone foliation, with steep to relatively shallow plunges (fig. 4.9).

The trend of the main shear zone lineations varies somewhat, apparently a reflection of the slightly anastomosing nature of the shear

Fig. 4.10. A photo from a large-scale mixed felsic-mafic lens within the shear zone (the Bredskär lens in fig. 4.6). Throughout the lens, the felsic and mafic rocks alternate, the foliation of the felsic rocks often being deflected around the mafic lenses, or complexly folded against the rheologically stronger mafic layers. View towards east, the length of the compass ca. 15 cm.

Fig. 4.9 (next centrefold). Simplified structural overview map of the study area with a compilation of the structural observations (stereographic projections) and sketches illustrating the 3D structural interpretations of the area. Most of the smaller islets and skerries have been omitted for clarity The stereonets are lower hemisphere, equal area projections. The 3D sketches are illustrated in a greater detail in the following figures.

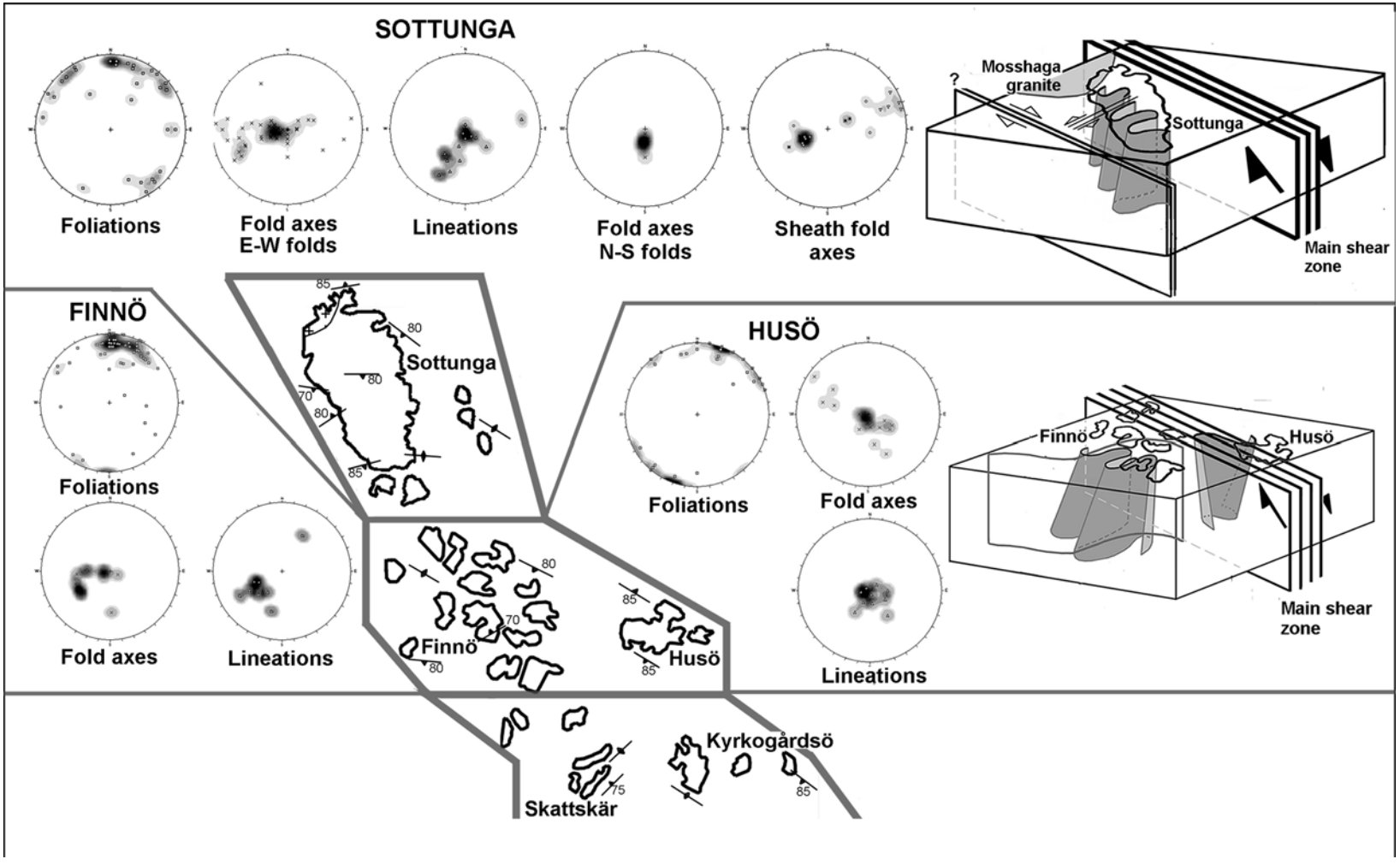
SOTTUNGA
Foliations
Fold axes
E-W folds
Lineations
Fold axes
N-S folds
Sheath fold
axes
Mosshaga
granite
?
Sottunga
Main shear
zone
FINNÖ
Foliations
Fold axes
Lineations
Sottunga
Finnö
Husö
HUSÖ
Foliations
Fold axes
Lineations
Finnö
Husö
Main shear
zone
Skattskär
Kyrkogårdsö

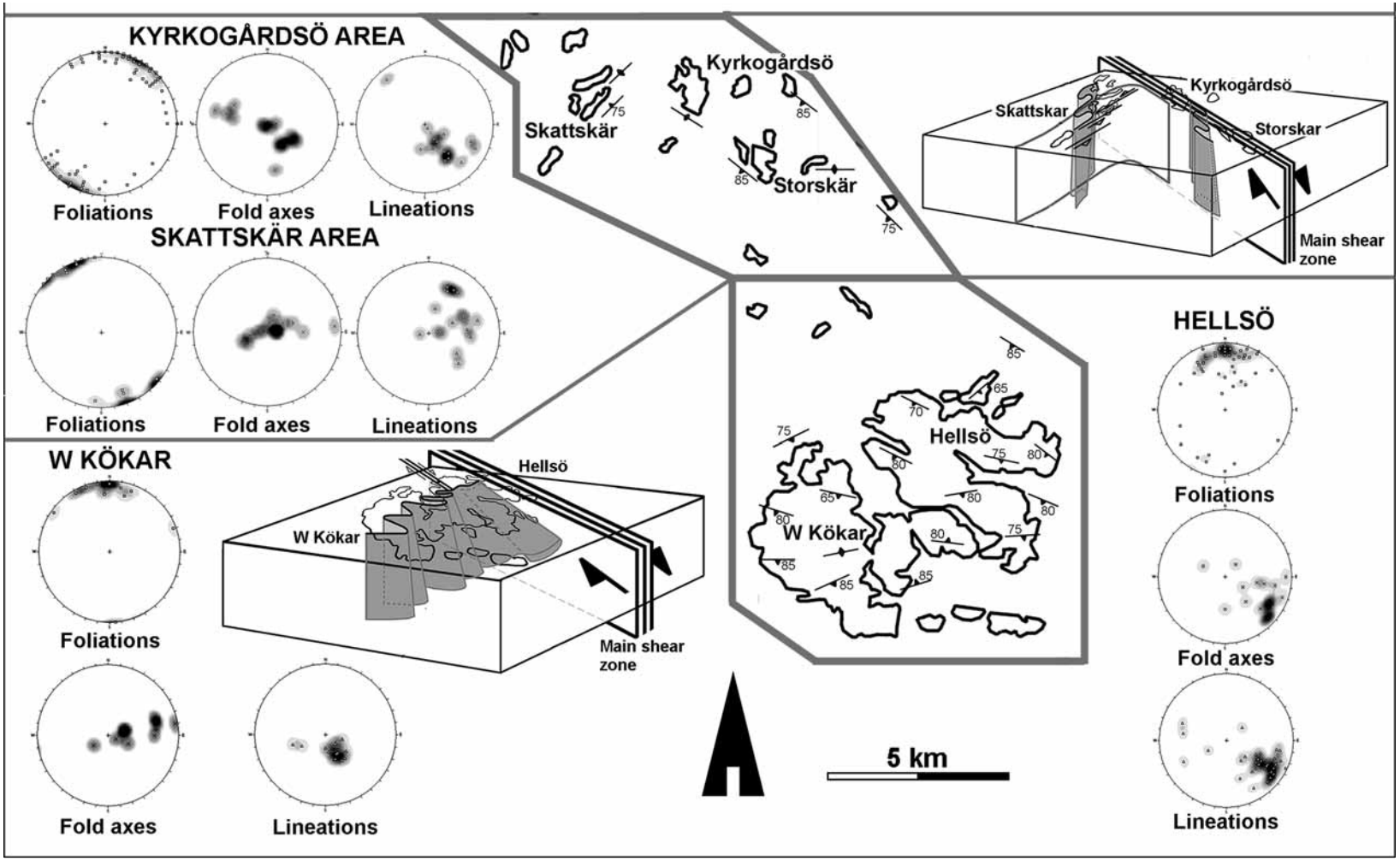
KYRKOGÅRDSÖ AREA
Foliations
Fold axes
Lineations
SKATTSKÄR AREA
Foliations
Fold axes
Lineations
Skattskär
Kyrkogårdsö
Storskär
75
85
85
75
Kyrkogårdsö
Skattskar
Storskar
Main shear zone
HELLSÖ
Foliations
Fold axes
Lineations
85
65
70
75
Hellsö
80
75
80
65
80
80
80
W Kökar
80
75
85
85
85
W KÖKAR
Foliations
Fold axes
Lineations
Hellsö
W Kökar
Main shear zone
5 km

zone. South and southwest of the shear zone (most observations from S and SW Kökar), the lineations likewise have a southeasterly trend, however being more concentrated (less variation in trend directions) and displaying a steep plunge.

Kökar and Hellsö areas

The foliations and, especially, fold axes measured from W and S Kökar display different trends compared to the measurements from Hellsö, northern Kökar (fig. 4.11). The differences reflect the structural transition from the less deformed gneisses in the SW toward the shear zone margin exposed on Hellsö as described below.

In W and S Kökar, the rocks are dominantly granites and granodiorites, with occasional lenses/horizons of amphibolite-rich intermediate rocks and basic diorites/gabbros. The foliations dip steeply toward south, striking dominantly E-W to ENE-WSW (fig. 4.11). The measured folds have ENE plunging axes that seem to cluster in two groups, one with steep axes and one with shallow axes. The shallow axes are interpreted to represent the F_1 fold axes that possibly formed during co-magmatic deformation/compression (D_1), while the steeper axes are measured from F_2 folds that refold the S_1 foliations. All measured foliation poles are slightly scattered along a great circle, revealing a slight tendency toward gentle (F_3?) folding along steep, approximately SSE plunging fold axes that has not, however, been directly observed in the field.

Toward Hellsö (NE Kökar), the mainly granitic and granodioritic rocks become clearly more intensely deformed, although there is a larger, less deformed lens NE of Hellsö (the Kuggholma lens in fig 4.6) where tonalitic and dioritic rocks are common. Within the lens, the foliations are clearly oblique with respect to the main shear zone foliation strike (fig. 4.12). Compared to W Kökar, the strikes of the foliations in Hellsö granitoids rotate slightly counter clockwise and become less steep. The folding pattern along the shear zone margin that refolds the F_2 folds around the approximately SE plunging F_3 fold axes becomes clear (fig. 4.11a and b). The Hellsö F_3 fold axes show some scatter, possibly reflecting the presence of refolded F_2 folds that can in places be visually observed, or a slight rotation and/or continued folding of the F_3 folds during shearing and/or during the last D_4 deformation phase. The F_3 folds have been observed in both meso- and macroscale; for example, the cape of Sväleholm on W Hellsö is essentially a large, synclinal open fold with a SE plunging fold axis (appendix 1). The flanks of the F_3 folds are often marked by minor (m-scale), NW-SE striking, steeply dipping shear zones, which in turn are often intruded by slightly deformed pegmatite dykes (fig. 4.11 and 4.11a).

Fig. 4.11. The stereographic projections and a simplified 3D sketch illustrating the structural interpretation of the Kökar area (see text for discussion). The stereonets are lower hemisphere, equal area projections. **a)** A photo from Hellsö of a flat lying fold with a gently toward SE plunging fold axis. On the northern side (left side of the picture), the fold is bounded by a local shear zone with a steeply dipping foliation in which a pegmatite dyke is intruded; the southern contact cannot be observed (under water). The same structural pattern (flat folds with SE plunging axes bound by steep, local deformation zones) is repeated throughout Hellsö. Length of compass ca. 15 cm,

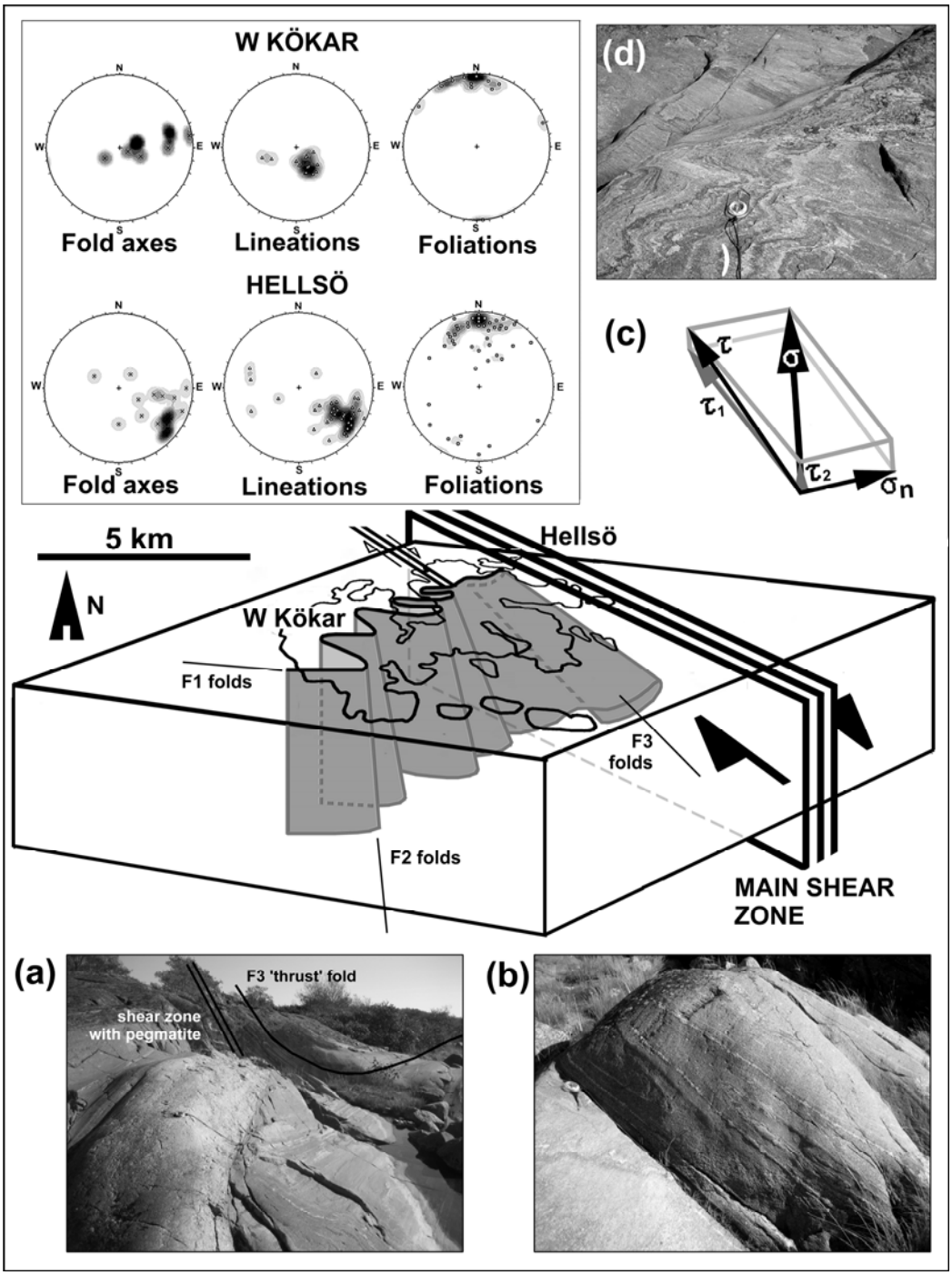

view toward SE. **b)** Refolded F_2 folds on Hellsö; the southern flank of the synclinal flat F_3 fold is not visible in the photo (to the right of the photo) Length of compass ca. 15 cm, view toward E. **c)** Qualitative representation of the stress components during D_3 deformation on Hellsö; σ = total stress, τ = shear stress (τ_1 = horizontal component, τ_2 = vertical component), σ_n = compressive stress. The F_3 folds are thought to have been formed as a response to the σ, while the partitioning of τ facilitated the formation of the local and regional shear zones. **d)** The lineations in Hellsö are dominantly mineral (stretching) and crenulation lineations, associated with the flat folds. Length of the compoass ca. 15 cm.

The stretching lineations on S and W Kökar plunge steeply and consistently toward SE, i.e. do not appear to follow the F_2 folding pattern (fig. 4.11). The lineations were there-fore formed (or the earlier L_1-L_2 line-ations rotated) after the D_1-D_2 deformation phases. Besides the gentle folding described earlier, the SE plunging lineations are the only observed indications of the D_3 deformation phase affecting S and W Kökar. D_3, in other wods, did not considerably affect this area. The mineral and stretching lineations on Hellsö are also less steep than in S and W Kökar and slightly scattered along a great circle, although in the field they are still clearly associated with the fold axis directions (fig. 4.11d). The gentle plunges of the Hellsö lineations can most likely be connected to the shear stress (stretching) component associated with the local stress field (τ in fig. 4.11c) along the shear zone, producing a thrust or a lateral flow toward NW along the margin of the shear zone. On the other hand, the F_3 margin folds themselves are interpreted to have formed as a response to the normal stress (flattening) component of the D_3 defor-mation (σ in fig. 4.11c). Deformation partitioning has thus lead to enhance-ment of one deformation type in one part of a rock volume, and of the other in other parts of the same rock volume, thus producing areas where either pure shear or simple shear deformation is dominant. The slight scatter of the lineations may reflect a briefly continued tightening of the F_3 folds during subsequent deformation, or result from a slight rotation of the stress field during the last folding and shearing phase. In any case, the southeasterly direction of the flat fold axes and lineations, combined with the dextral kinematics of the entire shear zone, indicate overall thrusting toward NW such that the block SW of the shear zone moved upwards relative to the block NE from the shear zone.

Kyrkogårdsö and Skattskär areas

In the Kyrkogårdsö area within the main shear zone, the gently anastomosing pattern of the shear zone is reflected in the slight scatter along a great circle of the poles to the foliations (fig. 4.13). The F_3 margin folds with shallow axes have not been observed within the shear zone where the deformation is more intense, so they are either absent or become tight to isoclinal, thus indistinguishable from the shear zone foliation. Small shear and buckle-type folds that formed due to a competence difference between layers and lenses with different compositions (e.g. granitic/granodioritic vs. tonalitic) are common within the shear zone, while observations of large-scale folds are relatively uncommon. The larger folds that have been measured, however, show axes plunging relatively steeply toward SE (fig. 4.13). These folds are commonly shear folds with dextral geometry (z-folds) that possibly started to form already during D_2, although the folds probably continued to tighten and were slightly refolded during subsequent deformation phases. The measured fold axes are slightly rotated towards south (130-140º) compared to the direction of the main foliation within the shear zone (ca. 120º). The stereographic projection of the measured fold axes shows some axis polarity; fold axes plunging in opposite directions have been observed relatively close to of the fold axes during transpressive deformation with a vertical

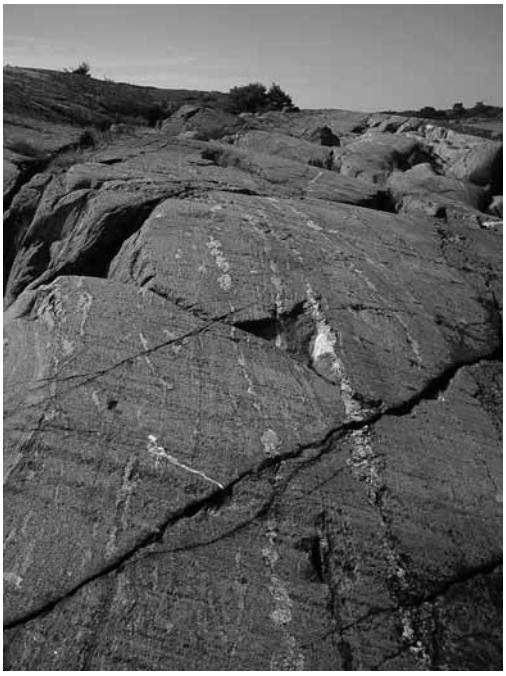

Fig. 4.12. A photo from Kuggholma on NE side of Hellsö, Kökar (see also fig. 4.6.). The Kuggholma lens within the shear zone is dominantly composed of dioritic and gabbroic rocks. The foliations within the lens strike ca. SW-NE, i.e. oblique to the main shear zone foliation. The granitic and pegmatitic dykes within the mafic rocks are boudinaged. View toward SW.

component, producing slightly conical folds or sheath folds.

The vertical shear component (figs. 4.13a and b) apparently becomes stronger in Kyrkogårdsö-Skattskär area, as opposed to Kökar and Hellsö areas further SE. This may be due to the increasing amount of amphibole-rich rocks as the NW part of the study area is approached; as the amphibole-rich rocks are, in the metamorphic conditions the prevailed in the area, rheologically stronger than more felsic rocks that are common in Kökar and Hellsö, they can be expected to be more resistant to the lateral flow along the shear zone margin. In other words, the increasing vertical component and the rheologically stronger rock types in the NW may have contributed to stronger strain partitioning, so that the flatly lying margin folds common on Hellsö are absent further NW, the strain having been partitioned into local and large-scale shear zones and sheath/conical folds in instead. At the shear zone margin, however, the large-scale F_3 margin folds do exist, but are less pronounced and only observable as a rotation of gneissose foliations around steep, NW-SE trending fold axes as the main SJSZ is approached (fig. 4.11, appendix 1).

The stretching lineations within the main shear zone, i.e. in the Kyrkogårdsö area, dominantly plunge steeply to gently toward SE (fig. 4.13). The slight scatter of the lineations around a NW-SE axis possibly reflects the complex 3D (re)folding pattern within the shear zone during which conical and sheath folds formed. In other words, the lineations were probably mostly formed earlier and were subsequently slightly folded and rotated as the shearing proceeded.

In Skattskär and neighbouring skerries, SW of the Kyrkogårdsö area of the main shear zone, the foliations are steep, striking roughly NE-SW but slightly anastomosing (fig. 4.13). The deformation of the granodioritic and tonalitic rocks is intense, in places mylonitic (fig. 4.13c). Three types of folds have been observed in the Skattskär area. Firstly, the gneisses were folded, possibly already during D_2 to form mesoscale, sinistral shear folds ('s-folds'), the axes of which plunge rather steeply toward SW (fig. 4.13d). These folds probably continued to tighten during D_3. Secondly, it is evident from the field observations (fig. 4.13) and the

geological maps (appendix 1) that the fold axes in the area were subsequently refolded along the large-scale F_3 margin folds with NW-SE axial planes, although the fold axes are much steeper in Kyrkogårdsö-Skattskär area than on Hellsö. The slightly anastomosing pattern of the foliations in Skattskär area may at least in part be a result of this folding. The third type of folds is represented by mostly mesoscale F_3 folds with steep, approximately NW-SE axial planes (figs. 4.13 and 4.13e). These are interpreted to be 'step-over folds', formed at step-over sites between two local sinistral, mylonitic shear zones. An interesting observation especially evident with these folds is that earlier boudines are frequently refolded as the step-over folds were formed (fig. 4.13e). This indicates that a period of extension that produced the boudines preceded the compression phase during which the folds were formed.

Also in Skattskär area, the trends of the stretching lineations are scattered, indicating a similar history for the development for Skattskär lineations compared to the Kyrkogårdsö lineations. The lineations are in other words interpreted to have formed during an early deformation phase (D_2?) and subsequently rotated as the rocks were refolded. However, despite the scatter, both the Kyrkogårdsö and Skattskär lineations display general trends towards SE and NE, respectively, indicating that the shear zones in both areas have some control of to which positions the lineations rotated.

The Kyrkogårdsö and Skattskär areas add to the structural evidence of large-scale deformation partitioning into a compressive component that resulted in multi-phase folding, and into a simple shear component that simultaneously produced flow along the fold axial planes and along the margin of the SJSZ. The evidence implies, in agreement with the previously discussed Kökar and Hellsö areas, that the relative movement of the crustal block SW of the shear zone was upwards compared to the crustal (LSGM) block NE of the zone. However, there are some obvious differences compared to the Kökar and Hellsö areas. The simple shear component of the deformation was dominantly but not entirely accommodated by the main shear zone (SJSZ) and parallel minor shear zone like on Hellsö, but conjugate strike-slip (NE-SW) sinistral high-strain zones along the southwestern F_3 margin fold limbs (Skattskär) developed instead. Further toward NW along the SJSZ, the structures show increasingly different characteristics, as will be demonstrated below.

Fig. 4.13. The stereographic projections and a simplified 3D sketch illustrating the structural interpretation of the Kyrkogårdsö-Skattskär area (see text for discussion). The stereonets are lower hemisphere, equal area projections. The sinistral shear zones and stepover folds in Skattskär area are moved from their actual position for clarity. **a)** and **b)** Qualitative representation of the stress components during D_3 deformation in Skattskär area (a) and Kyrkogårdsö area (b); σ = total stress, τ = shear stress (τ_1 = horizontal component, τ_2 = vertical component), σ_n = compressive stress. The compressive stress component was accommodated by the folds (both by the shear folds within individual deformation zones and by the large-scale F_3 margin folds), while the shear stresses were partitioned into shear zones. **c)** Mylonitic sinistral shear zone on Skattskär. Length of the compass ca. 15 cm. **d)** Minor sinistral shear folds ('crenulation') on Skattskär. Also meter-scale folds of this type are common. Length of the

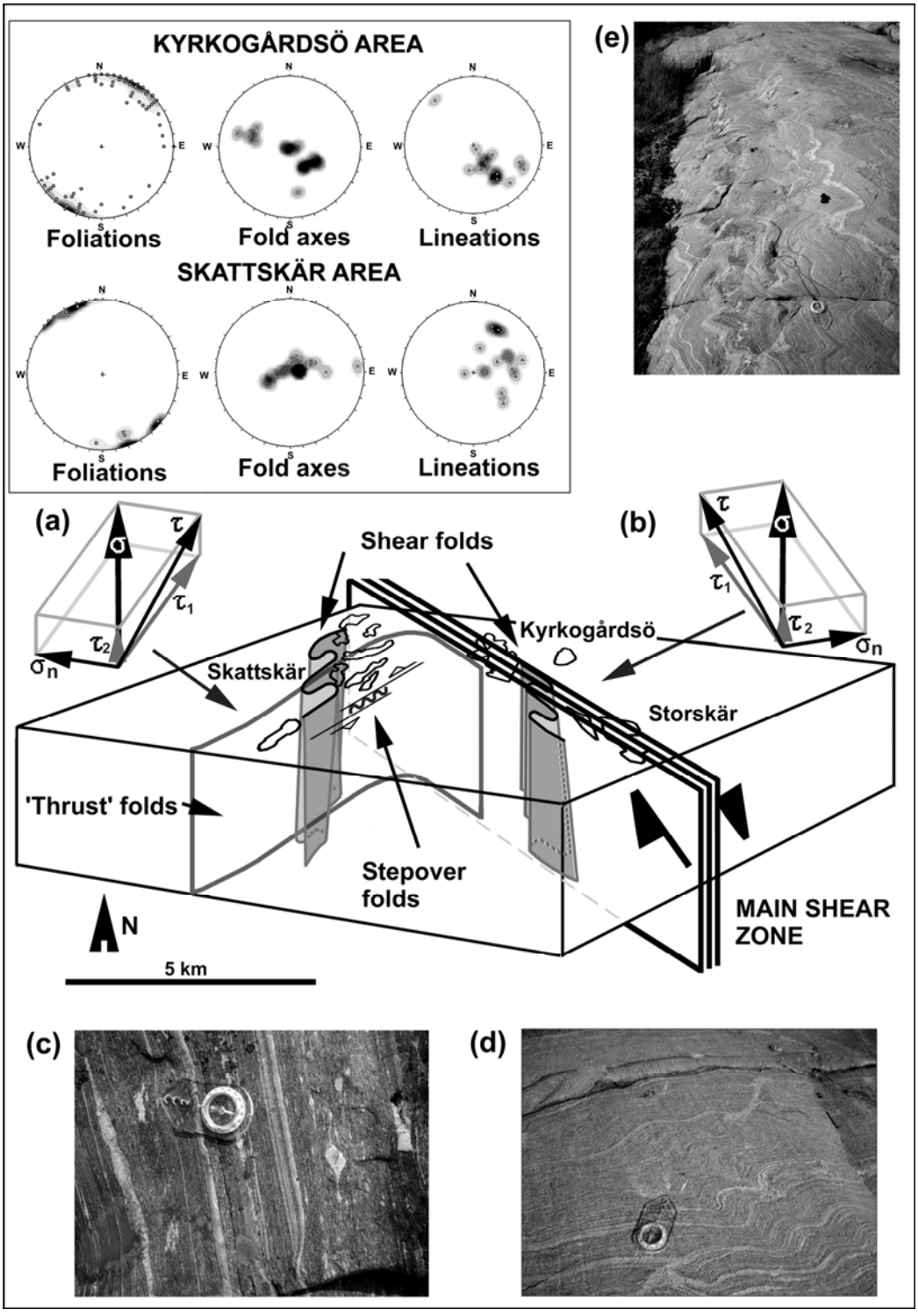

compass ca. 15 cm. **e)** 'Step-over' folds between two local deformation zones on Skattskär. Note the folded mafic boudines, indicating a change from earlier extension that formed the boudines, to compression that resulted in folding. Length of the compass ca. 15 cm

Husö and Finnö areas

The structural measurements in the Finnö area were made by Suominen (1972) and are reproduced from his thesis and reinterpreted here.

In Husö and, especially, Finnö areas, the granodiorites that are dominant in the SE part of the study area, give partly way to the more competent, amphibolite-rich tonalites, quartz-diorites and diorites (appendix 1). This clearly affects the deformation style and folding patterns within the area, the folds commonly being less rotated and more open than the folds towards the SE parts of the study area where granites and granodiorites dominate. In addition to the gneisses, dykes of postorogenic microcline granites that are very common further NW in Sottunga make their first appearance in Finnö area.

On the island of Husö, situated in the middle of the main shear zone, the foliations follow the same anastomosing pattern as in the Kyrkogårsö area (fig. 4.14). The exposed rocks are still frequently granodiorites, although the amphibolite-rich tonalitic and dioritic gneisses become increasingly common. The rocks are intensely deformed, showing steep lineations and strongly sheared fabrics as well as narrow mylonitised zones both along and cutting the gneissose foliation (figs. 4.14a and b). In places there are dioritic lenses that seem to intrude the ductile gneisses (fig. 4.14c). A calc-silicate horizon follows the gneissose foliation on the SW side of the main island (appendix 1). The folds on Husö show dominantly steep fold axes, with a very slight tendency to polarity as a result of the vertical SW-side up component of the transpressive deformation; fold axis plunging in opposite directions (NW and SE) have also been measured from Husö main island (appendix 1). Further NW from Husö area, conical and sheath folds become increasingly common as the vertical component of the regional shearing increases.

In Finnö area, the amphibolite-rich rocks are even more common than in the Husö area. The relatively steeply dipping foliations strike mainly toward ESE-SE (fig. 4.14, appendix 1). Together, all of the poles to the foliations show a slight scatter around a great circle, reflecting the large-scale folding around SW-NE trending axial planes. The main SJSZ is exposed in northern parts of Finnö area as the shear zones starts to widen and divide/splay itself, and the foliations in this area therefore show a NW-SE strike instead of the E-W strikes in S and SW Finnö.

The folds that have been measured in Finnö area are dominantly sinistral shear folds that show fold axes plunging moderately to steeply toward SW-W. The fold axes plot into a small semi-circle, indicating a half-cone –type refolding of the measured fold axes. The measured fold axes of the sinistral shear folds are interpreted to represent F_2 folds, while the conical folding pattern that emerges in the stereographic projection is here interpreted to have been formed during D_3, i.e. that the sinistral folds were subsequently refolded into the conical folds as the deformation progressed. The refolding of the rocks to form the conical folds is closely related to the formation of the large-scale F_3 margin folds (fig. 4.14). This scenario might imply that the vertical component of the shearing that was

caused by the τ_2 component of the local stress field (fig. 4.14d) increased from D_2 to the D_3 deformation phase, although the possible conical appearance of the first sinistral shear folds might also have been destroyed as the deformation proceeded. The stretching lineations observed in Husö are almost invariably steep and relatively unscattered, thus appearing to be related the last ductile deformation phase within the Husö area (fig. 4.14) Also in Finnö area, most of the lineations plot in a quite tight cluster and seem to be related to the fold axes as they plunge dominantly toward SW. The steepness of the observed lineations and fold axes, especially in Husö area, may reflect a dominating pure shear component of the last deformation phases (Dewey et al. 1998). Also, field observations of wide, relatively high-T mylonite zones indicating strong deformation partitioning within the ductile regime are much less common in Husö area than in e.g. Kyrkogårdsö and Skattskär areas. Instead, the mylonite zones in the Husö-Finnö area are almost invariably narrow, indicating higher strain rates and more intense deformation partitioning into simple and pure shear components, probably due to presence of rheologically stronger rock types. The increasing pure shear component is also preliminary allocated to the different rheology of the amphibole-rich rocks compared to the more granite-granodiorite –rich lithologies in the SE parts of the study area. It is also possible that the NW parts of the study area represent a somewhat deeper crustal level than the SE parts, which would explain both the pure shear dominated deformation style and the widening of the shear zone toward NW.

Sottunga

Like in Husö-Finnö area, the amphibolite-rich rocks are clearly more common in Sottunga than in the Kyrkogårdsö-Skattskär and Kökar-Hellsö areas, thus contributing to a higher competence of the rocks as a whole. Therefore, especially the folding patterns are slightly different compared to the granite and granodiorite-dominated areas towards SE. The island of Sottunga displays some structural characteristics such as D_3 (D_2?) sheath folds not directly observed and measured elsewhere (fig. 4.15 and 4.16). This may imply that the vertical shear stress component τ_2 is even stronger in Sottunga than elsewhere within the study area (fig. 4.16a). The shear zone also seems to split up or anastomose around the island such that the main shear zone continues around the island along its northwestern shore, while to the SW side there is a fault zone that separates Sottunga island from Föglö islands (appendix 1, fig. 4.6). The island of Sottunga may represent a tectonic lens within the shear zone, in a similar manner to, although in a larger scale than the Bredskär and Kuggholma lenses further SE (fig. 4.6). The late- and post-orogenic granites (ca. 1.79 Ga Mosshaga pluton and associated dykes) intruded the bedrock in this area, probably because a local stress minimum formed within the anastomosing shear zone.

The rocks that form the approximately 10 km long and 3 km wide island consist of granodioritic, tonalitic and dioritic gneisses and

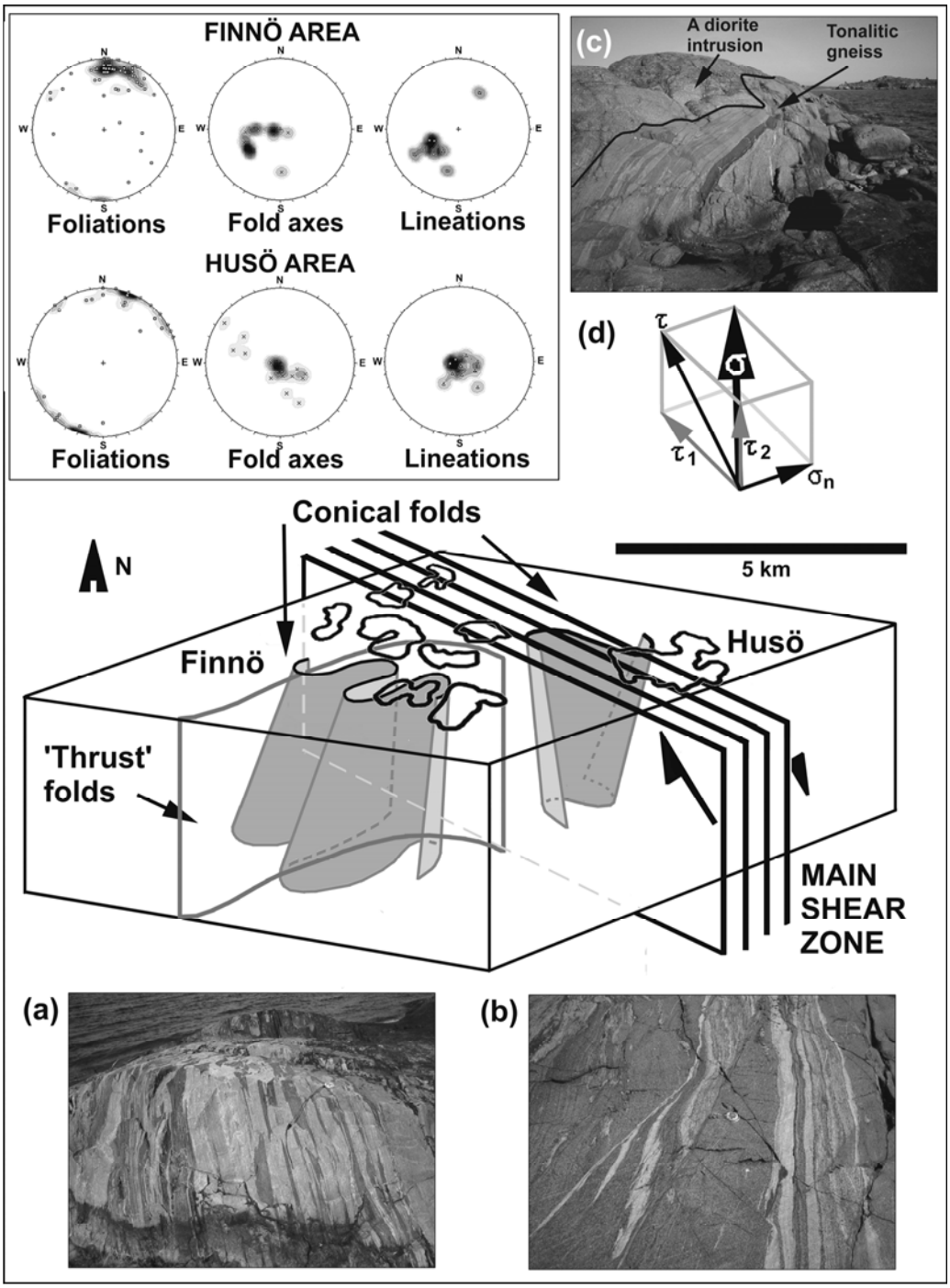

Fig. 4.14. The stereographic projections and a simplified 3D sketch illustrating the structural interpretation of the Husö-Finnö area (see text for discussion). The stereonets are lower hemisphere, equal area projections. **(a)** Tonalite gneiss with strongly flattened dioritic fragments. The steep stretching lineation in the Husö gneisses is reflected in the vertical stretching of the fragments. View toward NW, length of the compass ca. 15 cm. **(b)** A narrow fine-grained mylonite band cutting the gneiss, Husö. View toward E, length of the compass ca. 15 cm. **(c)** A diorite intruding the tonalitic gneisses on Husö. View toward W. **(d)** Qualitative representation of the stress components during D_3 deformation in Skattskär area (a) and Kyrkogårdsö area (b); σ =

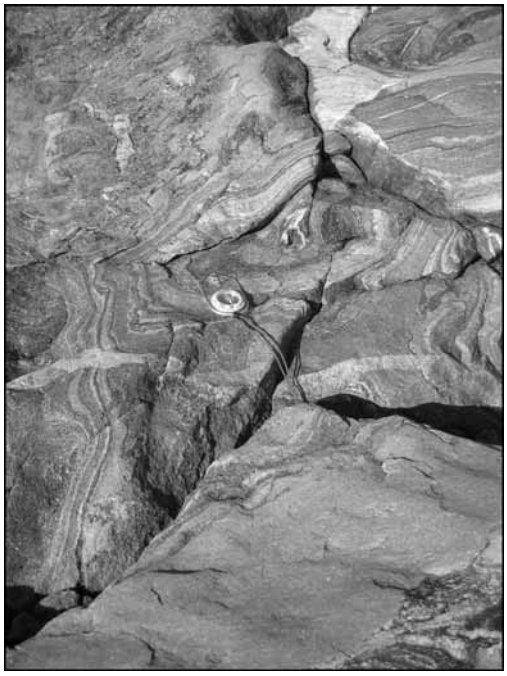

Fig. 4.15. A minor sheath fold in granodioritic gneiss in SW Sottunga. The postorogenic microcline granite dyke in the foreground is only very weakly deformed. The length of the compass ca. 15 cm.

amphibolites which, especially toward the Mosshaga pluton, are intruded by slightly deformed postorogenic microcline granite veins and dykes dated at ca. 1.79 Ga (Ehlers et al. 2004). The granite veins may reflect the early, less voluminous stages of the approximately coeval Mosshaga plutonism, and they appear to intrude the gneisses in pulses as the granites show slightly different appearances (colour, grain size). The granites probably intruded more or less simultaneously since their cross-cutting relationships do not show any consistent age relationships, i.e. two granite types of which one is at one location cut by the other, may at another location show opposite relationships (fig. 4.15).

Due to the abundant and complex folding and dyking on Sottunga, the measurement of foliation strikes and dips is relatively difficult. The scatter of the poles to the foliations measured on Sottunga reflects the complex folding patterns in the area (fig. 4.16). However, there appears to be a slight tendency of the foliations to bend around N-S directed axial planes. On the other hand, field observations reveal approximately SW-NE directed deformation zones that in many places cut and misplace some of the earlier folds, and that are interpreted to represent the last ductile deformation phase D_4 (fig. 4.16c).

At least three different fold types can be observed in the field. The tight to open folds with dominantly toward E-W to ENE-WSW plunging fold axes, interpreted to represent folding during D_2 deformation phase, occur throughout the island. These E-W fold axes show a tendency to plot in small circles in a manner that very much resembles that observed in the Finnö area, indicating a refolding of the E-W axial planes around relatively steep, WSW but also NNE plunging cone and sheath fold axes (fig. 4.16). These conical folds as well as the sheath folds are interpreted to have been formed during D_3. The sheath folds are measurable in the field, their symmetry planes trending dominantly ENE-WSW (fig. 4.16b). The sheath fold axes do not show any significant refolding when plotted on a stereographic projection, although in the field a slight tendency of the

total stress, τ = shear stress (τ_1 = horizontal component, τ_2 = vertical component), σ_n = compressive stress. The increasing vertical component (τ_2) of the shear stress has lead to the formation of conical and sheath folds in the area.

sheath folds to bend along SSE directed axial planes can be observed. The small amount of refolding suggests that the sheath folds were formed at a relatively late stage during the deformation history of the area. The third type of folds are the gentle to open folds with steeply southward plunging fold axes; these refold all of the earlier fold types, including the sheath folds as mentioned above (fig. 4.16d and 4.17). It is unclear whether these late, open folds with N-S axial planes formed during late stages of the D_3 deformation phase, representing what in other areas are called F_3 margin folds, or whether these folds were formed separately during D_4. However, in NE Sottunga close to the southern margin of the main SJSZ, the N-S axial planes appear to rotate toward NW-SE, and the folds themselves become tighter. Thus, the 'N-S folds' can probably be most closely related to the F_3 margin folds observed in the more southeasterly parts of the study area.

The bulk of the stretching lineations on Sottunga plunge moderately to steeply toward SW (fig. 4.16). They appear to follow the conical E-W folds to some extent, but are in the field rather associated with the approximately SW-NE directed deformation zones (fig. 4.16c). These sinistral deformation zones again form a conjugate pattern to the main shear zone, in a similar manner to those in Skattskär area. The shear zones may have initiated during D_3, although it is likely that significant amount of deformation along these zones occurred during D_4 since they have apparently not been folded in any great extent. The 'N-S folds' and the sinistral shear zones seem to be connected such that the regional N-S directed transpressive stresses were in part accommodated by shear strain along the sinistral shear zones as well as the main SJSZ, and in part by partitioning of the compressive deformation into the open folds with N-S axial planes.

Other structures

Within the main shear zone, but also in places along its southern margin, competency difference between the mafic and felsic rock layers have led to formation of different mesoscale structures such as boudines and layer pinching, 'drag' folding (e.g. the step-over folds in Skattskär), and to development of brittle cracks *en echelon*. Most commonly, the mafic rock layers behaved in a more brittle manner than their more felsic neighbours, but there are some exceptions.

Fig. 4.16. The stereographic projections and a simplified 3D sketch illustrating the structural interpretation of Sottunga area (see text for discussion). The stereonets are lower hemisphere, equal area projections. **(a)** Qualitative representation of the stress components during D_3 deformation in Skattskär area (a) and Kyrkogårdsö area (b); σ = total stress, τ = shear stress (τ_1 = horizontal component, τ_2 = vertical component), σ_n = compressive stress. The increasing vertical component (τ_2) of the shear stress has resulted in the formation of the abundant sheath folds in the area. **(b)** Schematic representation of the sheath folds observed in Sottunga. The sheath fold axes plunge relatively steeply toward ENE; the sheath folds seem to have been formed at relatively late stages (F_3) as the stereographic projections do not reveal any significant refolding of the sheath folds. **(c)** Sinistral, steeply dipping SW-NE striking D_4 shear zones can be found in many places, cutting and obscuring the earlier folds and foliations. Photo from SW Sottunga. At this locality, a postorogenic pegmatite dyke intrudes the shear zone (left side of the photo).

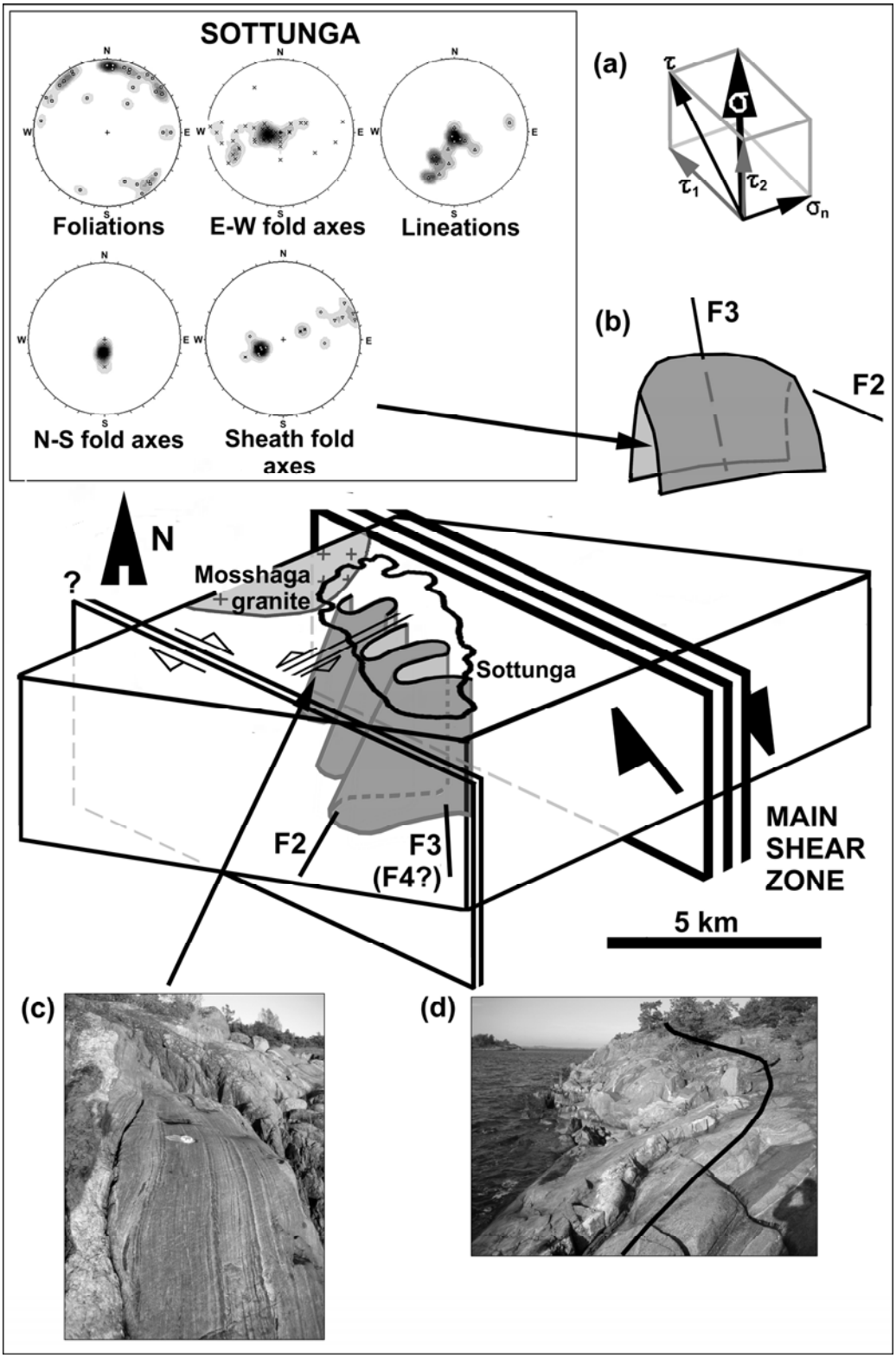

Length of the compass ca. 15 cm. **(d)** A large F_3 (F_4?) fold in S Sottunga with an approximately N-S fold axis. These N-S folds refold all of the other fold types. View toward W.

Both horizontal and vertical boudinaged ('chocolate-tablet' structure) and layer pinching along the strike of the shear zone is a common phenomenon (figs. 4.18a and b). Outside the main shear zone in Skattskär area the boudines have sometimes been folded (fig. 4.13e), indicating a change in the deformation style and the stress field from lateral extension to compression. Usually, the mafic layers within felsic rocks have been boudinaged, reflecting the higher competence of the mafic layers, although occasionally also the opposite case is observable and a mafic layer has behaved in a rheologically weaker manner (mullion-style deformation; e.g. Talbot & Sokoutis 1992). South of the shear zone, within the E-W to ENE-WSW gneissose F_2 foliation, boudinage is less common and also less intense. Mullion-type structures where the mafic layers were less competent than the granites seem instead to be a more common phenomenon, especially in W Kökar (fig. 4.18c). These 'fold mullions' (Talbot 1998) may have been formed at rather high temperatures, while the boudines and the pinched layers closer to and within the main shear zone were probably formed at somewhat lower temperatures. The presence of boudinaged and pinched layers within the main shear zone indicate that there was a significant flattening pure

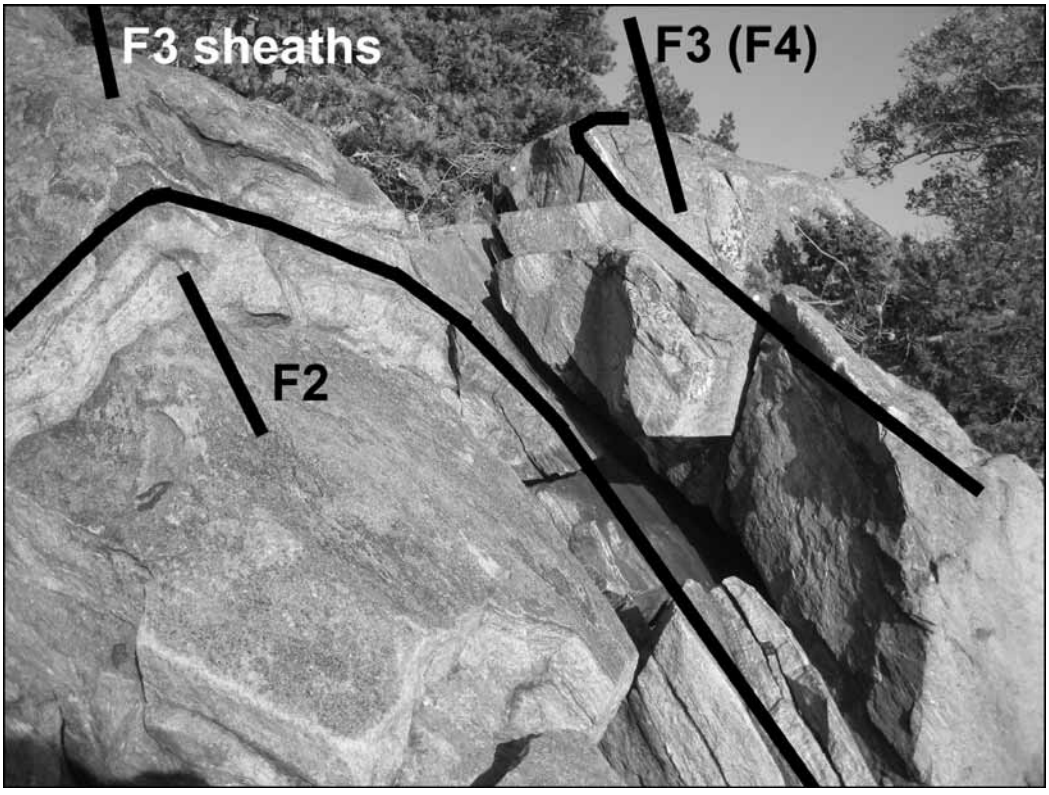

Fig. 4.17. In this locality in SW Sottunga, all three common fold types observable in the area are represented. The early, here relatively flatly lying F_2 folds are refolded into sheath folds during F_3. Both folds are subsequently refolded with the steep N-S directed open late F_3/F_4 folds. View toward E.

shear component involved to the overall ductile shearing, which implies that the shape of the total strain ellipsoid for the gneissose deformation may rather be oblate than prolate, also for the most parts of the main SJSZ. Only the latest, D_4 deformation phase during which most of the mylonites started to form seems to have been dominated by simple shear deformation. On the other hand, the coexistence of flanking structures with some boudinaged/pinched structures (fig. 4.18b) indicates simultaneous strong pure shear and simple shear components (i.e. general shear), confirming the earlier conclusions made e.g. by Ehlers et al. (1993) of the transpressive nature of the regional stress field.

Brittle cracks *en echelon* formed in many places within more competent, amphibolite-rich horizons and lenses during the ductile, gneissose deformation (fig. 4.18d). The presence of the cracks further witnesses of the strong competency difference between the different rock types within the prevailing conditions of (D_3) deformation.

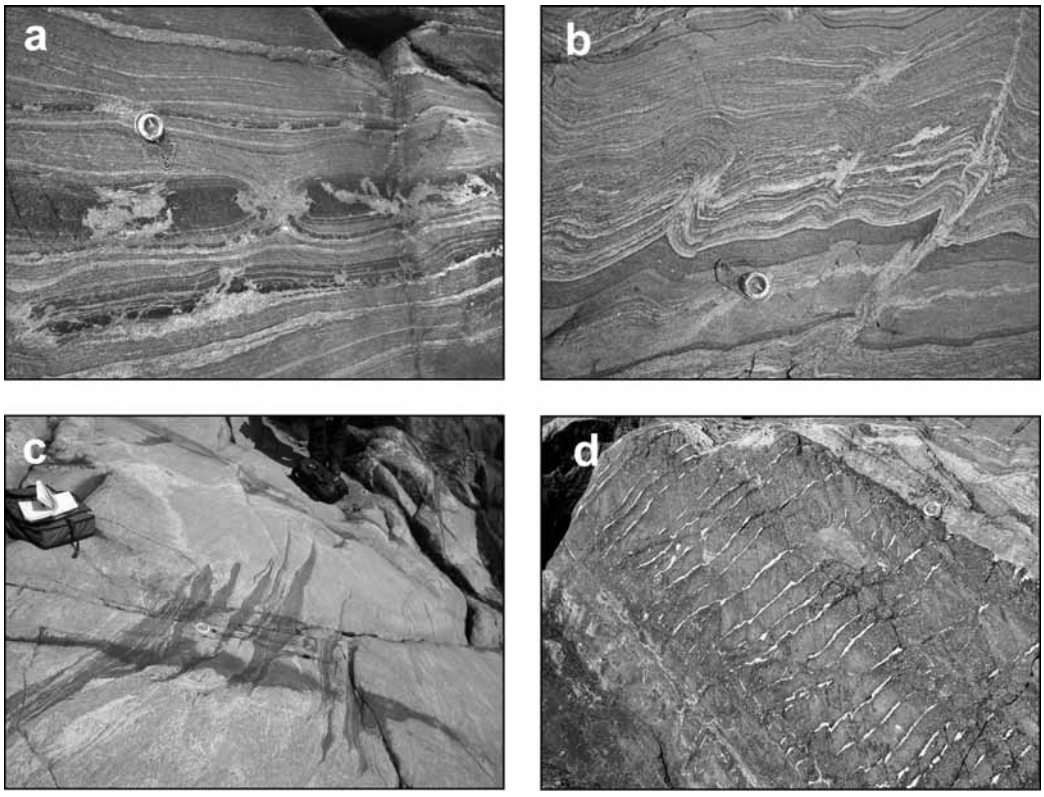

Fig. 4.18. (a) A boudinaged mafic layer within the main shear zone on Storskär, Kyrkogårdsö. The felsic rocks have straight, steeply dipping foliations. The length of the compass ca. 15 cm. **(b)** Layer pinching and flanking structures in a gneiss layer that is slightly more amphibole-rich than the surrounding granodioritic-granitic rocks. Storskär, Kyrkogårdsö, length of the compass ca. 15 cm. **(c)** Mullion-type deformation where the mafic dykes have been more incompetent than the granite gneisses. W Kökar. **(d)** Cracks *en echelon* in W Hellsö, filled with secondary quartz. The cracks formed during D_3 due to overall lateral extension within an amphibolite layer, while the surrounding granodiorite gneisses deformed more ductilely. Length of the compass ca. 15 cm.

4.2.2.2 *Mylonites*

Two mylonitisation styles can be observed: wide, decimetres to up to tens of meters wide mylonite zones that have the same strike as the foliation of the gneissose wall rocks; and narrow, centimetre-scale mylonitised shear bands that often cut the pre-existing gneissose foliation (fig. 4.19). Based on the field observations, it is therefore likely that mylonitisation occurred during at least two separate deformation phases. No location has however been found where the two mylonite types cut each other, so the relative age of the two types remains uncertain. On the other hand, since the wide mylonite zones include relatively coarse-grained mylonites as well as fine-grained ultramylonites, while the narrow mylonite zones are invariably fine-grained, it is likely that the wide zones were at least initially formed in higher-grade conditions than the narrow zones, although it is likely that the wide zones were repeatedly active during multiple deformation stages. In the field, the wider mylonite zones also commonly follow the gneissose foliation, also when the foliation is slightly folded; this is reflected in the stereographic projection of the poles to the strike and dip of the wider mylonite zones within the SJSZ (figs. 4.19e and f).

Mylonites thus record the late stages of the ductile and semi-ductile, late- to post-orogenic, high strain rate deformation. There seems to be a rather large jump in PT-conditions to the next, brittle deformation phase that locally produced pseudotachylytes; also cataclasites are only rarely observed. This may be due to rapid exhumation of rocks from the ductile and semi-ductile conditions into the brittle regime and/or indicate a pause in regional tectonic activity while the rocks were being exhumed.

4.2.2.3 *Pseudotachylytes*

Pseudotachylytes are widely accepted as witnessing the occurrence of fossil earthquakes, although other mechanisms for pseudotachylyte formation are recognised (see chapter 2.2). The relatively small volumes of melt that are generated during pseudotachylyte formation are cooled quickly due to the relatively low temperatures of the wall rock. Therefore, the melts are 'frozen' along tabular generation surfaces, or, very commonly, into veins branching from the melt generation surface into the wall rock. It is recognised that conjugate sets of brittle fractures often form between two sets of subparallel generation surfaces (or 'paired shears'), and that the injection veins commonly localise along these conjugate fractures (e.g. Grocott 1981). The blocks that are defined by the conjugate shears are often rotated during movement, although only small amounts of melt are normally generated on the conjugate surfaces (e.g. Grocott 1981).

Within the study area, pseudotachylytes have been found in two locations: on the islet of Storskär close to the island Kyrkogårdsö, and in Hellsö, northern Kökar (figs. 4.6 and 4.20). At both locations, the pseudotachylytes form steep (vertical) generation surfaces, which strike NW-SE (ca. 130º) on Storskär, and approximately E-W on Hellsö. The pseudotachylytes formed in the aforementioned two locations are here referred to in singular form as the 'Storskär pseudotachylyte' and the

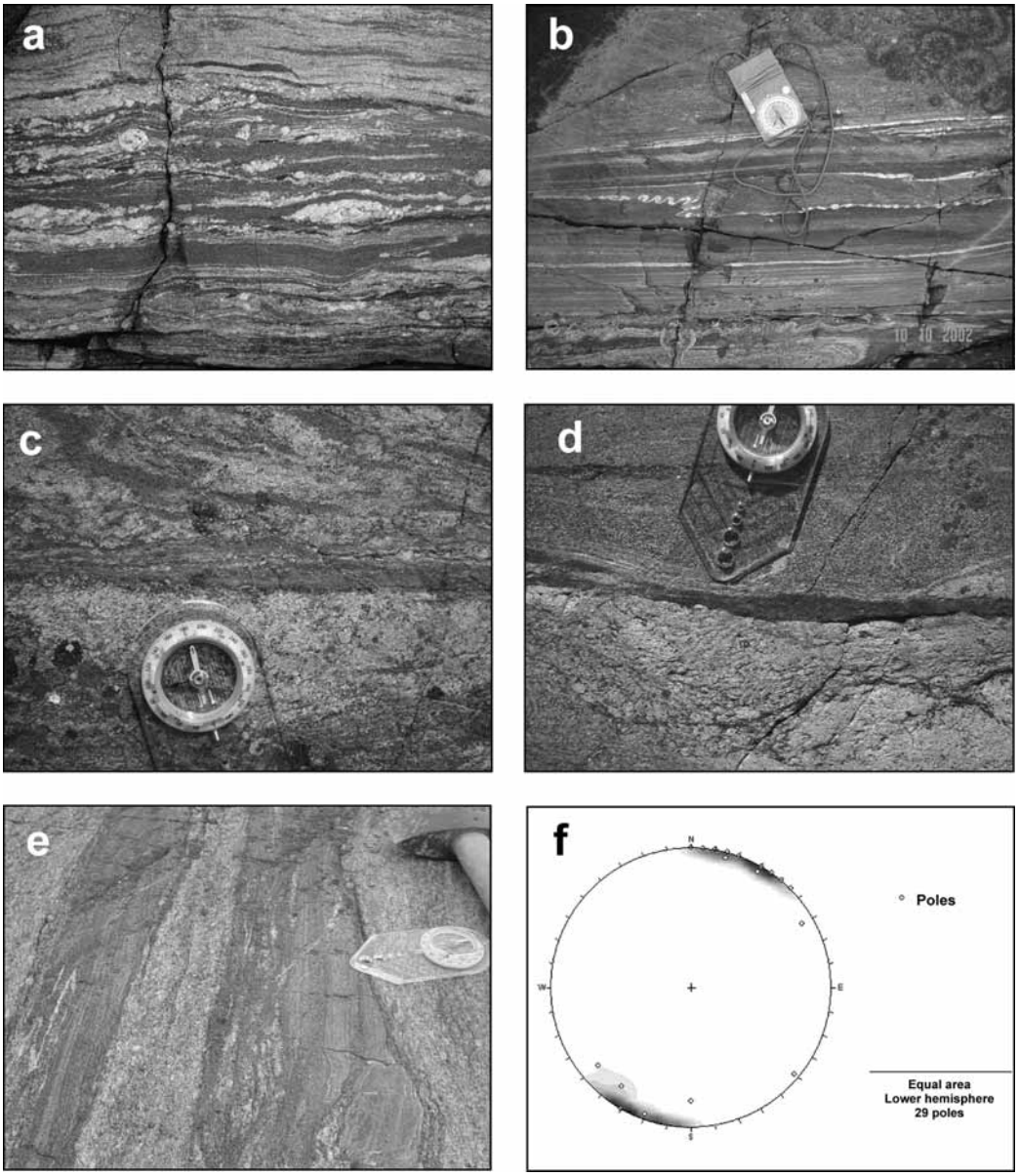

Fig. 4.19. Various mylonites within the study area. See also figures 4.5c, 4.6 and 4.13c. **(a)** A relatively wide, biotite-rich mylonite zone in a granodioritic gneiss, Kyrkogårdsö. Width of the photo ca. 40 cm, strike of the mylonitic foliation ca 120°. **(b)** A wide (>10 m) mylonite zone following the SW shore of Kyrkogårdsö island. Coarser mylonites and ultramylonites, both granodioritic and tonalitic, coexist within this zone. Length of the compass ca. 15 cm. **(c)** A narrow ultramylonite band in granodiorite. Kyrkogårdsö, length of the compass ca. 15 cm. **(d)** A narrow, biotite-rich ultramylonite zone in granodiorite. Husö, length of the compass ca. 15 cm. **(e)** A garnet-bearing, biotite-rich mylonite zone in a granodiorite gneiss. The mylonite zone is slightly folded together with the gneiss. It is probable based on the appearance and the mineralogical differences that this mylonite zone was initially a mafic dyke, intruded into the gneiss. Furthermore, due to differences in the rheological properties of the two rocks, the dyke mylonitized already at relatively high temperatures and during a relatively early deformation stage while the adjacent granodiorite still underwent gneissose deformation. Ejskär, Kyrkogårdsö, length of the compass ca. 15 cm. **(f)** Stereographic projection of the poles to the strikes and dips of the wider (>ca. 5 cm) mylonite zones along the main shear zone in Kyrkogårdsö area.

'Hellsö pseudotachlylyte', although in reality each location contains multiple sets of paired generation surfaces and associated conjugate shears. However, since all pseudotachylyte sets in each location show similar and comparable features, they are here treated as single units.

The Storskär pseudotachylyte is formed within the main shear zone, in a granodioritic wall rock showing steeply dipping, mostly regular and straight foliation striking ca. 120-130º. The pseudotachylyte formed without cataclastic or mylonitic precursors, the main generation surfaces being relatively straight and apparently parallel with the gneissose foliation in most parts of the studied rock volume (figs. 4.20 a-c and 4.21a). The Storskär pseudotachylyte shows sinistral offset along the main generation surfaces of ca. 4-5 m as evidenced by pegmatite dykes that are cut by pseudotachylyte (fig. 4.22). In this context it should be mentioned that generation of pseudotachylytes is suggested by some authors to be most effective along fault tips and fracture propagation fronts, and the apparent displacement does not therefore necessarily reflect the maximum fault displacement (Andersen & Austrheim 2006).

The Hellsö pseudotachylyte formed in a structurally more complex gneissose rocks at the SW margin of the main shear zone, i.e. not within the zone of the most intense shear deformation. In contrast to the Storskär pseudotachylyte, Hellsö pseudotachylyte is associated with mylonitic and/or cataclastic zones, the cataclasites and mylonites however predating the pseudotachylytes (figs. 4.20d-f). The mylonites and cataclasites may have had some local control on the orientation of the main generation surfaces although it appears from the field evidence that the pseudotachylytes formed largely independent of the previous fine-grained cataclastic/mylonitic zones (figs. 4.20d, e). The local control of the previous weakness zones may have resulted in the more irregular and strongly anastomosing appearance of the Hellsö generation surfaces compared to the generally relatively straight Storskär pseudotachylyte generation surfaces (fig. 4.21b). The kinematics of the Hellsö pseudotachylyte is not readily evident in the field due to the complex deformation style of the wall rocks.

For both Storskär and Hellsö pseudotachylytes, the melt generation surfaces are paired with conjugate sets of fractures that often serve as channels for injection veins cutting through the wall rock in between. The melt produced during the brittle failure was mostly deposited within the injection veins although in many places the melt also remained within the generation surface.

Fault orientation in general is dependable on the direction of the prevailing stress field so that conjugate fault sets commonly form oblique (20-45º) to the direction of the princi-

Fig. 4.20. Pseudotachylytes in the study area. **(a)** A slightly anastomosing pseudotachylyte generation surface running from the bottom left corner toward right side of the photo. An injection vein has intruded one of the conjugate shear fractures running from the generation surface toward the pen; this injection vein has also been sampled and dated (chapter 4.5). Sotrskär, Kyrkogårdsö, length of the pen ca. 15 cm. **(b)** A large melt pocket within a pseudotachylytegeneration surface. Storskär, Kyrkogårdsö, length of the compass ca. 15 cm. **(c)** Conjugate shear fractures with injected pseudotachylyte melt seen from a semi-vertical rock

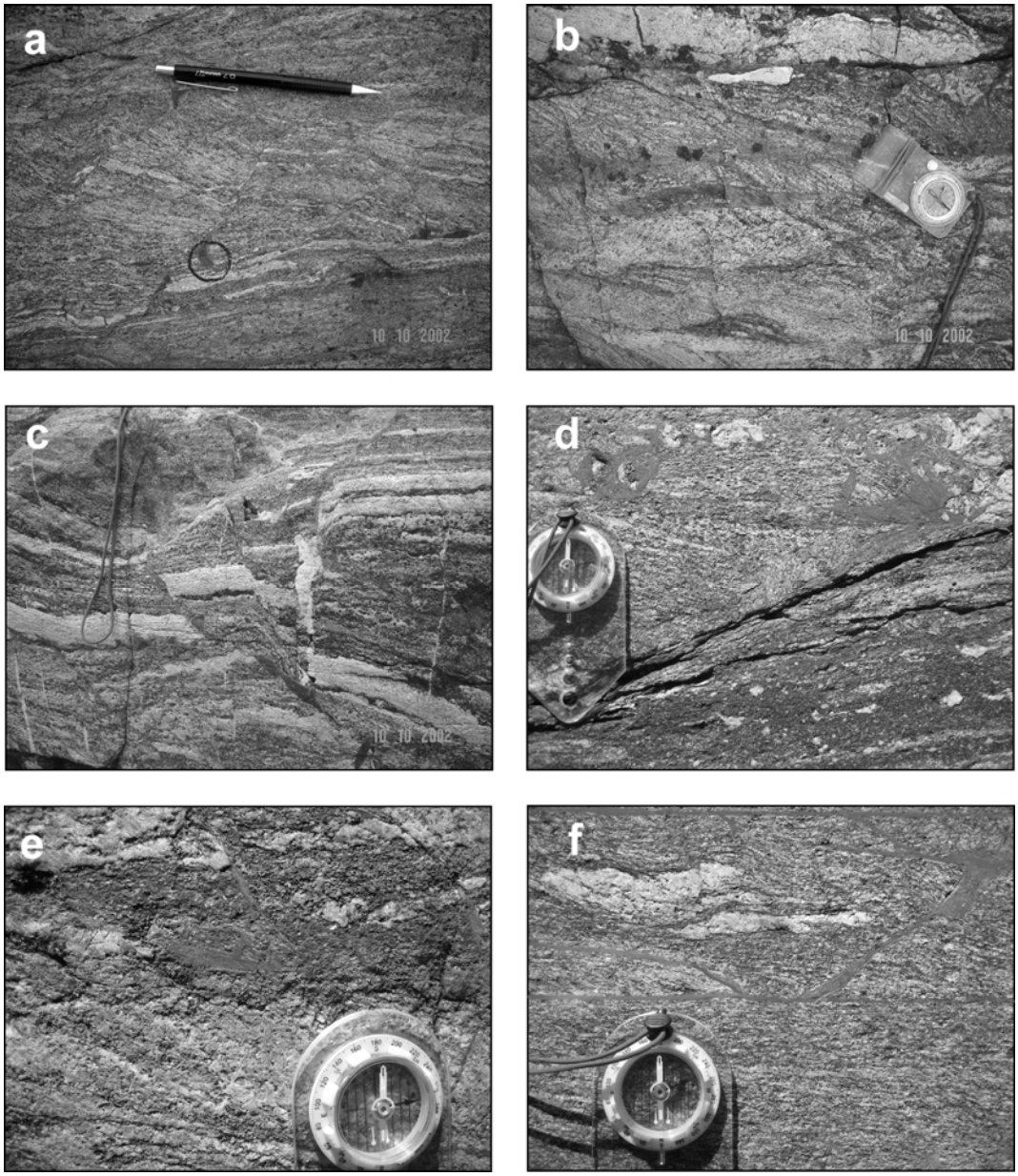

surface. Storskär, Kyrkogårdsö, width of the photo ca. 40 cm, view toward N. **(d)** Pseudotachylyte generation surface and large melt pockets (above compass). The cataclasite zone below the compass does not appear to control the pseudotachylyte generation surface. Hellsö, Kökar, length of the compass ca. 15 cm. **(e)** In this locality, the pseudotachylyte and the cataclasite (above the compass) are superficially associated; however, the generation surface (running from left to right just above the compass) cuts both the granodiorite gneiss and the cataclasite, and the pseudotachylyte conjugate shear fracture (running from the centre of the view upwards) cuts the cataclasite. Therefore, the cataclasite is older than the pseudotachylyte, and the pseudotachylitic deformation does not appear to be significantly controlled by the cataclasite zones. **(f)** A paired set of generation surfaces and associated conjugate shear fractures. The generation surfaces run from left to right, one just above the compass, the other at the uppermost margin of the view. A large melt pocket has formed within the conjugate shear fracture at the upper right corner of the view. Hellsö, Kökar, length of the compass ca. 15 cm.

pal stress σ_1, and intersect along the medium stress axis σ_2 (e.g. Park 1997). Among others, Grocott (1981) and Davidson et al. (2003) follow this principle in reconstructingthe approximate direction of the palaeostress field by measuring the directions of the conjugate fractures and the generation surfaces. This approach has been applied also for the purposes of this study. The strikes and dips of the pseudotachylyte generation surfaces as well as of the conjugate fractures were carefully measured in the two locations where pseudotachylytes have been found. Only those surfaces where the surface relationships (main generation, dextral conjugate or sinistral conjugate surface) were clearly observable and the strike/dip measurable with good accuracy were taken into account. The results of the measurements were plotted on stereographic projections (fig. 4.23a and c). Considering that i) the conjugate surfaces should intersect along σ_2; ii) that the principal stress axis σ_1 should bisect the angle α between the conjugate sets; and iii) that the other two stress axes σ_2 and σ_3 can be drawn at right angles from the σ_1, the approximate orientation of the palaeostress field is reconstructed for both Storskär and Hellsö pseudotachylytes (fig. 4.23b and d).

For Storskär pseudotachylyte, the main slip surfaces have a NW-SE, almost vertical strikes (mean orientation 272/86; i.e. dips slightly weighed towards NE). The sinistral conjugate surfaces strike almost E-W, while the average dextral conjugate shears strike ca. 10º. The fracture angle α between the mean conjugate surfaces is 83.3º. The calculated axes of the stress ellipsoid show that at the time of the pseudotachylyte formation, the local stress field had a SW-NE direction. The calculated direction of the σ_1 is slightly oblique to the mean orientation of the main generation surfaces (clockwise rotation), which is in agreement with the sinistral kinematics of the pseudotachylyte generation surfaces observed in the field. The σ_1-axis is almost horizontal with a slight SW plunge, indicating a nearly pure strike-slip faulting with only a minor SW side-up component in the slip.

Contrary to the Storskär pseudotachylyte, the main generation surfaces of the Hellsö pseudotachylyte are slightly less steep, showing a mean orientation ca. E-W (93/77). The sinistral conjugate surfaces strike on average 60/75, and the dextral surfaces 134/79 (SE-NW). The angle α is 108.1º, i.e. larger than 90º which is considered to be the maximum angle for shear fractures with respect to the direction of maximum stress (e.g. Park 1997). The pre-existing

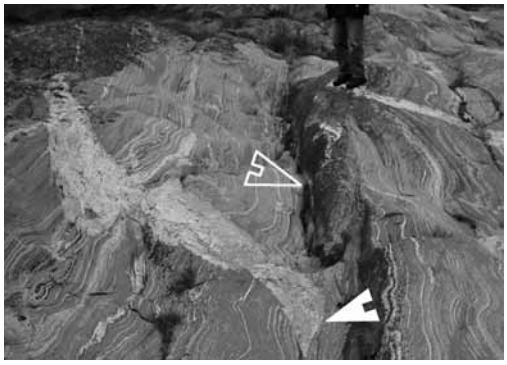

Fig. 4.22. A pseudotachylite generation surface (solid arrow) sinistrally offsetting a pegmatite dyke on Storskär, Kyrkogårdsö. A later brittle crack (no significant lateral movement; empty arrow) slightly oblique to the pseudotachylite in turn cuts the pseudotachylite generation surface. The foliation of the ductilely deformed granodioritic gneiss (dextral sense of shear) as well as the pseudotachylite generation surface strike 120º (NW-SE), view toward SE. The pegmatite has been dated at ca. 1.79 Ga (chapter 4.5).

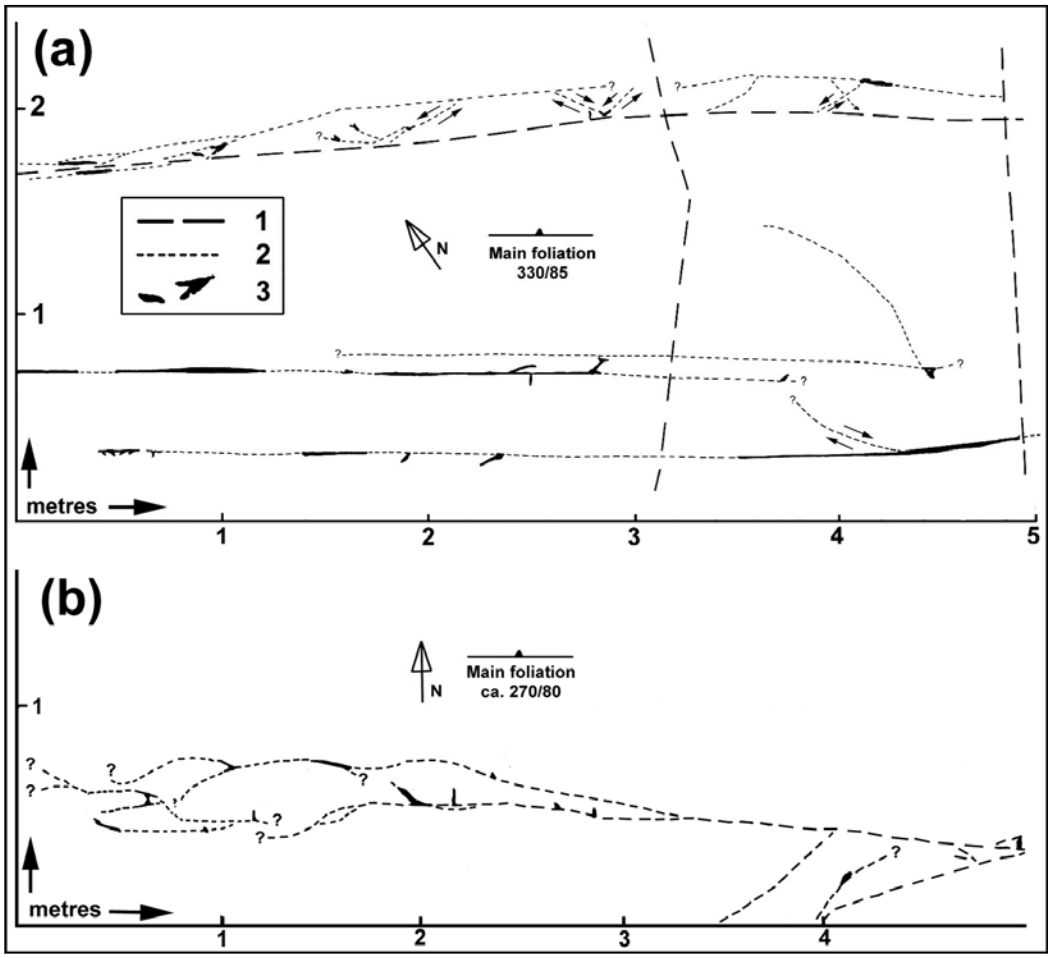

Fig. 4.21. Sketch of a part of a pseudotachylyte zone within granodiorite gneiss on **(a)** Storskär, Kyrkogårdsö, and **(b)** Hellsö, Kökar. The size of the melt pockets have been slightly exaggerated for clarity. On Storskär, the pseudotachylyte generation surfaces commonly run relatively straight (lower zone), (sub)parallel to the gneissose foliation, although also anastomosing zones are found (upper zone). In Hellsö, the pre-existing complex foliations patterns of the gneiss and the mylonites and cataclasites have controlled the formation of the pseudotachylyte generation surfaces somewhat so that the generation surfaces anastomoses considerably (see text). Key: **(1)** Brittle fractures (younger); **(2)** Pseudotachylyte generation surfaces and conjugate shear fractures; **(3)** Pseudotachylyte melts.

complicated rock structures and the resulting strongly anastomosing nature of the pseudotachylyte on Hellsö may have contributed to the distortion of the resulting fracture pattern, which in turn is reflected in the large fracture angle; the measurements from Hellsö should therefore be interpreted with some caution. The calculated stress ellipsoid shows a local stress field with an approximately N-S oriented compression. The orientation of σ_1 is very slightly but observably oblique to the orientation of the mean generation surface, indicating a dominantly sinistral kinematics for the mean generation surfaces. The σ_1-axis is slightly but clearly tilted towards N, indicating a relative N side-up component in the resulting slip.

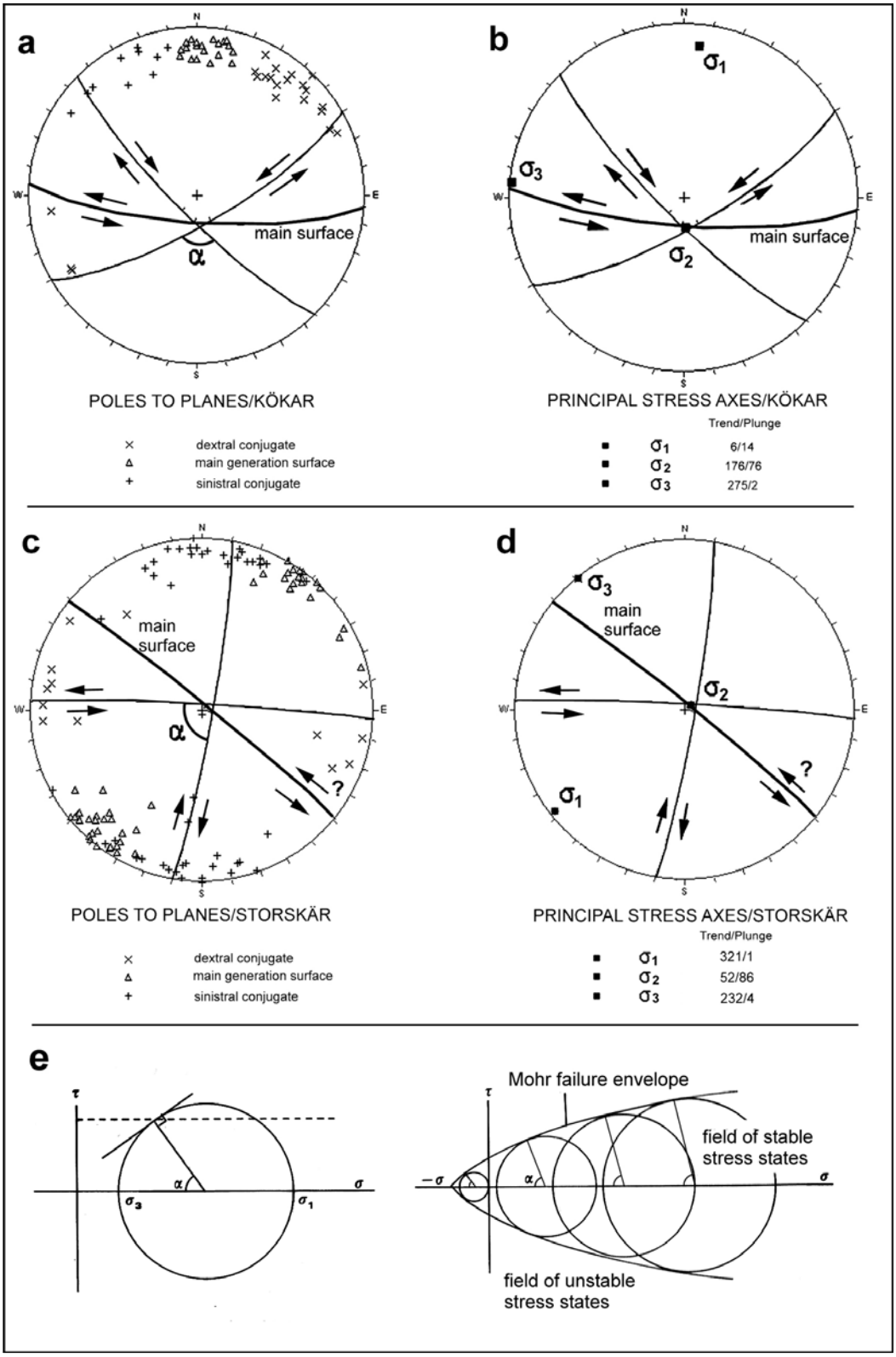
a
N
W
E
S
main surface
α
POLES TO PLANES/KÖKAR
× dextral conjugate
Δ main generation surface
+ sinistral conjugate
b
σ1
σ3
σ2
main surface
PRINCIPAL STRESS AXES/KÖKAR
Trend/Plunge
σ1 6/14
σ2 176/76
σ3 275/2
c
main surface
α
?
POLES TO PLANES/STORSKÄR
× dextral conjugate
Δ main generation surface
+ sinistral conjugate
d
σ3
main surface
σ2
σ1
?
PRINCIPAL STRESS AXES/STORSKÄR
Trend/Plunge
σ1 321/1
σ2 52/86
σ3 232/4
e
τ
σ
α
σ3
σ1
Mohr failure envelope
field of stable stress states
field of unstable stress states
−σ

Based on the crosscutting relationships between the mylonites, cataclasites and pseudotachylyte on Hellsö, the mylonites and cataclasites formed during an earlier deformation phase in more (semi)ductile conditions and/or with slower slip rates. The Storskär pseudotachylyteon the other hand lacks mylonite and cataclasite precursors, although the gneisses in many places approach a 'protomylonitic', augen gneiss –like appearance. On Storskär, the local palaeostress field is slightly more oblique with respect to the main generation surface than in Hellsö, suggesting initially higher slip rates that would have facilitated pseudotachylyte formation instead of cataclasis, which may partially explain the absence of the cataclastic and mylonitic precursors on Storskär. On the other hand, the aforementioned uncertainties regarding Hellsö pseudotachylyte do not necessarily justify making any definite conclusions about the relative direction of the Hellsö palaeostress field at the time of the pseudotachylyte formation. For Storskär pseudotachylyte, following the principles of the Mohr stress diagram (fig. 4.23e), the large fracture angle between the conjugate shear fracture surfaces suggests high values of shear stresses and relatively high hydrostatic stresses (i.e. relatively deep crustal levels). The microtextures of the Storskär pseudotachylyte indeed indicate that at least in this locality, the temperature remained relatively high at the time of the pseudotachylyte formation (chapter 4.3).

4.2.3 SUMMARY OF FIELD OBSERVATIONS

The ductile shearing along the main shear zone produced gneissose and mylonitic rocks that show an overall dextral kinematics on various scales. Based on the field evidence described above, the overall vertical kinematic movement along the shear zone was SW side up so that the rocks SW of the shear zone were thrusted toward NW.

The shear zone was probably formed due to partitioning of the strain caused by the approximately N-S to NNW-SSE directed regional, transpressive stresses. The first deformation phases (D_1-D_2) are best preserved in W and S Kökar. These phases produced tight to isoclinal upright folds with gently plunging (F_1) and steep (F_2) fold axes, respectively. During the subsequent deformation phases, the pre-existing structures were commonly refolded (conical and sheath folds and F_3 margin folds), but the regional strain was increasingly partitioned into planar deformation zones within the crust, and the SJSZ was formed. The scale of this zone is so large that it is suggested here, bearing in mind the lithological differences on both sides of the main shear zone, that the SJSZ possibly follows a pre-existing crustal discontinuity. Besides the main shear zone, an approximately SW-NE directed, conjugate set of zones of intense deformation exist, indicating

Fig. 4.23. Stereographic projections of the poles to planes and the calculated mean planes for Kökar **(a)** and Storskär **(c)** pseudotachylyte main generation surfaces and conjugate shear fractures. **(b)** and **(d)** show the calculated mean planes and associated principal stress axes for Kökar and Storskär pseudotachylytes, respectively.

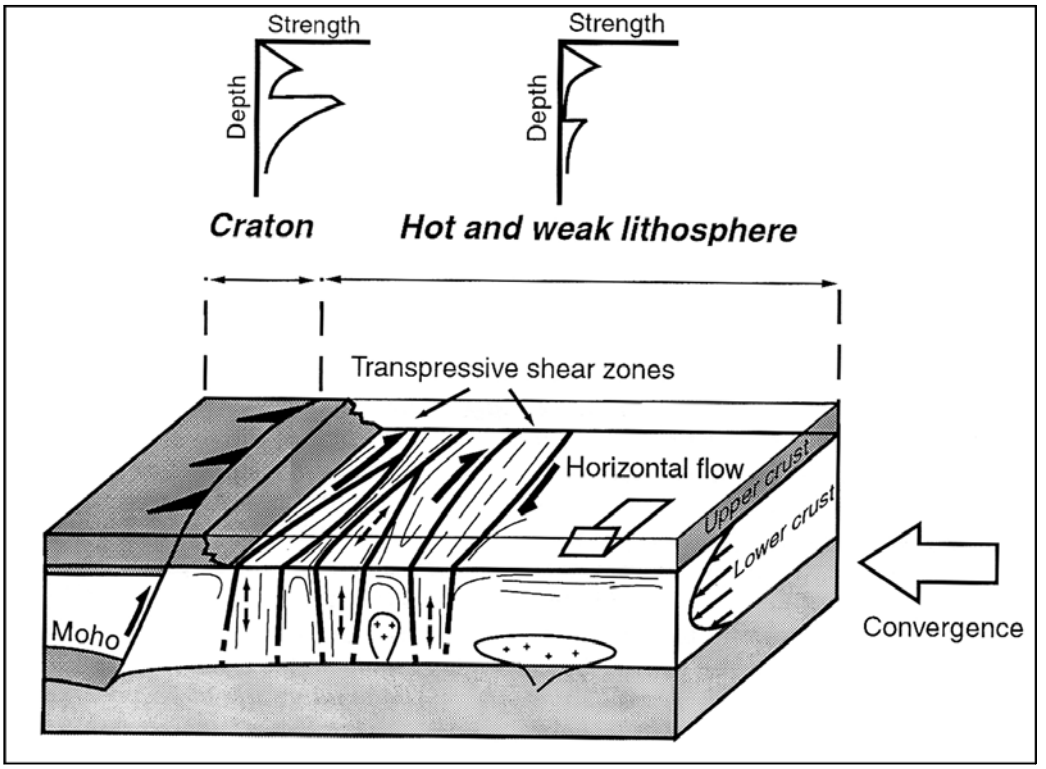

Fig. 4.24. A model by Cagnard et al. (2006) illustrating a possible behaviour of a weak lithosphere colliding or accreting against a more resistant domain.

that the shear component of the transpressive deformation was not entirely accommodated by the main shear zone. These conjugate zones were formed along planar zones defined by the southwesterly flanks of the regional F_3 margin folds. In other words, some thrusting, or flow apparently occurred parallel to the strike of the main shear zone, evidenced by the southeastwards gently dipping mineral and stretching lineations (L_3) that generally developed on the folded surfaces of the major F_3 margin folds. The large-scale margin folds formed after the F_2 shear folds had begun to form, and this type of folding was probably most active during D_3 although the two folding processes may have been active simultaneously during late D_2. On the other hand, the observed L_3 lineations often show a weak trend along a great circle, which may indicate that the F_3 margin folds locally continued to tighten somewhat during later deformation phases (D_4).

Högdahl (2000) concluded that due to the transpressional nature of deformation, the strain was partitioned into pure shear and simple shear-dominated components within Hassela shear zone, the latter producing dextral strike-slip anastomosing zones. It is likely that deformation dominated by pure shear occurred earlier, being subsequently followed by partitioning of strain into increasingly simple shear-dominated deformation, since the U-Pb titanite ages from Forsaån, a dominantly pure shear zone, gave the oldest age of 1816±2 Ma of the investigated shear

zones, while the strike-slip zones within the study give ages of ca. 1794-1801 Ma. Summarising the results of the field observations, a similar development is likely to have occurred within the SJSZ; an early pure shear dominated deformation was succeeded by increasing partitioning into simple shear dominated, lateral-slip transpressive shear zones.

Cagnard et al. (2006) noted that according to their experiments, deformation of weak lithospheres results in accommodation of horizontal shortening by strain localisation in transpressive zones and/or along fold limbs in such manner that involves significant vertical stretch as well as lateral flow. According to them, vertical stretch is observed in many Precambrian orogenic belts, which may indicate that the lithosphere was at least locally weaker than at present, probably due to higher heat flow. The results of their experiments suggest that the lithospheric strength plays an important part in whether folds are formed, or whether shear zone dominated structures are formed in a transpressive orogen. They further suggest a model for the Svecofennian orogen in Southern Finland in which, due to the low lithospheric strength of the lithosphere, the mantle was able to flow horizontally along the margins of the transpressive shear zones (fig. 4.24). The field observations of this study give some support to the model by Cagnard et al. (2006); the large-scale F_3 margin folds with gently SE plunging fold axes that have been formed along the southern margin of the SJSZ may have been a result of lateral ductile flow, combined with a slight south side-up thrust component. However, the model implies that the lithosphere-scale flow affect a relatively large area, while within the area of this study, the width of the band of open folds with shallow plunging fold axes is relatively small (in the order of 5 km). Furthermore, applying the model to the SJSZ (and SFSZ) and the rocks south of it would require that the rocks north of the present SJSZ (i.e. the area of the LSGM) was already more rigid than the lithosphere south of the LSGM by the time of their convergence. This in turn implies that there was a separate collisional/convergent event between the LSGM and an unknown, weaker lithospheric block to the south. So far, no concrete evidence for or against a model involving a weak block to the south has been presented in literature, although the model for the Svecofennian orogeny by Korja & Heikkinen (2005) requires that an unknown continental mass existed to the south (see also chapter 1.1). However, regardless of the truthfulness of these notions, the author considers that a thrust or flow component directed along the axial planes of the present open F_3 margin folds is required in order to produce the structures observable in the outcrops.

The relative steepness of the lineations and fold axes in Husö and Kyrkogårdsö areas compared to those in Hellsö may reflect a larger pure shear component to the overall deformation in the NW parts as opposed to the SE parts of the study area. This in turn may be related to the different rheology of the amphibole-rich rocks that are more common toward Husö-Finnö and Sottunga, thus making the lithosphere locally more rigid. High-T mylonite zones indicating strong deformation partitioning are indeed less common in Husö area than in Kyrko-

gårdsö and Skattskär. Furthermore, the zone seems to widen as NW parts of the study area are approached, which also suggests that pure shear strain component was stronger than in the SE parts. It therefore appears that the deformation was not partitioned only across the shear zone and shear zone margins into dominantly pure shear and simple shear domains (shear zones vs. folds), but also along the zone so that in the NW, compressive structures are more common while in the SE, simple shear dominated structures are more frequently encountered with.

The ductile to semi-ductile mylonites represent late stages of the ductile deformation and extreme strain partitioning that was necessary to accommodate the strike-slip component of the regional, late-orogenic deformation affecting the cooling crust. The clear dominance of mylonites over more brittle cataclasites implies that the exhumation of the rocks from ductile and semi-ductile conditions into a brittle regime was rapid and/or there was no significant regional tectonic activity while the rocks were being exhumed.

Regarding the brittle deformation phase, both Hellsö and Storskär pseudotachylytes show sinistral kinematics along their main generation surfaces, in contrast to the overall dextral kinematics of the ductile shear zone. In Hellsö, the palaeostress field is only slightly rotated compared to the overall N-S to NW-SE direction of the D_4 deformation in SW Finland, although bearing in mind the uncertainties discussed above regarding Hellsö fracture surfaces, the true orientation of the palaeostress field in Hellsö may remain unsolved. On Storskär, however, the measurements can be considered more reliable, and the directions of the pseudotachylyte generation and conjugate surfaces indicate a considerable difference in the stress field compared to the Svecofennian D_4. This suggests either that the stress field of the late stages of the Svecofennian orogeny had rotated by the time of the pseudotachylyte formation or, more likely, that the stress field was a product of a separate geological event other than the Svecofennian orogeny. The pseudotachylytes may have been formed within the brittle-ductile transition zone rather that entirely within the brittle regime, since indications of possible coeval mylonitic and pseudotachylitic deformation are found.

As a summarizing statement, it is suggested that i) the main shear zone (SJSZ) follows a pre-existing crustal zone of weakness and may thus represent a terrain boundary between the volcanic arc system (LSGM) of southern Finland and the amphibolite facies rocks SW of the SJSZ; ii) that the deformation within the area occurred in several phases D_1 – D_4; and iii) the deformation during the structural development of the study area was partitioned so that the early, pure shear dominated deformation phases produced the large-scale F_1-F_3 folds observable in the field while simultaneously - latest during D_3 and probably even earlier - there was a significant simple shear component involved that was mainly accommodated by the SJSZ and the conjugate local high-strain lateral-slip zones such as Skattskär. During late-orogenic D_4, the deformation was almost completely partitioned into the simple shear dominated shear zones, although some tightening of the earlier (F_3) folds probably occurred.

4.3 MICROSTRUCTURES IN DIFFERENT ROCK TYPES

4.3.1 GNEISSOSE ROCKS

The petrographic study of the gneissose rocks confirms their nature as mainly quartzo-feldspatic, relatively high-grade gneisses with igneous origins. They are medium-grained rocks with relatively strong internal deformation fabrics, consisting mainly of quartz, plagioclase and either biotite together with potassium feldspar (granites and granodiorites) or biotite and/or hornblende (tonalites and the less common diorites; tab. 4.1). Very locally, the granodiorites and tonalites have some prograde garnet. Titanite is a relatively common mineral, especially in the tonalites. The mafic varieties (metadiorites and –gabbros) usually consist of hornblende, plagioclase and mica (dominantly biotite), with some accessory opaques and occasional quartz. In some individual mafic lenses the dominant mafic mineral is clinopyroxene instead of hornblende, with some coexisting olivine, although the pyroxene is usually extensively altered to uralite with an exolution of an opaque phase (see chapter 4.4. for a more detailed description).

The gneissose foliation in the K-feldspar gneisses is commonly defined by mica (biotite), while in tonalitic gneisses the foliated fabric is mainly a result of the slightly elongate hornblende, with or without biotite. In both rock types, the feldspar and quartz are relatively equigranular, defining bands and/or lenses between the biotite-rich layers. Where dynamic recrystallisation has been most intense and static recovery has not completely removed the dynamic textures, the feldspars also occur as rounded grains displaying core-and-mantle -textures. Also feldspar-quartz myrmekites are locally common in the K-feldspar gneisses. As a rule, in all of the gneissose rock samples, there are at least lenses and layers where the mineral grains are internally relatively strain-free despite the evidently strong deformation, indicating a period of static re-crystallisation in relatively high-T conditions at some time during the deformation history of the rocks. However, especially when the main shear zone is approached, micro- and mesoscopic layers and zones where the mineral grains are more dynamically deformed become increasingly common, the grains retaining much of the internal strain of the last ductile deformation phase(s). This may evidence of deformation partitioning and/or fluid channelling not only on meso- and macroscale, but also on grain- and thin section scale. Extensive retrograde reactions are mostly absent in the gneisses, indicating that the temperature decreased rather rapidly after the last gneissose deformation phase recorded by the minerals, and/or there were not enough fluids present to facilitate retrograde hydration reactions. However, there are exceptions, as it seems that locally some retrograde metamorphism was enabled, suggesting that fluid channelling may have been of a significant importance during or after the last deformation phase(s).

The thin sections were cut parallel to lineation (where observable) and perpendicular to foliation.

4.3.1.1 Gneisses outside SJSZ

The rocks outside the main shear zone (western and southern Kökar) show distinctly different microstructures compared to the rocks at the margin of and within the main shear zone (Hellsö and Kyrkogårdsö areas, respectively). Microstructural differences between the mafic and the felsic rock types are relatively small, as both have commonly undergone extensive post-deformation static recrystallisation in relatively high-T conditions. However, the felsic rocks do show many features typical for dynamic deformation that are absent in the mafic rocks because the lack of quartz and K-feldspar made the mafic rocks rheologically stronger; amphibole, for example, deforms mainly by brittle fracturing rather than dynamic recrystallisation in temperatures below ca. 650-700ºC (e.g. Imon et al. 2002, Berger & Stünitz 1996). On W and S Kökar, the thin sections from felsic gneisses show relatively high-T (500-700°C) dynamic recrystallisation microstructures; the differences in the rheological behaviour between quartz and feldspars in the prevailing conditions are observable. In quartz, slightly lobate grain boundaries formed due to grain-boundary migration processes (GBM) and some indication of sub-grain rotation recrystallisation (SGR) are observable, although the grains are nevertheless relatively strain-free due to rapid recovery and recrystallisation (e.g. Passchier & Trouw 2005, Stipp et al. 2002; fig. 4.25a). In feldspars, relatively high-T (500-600ºC) indicators such as myrmekites are abundant and undulose extinction occurs; also 'core-and-mantle' structures where a fine-grained feldspar mantle has developed around a core of an old grain due to bulging recrystallisation (BLG) are frequently encountered (e.g. Tullis & Yund 1991, Gapais 1989; figs. 4.25b, c). Areas and layers where dominantly post-deformation, high-T static recrystallisation and recovery dominate are common, and monomineralic quartz ribbons with relatively strain-free grains and polygonised grain boundaries have formed as a result of static grain boundary area reduction processes (GBAR; e.g. Passchier & Trouw 2005, Evans et al. 2001, Kruhl 2001; figs. 4.25a, d). Retrograde hydrous mineral reactions such as chloritisation are rare or absent in the thin sections, indicating a fast temperature drop from hornblende facies conditions, and/or a lack of fluids during retrogression. The macroscale structural investigations (chapter 4.2) suggest the regional deformation was by D_3 largely partitioned into relatively narrow high-strain zones within and at the margins of SJSZ, since late deformation-related microstructures are mostly absent in the rocks of W and S Kökar. However, it is feasible that the continuing convergence still affected the rocks outside the main shear zone in order to accommodate the flattening component of the regional transpressive stress field. Consequently, the dynamic micro-structures that remain observable in these rocks probably mostly reflect the D_3 deformation, despite the fact that deformation at this stage was not very intense in S and W Kökar. If some D_2 microstructures are present on S and W Kökar, they are indistinguishable from D_3 micro-structures, or they have been removed by extensive post-D_2 static recovery and recrystallisation.

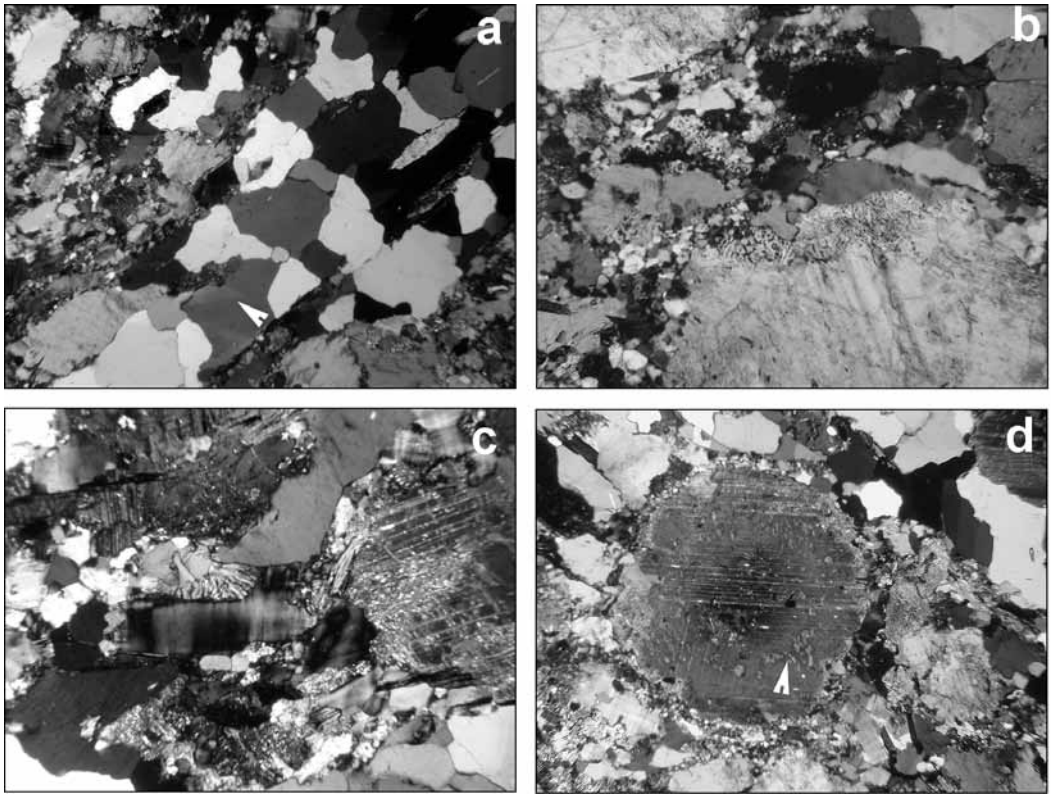

Fig. 4.25. Microstructures in the gneisses outside the main SJSZ (W and S Kökar). Key: PPL = plain-polarized light, CPL = cross-polarized light **a)** A monomineralic quartz ribbon in a granite gneiss, W Kökar (sample Geochemistry 3). Most of the dynamic structures in quartz have been erased by post-deformational high-T static recrystallisation, so the grains are relatively strain-free (few sub-grain boundaries or undulose extinction) and the grain boundaries relatively straight. However, the grain boundaries are slightly lobate in places and in one grain, a weak sub-grain rotation recrystallisation structure (*white arrow*) remains. Width of the view 4.5 mm, CPL. **b, c)** K-feldspar – plagioclase myrmekites (*centre*) in a granite gneiss, W Kökar (sample SW-1). The margins of the larger feldspar grains in b) have been partly dynamically recrystallised by bulging (BLG), producing a rim consisting of very small feldspar crystals around the larger grain cores. Width of the view 1.8 mm, CPL. **d)** A largish, rounded plagioclase grains in a granite gneiss, W Kökar (sample Geochemistry 3). The grain shows undulose extinction and remnants of an earlier zoning (*white arrow*), as well as a narrow rim formed by BLG. Also the smaller feldspar grains around the large one have developed subtle BLG rims (*lower left and right*). The quartz ribbon (*upper right*) shows some lobate grain boundaries and undulose extinction, but is all-in-all relatively strain-free. Width of the view 4.5 mm, CPL.

D_1 microstructures have not been found because if they ever existed they were apparently destroyed due to high-T static recrystallisation between deformation phases and/or overprinted by the subsequent deformation textures. Lower-T microstructures of the last ductile deformation phase (D_4) have not been observed on W and S Kökar, confirming that the D_4 dominantly affected the main shear zone and its margins.

4.3.1.2 Gneisses at SJSZ margin

As the main shear zone is approached, the difference between the deformation styles of the K-

feldspar and tonalitic rocks vs. quartz-poor rocks becomes more obvious. The basic rocks are commonly brecciated and form lenses within the quartz-rich rocks, i.e. they show very little deformation compared to the acid and intermediate gneisses. Toward the main shear zone, somewhat lower-grade micro-structures and retrograde mineral reactions become increasingly common in all rock types, especially in the narrow high-strain zones within the felsic gneisses ('minor shear zones'; chapter 4.2, fig. 4.11), although all in all the earlier, higher-T mineral assemblages and micro-structures still dominate. The lower-grade mineral reactions are interpreted to mostly represent the development at late stages and after the last ductile (D_4) phase, as will be shown below. All dynamic textures appear considerably better preserved e.g. on Hellsö than on S and W Kökar, although locally significant static recrystallisation occurs. The higher abundance of dynamic struct-ures is probably due to higher intensity of both D_3 and D_4 de-formation phases closer to the main shear zone as opposed to W and S Kökar.

The $D_{3(-4)}$ microstructures are frequently observed in felsic Hellsö rocks, but are not equally common everywhere. Because the deformation was by D_3 already largely partitioned into local high-strain zones ('minor shear zones') where the deformation was more intense, and because the minor shear zones may have been reactivated during D_4, the static recovery and recrystallisation pro-cesses after D_3 (and D_4) were not sufficient to completely remove the dynamic fabrics from the rocks within the high-strain zones. Between the minor shear zones, in areas dominated by pure shear deformation style (i.e. within the F_3 margin folds of chapter 4.2), static recovery and recrystallisation is a considerably more frequent phenomenon, and the earlier dynamic textures have in places been almost completely erased. The static recovery affected especially quartz, as grain-boundary area reduction (GBAR; Passchier & Trouw 2005) resulted in strain-free, polygonal quartz grains (e.g. Evans et al. 2001, Kruhl 2001; fig. 4.26a). These rocks, i.e. other than those within the minor shear zones, do however retain some of the higher-grade (500-700ºC; e.g. Stipp et al. 2002) $D_{3(-4)}$ dynamic recrystallisation textures. They typically show SGR and GBM recrystallisation, resulting in grain size reduction and lobate grain boundaries in quartz (500-700ºC). Additionally, some feldspar grains show remnants of myrmekitic and core-and-mantle textures (500-600ºC) and, locally, undulose extinction (ca. 500ºC; Tullis & Yund 1991, Gapais 1989; fig. 4.26a-c). Another noteworthy microstructure that can be observed in the Hellsö rocks is the foliation deflection around the occasional garnets, indicating that the garnet is prograde and developed during or before active deformation, probably during D_3 (fig. 4.26d). The garnet is sometimes, but not always, somewhat altered to biotite or, in some samples, slightly retrogressively chloritised. The garnets show inclusions that however do not appear to reflect any previous deformation phase, i.e. they do not define a relict foliation pattern within the garnets that deviates from the foliation in the rest of the sample. The garnets were probably formed during the

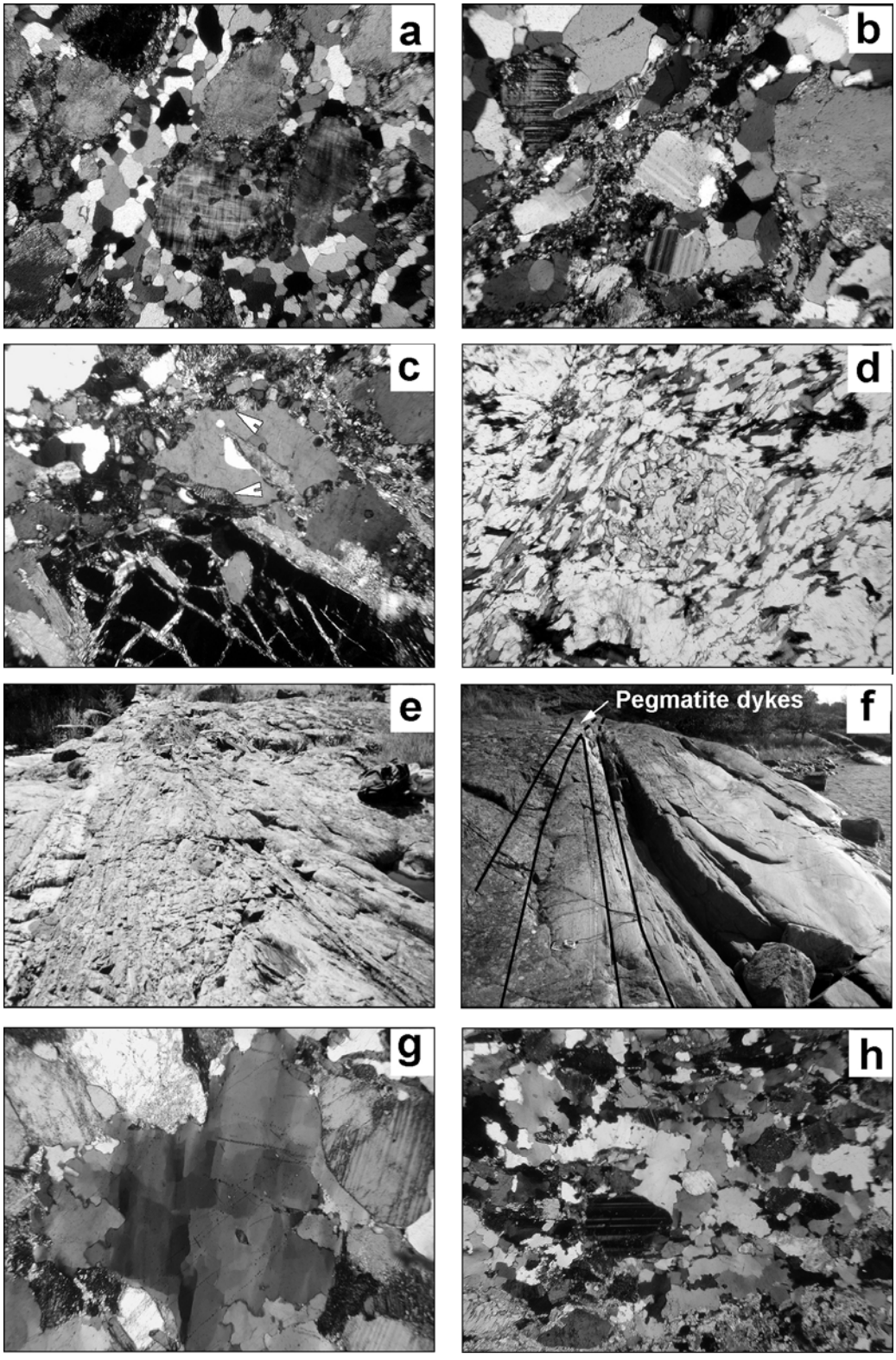
a
b
c
d
e
Pegmatite dykes
f
g
h

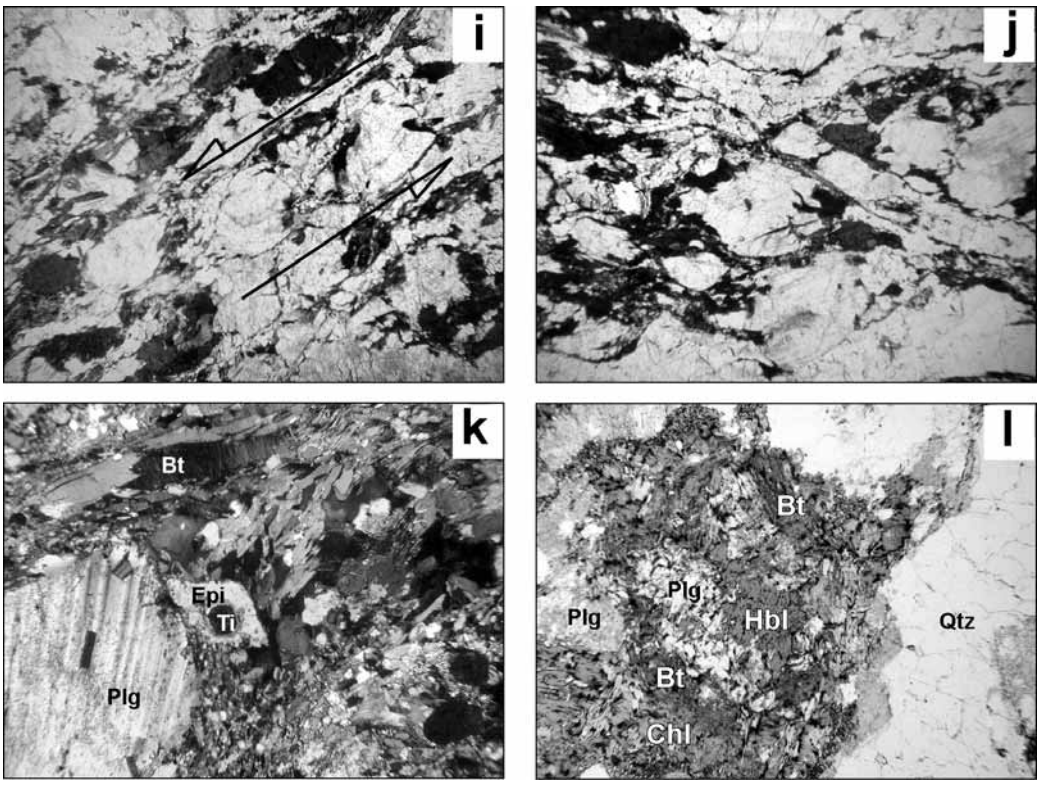

Fig. 4.26. Microstructures in gneisses at the margin of the main SJSZ (Hellsö). Key: Epi = epidote, Ti = titanite, Plg = plagioclase, Bt = biotite, Gt = garnet, Qtz = quartz, PPL = plain-polarized light, CPL = cross-polarized light. **a)** Static recovery of quartz in granite gneiss, Hellsö (sample K-4/02). GBAR resulted in strain-free, polygonal quartz grains in this quartz ribbon surrounding the central feldspar aggregate. The feldspars show rim-and-mantle textures. Width of the view 4.5 mm, CPL. **b, c)** Dynamic structures in feldspars, granodioritic gneiss, Hellsö (samples K-3/02 and K-3/03, respectively). In b), BLG recrystallisation of feldspars has resulted in core-and-mantle structures; the grains in the centre of the view even have developed weak 'wing' structures along the plane of the gneissose foliation. Note also the strain-free, polygonal quartz grains. Width of the view 1.8 mm, CPL. In c), some remnants of feldspar myrmekite can be seen in the centre of the view (*white arrows*). The quartz in this sample (*upper left*) has more irregular grain boundaries than in b) and shows some undulose extinction, but is still clearly more strain-free than the typical quartz grains within the narrow high-strain zones (see text). The large isotropic grain in lower centre is garnet. Width of the view 1.8 mm, CPL. **d)** Deflection of the gneissose foliation around a prograde garnet porphyroblast, granodioritic gneiss, Hellsö (sample K-5/02). The mica is red-brown biotite, unchloritized in this sample. Width of the view 4.5 mm, PPL. **e)** A narrow shear zone in granodioritic gneiss, Hellsö; view toward SE. A pegmatite dyke intrudes the deformation zone (*centre left*). Samples Geochemistry 9 (outside the shear zone), 10 and 11 (within the shear zone; figs. 4.26g, h) are taken from this locality. Photo: Elin Siggberg. **f)** A narrow shear zone along the northern limb of an open synclinal F_3 margin fold with gently toward SE plunging stretching lineations and fold axis. Hellsö. The shear zone is truncated by two pegmatite dykes, the one to the right being slightly deformed. View toward SE; compass pointing north. **g, h)** Dynamic medium- to high-T structures in a narrow (30-40 cm) shear zone in granodioritic gneiss, Hellsö (samples Geochemistry 10 and 11). In f), the quartz displays 'chessboard extinction', typical for quartz deformed at middle to upper amphibolite facies conditions (Passchier & Trouw 2005). Also the grain boundaries are clearly irregular and lobate due to grain boundary migration (GBM) processes. Width of the view 4.5 mm, CPL. g) shows an almost monomineralic quartz band (*centre left to centre right*) where all quartz grains have been deformed by GBM, resulting in highly lobate grain boundaries. Width of the view 1.8 mm, CPL. **i)** Granodioritic gneiss with weak sinistral shape symmetry of feldspar grains (sample K-1/05). The

progressive phase of D_3, but possibly earlier.

The minor high-strain zones within the K-feldspar and tonalitic gneisses show a significant simple shear component and are relatively narrow (some tens of centimetres to a couple of meters wide). They developed dominantly along the the limb regions of the open F_3 margin folds common on Hellsö (chapter 4.2; fig. 4.26e), and/or at the contact zones of two different rock types. The rocks within these local shear zones frequently contain relatively high-grade dynamic microstructures associated with temperatures around 500-700ºC, such as highly lobate grain boundaries and 'chessboard extinction' of quartz grains within the zones (fig. 4.26g, h; Passchier & Trouw 2005, Stipp et al. 2002, Kruhl 1996, Mainprice et al. 1986). Also myrmekitic and rim-and-mantle structures are common. It is difficult to conclude whether the zones were formed mainly during D_3 or D_4, since several indications from both within and outside the shear zone indicate that the rocks cooled slowly and during D_4, the rocks were still within a relatively high-T, ductile regime (chapters 4.3.1.3 and 4.5). Late- to post-orogenic, slightly deformed pegmatites often intrude the narrow deformation zones, which may serve as an indication of the relatively young (D_{3-4}) age of the zones (fig. 4.26f). The microstructures observed within the narrow shear zones on Hellsö indicate somewhat higher deformation temperatures than those preserved dynamic structures that can be seen within the main SJSZ; this would imply that the Hellsö narrow shear zones formed mainly during D_3.

Kinematic indicators with monoclinic symmetry in gneisses are largely absent in W and S Kökar, but become more abundant within the high-strain zones of Hellsö as the pure shear component that dominates on Kökar gradually gives way to simple shear dominated deformation toward the main shear zone. For example, the strongly sheared limb regions of the F_3 margin folds (chapter 4.2.2.1) show weak C' -type fabrics that are kinematically consistent with the macrostructural interpretation that involves a NW –directed flow along the fold axial planes (figs. 4.26i). Some samples even seem to be transitional to mylonites, and could in mesoscale be defined as 'augengneisses', as small mica (mainly biotite) and recrystallised feldspar grains have concentrated along the foliation plane between

---

sample is from the northern limb of an open F_3 margin fold with a gently dipping fold axis (fig. 4.26f), and the sinistral kinematics seen in thin section is in accordance with field observations. Width of the view 4.5 mm, PPL. **j)** Fine-grained biotite around roundish feldspar grains (*centre*) in a granodioritic gneiss (sample K-5/02). This type of strongly sheared rocks showing weak monoclinic shape symmetries, 'augen-gneisses', are probably precursors to the mylonitic deformation style. Width of the view 4.5 mm, PPL. **k)** An epidote crystal is pseudomorphing an older titanite grain, the titanite remaining as a core within the epidote. The titanite alteration probably occurred during or soon after D_4. The quartz in this sample is typically strain-free and polygonal (not visible), indicating post-deformation static recrystallisation. Tonalitic gneiss, at a sheared contact between tonalite and granite, Hellsö (sample K-3/02). Width of the view 1.8 mm, CPL. **l)** Hornblende altered to biotite and chlorite, tonalitic gneiss, Hellsö (sample K-1/02). This sample is one of the most altered ones, the retrograde reactions are normally much less pronounced or, more commonly, completely absent. The monomineralic quartz ribbon (*right*) shows strain-free, polygonal grains (not visible). Width of the view 4.5 mm, PPL.

larger, often roundish feldspar grains and elongate quartz aggregates/ribbons (fig. 4.26i, j).

During the D_4 deformation phase, abundant metamorphic titanite formed. It is almost always associated with amphibole, and usually also with abundant epidote and an opaque to almost opaque, very dark brown phase. The opaque phase probably consists of ilmenite as it is together with epidote a common alteration product of titanite (Broska et al. 2007), or magnetite that often (re)crystallises together with magmatic and metamorphic titanite (Xirouchakis et al. 2001). In some rocks, also an older (?) titanite generation can be observed, the older titanite commonly being smaller, darker brown and more turbid (see also chapter 4.5). According to Xirouchakis et al. (2001), titanite (and magnetite) associated with amphibole, a common occurrence in plutonic quartz-rich rocks, is indicative of a high water activity (a_{H2O}) and high oxygen fugacity (f_{O2}) in igneous and metamorphic rocks, and that the titanite-forming process is most efficient at slow cooling rates, at temperatures relatively high compared to solidus-temperatures of the magmas (up to upper amphibolite facies). Also the presence epidote in many samples suggests a high f_{O2} (fig. 4.26k; Moody et al. 1982). According to experiments by Moody et al. (1982) and Liou et al. (1974), epidote can be stable at temperatures as high as 600ºC at high f_{O2}, especially in basic rocks. As mentioned above, the presence of epidote can be allocated to titanite alteration processes, where titanite is replaced by ilmenite, quartz, epidote (REE-bearing) and allanite according to the reaction

titanite + anorthite + annite + H2O = ilmenite + clinozoisite + muscovite + quartz,

in the system KCFATSHO (Broska et al 2007).

Late- to post-D_4 meso- and microstructures are locally present at the shear zone margin on Hellsö as lower-grade, retrograde mineral reactions. As described above, it appears that after D_4, there was a short period when temperatures remained sufficiently high in order to allow static recrystallisation and recovery, which however was insufficient in completely removing the dynamic structures from the rocks, especially those of the narrow shear zones. During this late- to post- D_4 period, the Hellsö rocks (and also rocks within SJSZ; chapter 4.3.1.3) passed through retrograde, lower amphibolite facies conditions where hornblende and the occasional garnet start to alter to biotite and, locally, further to chlorite in hydrous conditions (fig. 4.26l). The chloritisation reaction occurs at ca. 550ºC in siliceous alkali-calcic rocks, alkalic rocks and basic rocks, although in basic rocks chlorite can at high f_{O2} appear even at higher temperatures than this (e.g. Evans 1990, Moody et al. 1982). As stated above, the abundant presence of titanite + amphibole and epidote in many rocks suggests a high f_{O2} in the studied rocks. The retrograde reactions are not present everywhere, and in many samples such reactions seem to be completely absent. This probably reflects the high oxygen

fugacity, so that retrograde alteration was more efficient in the more mafic rocks, and/or fluid channelling within the rocks so that in some places there may have been insufficient amounts of fluids present to enable retrograde mineral reactions within the prevailing crustal conditions. Moreover, the temperature drop soon after the late- to post- D_4 period must have been quite fast after the rocks reached the amphibolite-greenschist facies transition, since even when retrograde reactions do occur, they are seldom very extensive.

4.3.1.3 Gneisses within SJSZ

The microstructures within the SJSZ gneisses resemble those of the Hellsö rocks, the most significant difference being the higher deformation intensity. This is most obviously observed as a somewhat smaller overall grain size, better preserved dynamic microstructures and more clearly defined foliations due to the abundant presence of quartz ribbons and bands, biotite-rich layers and slightly oblong feldspar, hornblende and titanite crystals along the foliation plane (fig. 4.27a). Gneisses approaching augen-like texture are relatively common within the shear zone. Like on Hellsö, the rocks have undergone several deformation phases within relatively high-grade conditions, with periods of static recovery and recrystallisation in between. Probably due to the higher deformation intensity within the shear zone, the static microstructures are markedly less common within the SJSZ compared to the shear zone margins (fig. 4.27b). Some influence of recovery can however be seen in most rocks as even the dynamically recrystallised grains often have a relatively strain-free appearance. This supports the notion presented in the previous chapter that there may have been a brief period of static recrystallisation at relatively high-T (ca. 500-550ºC) during late- or post-D_4 before the rocks were rapidly cooled and exhumed.

The dynamic fabrics that can be observed in the SJSZ rocks most probably represent the D_4 deformation phase, and witness of temperature conditions around 500-600ºC; the quartz commonly shows somewhat lobate grain boundaries (GBM) and subgrain rotation recrystallisation (SGR), while the feldspars frequently exhibit remnants of myrmekites and core-and-mantle structures, while also lower-T structures such as deformation twins (plagioclase), flame-perthites (=tapering albite lamellae in K-feldspar) and rare microfractures are present (fig. 4.27c-g). Deformation twins, microfractures and flame-perthites in plagioclase indicate deformation temperatures between ca. 400- 500ºC (Pryer & Robin 1995, Pryer 1993, Tullis & Yund 1987). Since the deformation twins have not generally been further deformed (bent), their presence indicates that the relatively low-T deformation occurred during the last stage of D_4, thus giving a temperature estimate for the late D_4 deformation. Deformation twins have not been commonly observed at the shear zone margin on Hellsö where D_4 was considerably less intense.

During D_4, abundant titanite and, locally, epidote formed much similarly to Hellsö, especially in the tonalitic rocks (fig. 4.27h). Two titanite generations are present in many titanite-rich rock samples, the presumably older one being darker

brown and more turbid in thin section. Some of the SJSZ rock samples containing two titanite generations have been dated during this project (chapter 4.5).

4.3.2 MYLONITES AND CATACLASITES

Mylonites occur mainly within the main shear zone and the conjugate shear zones (e.g. Skattskär, chapter 4.2.2.1), although local, narrow mylonite zones have also been observed at the SJSZ margin (Hellsö; fig. 4.28a, b). Two dominating mylonite types have been observed in the field: the wide mylonite zones (width > ca. 1 m) that commonly follow the gneissose foliation and are sometimes slightly folded; and the narrow mylonites (width < 1m, usually 1-10 cm) that commonly, but not always, cut the gneissose foliation. The most prominent wide mylonite zones have been encountered with on and in the vicinity of the island of Kyrkogårdsö, within the main shear zone, and within the conjugate deformation zone of Skattskär, outside the main SJSZ.

The mylonites within the wide zones can be subdivided into protomylonites, locally gradational to the augen gneisses, with 10-50% matrix; mylonites with ca. 50-90%; and ultramylonites with a large percentage (> ca. 90%) of matrix (figs. 4.28b-d). None of the different mylonite types commonly have much chlorite in the fine-grained matrix,

---

Fig. 4.27. Microstructures in gneisses within the SJSZ. Key: Ti = titanite, Il = ilmenite/ilmenorutile, Hbl = hornblende, Plg = plagioclase, Bt = biotite, Qtz = quartz, PPL = plain-polarized light, CPL = cross-polarized light. **a)** A granodioritic-tonalitic gneiss, Storskär, Kyrkogårdsö (sample KY-9/03). In the area of Storskär, the gneissose deformation is at its most intense within the study area. The sample shows quartz bands and ribbons, and oblong hornblende and titanite grains, which together with biotite define the gneissose foliation. Width of the view 4.5 mm, PPL. **b)** A granite gneiss, Storskär, Kyrkogårdsö (sample KY-7/03). In some places within the shear zone, static recrystallisation and GBAR of especially quartz has removed most of the dynamic microstructures, leaving relatively strain-free, polygonized grains. This is, however, much less common than e.g. on Hellsö, at the shear zone margin. Width of the view 3.0 mm, CPL. **c)** A granite gneiss, Storskär, Kyrkogårdsö (sample Geochemistry 15). The quartz grains in the ribbon at the centre (and lower left) of the view have irregular and lobate grain boundaries due to GBM recrystallisation. The grains are internally relatively strain-free, although some undulose extinction can be observed (*lower right*). Note also the K-feldspar grain at lower left displaying flame-perthite. Width of the view 1.8 mm, CPL. **d)** Remnants of a feldspar myrmekite (*white arrow*) in a granite gneiss, Storskär, Kyrkogårdsö (sample KY-7/03). Note also the undulose extinction of the larger feldspar grains (*centre and lower left*). Width of the view 3.0 mm, CPL. **e)** Remnants of a core-and-mantle structure in feldspar, formed by SR recrystallisation (*lower centre*) in a granite gneiss, Storskär, Kyrkogårdsö (sample KY-7/03). Width of the view 3.0 mm, CPL. **f)** Flame perthite in a K-feldspar grain (*lower centre*) of a granite gneiss, Storskär, Kyrkogårdsö (sample Geochemistry 15). Note also the smaller quartz grains, presumably initially deformed by SGR but subsequently experienced some static recovery, which resulted in a relatively strain-free appearance of the grains. Width of the view 1.8 mm, CPL. **g)** Deformation twins superimposed on the original growth twins of a plagioclase crystal (*centre*) in a granodioritic-tonalitic gneiss, Storskär, Kyrkogårdsö (sample KY-9/03). Width of the view 1.8 mm, CPL. **h)** Metamorphic (D_4) titanite in a metadiabase dyke on Kyrkogårdsö (sample KY-1/03). This type of late-orogenic titanite is much more common within the SJSZ than at its margin, confirming that the D_4 deformation was largely partitioned into the main shear zone while the adjacent areas were markedly less affected. Titanites in this sample have been dated (chapter 4.6). Width of the view 3.0 mm, PPL.

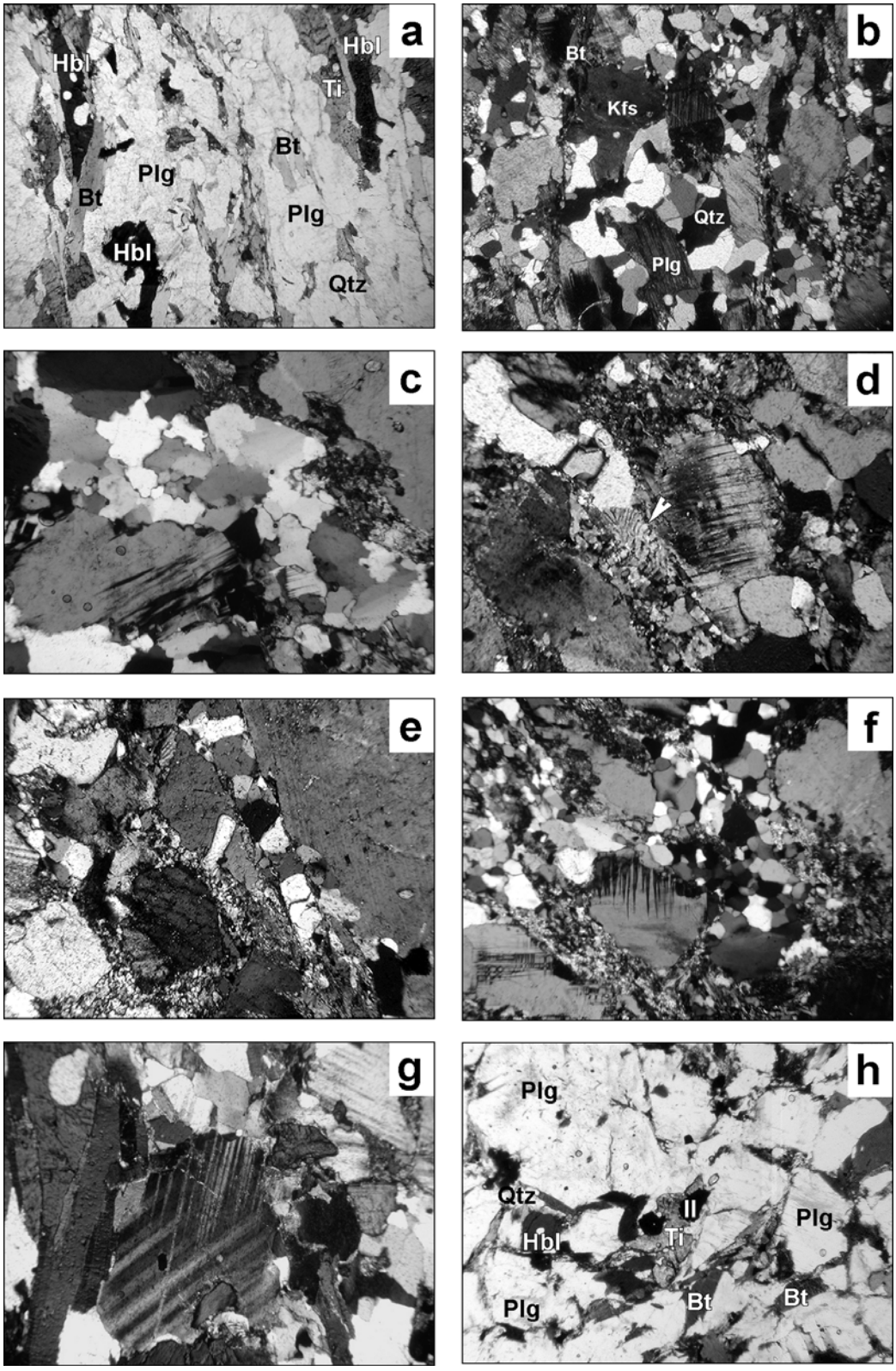
a
Hbl
Hbl
Ti
Bt
Plg
Bt
Plg
Hbl
Qtz
b
Bt
Kfs
Qtz
Plg
c
d
e
f
g
h
Plg
Qtz
Il
Plg
Hbl
Ti
Plg
Bt
Bt

suggesting that either there were an insufficient amount of fluids present at the time of the mylonitisation or that the wide mylonite zones formed at relatively deep crustal conditions (above or around ca. 500-550ºC; chapter 4.3.1.2). As 'early-protomylonitic' rocks exist both in the form of augen gneisses, often with a slightly mylonitic appearance in thin section, and in the form of coarse-grained protomylonites, it can be assumed that the wide mylonite zones were probably in many cases formed in several stages as a result of extreme deformation partitioning and reactivation of the zones. It is here postulated that the gneisses successively deformed to form augen gneisses and, with further deformation partitioning, proto-mylonites, mylonites and, finally, ultramylonites. The original lithotype (granitic/granodioritic vs. tonalitic) of the gneissose rock did not seem to have much influence on the rheo-logical behaviour, i.e. the tendency of the rock to form mylonite or ultra-mylonite, as both bulk chemistries are represented in the wide mylonite zones. The degree of and tendency for mylonitisation seems instead to be controlled by the amount of quartz and possibly also by the plagioclase contents of the original rock. However, it is obvious that the K-feldspar porphyroclasts behaved more plastically in the mylonite-forming conditions, commonly forming σ- and δ-clasts, compared to the hornblende porphyroclasts which display rigid behaviour (figs. 4.28e, f).

In the protomylonites and mylonites, the deformation is partitioned into relatively thin shear bands in thin section scale, observable as biotite-rich layers and quartz ribbons, leaving porphyroclasts and/or lenses and bands retaining the gneissose fabric in between (figs. 4.28c, g). In the protomylonites, the microtextures evidence of relatively high-T deformation (500-600ºC) at least during the last gneissose deformation phase, as SGR and lobate quartz grain boundaries in monomineralic quartz ribbons are common (fig. 4.28h). The tonalitic mylonites have abundant titanite, formed during the last ductile deformation phase (fig. 4.28g). The protomylonitic and mylonitic rocks do not generally show extensive chloritisation of the mafic minerals, which further pinpoints the temperature conditions of this de-formation phase to around 550-600ºC (Moody et al. 1982, Laird 1980; chapter 4.3.1.2). It is therefore unlikely that the protomylonites (and mylonites) of e.g. Skattskär and Kyrkogårdsö would have been formed long after the D_4 deformation phase. Instead, it is suggested that the (proto)mylonites formed during main D_4 or latest during late-D_4, the reason for their rheologically different behaviour compared to the gneisses being that of a strong strain par-titioning, with or without extensive fluid channelling, into relatively narrow zones; in other words, locally higher strain rates and thereof resulting enhancement of strain softening processes caused relatively high-T mylonitisation more or less simultaneously with the last gneissose deformation (Passchier & Trouw 2005, White et al. 1980).

The conditions of the ultramylonitic deformation within the wide zones are a more difficult matter as they typically contain minerals more common in greenschist facies

rocks, such as epidote – on the other hand, epidote can at high oxygen fugacities be stable at temperatures up to ca. 600ºC (Moody et al. 1982, Liou et al. 1974). They do not commonly have large amounts of chlorite, brown biotite being the dominant matrix material, which would imply that the temperatures were too high to allow for extensive chloritisation (fig. 4.28d, f). The abundance of hydrous minerals and minerals requiring high f_{O2} (biotite, titanite, hornblende, epidote) suggest that fluids were present during mylonitisation, so the absence of chlorite should not be caused by lack of fluids to facilitate the retrograde chloritisation reactions. As the chloritisation reaction occurs from ca. 550ºC downwards in siliceous alkali-calcic rocks and alkalic rocks, the higher temperatures being favoured by a high f_{O2} (e.g. Evans 1990, Moody et al. 1982), it is necessary to conclude that the ultramylonites must have been formed at relatively high-T conditions (up to 500-600ºC), and that the temperature dropped fast soon after the mylonitisation. It is unclear whether the ultramylonites of the wide mylonite zones formed simultaneously with the protomylonites and mylonites during D_4 due to extreme deformation partitioning and/or higher strain rates, or if they formed separately during late-D_4 (or soon after) as a result of deformation localisation and continued mylonitisation of the previously deformed rocks. The first alternative seems more likely since the fast temperature drop soon after D_4 would have rapidly brought the rocks well within greenschist facies conditions where chloritisation reactions would have been considerably more abundant.

The narrow mylonite zones are a few to some tens of centimetres wide structures deflecting and, more rarely, cutting the gneissose foliation (fig. 4.28a). Microscope study of these mylonites reveals that the mylonitic texture is frequently a result of biotite-rich layers anastomosing between feldspar/amphibolite porphyroclasts and quartz lenses and ribbons (fig. 4.28b, i). They are therefore relatively coarse-grained, very rarely approaching the ultramylonitic appearances observed within the wide mylonite zones. The narrow mylonites are not typically extensively chloritised, implying that they were formed at relatively high temperatures, probably in lower amphibolite facies conditions before significant chloritisation could take place. This further supports the idea that the temperature dropped fast after the rocks reached amphibolite-greenschist facies transition (ca. 500-550º; e.g. Raymond 1995).

Occasional cataclasites have been observed, most frequently on Hellsö at the SJSZ margin (fig. 4.28j). On Hellsö, the cataclasites mainly formed within the gneisses along weakness zones (sometimes protomylonitic) that during later, brittle movements hosted pseudotachylytes. The cataclasites are usually amphibolite-rich, reflecting the more rigid behaviour of the tonalitic gneisses compared to K-feldspar gneisses within the increasingly brittle crustal conditions. The age of the cataclasites is unknown, but they are certainly younger than the gneisses and very probably younger than the mylonites. Some authors place the upper temperature limit for cataclastic deformation to ca. 300ºC (e.g. Scholz

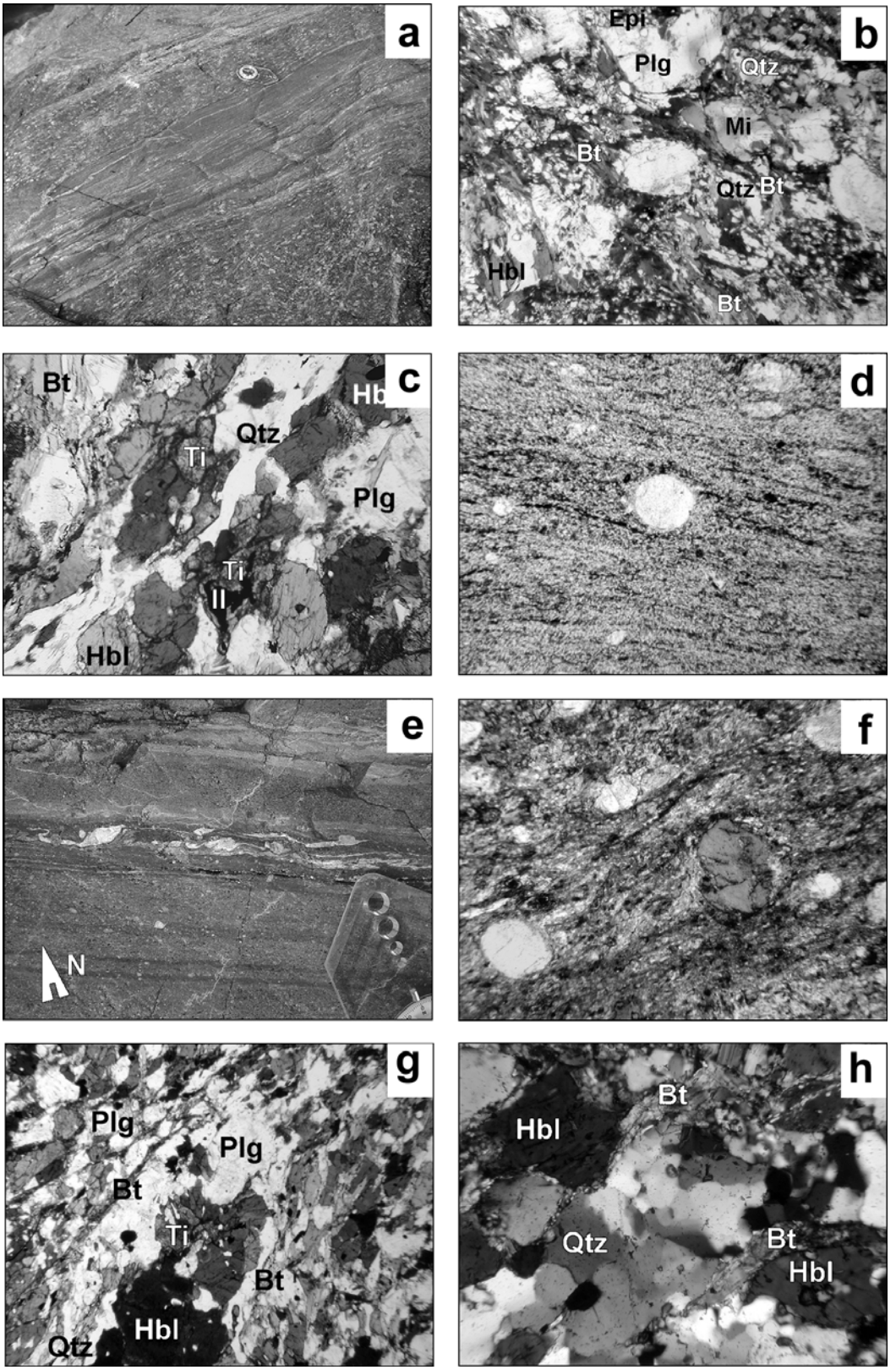
a
b
Epi
Plg
Qtz
Mi
Bt
Qtz
Bt
Hbl
Bt
c
Bt
Hb
Qtz
Ti
Plg
Ti
Il
Hbl
d
e
N
f
g
Plg
Plg
Bt
Ti
Bt
Qtz
Hbl
h
Bt
Hbl
Qtz
Bt
Hbl

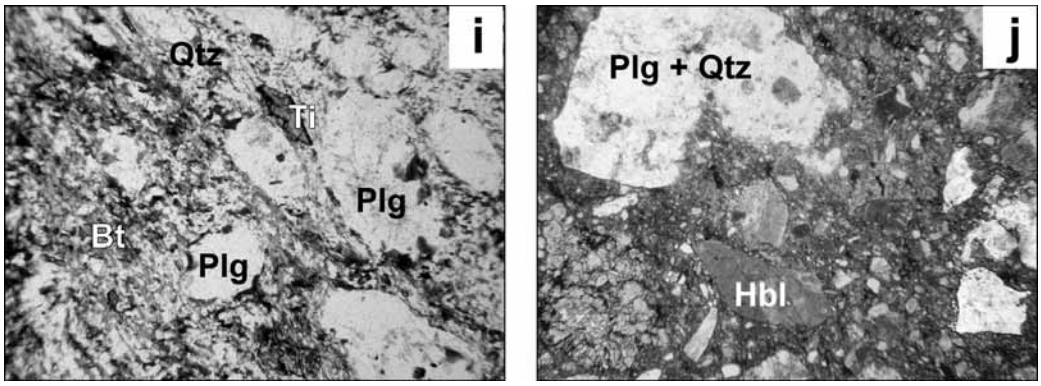

Fig. 4.28. Different mylonites within the study area. Key: Epi = epidote, Ti = titanite, Il = ilmenite/ilmenorutile, Hbl = hornblende, Plg = plagioclase, Mi = microcline, Bt = biotite, Qtz = quartz, PPL = plain-polarized light, CPL = cross-polarized light. **a)** A narrow mylonite zone in a porphyritic granite gneiss/augen-gneiss, N Hellsö. Compass pointing toward N. **b)** A narrow (3 cm) mylonite zone in a granodiorite gneiss, Hellsö (sample K-2/02). The mylonite is of a relatively coarse variety and it follows the earlier gneissose foliation. Width of the view 3.0 mm, PPL. **c)** A tonalitic protomylonite, Kyrkogårdsö (sample KY-2/03). The mylonitic appearance is defined mainly by the monomineralic quartz ribbons (*lower left to upper right*) and narrow layers of very fine-grained biotite (fig. 4.28g, h). This titanite-rich sample has been dated (chapter 4.6). Width of the view 4.5 mm, PPL. **d)** A rounded plagioclase σ-clast with poorly developed wings in a granodioritic ultramylonite, Kyrkogårdsö (sample KY-2/02). The matrix consists mainly of quartz/feldspar, biotite and opaque minerals, with minor chlorite and epidote. Width of the view 4.5 mm, PPL. **e)** An ultramylonite with dextral σ-porphyroclasts of K-feldspar within a 30-m wide mylonite zone, Kyrkogårdsö. This ultramylonite with a granitic/granodioritic protolith demonstrates the plastic behaviour of the feldspar in the crustal conditions in which the mylonites were formed as well as the high amount of dextral simple shear within the mylonite zone. Width of the view ca. 10 cm. **f)** A tonalitic mylonite/ultramylonite within a 30-m wide mylonite zone, Kyrkogårdsö (sample KY-8/04 = Geochemistry 17). The typical rigid behaviour of the hornblende porphyroclast (*centre right*) in the mylonite-forming conditions is clearly observable. The matrix consists mainly of plagioclase/quartz, biotite and opaque minerals, with minor chlorite and epidote. Width of the view 1.8 mm, PPL. **g)** A tonalitic protomylonite, Kyrkogårdsö (sample KY-2/03), the mylonitic appearance resulting from quartz ribbons and thin biotite-rich layers. A larger lens retaining the earlier gneissose fabric has been left intact (*lower left to centre*). Width of the view 4.5 mm, PPL. **h)** Abundant subgrain rotation recrystallisation (SGR) and somewhat lobate grain boundaries formed in response to grain boundary migration recrystallisation (GBM) in a quartz ribbon within a tonalitic protomylonite, Kyrkogårsö (sample KY-2/03). Apart from the subgrain boundaries, the quartz has a strain-free appearance due to rapid recovery in relatively high-T. Width of the view 74 µm, CPL. **i)** A relatively coarse mylonite in a narrow (ca 10 cm) garnet-bearing mylonite zone with a granodioritic country rock, Ejskär, Kyrkogårdsö (sample E-2/03). The mylonite itself is rich in biotite and titanite and is slightly folded together with the gneiss; it has probably originally been a mafic dyke within the granodiorite. The matrix consists mainly of biotite, plagioclase and quartz with some minor epidote. The titanite in this sample has been dated (chapter 4.6). Width of the view 4.5 mm, PPL. **j)** Cataclasite from Hellsö with abundant rock fragments from the tonalitic protolith (sample K-1/03). The groundmass is mainly brown mica and iron oxides, with some epidote and plagioclase/quartz. Width of the view 4.5 mm, PPL.

1988). However, the biotite in the Hellsö cataclasites is not extensively chloritised, which may imply that they were formed in relatively high-T conditions.

4.3.3 PSEUDOTACHYLYTES

In thin section, the pseudotachylytes are mainly composed of a very fine-grained (aphanitic), close to isotropic matrix with tiny porphyroclasts of

quartz and/or feldspars. Some larger (up to 3 cm) melt pockets show zoning, probably indicating a sequence of crystallisation where the outer parts of the melt pockets crystallised/froze slightly more rapidly than the inner parts (fig. 4.29a). In thin section, the crystallisation zones do not appear to differ mineralogically; only a slight colour change can be observed. The larger melt pockets also show a very narrow chilled margin against the gneissose host rock (fig. 4.29b). Some of the Hellsö pseudotachylytes show flow structures, which probably formed when the melts moved along the generation surfaces (fig. 4.29c).

Locally, especially in Hellsö pseudotachylytes, cracks were formed along the pseudotachylyte main generation surface, either as a result of volume contraction as the melts escaped the generation surface and cooled down, or during a later, brittle, small-scale faulting of the rocks (fig. 4.29c). The hydrothermal minerals mainly of the epidote group that crystallised into the cracks may favour the former mechanism.

The depth of the pseudotachylyte formation within the study area remains unclear. However, there are some features that indicate that the pseudotachylytes were not formed very close to the surface. Firstly, the matrix in the observed pseudo-tachylytes is not glassy but very fine-grained and commonly contains abundant, small spherulites, in places even plagioclase microlites close to the pseudotachylyte margin (figs. 4.29a-c). On the other hand, the aphanitic rather than glassy grain size and the spherulitic textures may result from devitrification processes instead of melt crystallisation processes; devitrification being a process where pseudotachylyte glass alters to stable crystalline material in near-surface conditions (e.g. Lin 1994). Aphanitic grain size and small spherulites are indeed common in the studied pseudotachylytes (fig. 4.29c), but it is difficult to determine whether they were formed during melt crystallisation or due to devitrification. While the spherulites observed in the thin sections may indeed have been formed as a response to devitrification, it is not likely that the acicular plagioclase microlites in some pseudotachylyte samples (fig. 4.29b) formed due to complete recrystallisation by means of devitrification processes, but that they rather crystallised directly from the pseudotachylyte melt. Secondly, the larger melt pockets, as described above, show some crystallisation zoning (fig. 4.29a). Thirdly, the ratio clasts/melt (W/M) is quite low; when the microscope photos of Kökar and Kyrkogårdsö pseudotachylytes are analysed with image analysis software (Digimizer 3.0 by Frank Schoonjans), the obtained W/M commonly lies between 0.2-0.35. According to O'Hara (2001), W/M of pseudotachylytes in general lie between 0.1-0.7, a low ratio indicating a high temperature for the pseudotachylyte-hosting country rock at the time of pseudotachylyte formation, and vice versa. In other words, if the country rock temperature is relatively high when the pseudotachylyte melt is formed, the resulting pseudotachylyte will have fewer clasts than if the country rock temperature was lower. O'Hara (2001) further presented a pseudotachylyte geothermometer, where $T(K)_{crust} = (1-W/M)T(K)_{melt}$ (the accuracy of the method is $\pm$70ºC).

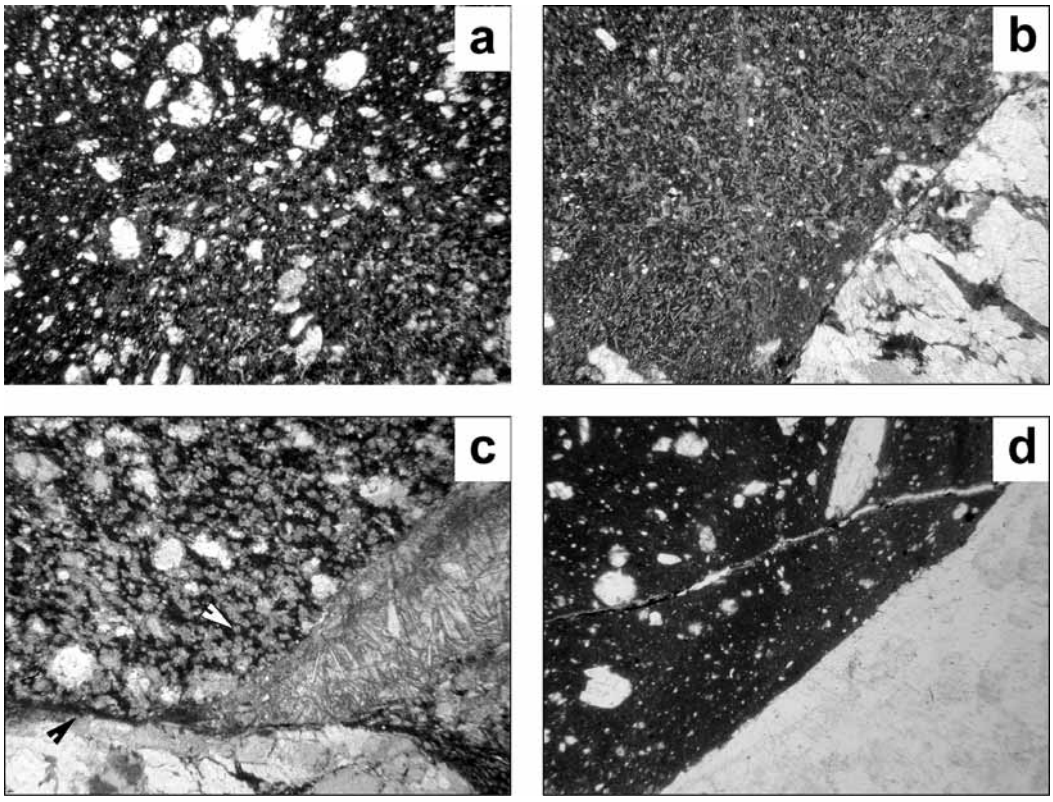

Fig. 4.29. Pseudotachylytes within the study area. Key: PPL = plain-polarized light, CPL = cross-polarized light. **a)** A zoned pseudotachylyte injection vein on Storskär, Kyrkogårdsö (sample KY-11/03). The melt further away from the vein walls probably crystallised slightly more slowly, resulting in a somewhat less glassy matrix with a lighter colour (*centre to lower right*). The clast/matrix ratio in this sample is 0.35. Width of the view 4.5 mm, PPL. **b)** A pseudotachylyte injection vein from Storskär, Kyrkogårdsö (sample KY-4/02). The pseudotachylyte has a slightly more fine-grained 'chilled margin' against the granodioritic wall rock. Note also the abundant small, needle-shaped plagioclase microlites within the pseudotachylyte melt close to the contact with the gneiss, and how the microlites gradually become less abundant toward the centre of the vein (*upper left*). This sample has been dated (chapter 4.6). Width of the view 4.5 mm, PPL. **c)** A pseudotachylyte formed along a main fault vein (generation surface), Hellsö (sample K-8/02). The pseudotachylyte melt shows a weak flow texture (*from upper left toward centre*), probably formed as the melt moved along the surface. The melt is rich with small, reddish feldspar spherulites (*white arrow*), making the determination of the clast/melt ratio very difficult. A later crack (or a cooling crack) cutting the pseudotachylyte is filled with mineral crystals from the epidote group – in other locations, the same crack follows the wall of the main fault vein. The epidote crack is here in turn offset by a later, brittle microfracture (*black arrow*). Width of the view 4.5 mm, PPL. **d)** A pseudotachylyte within a granitic gneiss, Torsholma (sample To-MLN-1). The matrix is glassy and largely unvitrified, and the clast/melt ratio is calculated to 0.2. This sample has been dated (chapter 4.6). Width of the view 4.5 mm.

Using his formula, temperatures of ca. 400 and 530ºC can be calculated for country rocks hosting pseudotachylytes with clast/melt ratios of 0.35 and 0.2, respectively, if a pseudotachylyte melt temperature of 750ºC is assumed. The assumed melt temperature is very low, since pseudotachylyte melts are usually considered to have temperatures between 750-1600ºC (e.g. DiToro & Pennacchioni 2004, O'Hara 2001, Lin

& Shimamoto 1998), but using higher melt temperatures would give even higher country rock temperatures, completely unrealistic for the study area. On the other hand, the country rocks are quartzo-feldspatic and rich in hydrous minerals, so relatively low melt temperatures could be expected, even in a case of non-equilibrium melting associated with pseudotachylyte formation. Nevertheless, the country rock temperature calculated for W/M of 0.2 (530ºC) seems high considering the structural and petrographical evidence, while the temperature calculated for ratio 0.35 (400ºC) seems more realistic. Possible devitrification processes (spherulites) observed in thin section could have obscured the true abundance of especially the smaller clasts in some samples. The image analysis would consequently give too low clast/melt ratios for the studied devitrified samples. On the other hand, a largely undevitrified pseudotachylyte sample from Torsholma, ca. 40 km north of Kökar (outside the area of this study), was analysed for comparison, and a clast/melt ratio of 0.2, i.e. within the same range as for Kökar and Kyrkogårdsö pseudotachylytes, was obtained (fig. 4.29d). All in all, despite their uncertainties, the temperature calculations give an indication that the pseudotachylytes were formed at relatively high crustal temperatures (country rock temperatures in the order of 400ºC).

In summary, the aforementioned features imply that the crystallisation temperature of the pseudotachylyte melts was relatively high, and the rocks therefore may have remained well within the ductile-brittle transition zone during the pseudotachylyte-forming event. The depth of this transition varies greatly depending mostly on temperature but also on lithotype, strain rate, fluid pressure, operative slip systems and grain size (e.g. Passchier & Trouw 2005, McNulty 1995). The transition zone is by many authors placed between ca. 300-500ºC, i.e. 10-15 km, for pelitic and quartzofeldspatic rocks, the upper limit roughly corresponding to the cessation of feldspar plasticity (e.g. Pennacchioni & Cesare 1997, McNulty 1995, Tullis & Yund 1987). No overprinting of the pseudotachylytes by more ductile phases (mylonites) have been observed, which would be a definite, but not required, indication of a high country rock temperature, so the conditions may have been closer to brittle than to ductile regime and the temperatures therefore well below 500ºC. Some authors place the lower temperature limit of the first occurrence of crystalline (microlitic) pseudotachylyte to 150-200ºC (e.g. Scholz 1988).

4.3.4 SUMMARY OF MICROSTRUCTURES

Based on the microstructural evidence, at least the last two ductile deformation phases (D_3 and D_4) took place in amphibolite facies conditions, while indications of earlier deformation phases have been erased from the rocks. Substantial static recovery took place also during and after D_3 and D_4 deformation phases, quite effectively erasing the dynamic structures in all but the most intensely deformed rocks. The temperature dropped rapidly after main D_4 and a possible subsequent short period of static recrystallisation, probably due to post-orogenic rapid uplift and exhumation.

During D3 and D4, the temperatures were between 500-700°C, based on the preserved dynamic microstructures observed in the studied samples. Evidence from the narrow shear zones of Hellsö, preserving the highest-T dynamic microstructures, implies that the temperature was somewhat higher during D3 than during main D4, although the difference in temperature (and microstructures) seems quite small. The presence of two titanite generations in some rocks supports the notion that the rocks were within approximately the same temperature regime during D3-4, and that relatively little temperature chance occurred between D3 and main D4, as the abundant titanite (+amphibole) is indicative of a slow cooling rate. It is postulated here that most of the mylonites within the study area formed during the main or the late stages of D4, although especially some of the protomylonitic varieties may have formed earlier. Latest soon after D4 and a possible subsequent short period of static recovery the rocks reached the amphibolite-greenschist facies transition (500-550°C), mostly indicated by the occasional chloritisation reactions. After D4 the rocks cooled more rapidly and without extensive deformation, probably due to uplift and exhumation, although some gneisses within the SJSZ show that limited semi-ductile deformation may have taken place during late- to post-D4 period in temperatures between ca. 400-500ºC. Semi-brittle and brittle structures are consequently rare within the study area. The pseudotachylytes and cataclasites that nevertheless are observed are here suggested to have formed at relatively high crustal temperatures, however probably well below 500°C.

4.4 GEOCHEMISTRY

For the purposes of this study, 17 samples were collected and analysed in order to establish a general picture of the geochemistry of the igneous rocks in the area. The selected samples were grinded at the Åbo Akademi University and analysed at the Acme Laboratories in Canada (whole rock and REE analysis with ICP-MS and ICP-ES; tab. 4.2). The analysis data were processed with Igpet2001 software (Terra Softa). Of the samples, five represent the mafic rocks, commonly occurring as lenses within the study area; two samples are from tonalitic rocks, one of them being an ultramylonite; and ten samples were taken from granitic to granodioritic (quartz-feldspar) gneisses. The small amount of geochemical data collected within the scope of this study does not justify speculation of the petrogenesis of the rocks; nevertheless, the data that was obtained is briefly summarised below.

Most of the mafic rock samples (1, 2, 5, 12) are dominantly composed of very large hornblende crystals, the texture of the rock being in places almost pegmatitic (fig. 4.30a). Other minerals present in these rocks include plagioclase and mica (dominantly biotite), with some accessory opaques. The minerals do not show strong deformation fabrics or retrograde alteration, suggesting that the (re)crystallisation of the mafic rocks occurred at high temperatures at early stages of the regional deformation, and that at lower temperatures the rock was rheologically sufficiently strong to resist deformation and/or there were not enough fluids present during retrogression for the lower-T reactions to take place. Since the dominating mineral is the seemingly primary hornblende, it is unlikely that the rocks represent oceanic tholeiites, as the f_{H2O} and F_{O2} would generally be too low for primary amphibole to crystallise from oceanic tholeiitic magmas (Deer et al. 1992). Sample 14 differs considerably from the other four mafic rock samples. It consists mainly of pyroxene, extensively altered to uralite (a secondary, very fine-grained blue-green amphibole with a undeterminable composition, but usually of tremolite or cummingtonite chemistry; Deer et al. 1992) with exolution of an opaque phase; biotite which is often altered to hydrothermal, medium-grained chlorite; some olivine, in places altered to red-brown iddingsite with an opaque (magnetite?) rim; and minor plagioclase, that is extensively sericitised and in places shows retrograde exolution of calcite/dolomite (figs. 4.30b-d). Also spinel (?; deep green, isotropic) symplectites associated with olivine, plagioclase and pyroxene/uralite occur, probably as remnants from earlier high-T conditions (fig. 4.30d). This olivine-gabbroic rock has, in other words, undergone extensive hydrothermal alteration.

The tonalitic rock samples (samples 16 and 17) were collected from Kyrkogårdsö area. Sample 16 is a medium-grained, equigranular tonalite gneiss, consisting mainly of hornblende, plagioclase, quartz, biotite and some titanite. Sample 17 is an ultramylonite with a tonalitic protolith. It contains porphyroclasts of plagioclase and hornblende, the very fine-grained matrix consisting mainly of mica, plagioclase/quartz, epidote and some chlorite with occasional narrow quartz ribbons (fig. 4.28f).

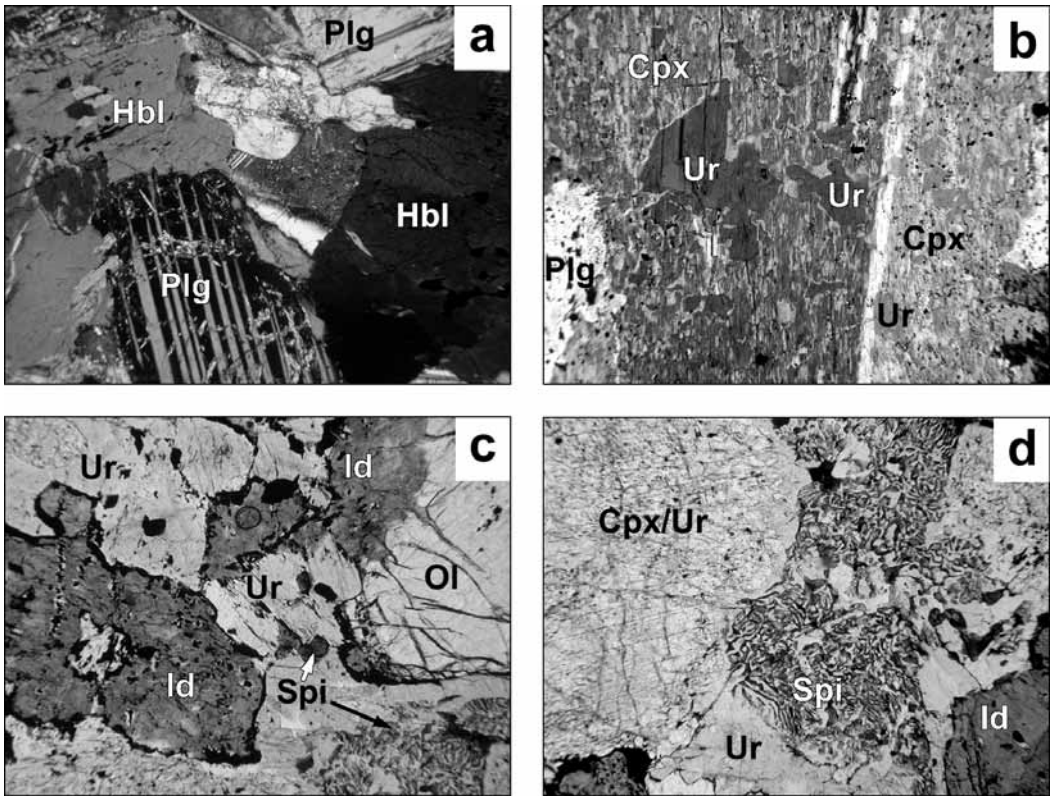

Fig. 4.30. Selected microscope photographs from the geochemistry samples. Key: Ur = uralite, Cpx = clinopyroxene, Ol = olivine, Id = iddingsite, Spi = spinel, Epi = epidote, Ti = titanite, Il = ilmenite/ilmenorutile, Hbl = hornblende, Plg = plagioclase, Mi = microcline, Bt = biotite, Qtz = quartz, PPL = plain-polarized light, CPL = cross-polarized light. **a)** An amphibolite lens, W Kökar (sample Geochemistry 5). Width of the view 4.5 mm, CPL. **b-d)** An ultramafic lens within SJSZ on Storskär, Kyrkogårdsö (sample Geochemistry 14). b) The pyroxene is commonly partly or wholly altered to uralite (*see text*) with an exolution of an opaque phase (tiny black dots within the Cpx, best visible on the right side of the view). Width of the view 4.5 mm, CPL. c) The olivine is often altered to iddingsite with opaque magnetite rims (*see text*). A spinel(?)-uralite symplectite can be seen on lower right. Width of the view 1.8 mm, PPL. d) A detail of a spinel-uralite symplectite. Width of the view 1.8 mm, PPL.

The granitic and granodioritic rock samples (samples 3, 4, 6-11, 13 and 15) represent quartz-feldspar gneisses deformed to various degrees (figs. 4.25a, d; 4.26g, h; 4.27c, f). The least deformed samples 3 and 4 are from W Kökar (granite gneiss; fig. 4.25a, d). Samples 7-11 (W Hellsö) and 15 (Storskär, Kyrkogårdsö) are most deformed, representing intensely deformed rocks from local and large-scale deformation zones, respectively (fig. 4.26g, h; 4.27c, f). All of the rocks belonging to this sample group are mainly composed of quartz, K-feldspar, plagioclase and biotite in varying proportions, with some accessory apatite.

Following the classification of volcanic rocks by LeBas et al. (1986), plotting all geochemical analysis on a Na_2O+K_2O/SiO_2 diagram reveals that the rocks within the study area form an almost linear trend from ultrabasic and basic rocks through intermediate compositions to granites (fig. 4.31a).

This is typical for volcanic arc systems (Eichelberger et al. 2006). The same trend is observable also in the Nb/Y vs Zr/Ti diagram (Pearce 1996; fig. 4.31b).

The mafic rocks are ultrabasic to basic in composition (tab. 4.2, fig, 4.31). Samples 1, 2 and 12 from W and NW Kökar show SiO_2 contents of <45%. Sample 14 from Storskär is basic-ultrabasic with 45.2% SiO_2. Sample 5 from NW Kökar contains most SiO_2 of the five mafic rock samples (48.4%). The mafic samples

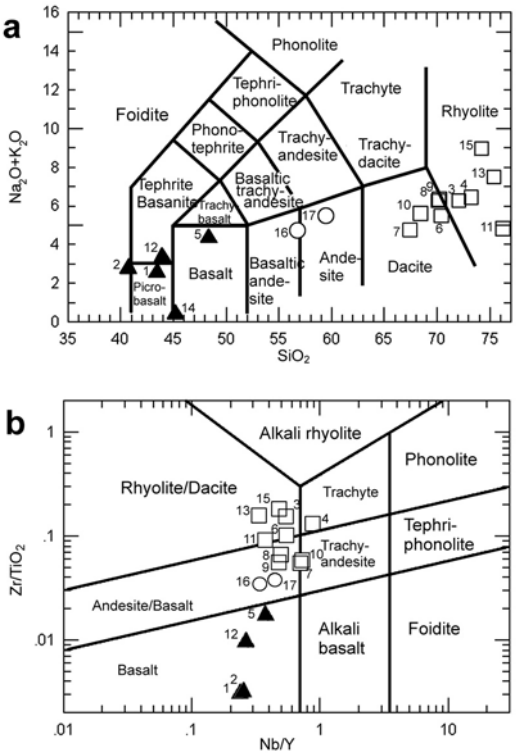

Fig. 4.31. Examples of geochemical data plots for the whole-rock ICP-MS analysis data of samples collected from the study area, illustrating the overall geochemical composition of the analysed rocks. **a)** A Na_2O+K_2O/SiO_2 diagram according to LeBas et al. (1986). **b)** Zr/TiO_2 vs. Nb/Y diagram according to Winchester & Floyd (1977). Sample 14 is not plotted since the amount of Nb in the sample was under the detection limit (0.5 ppm).

are relatively low in Al, the Al_2O_3 content being as low as 3.9% in sample 14, the other four samples displaying Al_2O_3 contents between 15.2% and 16.6%. The samples are also low in alkalis, showing subalkaline (sample 14) to borderline alkaline affinities (fig. 4.32). Sample 14 contains as much as 20% MgO but little TiO_2 (0.44%), while in the other mafic samples MgO is quite low (3.7-8.7%) and TiO_2 ranges from 1.1 to 2.3% (tab. 4.2). All in all, sample 14 hows very different geochemical characteristics compared to the other basic rocks (tab. 4.2). A REE plot of the mafic rock samples (fig. 4.33a) shows that sample 14 is slightly depleted in LREE, while the rest of the mafic samples are LREE enriched. Also in an incompatible trace element 'spider' plot (fig. 4.33b) sample 14 stands out from the other four basic samples. All of the mafic samples, especially sample 14, show clear negative Nb-Ta anomalies and positive U and K anomalies, generally interpreted being indicative of a subduction environment (e.g. Best & Christiansen 2001).

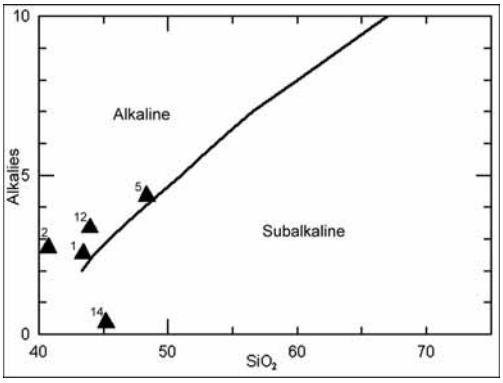

Fig. 4.32. Alkalis vs. SiO_2 diagram illustrating the affinities of the analysed mafic rock samples. See text for discussion.

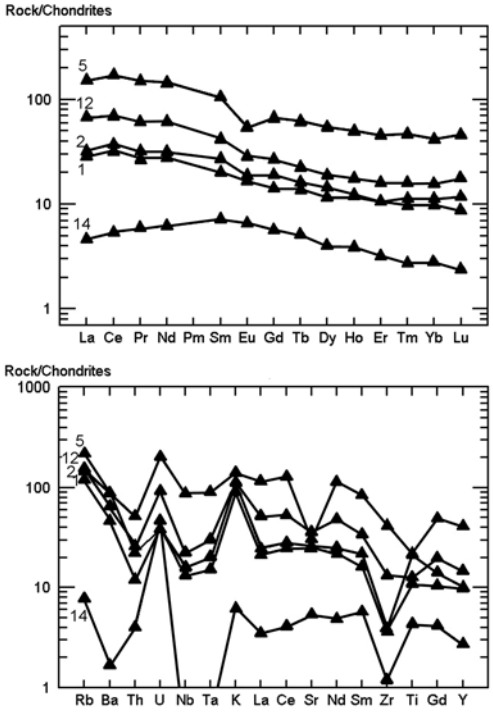

Fig. 4.33. a) REE diagram and **b)** incompatible element spider diagram for the tonalitic rock samples by Sun & McDonough (1989) and Sun (1980), respectively.

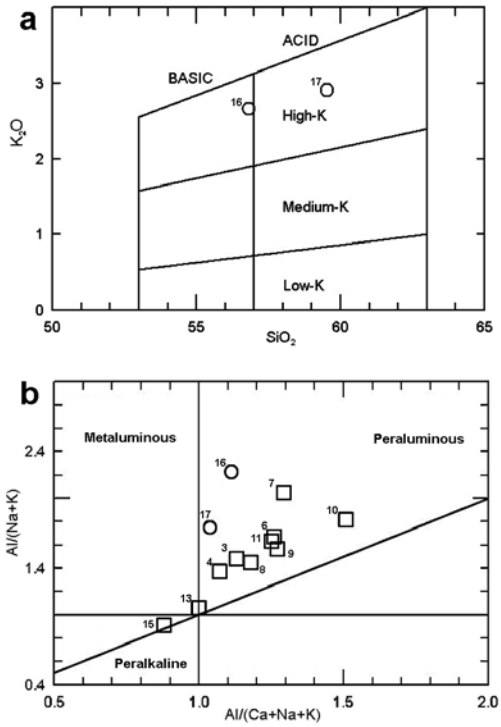

Fig. 4.34. a) K_2O vs. SiO_2 diagram for the analysed tonalitic rock samples. **b)** Shand's index for the analysed intermediate and acid rock samples (Maniar & Piccoli 1989).

The tonalitic rocks (samples 16 and 17) plot in the intermediate field with respect to their SiO_2 contents (56.8% and 59.5%, respectively). The rocks have high K_2O/SiO_2 ratios (fig. 4.34a). Despite the fact that both samples plot into a peraluminous field (fig. 4.34b), they do not contain Al-rich minerals such as Al_2SiO_5 polymorphs (e.g. kyanite), and even muscovite and garnet are very rare. The REE plot against upper continental crust does not show any significant anomalies for the tonalitic rocks, although sample 16 (tonalite gneiss) is slightly depleted in LREE (fig. 4.35a). The trace element pattern of the samples displays slight positive anomalies for U and small negative anomalies for Nb, Ta, Hf and Zr (fig. 4.35b).

The granitic and granodioritic gneisses (samples 3, 4, 6-11, 13 and 15) have SiO_2 contents of up to 75.4% (tab. 4.2). None of the acid rocks contain Al_2SiO_5 polymorphs and also garnet and muscovite remain very uncommon, although they mostly plot into a peraluminous field (fig. 4.34b) and have obviously been metamorphosed within upper amphibolite facies conditions. A REE plot of the acid rocks show a slight trend of HREE depletion compared to the mean upper continental crust (fig. 4.36a; Taylor & McLennan 1985). The samples do not show any significant Eu anomalies. The trace element pattern reveals that even the acid

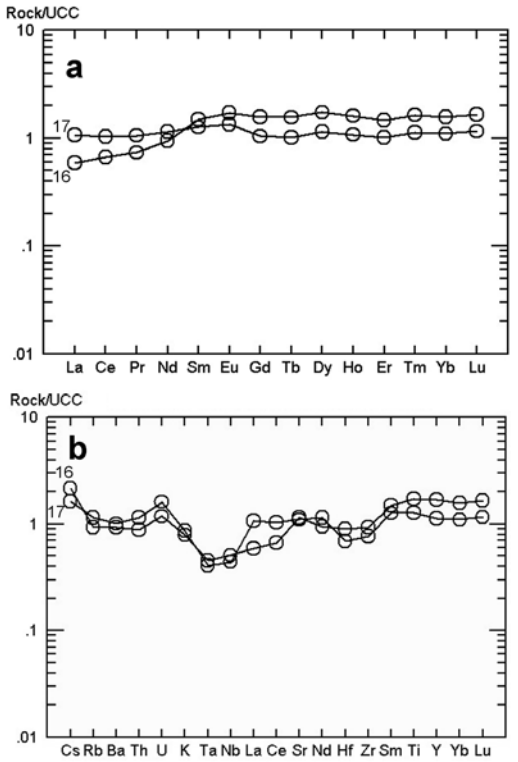

Fig. 4.35. a) REE diagram and **b)** incompatible element spider diagram by Taylor & McLennan (1985), normalised for upper continental crust, for the tonalitic rock samples. See text for discussion.

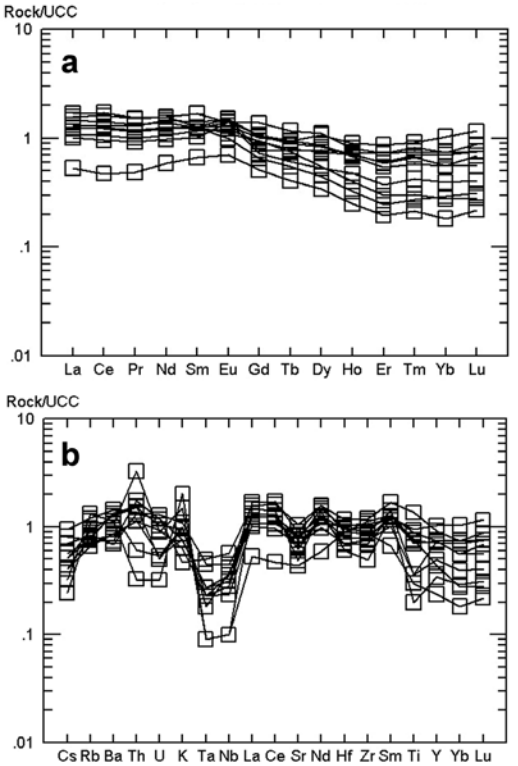

Fig. 4.36. a) REE diagram and **b)** incompatible element spider diagram by Taylor & McLennan (1985), normalised for upper continental crust, for the granodioritic to granitic rock samples. See text for discussion.

rocks have clear negative Nb-Ta anomalies and several also show negative Ti anomalies, suggestive of a subduction-related environment (fig. 4.36b). Several samples also show slightly positive Th and K, especially sample 13; on the other hand, sample 15 also displays negative Th-U anomalies.

As a summary, the rocks are geochemically complex, which can be expected as they have undergone several periods of intense deformation, alteration and metamorphism. The scarcity of the data does not allow deductions of the petrogenesis of the rocks, although some indications of a presence of a subduction zone exist.

Table 4.2. Whole-rock ICP-MS geochemistry of selected rock samples from the study area (SJSZ and Kökar), Åland, Finland.

Sample	1	2	3	4	5	6	7	8	9	10	11	12	13	14	15	16	17
Location	W Kökar	W Kökar	W Kökar	W Kökar	NW Kökar	NW Kökar	W Hellsö	W Hellsö	W Hellsö	W Hellsö	W Hellsö	NW Kökar	Kökar kyrka	Storskär	Storskär	Storskär	Kyrko-gårdsö
Rock type	Amphi-bolite Mafic lens	Amphi-bolite Mafic lens	Granite gneiss	Granite gneiss	Amphi-bolite Mafic lens	Granod. gneiss	Granod. gneiss Local shear zone	Granod. gneiss Local shear zone	Granod. gneiss Local shear zone	Granod. gneiss Local shear zone	Granod. gneiss Local shear zone	Amphi-bolite Mafic lens	Granod. gneiss	Amphi-bolite Mafic lens	Granite gneiss	Tonalite gneiss	Ultra-mylonite =KY-8/04[a]
wt.%																	
SiO[2]	43.43	40.73	72.05	73.25	48.36	70.39	67.49	70.21	70.11	68.4	76.24	43.95	75.41	45.2	74.21	56.82	59.54
Al2O3	16.55	16.27	13.83	13.18	15.19	13.55	14.18	13.76	14.44	15.29	11.62	16.13	12.01	3.9	12.49	15.7	14.23
Fe2O3	13.03	16.91	3.07	2.97	14.99	5.02	5.75	4.18	4.07	4.75	3.06	14.65	1.88	12.31	2.02	8.96	7.02
MgO	8.72	8.18	0.43	0.36	3.74	0.96	1.96	1.23	1.49	1.73	0.9	6.97	0.4	20.49	0.26	4.45	5.31
CaO	11.19	10.02	2.13	2.01	7.95	1.94	2.98	1.6	1.59	1.28	1.59	10.38	0.5	13.76	0.36	5.23	4.12
Na2O	1.25	1.12	2.97	3.06	2.31	2.93	3.19	2.68	3.75	2.37	2.67	1.7	2.47	0.29	2.11	2.05	2.55
K2O	1.3	1.61	3.31	3.38	2.03	2.56	1.57	3.66	2.53	3.24	2.15	1.65	5.02	0.09	6.85	2.66	2.91
TiO2	1.11	2.16	0.18	0.18	2.27	0.35	0.68	0.47	0.44	0.38	0.37	1.3	0.1	0.44	0.15	0.86	0.64
P2O5	0.09	0.06	0.04	0.03	0.65	0.1	0.09	0.09	0.08	0.07	0.06	0.34	0.03	0.02	0.02	0.26	0.19
MnO	0.18	0.16	0.04	0.04	0.24	0.07	0.05	0.04	0.04	0.02	0.02	0.22	0.03	0.16	0.02	0.14	0.11
Cr2O3	0.011	0.007	0.006	0.006	0.003	0.008	0.012	0.01	0.011	0.011	0.009	0.009	0.006	0.205	0.006	0.016	0.05
TOT.	96.86	97.23	98.06	98.47	97.73	97.88	97.95	97.93	98.55	97.54	98.69	97.30	97.86	96.87	98.50	97.15	96.67
ppm																	
Ni	23	36	9	10	21	15	30	29	22	25	17	13	11	236	5	31	101
Sc	45	73	5	6	42	9	11	8	5	2	7	41	2	74	4	28	20
Ba	176.8	334.4	733.1	734	332.1	452.8	403.9	789.9	381.7	694.5	474.4	245.3	591	6.3	624.1	508.5	553.8
Be	<1	1	1	1	2	1	1	1	3	4	1	1	1	<1	1	2	2
Co	39.9	47.9	4.5	3.5	26.4	6.1	13.2	9.4	7.7	15.9	6.9	35.9	2.5	71	2.7	20	22.5
Cs	2.2	1.6	1.9	1.5	3.8	2.1	3	3.5	2.6	1.9	1.5	2.5	0.9	0.1	1.2	8	6

Table 4.2. *(Continued)*

Sample	1	2	3	4	5	6	7	8	9	10	11	12	13	14	15	16	17
Ga	19.2	22	17.4	18	23.2	18.1	17.8	16.7	18.3	17.9	12.8	19.6	12.7	5.5	14.3	21.5	18
Hf	0.9	0.9	5.7	4.1	6.5	5.2	6.8	5.5	4.5	4	6	2.2	3.5	<.5	5.2	5.2	4
Nb	4.6	5.5	8.9	9.5	30.7	8.9	14.2	11.1	7.8	7	5.9	7.7	2.5	<.5	2.5	12.7	11
Rb	41.7	50.7	87.8	90.2	76.6	85	84.2	134.3	93	104.7	74.6	53.4	127.1	2.7	148.3	103.9	128.8
Sn	3	2	<1	1	4	2	1	1	<1	<1	<1	2	<1	<1	<1	2	2
Sr	272.9	286.9	262.8	240.4	331.2	316.3	364.5	294.7	234	218.8	285.3	389	169	58.6	153.8	399.2	385.4
Ta	0.3	0.4	0.5	0.4	1.8	0.6	1.1	1	0.6	0.5	0.5	0.6	0.2	<.1	0.2	1	0.9
Th	0.6	1.1	16.5	6.5	2.6	12.3	18.8	14.7	14.1	16.3	12	1.3	35	0.2	3.5	9.4	12.2
U	0.5	0.5	1.4	1.5	2.6	1.5	3.3	3.6	3.3	2.9	2.6	1.2	2.5	0.6	0.9	3.3	4.5
V	544	887	25	20	256	34	88	59	62	74	46	279	21	274	12	170	113
W	10.2	11.5	36.7	33.3	15.3	42.4	24.7	23.3	23.3	20.1	22.3	32.5	30.3	14.9	32	22.4	20.1
Zr	20.5	21.7	166.8	142.3	235.2	214.2	225.7	186.1	147.3	133	204.1	74	93.7	6.6	163.1	175.7	144.9
Y	19.4	20.1	16.3	10.9	81.6	16.3	20.2	22.5	16.4	9.6	15.8	29.2	7.5	5.4	5.2	37	24.7
La	6.8	7.7	39.4	30.4	36.2	50.4	47	37.4	36.9	36.9	31.8	16.2	44.1	1.1	15.9	17.7	32.2
Ce	19.9	22.8	82.4	61.7	104.7	110.1	103.5	78.7	80	78.7	68.2	43.1	91.2	3.3	30.3	42.4	66.2
Pr	2.61	3.07	9.27	6.55	14.31	10.87	10.69	8.15	8.36	8.12	7.11	5.84	9.45	0.56	3.47	5.22	7.51
Nd	13.1	14.8	38	25.4	68	40.5	40.8	32.8	32.3	31.8	28	28.8	36.1	2.9	15.4	24.6	29.8
Sm	3.1	4.2	6.4	4.6	16	5.7	7.6	5.5	5.7	5.7	5.2	6.5	5.6	1.1	3	6.7	5.7
Eu	0.97	1.1	1.32	1.24	3.13	1.33	1.22	1.25	1.14	0.97	1.07	1.68	0.87	0.38	0.62	1.51	1.18
Gd	2.91	3.93	3.97	2.76	13.82	2.96	5.25	4.05	3.86	3.6	3.52	5.51	2.47	1.16	1.94	5.98	3.96
Tb	0.52	0.61	0.57	0.39	2.33	0.49	0.75	0.61	0.6	0.48	0.51	0.85	0.35	0.19	0.26	1	0.65
Dy	2.98	3.69	2.91	1.85	13.86	2.75	3.91	3.76	3.04	1.94	2.61	4.86	1.57	1.02	1.19	6.07	4
Ho	0.67	0.7	0.57	0.38	2.84	0.59	0.65	0.72	0.54	0.32	0.56	1	0.26	0.22	0.2	1.29	0.86
Er	1.74	1.75	1.36	0.86	7.51	1.66	1.67	2	1.25	0.68	1.37	2.67	0.56	0.53	0.45	3.36	2.34
Tm	0.29	0.25	0.22	0.14	1.2	0.27	0.25	0.3	0.19	0.1	0.23	0.41	0.09	0.07	0.07	0.54	0.37
Yb	1.92	1.67	1.22	0.87	7.1	1.63	1.63	2.28	1.22	0.61	1.54	2.66	0.64	0.47	0.4	3.45	2.42

Table 4.2. *(Continued)*

Sample	1	2	3	4	5	6	7	8	9	10	11	12	13	14	15	16	17
Lu	0.3	0.22	0.22	0.13	1.17	0.24	0.28	0.37	0.18	0.09	0.24	0.45	0.1	0.06	0.07	0.53	0.37
Mo	1.4	1.5	4.4	4.3	2.4	5.1	2.8	2.6	3.1	4	2.3	1.2	4.7	1.6	3.6	2.7	2.6
Cu	29.8	54.7	5.6	4.8	17	4.8	6.9	7.6	13.9	46.4	7.5	23.7	3.7	95.4	3.2	17.5	4.4
Pb	5.6	8.4	3.3	3.5	8	5.2	6.2	5.8	4	8.7	7.1	5.7	20.5	3.1	3.7	5.2	3
Zn	52	91	29	35	128	49	81	58	56	65	32	72	19	30	17	94	85
As	1	1	0.5	0.6	0.8	0.7	<.5	2.5	<.5	1.2	0.7	1.5	<.5	2.2	0.6	0.7	<.5
Sb	0.1	0.1	0.1	0.1	0.2	0.1	<.1	0.1	<.1	0.1	0.1	0.1	0.1	0.1	0.1	0.1	<.1
Au	3.4	2.2	2.1	3	1.8	0.8	1	1.9	2.4	5.7	2.2	1.1	1.3	2.7	1.2	0.8	1.4
Tl	0.1	0.3	0.2	0.1	0.3	0.1	0.4	0.4	0.4	0.3	0.2	0.1	0.1	0.3	0.1	0.4	0.4

a) This is the same sample as KY-8/04 used for geochronology (chapter 4.6).

4.5 AGE DETERMINATIONS – TIMING THE ACTIVITY OF THE SHEAR ZONE

Large parts of the following chapters are reproduced from the article Torvela et al. (accepted). Especially the calculation procedures and the interpretation of the results of the U-Pb isotope analyses and the $^{40}Ar/^{39}Ar$ analyses described in chapter 4.6.3 rely heavily on the expertise of Mänttäri and of Hermansson and Page, respectively.

4.5.1 TIMING OF THE SHEARING – PREVIOUS STUDIES

Previous studies close to the area of this study have been successful in giving an overall time frame for the deformation within the study area and the formation of the SJSZ (e.g. Ehlers et al., 2004; Suominen, 1991). The ages frequently encountered within these studies cluster in three distinctive groups of ca. 1.88 Ga, 1.83 Ga and 1.79-1.80 Ga.

The first group with the highest obtained ages of ca. 1.88 Ga have been interpreted to represent the approximate intrusive ages of the rocks in the area, the ages being synorogenic in respect to the Svecofennian orogeny in SW Finland. For example, the striped granodioritic gneisses at the southern margin of the SJSZ on Hellsö, northern part of the island of Kökar (ca. 10 km SE of the area of this study), give a magmatic age of 1885 Ma, thus indicating the maximum age for the earliest ductile shearing (Ehlers et al. 2004). The zircons in the sample in question also showed some metamorphic overgrowths, none of which was younger than ca. 1860 Ma (Ehlers et al. 2004). This age is the only one south of the study area that indicates any metamorphism outside the main SJSZ at ca. 1.85-1.86 Ga. This in turn may suggest that the SJSZ was already relatively well developed at that time so that the deformation and metamorphism was already concentrated into the present SJSZ.

The extrusive age of the volcanic supracrustal rocks north of the SJSZ is approximately the same as that of the igneous rocks south of the shear zone, i.e. 1.89-1.88 Ga (e.g. Huhma 1986). However, the volcanic and sedimentary supracrustal units underwent extensive migmatisation at ca. 1.84-1.83 Ga as the (e.g. Suominen 1991, Huhma 1986). Indications of a regional migmatising heat pulse around 1.83 Ga are also recorded by late-orogenic intrusions in southwestern Finland as reported by e.g. Kurhila et al. (2005) and Suominen (1991). In literature, the migmatised belt is referred to by different names, the term Late-Svecofennian Granite-Migmatite Zone (LSGM; Ehlers et al. 1993; fig. 4.1) being adopted by the author. The possible connection of the SJSZ and other crustal-scale shear zones in southern Finland to the LSGM is unknown, although an obvious spatial relationship can be observed: the SJSZ, for example, closely corresponds to the southern margin of the LSGM, the migmatization being limited within and completely absent south of the shear zone itself. Stålfors & Ehlers (2005) suggest that the ca. 1.83 Ga granites in Nagu area, close to SJSZ, were emplaced along sub-vertical shear zones, the fractionation of the melts being a shear-assisted process. This implies that the SJSZ was well developed by 1.83 Ga.

Table 4.3. Summary of the dated rock samples from SJSZ, Kyrkogårdsö area.

	Sample number	Rock type	Sample description	Figures
Gneisses	**KY-7/03**	Granodioritic gneiss	Medium-grained, relatively granoblastic, high-T static recrystallisation of quartz. Mineralogy: quartz, plagioclase, K-feldspar, biotite, minor chlorite and apatite.	Fig. 4.38a
	KY-6/04	Tonalitic gneiss	Medium-grained, relatively granoblastic, static recrystallisation present but less evident than in the granodiorite. Mineralogy: Plagioclase, quartz, hornblende, biotite, titanite, epidote, opaques (ilmenite/ilmenorutile?), minor chlorite and apatite.	Fig. 4.38b
	KY-1/03	Metadiabase dyke	Meduim-grained, relatively granoblastic, relatively strain-free plagioclase grains indicate some static recrystallisation. Mineralogy: Plagioclase, hornblende, biotite, titanite, epidote, ilmenite (ilmenorutile), minor quartz, chlorite and apatite.	Fig. 4.38c
Mylonites	**KY-8/04**	Ultramylonite *From a >20 m wide mylonite zone*	A mylonite with a tonalitic (amphibole-rich) protolith. Very fine-grained matrix with rounded porphyroclasts. Matrix mineralogy: biotite, plagioclase/ quartz, chlorite, epidote, zircon, opaques (ilmenite). Porphyroclasts: plagioclase, hornblende, titanite.	Fig. 4.48g
	KY-2/03	Protomylonite *From a >20 m wide mylonite zone*	A relatively coarse-grained mylonite variety (20-30% fine-grained matrix) with medium-grained porphyroclasts. Matrix mineralogy: biotite, quartz. Porphyroclasts: Plagioclase, hornblende, titanite, ilmenite (ilmenorutile), some smaller biotite and quartz.	Figs. 4.38e and f
	E-2/03	Mylonite *A 10 cm wide mylonite band*	Mylonite with 50-60% fine-grained matrix. Some static recrystallisation structures in quartz ribbons within matrix. Matrix mineralogy: biotite, quartz, epidote, minor chlorite. Porphyroclasts: Plagioclase, quartz, titanite, ilmenite (ilmenorutile).	Fig. 4.38d
Pegmatite dykes	**KY-1/04, KY-4/04**		30-40 cm wide pegmatite dykes cutting the foliation of granodioritic gneiss.	Fig. 4.39
Pseudotachylyte	**KY-4/02**		A pseudotachylyte injection vein in a granodioritic wall rock.	Fig. 4.38h

Furthermore, metamorphic ages from this group (ca. 1.83 Ga) have not been reported from the area SW of the SJSZ and the study area, i.e. from within the unmigmatised granitoids, although they are common in the supracrustals, migmatites and granitoids north of the SJSZ. This supports the notion that within and SW of the study area, the regional deformation was dominantly partitioned into the main SJSZ by ca. 1.83 Ga.

The third age group of ca. 1.79-1.80 Ga is also common in the granitoids and migmatites close to the study area and also elsewhere in SW Finland (e.g. Lahtinen & Huhma 1997, Suominen 1991). Suominen (1991) interpreted the ca. 1.80 Ga titanite ages from Åland islands and Tammisaari to indicate a postorogenic regional metamorphic event or the end of such an event, the cause and nature of which was however not speculated. Of results closest to the area of this study, Suominen (1991) reported a titanite age of ca. 1.80 Ga in a 1.88 Ga granite in Mörskär, Kökar. Furthermore, Ehlers et al. (2004) identified a population of ca. 1.79 Ga metamorphic titanites within the 1.88 Ga granodioritic gneisses of Hellsö (northern Kökar); the implications of the obtained U-Pb ages and the relation of the titanite growth to the regional shearing were, however, not assessed. Finally, the weakly foliated granitic dykes that intrude and crosscut the gneisses of the SFSZ on the island of Sottunga, near the Mosshaga granite pluton (fig. 4.3), show U-Pb zircon ages of 1.79 Ga (Ehlers et al. 2004). According to their interpretation, the relatively weak deformation in the dated dykes indicates that the large-scale ductile deformation within the shear zone had reached a waning stage by 1.79 Ga.

The purpose of this study is to define the time span over which the SJSZ was active. Further attempts were made for timing of the different deformation phases observed in the field, i.e. ductilely deformed granoblastic gneisses, ductile to semi-ductile mylonites and ultramylonites, and brittle pseudotachylites. Direct dating of shear zone deformation is possible, as many radiometric isotope systems such as U-Pb and Rb-Sr are sensitive to metamorphism and deformation in the presence of recrystallisation processes (e.g. Resor et al. 1996). Indeed, many shear zones and their deformation phases in Fennoscandia have already been successfully dated (e.g. Hermansson et al. 2007, Högdahl & Sjöström 2001, Ploegsma 1991), and some of these shear zones may also have a direct relation to the SJSZ.

4.5.2 SAMPLE DESCRIPTION

The main petrographic and mineralogical features of the samples that were dated within the scope of this study are summarised in table 4.3. The entire study area is very well exposed and structurally homogeneous, so it can be stated with good confidence that all collected samples, despite their distance, belong to the same shear zone.

Based on field and petrographic studies as well as on the previous age determinations compiled above, the deformation within the study area partitioned into the main shear zone at a relatively early stage. As metamorphic ages of ca. 1.85 Ga are rare outside (SW) the shear zone it is here suggested that the deformation

partitioning initiated, i.e. the shear zone formed, approximately at this time. In any case, as demonstrated in the previous chapters, the overall deformation in the area was dominantly lateral-slip style and the

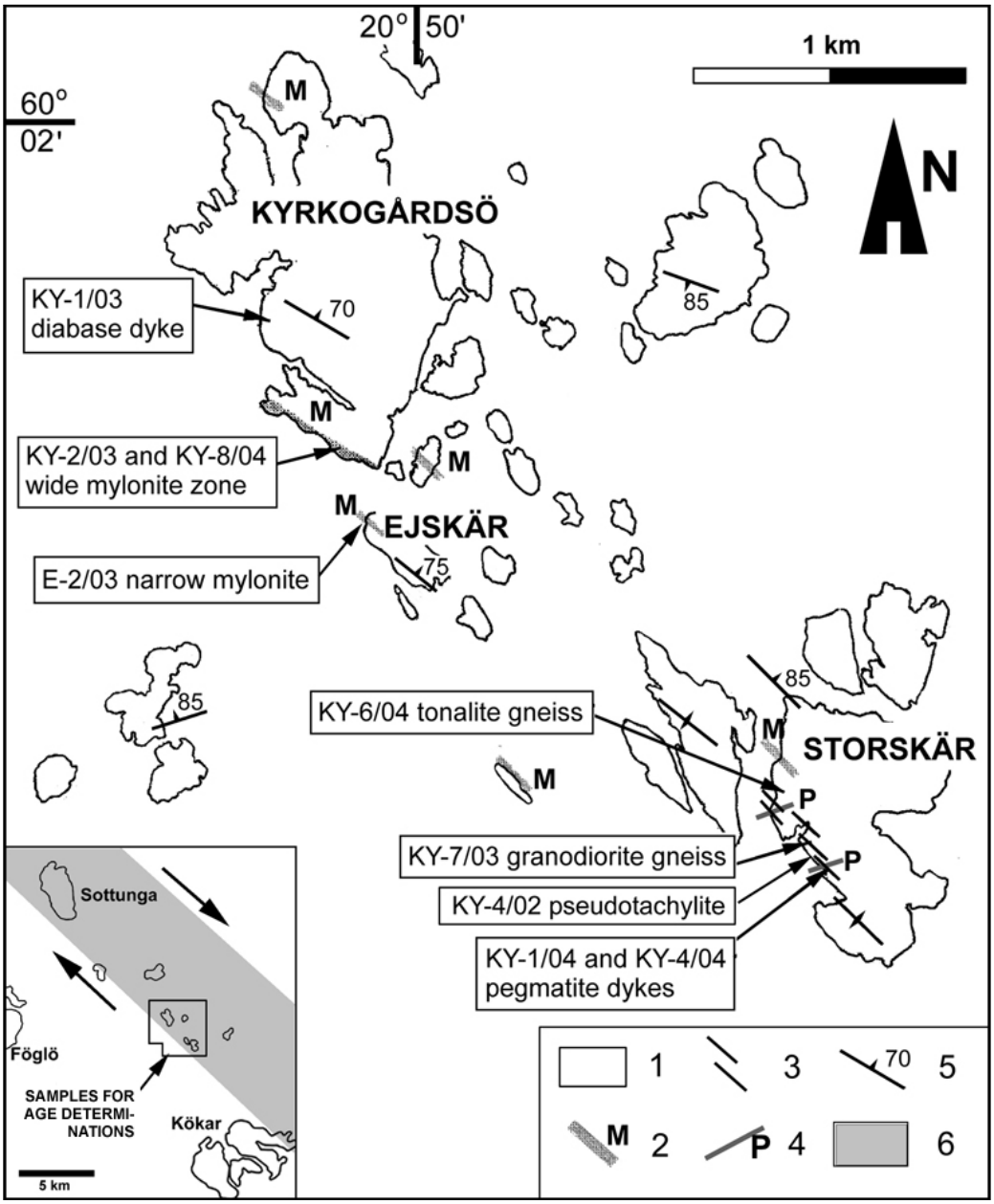

Fig. 4.37. Study area and sampling locations for age determinations. The overall strike of the foliation in the area is 120º (NW-SE). The mylonite zones mainly follow the main foliation within the shear zone. Key: (1) Granodioritic and tonalitic gneisses, (2) Mylonites and ultramylonites, (3) Pseudotachylites, (4) Pegmatite dykes, (5) Mean strike and dip of the gneissose foliation; note that the SW part of the study area is outside the main shear zone, the foliation thus displaying E-W to SW-NE direction typical for areas SW of the shear zone (6) Inset: the general location of the main shear zone.

SJSZ well developed latest by ca. 1.83 Ga. On the other hand, ca. 1.79 Ga metamorphic titanite ages are present SW of the SJSZ, indicating that at some deformation / metamorphism affected the entire area at that time.

4.5.2.1 Gneisses

Three rock samples representing the ductile gneissose phase were dated using zircon U-Pb and titanite U-Pb methods (fig. 4.37, Tab. 4.3). The rocks are medium-grained, granoblastic and intensely deformed, nevertheless showing relatively strain-free quartz grains due to high-T static recrystallisation indicating that there was a pause in deformation while the rocks were still within a relatively high-T regime (figs. 4.38a). In the granodiorite gneiss sample KY-7/03 (fig. 4.38a), fabric of the gneissose deformation is closely associated with the occurrence of zircons within the rock fabric: the few zircons that could be observed in thin section occurred in association with, but not as inclusions within, biotite grains, both aligned parallel to the gneissose foliation. In the tonalite gneiss sample KY-6/04 (fig. 4.38b), the titanites occur in close association with the hornblende. Epidote is also commonly present, probably as an alteration product from titanite (Broska et al. 2007). Again, the hornblendes and the associated titanites are aligned parallel to the gneissose fabric. The third sample representing the ductile gneissose phase (KY-1/03) is from a metadiabase dyke that intrudes granodioritic gneiss in a semi-discordant style, so it is clearly younger than the surrounding gneiss. In the metadiabase, two different titanite populations could be observed in thin section and in the separates; one comprised of abundant, homogeneous, light brown, transparent titanite that have a clear

Fig. 4.38. Photos of thin sections from SJSZ. Key: Ti = titanite, Pl = plagioclase, Kfs = alkali feldspar, Qtz = quartz, Bt = biotite, Epi = epidote, Hbl = hornblende, Il = ilmenite (ilmenorutile), Zr = zircon, PPL = plain-polarized light, CPL = cross-polarized light. **a)** Sample KY-7/03 (granodioritic gneiss). Grain boundary area reduction and the relatively strain-free grains (straight grain boundaries and foam structure) of the quartz indicate high-T static recrystallisation. CPL. **b)** Sample KY-6/04 (tonalite gneiss). Note the large titanite grown along the gneissose fabric. PPL. **c)** Sample KY-1/03 (semidiscordant metadiabase dyke). Two titanite generations can be observed in this rock: Ti1 (older) occurs sporadically in thin section compared to Ti2 (younger) that has a clear association to the metamorphic fabric. PPL. **d)** Sample E-2/03 (narrow mylonite zone). The photo shows two titanite grains within the mylonite. Note the epidote rim around the titanite grain located within the fine-grained biotite-rich matrix. PPL. **e)** Sample KY-2/03 (coarse tonalitic mylonite). The photo shows some of the older titanites in this sample (ca. 1849 Ma), often surrounded by an epidote reaction rim. One titanite grain also appears to have an opaque core (ilmenite/leucoxene?). PPL. **f)** Sample KY-2/03 (coarse tonalitic mylonite). The younger titanites in this sample (ca. 1795 Ma) are associated with the deformation fabric together with hornblende and ilmenite (ilmenorutile). PPL. **g)** Sample KY-8/04 (wide mylonite zone). Note the large zircon beneath the hornblende porphyroclast. Matrix consists mainly of biotite and quartz/plagioclase with some epidote and chlorite. PPL. **h)** Sample KY-4/02 (pseudotachylite). The pseudotachylite consists mainly of newly crystallised grains of plagioclase, biotite, K-feldspar and quartz although individual minerals may be difficult to distinguish. In addition to the new grains, tiny, rounded relict grains consisting mainly of quartz, but possibly also of plagioclase and/or K-feldspar can be seen within the pseudotachylite melt. Note the slight overall decrease in grain size toward the quartz-rich, granodioritic wall rock (chilled margin). PPL.

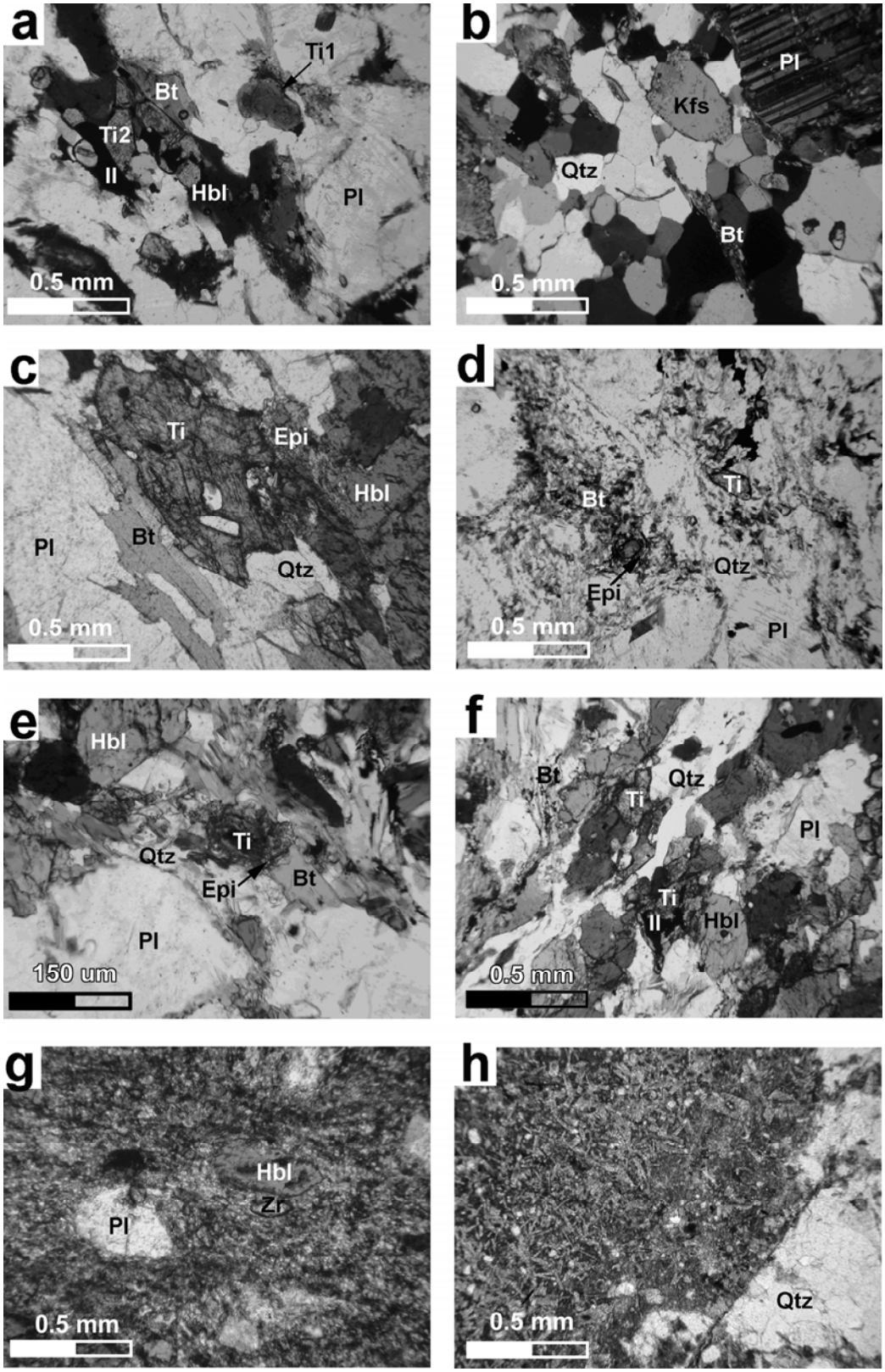
a
Ti1
Bt
Ti2
Il
Hbl
Pl
0.5 mm
b
Pl
Kfs
Qtz
Bt
0.5 mm
c
Ti
Epi
Hbl
Pl
Bt
Qtz
0.5 mm
d
Bt
Ti
Qtz
Epi
0.5 mm
Pl
e
Hbl
Ti
Qtz
Epi
Bt
Pl
150 um
f
Bt
Qtz
Ti
Pl
Ti
Il
Hbl
0.5 mm
g
Hbl
Zr
Pl
0.5 mm
h
Qtz
0.5 mm

association to the ductile gneissose fabric; the other consisting of more sporadically occurring, darker and more turbid titanite (fig. 4.38c).

4.5.2.2 Mylonites

From the mylonites, three rock samples were collected for U-Pb dating (fig. 4.37, tables 4.3 and 4.4). Zircon and titanite were separated from a sample collected from narrow (ca. 15 cm) mylonite zone within a gneissose wall rock (sample *E-2/03*). The other two rock samples represent a >20 m wide, intensely mylonitised zone (samples *KY-8/04* and *KY-2/03*). Zircon was extracted from the ultramylonitic sample *KY-8/04*, while titanite was separated from the protomylonite sample *KY-2/03*.

The *narrow mylonite zone* (*E-2/03*; figs. 4.28i, 4.38d) is slightly folded, following the foliation of the wall rock, suggesting that the mylonite zone and the wall rock at some point deformed simultaneously. In outcrop scale, the mineralogy of the narrow mylonite zone seems to differ from that of the wall rock, showing a more mafic assemblage compared to the granodioritic gneiss. In thin section, the mylonite zone shows significantly more abundant biotite, as well as some metamorphic garnet and abundant titanite that are absent in the gneiss. The mineralogical differences suggest that the mylonite zone was originally a dyke with a more mafic composition than the wall rock, although deformation has somewhat obscured the contact between the dyke and the wall rock. It is possible that due to different rheological properties between the two rock types, the dyke deformed in a mylonitic style while the wall rock simultaneously preserved a coarser, granoblastic fabric. Quartz ribbons within the mylonite matrix show some effects of high-T static recrystallisation in form of relatively strain-free, polygonised grains (Evans et al. 2001, Kruhl 2001). This is a further indication that the mylonite was formed at relatively high temperatures. The titanite within the mylonite zone is dark brown and translucent. The grains are usually situated rather sporadically within the matrix, appearing to be porphyroclasts, although many grains seem to have some association with the mylonitic fabric. Some titanite grains show an alteration rim of epidote. The few zircons observable in thin section occur within porphyroclasts, but possibly also within the fine-grained biotite-epidote-quartz -rich matrix.

The *wide mylonite zone* on the island of Kyrkogårdsö consists of alternating layers of protomylonites, mylonites and ultramylonites. For U-Pb dating, two rock samples were collected from the zone (sample KY-8/04 for zircon and sample KY-2/03 for titanite). Sample *KY-2/03* is from a *protomylonitic rock* with ca. 20% mica-rich matrix material, whereas sample *KY-8/04* is from an *ultramylonitic* variety with ca. 80-90% matrix (figs. 4.38e, f and 4.38g, respectively). The protolith of these samples has most probably been a tonalitic gneiss, the mineralogy of which is reflected in the mylonite porphyroclasts that are mainly composed of plagioclase and hornblende.

The ultramylonite sample KY-8/04 has some smaller titanite porphyroclasts in addition to the larger plagioclase and amphibole clasts. The

matrix in the ultramylonite is very fine grained, consisting mainly of brown mica, quartz and epidote. The hornblende clasts often show a retrograde reaction rim of biotite. The titanites appear unaltered, although occasionally a reaction rim of epidote is present. The matrix mineral assemblage is here interpreted to have formed mainly during mylonitisation, although some retrograde reactions may have taken place after the deformation ceased, producing the observed reaction rims in some porphyroclasts. Although titanites were clearly present in thin section, mineral separation did not yield enough good quality titanites for U-Pb dating. For dating, a small amount of zircon was separated instead.

The protomylonite sample KY-2/03 shows similar mineralogical features to the ultramylonitic variety. The fine-grained matrix, where present, is composed mainly of biotite, apparently formed as a result of alteration of the surrounding hornblendes, and very fine-grained quartz. Only very minor chloritisation can be observed. Two titanite populations can be seen in thin sections and separates of this sample. One population is brown, rounded and somewhat cloudy in appearance, the grains occurring rather sporadically in thin section. Many of the grains show an epidotic reaction rim which probably formed during subsequent deformation event(s) as the (older) titanite grains were corroded and altered, possibly to form new titanite. Indeed, the grains of the second titanite population do not show alteration rims and have a clear association with the slightly elongated hornblende grains of the youngest deformation fabric. Also, the titanites of the second population are much more abundant and larger in thin section than the grains of the first population and they are much lighter in colour - almost colourless in thin section. Many small opaque mineral grains (possibly ilmenite or ilmenorutile) present in thin section have a titanite rim of the colourless variety. In summary, the paler (colourless) titanites have clearly been formed as a product of a metamorphic reaction between hornblende, ilmenite ± the older titanite grains.

4.5.2.3 Pegmatites

In addition to the sheared rocks described above, two undeformed pegmatite dykes were sampled for U-Pb dating (samples KY-1/04 and KY-4/04; fig. 4.37). The dykes cut the gneisses and are in turn cut by pseudotachylytes (fig. 4.39). Hence,

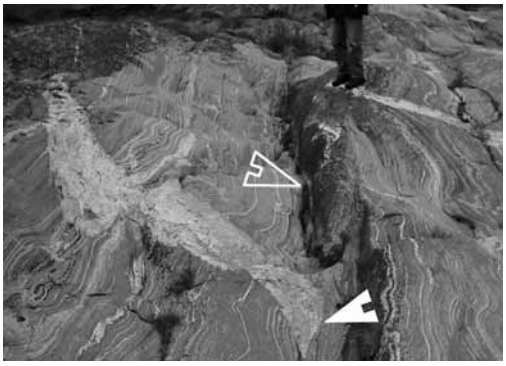

Fig. 4.39. A pseudotachylite generation surface (solid arrow) sinistrally offsetting a pegmatite dyke (sample KY-1/04, Storskär). A later brittle crack (no significant movement; empty arrow) slightly oblique to the pseudotachylite in turn cuts the pseudotachylite generation surface. The foliation of the ductilely deformed granodioritic gneiss (dextral sense of shear) as well as the pseudotachylite generation surface strike 120º (NW-SE), view toward SE.

the pegmatite ages determine the maximum age of the pseudotachylyte. The presence of the pegmatite dykes implies that the crust was relatively rigid at the time of their intrusion since the contact between the dykes and the wall rock is sharp.

4.5.2.4 Pseudotachylytes

For $^{40}Ar/^{39}Ar$ geochronology, a pseudotachylyte injection vein in Storskär, Kyrkogårdsö was sampled with a hand drill (sample *KY-4/02*; figs. 4.37, 4.38h). For comparison, a pseudotachylyte vein from a N-S striking shear zone in Torsholma (ca. 40 km NNW of the study area) was also analysed (sample *To-MLN-1*).

4.5.3 AGE RESULTS

The derived ages and their interpretations are summarised in table 4.4. All the zircon SIMS U-Pb, titanite ID-TIMS and pseudotachylyte whole-rock $^{40}Ar/^{39}Ar$ isotopic data are collected in tables 4.5, 4.6 and 4.7, respectively. See the tables when U concentrations, ages, individual spot ages, etc. are concerned. The descriptions below of the zircon and titanite morphology are largely written by I. Mänttäri.

The age results below are separated in three age groups: group I presents the magmatic ages of the protoliths; group II defines the ages of the ductile deformation, including three separate deformation phases within the group; and group III that includes estimations for the pseudotachylyte age.

4.5.3.1 Group I: protolith ages

Sample KY-8/04 (M584/n1801) from the *wide mylonite zone* (figs. 4.37 and 4.38g) contains two zircon populations: 1) magmatic, euhedral: translucent and brownish to transparent and quite colourless, short to long prismatic zircon and 2) rounded, extremely bright and colourless zircon. In BSE images, the rounded zircons are unfractured (healed?) and 'smoothly' zoned (zoning with obscure zone boundaries).

From the sample, a total of 37 zircon domains were dated. One of the analyses showed a high common lead content and was therefore rejected from the data (tab. 4.5). The majority of the U-Pb isotopic data from the euhedral zircons plot in a cluster on the concordia age of 1880 ± 3 Ma (fig. 4.40a). A few slightly.

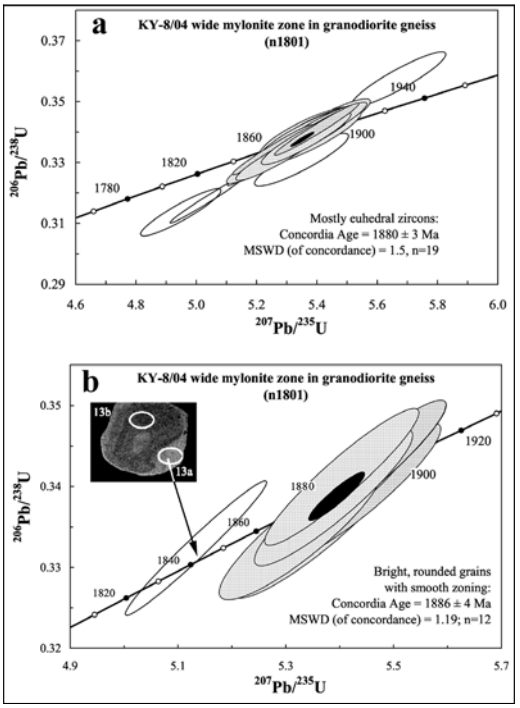

Fig. 4.40. Concordia plots of ion microprobe zircon U-Pb isotopic data for wide mylonite zone sample KY-8/04. **a)** Euhedral, magmatic zircons; **b)** Rounded, recrystallised zircons. Modified from original plots by I. Mänttäri.

Table 4.4. Summary of SIMS and ID-TIMS U-Pb age determinations from SJSZ, Kyrkogårdsö area.

	Sample number	Description	Analytical method	Ages (magmatic)	Ages (metamorphic)
Gneisses	**KY-7/03** Grano-dioritic gneiss	Euhedral zircon	Zircon SIMS	**1895±4 Ma**	**1850±12 Ma** (metamorphic rim)
	KY-6/04 Tonalitic gneiss	Dark brown, transparent titanite	Titanite ID-TIMS		**1823±8Ma**
	KY-1/03 Meta-diabase dyke	**A:** pale, transparent titanite	Titanite ID-TIMS		**A: ~1.79 Ga**
		B: darker, more turbid titanite		**B: 1831±5 Ma**	
Mylonites	**KY-8/04** Wide mylonite zone, ultra-mylonite	Euhedral zircon	Zircon SIMS	**1880±3 Ma**	
		Rounded, colour-less, smoothly zoned zircon		**1886±4 Ma** (recrystallised inherited?)	**1832±4 Ma** (metamorphic rim)
	KY-2/03 Wide mylonite zone	**A:** dark brown, translucent titanite	Titanite ID-TIMS		**A: 1849±5 Ma**
		B: pale, quite turbid titanite			**B: 1795±4 Ma**
	E-2/03 Narrow mylonite zone	Euhedral zircon	Zircon SIMS	**1888±4 Ma**	
		Dark brown, translucent titanite	Titanite ID-TIMS		**1824±5 Ma**
Pegmatite dykes	**KY-1/04, KY4/04**	Euhedral, magmatic zircon	Zircon SIMS	**1.78-1.79 Ga**	
Pseudo-tachylyte	**KY-4/02**	Whole-rock analysis	$^{40}Ar/^{39}Ar$	**>1.58 Ga**	

Table 4.5. Zircon ion microprobe U-Pb isotopic data for pegmatites, mylonite zones, and granodiorite gneiss, Kyrkogårdsö, Åland, Finland. Modified from the original data compiled by I. Mänttäri.

		Derived ages						Corrected ratios												
Sample/ spot #	Type of dated zircon domain	$^{207}Pb/^{206}Pb$	±σ	$^{207}Pb/^{235}U$	±σ	$^{206}Pb/^{238}U$	±σ	$^{207}Pb/^{206}Pb$	±σ %	$^{207}Pb/^{235}U$	±σ %	$^{206}Pb/^{238}U$	±σ %	r[1)]	Disc. %[2)]	[U] ppm	[Th] ppm	[Pb] ppm	$^{206}Pb/^{204}Pb$ measured	f_{206} %[3)]
KY-1/04 pegmatite, Storskär (KKJ coordinates 1492300, 6656200)																				
n1799-01a	metamorph, quite homog.	1872	7	1889	10	1904	17	0.1145	0.4	5.424	1.1	0.3436	1.0	0.93		209	95	90	1.92E+05	0.01
n1799-02a	zoned, dark altered	1148	10	662	6	528	6	0.0781	0.5	0.919	1.2	0.0854	1.1	0.91	-52.7	2787	129	260	3.71E+03	0.50
n1799-03a	*zoned, pale domain*	*1849*	*39*	*1923*	*21*	*1993*	*18*	*0.1131*	*2.2*	*5.648*	*2.5*	*0.3623*	*1.1*	*0.44*		*503*	*83*	*213*	*3.07E+02*	*6.09*
n1799-04a	zoned, pale unalt. rim domain	1830	4	1777	9	1732	16	0.1119	0.2	4.755	1.1	0.3083	1.0	0.98	-3.8	706	125	253	2.51E+04	0.07
n1799-04b	zoned, pale unalt. core domain	1883	8	1845	10	1811	16	0.1152	0.5	5.151	1.1	0.3243	1.0	0.91	-1.5	297	151	122	2.31E+03	0.81
n1799-05a	zoned, darker inner domain	*1896*	*22*	*1896*	*14*	*1896*	*17*	*0.1160*	*1.3*	*5.470*	*1.6*	*0.3419*	*1.0*	*0.63*		*292*	*111*	*123*	*7.95E+02*	*2.35*
n1799-06a	twice (?)altered grain	1542	5	1552	8	1559	14	0.0957	0.3	3.610	1.1	0.2735	1.0	0.97		7077	378	2150	1.20E+04	0.16
n1799-07a	zoned, dark altered	947	6	484	4	392	4	0.0706	0.3	0.610	1.1	0.0627	1.0	0.96	-58.0	5362	297	365	8.35E+03	0.22
n1799-08a	zoned, pale unalt. dom.	1774	2	1699	8	1640	15	0.1085	0.1	4.331	1.0	0.2896	1.0	0.99	-6.6	2886	101	935	6.20E+04	0.03
n1799-09a	zoned, pale unalt. dom.	1877	5	1835	9	1798	16	0.1148	0.3	5.093	1.1	0.3218	1.0	0.96	-2.5	596	208	234	3.12E+04	0.06
n1799-10a	zoned, dark alt. dom.	1430	6	897	6	697	7	0.0902	0.3	1.420	1.1	0.1141	1.0	0.96	-52.1	2666	123	336	6.25E+03	0.30
n1799-11a	zoned, pale unalt. dom.	1756	2	1759	9	1762	16	0.1074	0.1	4.655	1.0	0.3144	1.0	0.99		2494	136	882	7.34E+04	0.03
n1799-11b	zoned, partly alt. dom.	1638	2	1567	8	1516	14	0.1007	0.1	3.681	1.0	0.2650	1.0	0.99	-6.4	7906	483	2346	3.40E+04	0.06
n1799-12a	pale unaltered domain	1658	5	1559	11	1486	18	0.1019	0.2	3.642	1.4	0.2593	1.4	0.98	-8.9	4344	139	1252	4.24E+04	0.04
n1799-12b	pale unaltered domain	1694	3	1642	8	1601	14	0.1039	0.2	4.037	1.0	0.2819	1.0	0.99	-4.2	3557	137	1118	4.59E+04	0.04
n1799-13a	pale unaltered domain	1783	2	1795	9	1806	16	0.1090	0.1	4.860	1.0	0.3234	1.0	0.99		2309	53	833	1.13E+05	0.02
n1799-14a	pale unaltered domain	1729	3	1655	8	1597	14	0.1058	0.2	4.102	1.0	0.2811	1.0	0.99	-6.6	1544	73	486	4.02E+04	0.05
n1799-14b	partly altered domain	1446	5	1098	7	931	9	0.0910	0.3	1.948	1.0	0.1553	1.0	0.97	-36.4	5515	344	949	5.48E+04	0.03
n1799-15a	twice (?)altered grain	1641	4	1633	8	1627	15	0.1009	0.2	3.995	1.0	0.2871	1.0	0.98		11316	802	3641	4.80E+04	0.04
n1799-16a	quite unaltered domain	1783	5	1760	9	1740	15	0.1090	0.3	4.657	1.0	0.3098	1.0	0.97	-0.5	1393	44	483	5.14E+04	0.04
n1799-17a	partly altered domain	1583	6	1480	8	1409	13	0.0978	0.3	3.296	1.1	0.2443	1.0	0.95	-9.8	4159	175	1127	1.42E+04	0.13
n1799-18a	partly altered domain	1756	2	1617	8	1513	14	0.1074	0.1	3.916	1.0	0.2645	1.0	0.99	-13.6	3709	195	1101	7.73E+03	0.24
n1799-19a	*pale unalt. inner dom.*	*1808*	*28*	*1621*	*15*	*1481*	*14*	*0.1105*	*1.5*	*3.935*	*1.9*	*0.2583*	*1.0*	*0.56*	*-13.0*	*374*	*119*	*118*	*4.05E+02*	*4.62*

Table 4.5. *(Continued)*

		Derived ages						Corrected ratios												
Sample/ spot #	Type of dated zircon domain	$^{207}Pb/^{206}Pb$	±σ	$^{207}Pb/^{235}U$	±σ	$^{206}Pb/^{238}U$	±σ	$^{207}Pb/^{206}Pb$	±σ %	$^{207}Pb/^{235}U$	±σ %	$^{206}Pb/^{238}U$	±σ %	r[1)]	Disc. %[2)]	[U] ppm	[Th] ppm	[Pb] ppm	$^{206}Pb/^{204}Pb$ measured	f_{206} %[3)]
KY-4/04 pegmatite, Storskär (KKJ coordinates 1492110, 6656400)																				
n1800-01a	pale unaltered	1813	3	1747	9	1693	15	0.1108	0.2	4.588	1.0	0.3003	1.0	0.99	-5.5	1745	107	591	4.28E+04	0.04
n1800-02a	pale unaltered	1877	5	1867	9	1859	16	0.1148	0.3	5.291	1.1	0.3343	1.0	0.96		759	113	294	4.34E+03	0.43
n1800-03a	zoned, dark alt. dom.	*1559*	*77*	*1183*	*34*	*988*	*22*	*0.0966*	*4.2*	*2.205*	*4.9*	*0.1655*	*2.5*	*0.5*	*-18.1*	*1757*	*49*	*323*	*5.06E+02*	*3.69*
n1800-04a	pale unaltered	1853	5	1809	9	1771	16	0.1133	0.3	4.940	1.0	0.3162	1.0	0.97	-2.8	584	99	215	1.68E+04	0.11
n1800-05a	pale unaltered	1891	6	1901	9	1910	17	0.1157	0.4	5.502	1.1	0.3448	1.0	0.95		282	139	123	1.37E+04	0.14
n1800-06a	pale inner/core? dom.	1877	16	1877	11	1877	16	0.1148	0.9	5.352	1.3	0.3380	1.0	0.75		173	54	71	3.33E+03	0.56
n1800-06b	pale outer/rim domain	1886	6	1833	9	1787	16	0.1154	0.3	5.080	1.1	0.3194	1.0	0.96	-3.6	576	103	215	3.22E+04	0.06
n1800-07a	zoned, dark alt. dom.	1476	7	930	7	717	7	0.0924	0.4	1.498	1.1	0.1176	1.1	0.94	-51.9	2553	87	331	4.83E+03	0.39
n1800-08a	dark altered domain	708	13	434	4	385	4	0.0630	0.6	0.534	1.2	0.0615	1.0	0.86	-41.5	3854	169	256	2.46E+03	0.76
n1800-09a	pale unaltered	1897	5	1923	9	1946	17	0.1161	0.3	5.643	1.1	0.3525	1.0	0.96	0.5	566	369	261	2.39E+04	0.08
n1800-10a	mostly unaltered dom.	1786	3	1722	9	1670	15	0.1092	0.2	4.452	1.0	0.2958	1.0	0.99	-5.3	2227	72	737	6.84E+04	0.03
n1800-11a	slightly altered	1811	5	1754	9	1706	15	0.1107	0.3	4.626	1.1	0.3030	1.0	0.97	-4.3	624	69	216	1.74E+04	0.11
n1800-12a	mostly unaltered dom.	1779	3	1778	9	1776	16	0.1088	0.2	4.758	1.0	0.3172	1.0	0.98		2516	104	894	1.63E+04	0.11
n1800-13a	pale domain	1880	5	1821	9	1769	16	0.1150	0.3	5.010	1.1	0.3159	1.0	0.96	-4.4	496	245	198	5.12E+03	0.37
n1800-14b	pale inner domain	1887	6	1842	9	1802	16	0.1155	0.3	5.136	1.1	0.3226	1.1	0.96	-2.7	511	83	192	8.08E+03	0.23
n1800-15a	zoned dark inner domain	1741	21	1362	13	1134	13	0.1065	1.2	2.826	1.72	0.1924	1.3	0.73	-32.1	1577	686	370	1.06E+04	0.18
n1800-16a	pale unaltered domain	1834	4	1837	9	1839	16	0.1121	0.2	5.104	1.04	0.3302	1.0	0.97		1032	161	396	4.51E+05	0.00
n1800-17a	pale unaltered domain	1875	5	1863	9	1853	17	0.1147	0.3	5.265	1.08	0.3330	1.0	0.96		503	63	193	4.23E+03	0.44
n1800-18a	pale, quite homog. dom.	1875	5	1893	9	1910	17	0.1147	0.3	5.450	1.05	0.3448	1.0	0.96		491	194	208	5.51E+03	0.34
n1800-19a	quite homog. inner domain	1880	11	1913	10	1943	18	0.1150	0.6	5.578	1.21	0.3518	1.1	0.87	0.4	125	68	56	5.88E+04	0.03
KY-8/04 wide mylonite zone in granodiorite gneiss (KKJ coordinates 1490500, 6657700)																				
n1801-01a	dark inner dom., euh. grain with alt. zones	1879	9	1890	10	1899	17	0.115	0.5	5.430	1.1	0.3426	1.0	0.90		222	126	97	3.70E+05	0.01
n1801-02b	pale homog. outer domain, euhedral grain with altered zones	1884	3	1878	9	1872	16	0.1153	0.2	5.356	1.0	0.3370	1.0	0.98		1072	199	422	3.47E+04	0.05

Table 4.5. *(Continued)*

		Derived ages						Corrected ratios												
Sample/ spot #	Type of dated zircon domain	$^{207}Pb/^{206}Pb$	±σ	$^{207}Pb/^{235}U$	±σ	$^{206}Pb/^{238}U$	±σ	$^{207}Pb/^{206}Pb$	±σ %	$^{207}Pb/^{235}U$	±σ %	$^{206}Pb/^{238}U$	±σ %	r[1)]	Disc. %[2)]	[U] ppm	[Th] ppm	[Pb] ppm	$^{206}Pb/^{204}Pb$ measured	f_{206} %[3)]
n1801-02a	dark inner dom., euh. grain, alt. zones	1875	12	1881	11	1886	17	0.1147	0.7	5.375	1.2	0.3399	1.0	0.84		129	50	54	>1e6	0.00
n1801-03a	dark zoned, euhedral grain with alt. zones	1876	7	1881	9	1885	17	0.1148	0.4	5.374	1.1	0.3397	1.0	0.94		267	74	108	2.19E+04	0.09
n1801-04a	dark zoned inner domain, euhedral grain with altered zones	1890	9	1885	10	1880	17	0.1157	0.5	5.398	1.1	0.3385	1.0	0.90		133	53	55	1.44E+05	0.01
n1801-05a	pale homog. outer domain, euhedral grain with altered zones	1880	3	1859	9	1840	16	0.115	0.2	5.238	1.0	0.3304	1.0	0.98	-0.3	1288	245	497	1.14E+04	0.16
n1801-05b	*darker inner dom., euhedral with alt. zones*	*1823*	*62*	*1771*	*31*	*1728*	*15*	*0.1114*	*3.5*	*4.724*	*3.6*	*0.3074*	*1.0*	*0.28*		*179*	*71*	*69*	*8.85E+01*	*21.13*
n1801-06a	zoned dark, euhedr. grain	1887	5	1885	9	1883	17	0.1154	0.3	5.399	1.1	0.3392	1.0	0.96		377	135	156	1.38E+05	0.01
n1801-07a	quite homog. pale domain, euhedral grain	1878	8	1860	9	1844	16	0.1149	0.4	5.246	1.1	0.3312	1.0	0.92		276	100	112	7.03E+03	0.27
n1801-08a	pale outer domain, euhedral grain	1872	8	1879	10	1885	17	0.1145	0.5	5.363	1.1	0.3397	1.0	0.91		216	81	90	1.79E+05	0.01
n1801-09a	zoned dark, euhedral grain	1878	9	1881	10	1884	17	0.1149	0.5	5.377	1.2	0.3395	1.0	0.89		159	69	67	2.79E+05	0.01
n1801-10a	zoned dark, euhedral grain	1875	10	1879	10	1882	17	0.1147	0.5	5.361	1.2	0.3390	1.0	0.89		143	57	60	1.63E+05	0.01
n1801-11a	zoned dark inner domain	1915	9	1877	10	1843	17	0.1173	0.5	5.349	1.2	0.3309	1.1	0.90	-1.2	120	45	49	4.07E+05	0.00
n1801-11b	zoned pale outer domain	1871	8	1811	9	1758	16	0.1144	0.4	4.949	1.1	0.3136	1.0	0.92	-4.1	208	74	80	2.05E+04	0.09
n1801-12a	smoothly zoned, bright roundish grain	1894	9	1878	10	1863	18	0.1159	0.5	5.356	1.2	0.3351	1.1	0.91		131	56	54	>1e6	0.00
n1801-13a	rim domain, smoothly zoned bright roundish grain	1832	4	1842	9	1850	16	0.112	0.2	5.133	1.0	0.3324	1.0	0.98		715	52	269	9.13E+05	0.00
n1801-13b	smoothly zoned main domain, bright roundish grain	1899	8	1891	10	1884	17	0.1162	0.4	5.438	1.1	0.3394	1.0	0.92		167	77	71	>1e6	0.00
n1801-14a	smoothly zoned dark inner domain, subhedral bright	1884	8	1883	9	1882	17	0.1153	0.4	5.387	1.1	0.3390	1.0	0.92		183	95	79	>1e6	0.00

Table 4.5. *(Continued)*

		Derived ages						Corrected ratios												
Sample/ spot #	Type of dated zircon domain	$^{207}Pb/^{206}Pb$	±σ	$^{207}Pb/^{235}U$	±σ	$^{206}Pb/^{238}U$	±σ	$^{207}Pb/^{206}Pb$	±σ %	$^{207}Pb/^{235}U$	±σ %	$^{206}Pb/^{238}U$	±σ %	r[1)]	Disc. %[2)]	[U] ppm	[Th] ppm	[Pb] ppm	$^{206}Pb/^{204}Pb$ measured	f_{206} %[3)]
n1801-14b	pale outer domain, subhedral smoothly zoned bright grain	1888	7	1893	9	1898	17	0.1155	0.4	5.453	1.1	0.3423	1.0	0.93		219	81	92	1.63E+05	0.01
n1801-15a	quite homog. pale, translucent, yellowish grain, few fractures	1878	7	1884	9	1890	17	0.1149	0.4	5.395	1.1	0.3406	1.0	0.93		251	100	105	2.06E+05	0.01
n1801-16a	smoothly zoned, bright rounded grain	1881	8	1886	9	1891	17	0.1151	0.4	5.409	1.1	0.3410	1.0	0.92		175	99	77	>1e6	0.00
n1801-17a	smoothly zoned inner domain, bright grain	1887	8	1885	10	1883	17	0.1154	0.5	5.399	1.1	0.3392	1.0	0.91		168	67	70	2.84E+05	0.01
n1801-18a	pale rim domain, euhedr., fractured grain	1879	3	1826	9	1780	16	0.1149	0.2	5.040	1.0	0.3180	1.0	0.99	-4.0	1467	227	541	2.30E+04	0.08
n1801-19a	pale homog. euhedral grain with alt. zones	1885	3	1873	9	1863	16	0.1153	0.2	5.329	1.0	0.3351	1.0	0.99		1436	382	573	4.76E+05	0.00
n1801-20a	homog. core dom.,euh. grain with alt. zones	1865	4	1862	9	1859	16	0.1141	0.2	5.256	1.0	0.3342	1.0	0.98		1131	238	443	4.74E+05	0.00
n1801-21a	pale outer domain, euhedral grain	1886	7	1883	9	1881	16	0.1154	0.4	5.389	1.1	0.3388	1.0	0.93		351	124	145	2.59E+05	0.01
n1801-21b	darker inner domain, euhedral grain	1883	7	1865	9	1849	16	0.1152	0.4	5.276	1.1	0.3322	1.0	0.93		215	122	91	2.25E+05	0.01
n1801-22a	darker inner domain, translucent brownish euhedral grain	1883	7	1889	9	1894	17	0.1152	0.4	5.426	1.1	0.3415	1.0	0.94		230	87	96	4.17E+04	0.04
n1801-22b	pale tip dom., trans-lucent brownish euhedral grain	1883	8	1880	10	1877	17	0.1152	0.4	5.368	1.1	0.3379	1.0	0.92		358	125	147	1.08E+05	0.02
n1801-23a	pale outer domain, smoothly zoned bright elongated grain	1887	8	1873	9	1861	16	0.1155	0.4	5.327	1.1	0.3347	1.0	0.92		180	104	77	3.06E+05	0.01
n1801-23b	darker inner domain, smoothly zoned bright elongated grain	1888	7	1893	9	1897	17	0.1155	0.4	5.449	1.1	0.3422	1.0	0.93		216	70	90	6.99E+05	0.00
n1801-24a	rim domain, smoothly bright roundish grain	1888	10	1873	10	1859	17	0.1155	0.5	5.326	1.2	0.3344	1.0	0.89		115	37	46	1.42E+05	0.01
n1801-24b	inner domain, smoothly bright roundish grain	1887	6	1884	9	1881	17	0.1154	0.3	5.392	1.1	0.3388	1.0	0.95		362	95	146	2.92E+05	0.01

Table 4.5. *(Continued)*

		Derived ages						Corrected ratios												
Sample/ spot #	Type of dated zircon domain	$^{207}Pb/^{206}Pb$	±σ	$^{207}Pb/^{235}U$	±σ	$^{206}Pb/^{238}U$	±σ	$^{207}Pb/^{206}Pb$	±σ %	$^{207}Pb/^{235}U$	±σ %	$^{206}Pb/^{238}U$	±σ %	r[1)]	Disc. %[2)]	[U] ppm	[Th] ppm	[Pb] ppm	$^{206}Pb/^{204}Pb$ measured	f_{206} %[3)]
n1801-25a	smoothly zoned pale, euhedral grain with few fractures	1886	8	1883	10	1880	17	0.1154	0.5	5.387	1.1	0.3386	1.0	0.92		245	87	101	2.76E+05	0.01
n1801-26a	quite homog. pale dom., bright subhedral elongated grain	1877	7	1885	9	1893	17	0.1148	0.4	5.402	1.1	0.3412	1.0	0.94		230	96	97	1.96E+05	0.01
n1801-27a	pale outer domain, rounded yellowish grain with altered zone	1878	4	1885	9	1891	17	0.1149	0.2	5.403	1.1	0.3410	1.0	0.98		750	220	305	1.48E+05	0.01
n1801-27b	darker inner domain, rounded yellowish grain with altered zone	1882	8	1927	10	1969	17	0.1151	0.5	5.671	1.1	0.3573	1.0	0.91	2.4	154	70	69	1.28E+05	0.01
E-2/03 narrow mylonite zone in granodiorite gneiss, Ejskär (KKJ coordinates 1490600, 6657450)																				
n1802-01a	dark, zoned	1891	8	1819	9	1757	16	0.1157	0.4	4.999	1.1	0.3134	1.0	0.92	-5.3	279	110	109	2.48E+03	0.76
n1802-02a	dark zoned	1899	5	1889	9	1880	16	0.1163	0.3	5.427	1.0	0.3386	1.0	0.97		546	113	218	1.09E+04	0.17
n1802-03a	dark inner domain	1891	8	1892	10	1894	17	0.1157	0.5	5.448	1.1	0.3415	1.0	0.91		159	98	70	2.54E+05	0.01
n1802-03b	pale zoned, rim dom.	1877	5	1872	9	1867	16	0.1148	0.3	5.320	1.0	0.336	1.0	0.97		554	94	217	9.39E+04	0.02
n1802-04a	pale homog. inner dom	1888	3	1900	9	1911	17	0.1155	0.2	5.495	1.0	0.345	1.0	0.99		1478	529	622	5.48E+05	0.00
n1802-04b	pale homog. rim dom.	1887	3	1884	9	1882	16	0.1155	0.2	5.396	1.0	0.339	1.0	0.98		906	268	369	3.72E+05	0.01
n1802-05a	pale homoge. grain	1876	4	1894	9	1911	17	0.1147	0.2	5.460	1.0	0.3451	1.0	0.98		678	68	267	3.73E+05	0.01
n1802-06a	pale outer domain	1883	4	1904	9	1922	17	0.1152	0.2	5.520	1.0	0.3474	1.0	0.98	0.1	744	78	297	8.37E+05	0.00
n1802-06b	darker inner domain	1891	7	1896	9	1900	17	0.1157	0.4	5.470	1.1	0.3428	1.0	0.94		271	140	118	1.78E+05	0.01
n1802-07a	*pale outer domain*	*1869*	*23*	*1947*	*15*	*2020*	*19*	*0.1143*	*1.3*	*5.802*	*1.7*	*0.3681*	*1.1*	*0.65*	*2.9*	*968*	*109*	*416*	*5.49E+02*	*3.41*
n1802-07b	dark inner domain	1883	10	1853	10	1827	17	0.1152	0.6	5.204	1.2	0.3276	1.1	0.88	-0.2	208	73	83	5.15E+05	0.00
n1802-08b	pale tip domain	1865	5	1763	9	1679	15	0.1141	0.3	4.679	1.1	0.2974	1.0	0.96	-9.1	644	86	221	4.46E+03	0.42
n1802-08a	zoned darker core dom	1888	7	1947	9	2003	18	0.1155	0.4	5.804	1.1	0.3645	1.0	0.94	4.3	304	75	132	6.90E+03	0.27
n1802-09a	zoned darker inner domain	1892	5	1907	9	1922	17	0.1158	0.3	5.543	1.0	0.3473	1.0	0.97		729	176	301	8.61E+04	0.02
n1802-09b	pale homog. outer dom	1890	3	1931	9	1970	17	0.1156	0.2	5.699	1.0	0.3575	1.0	0.98	2.7	949	134	393	1.36E+05	0.01
n1802-10a	zoned domain	1892	5	1897	9	1901	17	0.1158	0.3	5.476	1.1	0.3430	1.0	0.96		531	253	229	1.04E+05	0.02
n1802-11a	darker inner domain	1888	8	1905	10	1922	18	0.1155	0.5	5.530	1.2	0.3473	1.1	0.92		151	54	64	1.92E+05	0.01
n1802-11b	pale outer domain	1890	4	1903	9	1915	17	0.1157	0.2	5.517	1.0	0.3460	1.0	0.98		731	69	289	5.61E+05	0.00

Table 4.5. *(Continued)*

		Derived ages						Corrected ratios												
Sample/ spot #	Type of dated zircon domain	$^{207}Pb/^{206}Pb$	±σ	$^{207}Pb/^{235}U$	±σ	$^{206}Pb/^{238}U$	±σ	$^{207}Pb/^{206}Pb$	±σ %	$^{207}Pb/^{235}U$	±σ %	$^{206}Pb/^{238}U$	±σ %	r[1)]	Disc. %[2)]	[U] ppm	[Th] ppm	[Pb] ppm	$^{206}Pb/^{204}Pb$ measured	f_{206} %[3)]
KY-7/03 granodiorite gneiss, Storskär (KKJ coordinates 1492240, 6656240)																				
n1803-01a	*zoned, inner domain*	*1860*	*21*	*1772*	*13*	*1699*	*15*	*0.1137*	*1.2*	*4.728*	*1.6*	*0.3016*	*1.0*	*0.64*	*-4.0*	*334*	*151*	*125*	*2.53E+02*	*7.39*
n1803-02a	zoned (enveloped with thin rim)	1886	10	1882	10	1878	16	0.1154	0.6	5.382	1.2	0.3382	1.0	0.88		258	80	105	7.59E+03	0.25
n1803-03a	zoned, darker inner domain	1896	8	1889	10	1883	17	0.1161	0.5	5.427	1.1	0.3391	1.0	0.92		161	72	68	4.20E+04	0.04
n1803-03b	zoned, pale rim domain	1874	4	1899	9	1922	17	0.1146	0.2	5.492	1.1	0.3475	1.0	0.98	0.6	697	91	279	1.52E+04	0.12
n1803-04a	zoned	1891	7	1944	9	1995	17	0.1157	0.4	5.787	1.1	0.3627	1.0	0.94	3.7	233	82	103	3.73E+05	0.01
n1803-05a	zoned	1903	8	1910	10	1916	17	0.1165	0.5	5.559	1.1	0.3461	1.0	0.91		192	54	79	7.87E+04	0.02
n1803-06a	zoned	1897	6	1904	9	1910	17	0.1161	0.4	5.522	1.1	0.3449	1.0	0.95		462	152	193	7.43E+04	0.03
n1803-07a	darker zoned inner domain	1882	7	1890	9	1897	17	0.1151	0.4	5.431	1.1	0.3422	1.0	0.94		379	145	159	4.04E+03	0.46
n1803-07b	pale homog domain	1893	5	1897	9	1901	17	0.1159	0.3	5.479	1.1	0.3430	1.0	0.96		546	142	223	5.08E+04	0.04
n1803-08a	zoned (enveloped with thin rim)	1890	5	1895	9	1899	17	0.1156	0.3	5.463	1.1	0.3426	1.0	0.96		447	151	186	5.02E+03	0.37
n1803-09a	darker inner domain	1896	6	1894	9	1893	17	0.116	0.3	5.461	1.1	0.3414	1.0	0.96		326	113	135	1.31E+05	0.01
n1803-09b	pale, homogeneous rim	1850	6	1831	9	1814	16	0.1131	0.3	5.070	1.1	0.3250	1.0	0.95		444	98	168	5.95E+03	0.31
n1803-10a	pale homogeneous outer domain	1886	2	1919	9	1950	17	0.1154	0.1	5.617	1.0	0.3531	1.0	0.99	1.8	2612	361	1067	>1e6	0.00
n1803-11a	pale homogeneous inner domain	1898	4	1903	9	1908	17	0.1162	0.2	5.515	1.0	0.3444	1.0	0.98		1015	322	423	3.66E+05	0.01
n1803-11b	*darker zoned outer domain*	*1900*	*20*	*1832*	*13*	*1772*	*16*	*0.1163*	*1.1*	*5.073*	*1.5*	*0.3164*	*1.0*	*0.67*	*-2.3*	*221*	*62*	*84*	*4.32E+02*	*4.33*
n1803-12a	zoned	1893	8	1903	10	1913	17	0.1159	0.4	5.517	1.1	0.3454	1.0	0.92		309	62	125	1.88E+05	0.01
n1803-13a	zoned	1894	6	1916	9	1936	17	0.1159	0.4	5.596	1.1	0.3502	1.0	0.94		286	65	118	6.57E+03	0.28

All errors are in 1 sigma level. Rejected data in italics.

[1)] Error correlation. [2)] Age discordance at closest approach of error ellipse to concordia (2s level).

[3)] Percentage of common ^{206}Pb in measured ^{206}Pb, calculated from the ^{204}Pb signal assuming a present-day Stacey & Kramers (1975) model terrestrial Pb-isotope composition.

discordant data are consistent with this age result. A zoned, BSE-dark inner domain of zircon 11 has a $^{207}Pb/^{206}Pb$ age of ca. 1.92 Ga (slightly discordant) and is considered as inherited. The U-Pb data of the cores of the rounded zircons plot in a tight cluster with a concordia age of 1886 ± 4 Ma (fig. 4.40b). These zircons have quite low U contents. The smoothly zoned main domain of the zircon 13 in fig. 4.40b has an age of ca. 1.90 Ga

Both zircon populations give an U-Pb age of ca. 1.88 Ga, despite their differing appearances. The 1880±3 Ma age for the euhedral, magmatic zircon is considered as the age of the protolith. The rounded, bright zircons are tentatively interpreted as originally inherited grains that recrystallised at the time of the intrusion. In any case, the obtained age represents the magmatic age of the mylonite protolith.

Sample E-2/03 (M584/n1802) is from the *narrow mylonite zone* (figs. 4.37 and 4.38d). The majority of the zircons in this sample show magmatic morphologies. Only a few possible metamorphic zircons were found. In BSE images, the euhedral zircons are occasionally quite structureless and pale. In some cases, the BSE-darker inner domains frequently exhibit zoning, while the outer domains are pale and structurally homogeneous. In addition to the zircon, some titanite was also separated.

18 zircon domains were dated from the sample. One analysis was rejected because of high common lead content (tab. 4.5). Regardless of the apparent differences in the dated zircon domains, all the age data are coeval (fig. 4.41). For the concordant data points, an age of 1888 ± 4 Ma is calculated. The few discordant data are in good agreement with this age. The 1888 ± 4 Ma age is marginally older than the age of 1880 ± 3 Ma for the protolith of the wide mylonite zone.

Sample KY-7/03 (M584/n1803) from the *granodiorite gneiss* (figs. 4.37 and 4.38a) contains translucent, pale brown, and prismatic zircons. In BSE images, the zircon mainly shows magmatic zoning, but a few structurally homogeneous pale rim phases and homogenised core

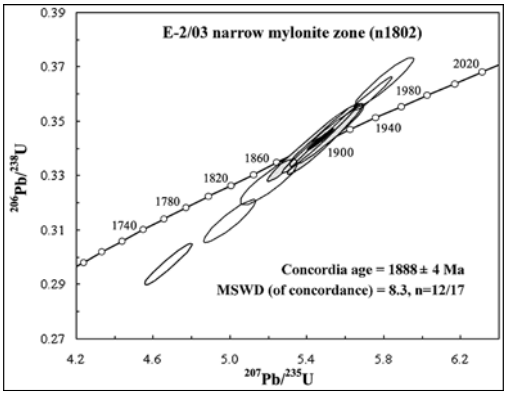

Fig. 4.41. Concordia plot of ion microprobe zircon U-Pb isotopic data for narrow mylonite zone sample E-2/03. Modified from an original plot by I. Mänttäri.

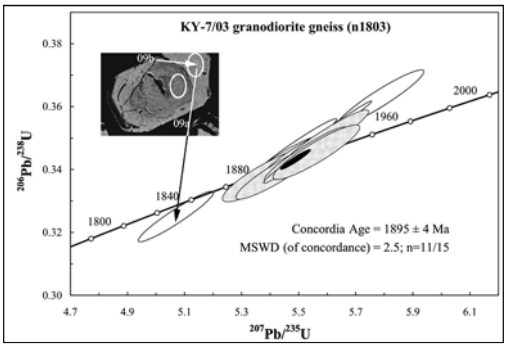

Fig. 4.42. Concordia plot of ion microprobe zircon U-Pb isotopic data for granodiorite gneiss sample KY-7/03. Modified from an original plot by I. Mänttäri.

Tab. 4.6. Titanite ID-TIMS U-Pb isotopic data for SJSZ rock samples. Modified from the original data compiled by I. Mänttäri.

Analysed mineral and fraction	Sample weight/ mg	U ppm	Pb ppm	$^{206}Pb/^{204}Pb$ mea-sured	$^{208}Pb/^{206}Pb$ radio-genic	ISOTOPIC RATIOS[1] $^{206}Pb/^{238}U$	±2σ%	$^{207}Pb/^{235}U$	±2σ%	$^{207}Pb/^{206}Pb$	±2σ%	r	APPARENT AGES / Ma ± 2σ $^{206}Pb/^{238}U$	$^{207}Pb/^{235}U$	$^{207}Pb/^{206}Pb$
[2]KY-1/03A diabase: pale brown titanite	1.55	19	10	142	0.36	0.3205	1.10	4.728	2.50	0.1070	1.89	0.67	1792	1772	1749±35
KY-1/03B diabase: dark brown titanite	0.89	30	18	150	0.48	0.3285	0.29	5.083	0.74	0.1122	0.58	0.70	1831	1833	1836±11
E-2/03 narrow mylonite zone: dark brown titanite	2.56	180	74	322	0.14	0.3272	0.40	5.028	0.50	0.1114	0.30	0.83	1825	1824	1823±5
KY-2/03A wide mylonite zone: medium brown titanite	1.35	106	48	198	0.12	0.3322	0.20	5.157	0.55	0.1126	0.44	0.71	1849	1846	1842±8
[2]KY-2/03B wide mylonite zone: translucent, pale titanite	1.31	52	20	373	0.12	0.3209	0.23	4.830	0.87	0.1092	0.74	0.67	1794	1790	1785±13
KY-6/04 tonalitic gneiss: dark brown titanite	2.88	29	18	179	0.71	0.3266	0.50	5.029	0.90	0.1117	0.65	0.67	1822	1824	1827±12

[1] Isotopic ratios corrected for fractionation, blank (30 pg), and age related common lead (Stacey & Kramers 1975; $^{206}Pb/^{204}Pb$±0.2, $^{207}Pb/^{204}Pb$±0.1, $^{208}Pb/^{204}Pb$±0.2).

[2] Used errors in common lead corrections: $^{206}Pb/^{204}Pb$±0.5, $^{207}Pb/^{204}Pb$±0.3, $^{208}Pb/^{204}Pb$±0.5 (Stacey and Kramers, 1975).

Table 4.7. $^{40}Ar/^{39}Ar$ analysis data for pseudotachylyte samples To-MLN-1 (Torsholma) and KY-4/02 (Kyrkogårdsö, SJSZ). Modified from original data compiled by T. Hermansson and L. Page.

Sample/ Run ID#[a]	Power (W)	$^{36}Ar/^{39}Ar$	$^{40}Ar^*/^{39}Ar$	^{39}Ar (Mol-14)	$\%^{39}Ar$[c]	Cum. $\%^{39}Ar$	$\%^{40}Ar^*$[d]	Age (Ma)	± 2σ
To-MLN-1, Run ID# 1504-01 (J = 0.009461 ± 0.000029):									
1504-01A	1.8	0.055415	64.560	0.045	2	2	79.8	860	1.2
1504-01B	1.9	0.011411	117.314	0.0471	2.1	4.2	97.2	1347	1.5
1504-01C	2.0	0.008189	143.252	0.2614	11.8	16	98.3	1546	0.7
1504-01D	2.1	0.002522	151.467	0.1292	5.9	21.9	99.5	1604	1.3
1504-01E	2.1	0.001107	149.409	0.3848	17.4	39.3	99.8	1590	0.7
1504-01F	2.2	0.000804	145.634	0.204	9.2	48.5	99.8	1563	1.0
1504-01G	2.2	0.000924	143.674	0.1898	8.6	57.1	99.8	1549	0.9
1504-01H	2.2	0.001001	142.449	0.1395	6.3	63.5	99.9	1540	1.2
1504-01I	2.2	0.001132	140.652	0.1119	5.1	68.5	99.8	1527	1.1
1504-01J	2.3	0.001273	135.327	0.073	3.3	71.8	99.7	1487	1.3
1504-01K	2.3	0.001357	138.122	0.0616	2.8	74.6	99.7	1508	2.1
1504-01L	2.4	0.001118	134.910	0.261	11.8	86.4	99.8	1484	3.3
1504-01M	2.5	0.001191	151.904	0.1991	9	95.5	99.8	1607	4.8
1504-01O	2.6	0.001102	158.177	0.0476	2.2	97.6	99.8	1651	3.6
1504-01P	2.8	0.002222	158.243	0.0156	0.7	98.3	99.6	1651	4.2
1504-01Q	3.2	0.001275	135.832	0.037	1.7	100	99.7	1491	9.3
Integ. Age=								1539	6.0
(•) Steps used in Age Calculation =					95.8			1556	6.0
KY-4/02, Run ID# 1480-01 (J = 0.009459 ± 0.00002):									
1480-01A	4	0.002882	127.525	1.1495	37.8	37.8	99.3	1428	1.3
1480-01B	4.1	0.000935	150.855	0.6738	22.2	60	99.8	1600	1.3
1480-01C	4.2	0.000697	152.022	0.3015	9.9	69.9	99.9	1608	1.2

Tab. 4.7. *(Continued)*

Sample/Run ID#[a]	Power (W)	$^{36}Ar/^{39}Ar$	$^{40}Ar^*/^{39}Ar$	^{39}Ar (Mol-14)	$\%^{39}Ar$[c]	Cum. $\%^{39}Ar$	$\%^{40}Ar^*$[d]	Age (Ma)	± 2σ
1480-01D	4.3	0.000614	150.158	0.3815	12.6	82.5	99.9	1595	1.2
1480-01E	4.4	0.0000001	148.344	0.1526	5	87.5	100	1582	1.1
1480-01F	4.5	0.000887	146.825	0.1004	3.3	90.8	99.8	1571	1.3
1480-01G	4.8	0.0000001	147.408	0.0161	0.5	91.3	100.9	1575	3.5
1480-01H	5.0	0.000275	146.625	0.0223	0.7	92.1	99.9	1570	2.5
1480-01I	5.4	0.002482	144.894	0.0221	0.7	92.8	99.5	1557	2.7
1480-01J	5.8	0.0000001	148.369	0.0273	0.9	93.7	100.5	1582	2.4
1480-01K	6.2	0.003155	144.099	0.0063	0.2	93.9	99.4	1551	8.7
1480-01L	8.0	0.000916	146.345	0.0605	2	95.9	99.8	1568	1.9
1480-01M	10.0	0.000723	145.399	0.1253	4.1	100	99.9	1561	1.2
Integ. Age=								1531	5.0
(•) Steps used in Age Calculation =					62.2			1583	5.0

domains were also detected. A total of 17 zircon domains were dated, of which two analyses were rejected due to high common lead contents (tab. 4.5). Excluding one data point, the data seem to be coeval regardless of the dated zircon domain type. Concordia age for the concordant U-Pb isotopic data is 1895 ± 4 Ma (fig. 4.42), and four slightly discordant analyses plot in this same cluster. The obtained magmatic age of this rock (1895 Ma) is marginally higher than the magmatic age of the narrow mylonite zone, but clearly higher than the protolith age of the wide mylonite zone. The age is nevertheless in good agreement with the overall magmatic ages of the study area and of granitoids in southern Finland in general (e.g. Ehlers et al. 2004, Väisänen et al. 2002).

4.5.3.2 Group II: timing of ductile deformation

Phase I ca. 1.85 Ga (D_2)

Sample KY-7/03 (M584/n1803) from the *granodiorite gneiss* (figs. 4.37 and 4.38a) yields, in addition to the magmatic age of ca. 1.89 Ga, a clearly younger concordant age of 1850 ± 12 Ma from a structurally homogeneous rim zircon phase (n1803-09b; tab. 4.5; fig. 4.42). The ~1.85 Ga age is interpreted as a metamorphic age.

Sample KY-2/03 from the *wide mylonite zone* (figs. 4.37 and 4.38e)

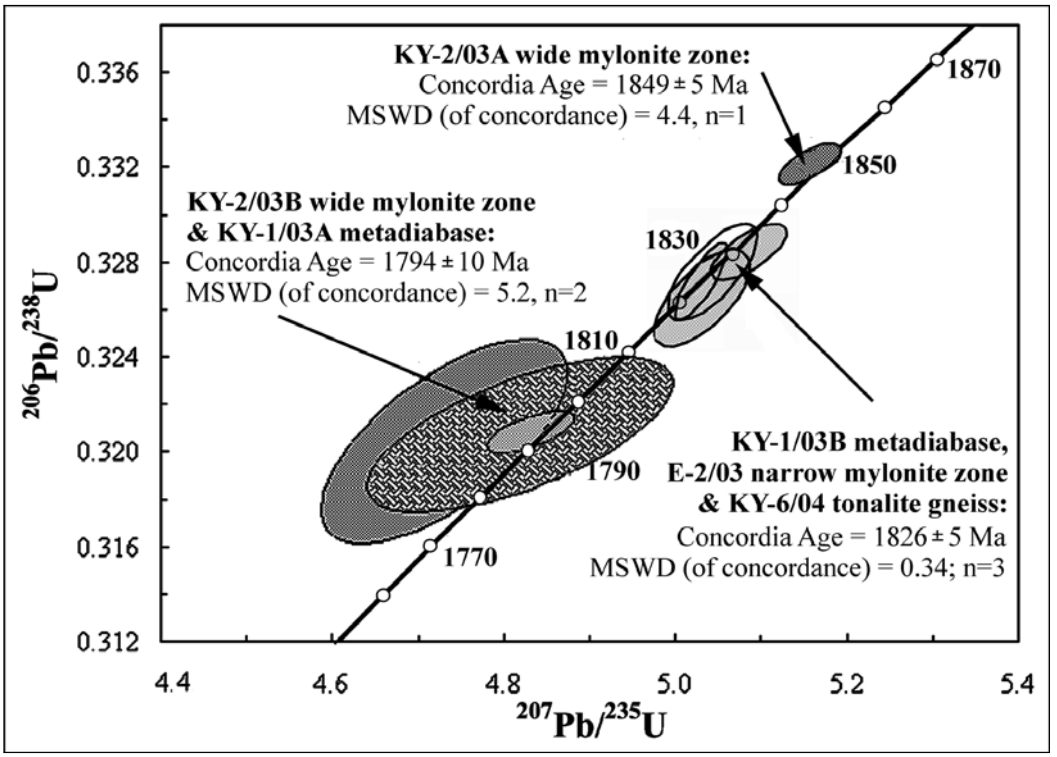

Fig. 4.43. Concordia plot of ID-TIMS titanite U-Pb isotopic data for samples tonalite gneiss KY-6/04, metadiabase dyke KY-1/03, wide mylonite zone KY-2/03 and narrow mylonite zone E-2/03. Modified from an original plot by I. Mänttäri.

contains two types of titanites of which the older, dark brown, translucent to transparent ones occurring sporadically within the rock volume give an age of 1849 ± 5 Ma (KY-2/03A; fig. 4.43). Assuming that the protolith is a ca. 1.88 Ga tonalitic gneiss, the ca. 1.85 Ga age is a metamorphic age. This is supported by the fact that the zircon in sample KY-7/03 exhibit ca. 1.85 Ga metamorphic rims with a low Th/U compared to the core domains, and it is therefore here suggested that the ca. 1.85 Ga age represents the first deformation phase within the study area.

Phase II ca. 1.82-1.83 Ga (D_3)

Several indications of an intensive deformation phase at this time exist, and the obtained ages are summarised in tab. 4.6 and fig. 4.43. Sample KY-6/04 from a *tonalite gneiss* (figs. 4.37 and 4.38b) yields a homogeneous titanite population consisting of transparent, quite dark brown titanite that give an age of 1823 ± 8 Ma. The rock is structurally closely associated to the granodiorite gneiss KY-7/03 dated at 1895 Ma, indicating that they were formed (and subsequently deformed) approximately simultaneously. The obtained titanite U-Pb age can therefore be considered metamorphic.

In sample KY-1/03 from the *semidiscordant metadiabase dyke* (figs. 4.37 and 4.38c), two titanite populations are present, of which the dark brown, turbid titanite is dated at 1831 ± 5 Ma (KY-1/03B; tab. 4.6). This age may represent the magmatic age for the dyke (compare sample KY-1/03A of phase III).

In the ca. 1.88 Ga zircons of the *wide mylonite zone* sample KY-8/04 (figs. 4.37 and 4.38g), a pale zircon rim domain with low Th/U ratio from a bright roundish zircon grain gives a younger zircon age of 1832 ± 8 (Pb/Pb age; grain 13a in fig. 4.40b). The age is interpreted to be metamorphic and the influence of this later event is present as thin, pale rims around many of the rounded, smoothly zoned ca. 1.88 Ga zircons, most of which were too narrow to be analysed.

Lastly, the *narrow mylonite zone* sample E-2/03 (figs. 4.37 and 4.38d) contains dark brown, translucent titanite that yields an age of 1824 ± 5 Ma (tabs. 4.4 and 4.6). The magmatic age for the protolith of the mylonite is ca. 1.89 Ga, so the obtained titanite age is interpreted as a metamorphic age. Using data from all of group II titanite samples a concordia age of 1826±5 Ma age is calculated (fig. 4.43).

Phase III ca. 1.79-1.80 Ga (D_4)

Besides the ca. 1.85 Ga dark brown titanites of phase I in the *wide mylonite zone* sample KY-2/03 (figs. 4.37 and 4.38f), the sample also contains pale, turbid titanite that yields an age of ca. 1.79-1.80 Ga (KY-2/03B; tab. 4.6). This type of titanite is much more abundant than the older titanites and have a clear connection to the metamorphic fabric in thin section. Therefore, the obtained age is considered to be a metamorphic age, reflecting the last ductile shearing phase along the SJSZ.

The younger titanite in the *semidiscordant metadiabase dyke* sample KY-1/03A (Figs. 2 and 7a) is pale to medium brown and transparent, forming a relatively homogeneous population with a clear

association to the deformational fabric in thin section. The titanite has an age of ~1.79Ga, but due to the large $^{207}Pb/^{206}Pb$ age error of the titanite (tab. 4.6) the age is not well defined. However, on the concordia diagram (fig. 4.43) the titanite U-Pb data plot roughly with the younger titanite KY-2/03B from the wide mylonite zone and using data from both the samples a concordia age of 1794±10 Ma age can be calculated. Thus, the ca. 1.79 Ga age is considered to be a proper age estimate for the KY-1/03A titanite and for the phase III (D_4) deformation. The U concentration of the KY-1/03A titanite is somewhat lower than that of the 1.83 Ga titanite from the same sample (KY-1/03B). This is in good agreement with the metamorphic origin for the younger titanite.

4.5.3.3 Group III: Pseudotachylyte age

Pegmatite magmatic ages

Two undeformed pegmatite dykes, samples KY-1/04 and KY-4/04 (figs. 4.37 and 4.39) were dated in order to obtain a maximum age for the pseudotachylytes. The zircons in both samples are magmatic, quite large, turbid to translucent, pale brown and prismatic. In BSE images, they show partial or total alteration. The low Th/U and high U (tab. 4.5) in the samples typical for pegmatite granite zircon.

From sample KY-1/04, 23 zircon domains were dated (fig. 4.44a). Of these, three were rejected because of too high common lead contents (tab. 4.5). The U-Pb isotopic data can be divided roughly in the following four groups.

1. Data points (01a, 04a, 04b, 09a) with quite low U concentrations and high Th/U as well as clearly higher ages than the other data, interpreted as inherited Svecofennian zircons.
2. Six (08a, 11a, 13a, 14a, 16a, 18a) concordant to slightly discordant data with high U and low Th/U, typical for pegmatite zircon, have $^{207}Pb/^{206}Pb$ ages between 1.78 Ga and 1.73 Ga. These are mostly from unaltered zircon domains. The age data deviate, but their upper intercept age of ca. 1.77-1.78 can be considered as the age for the pegmatite.
3. Six concordant or slightly discordant data points (06a, 11b, 12a, 12b, 15a, 17a) deviate roughly between 1.70 Ga and 1.55 Ga. The highest Pb/Pb ages (approaching 1.70 Ga) are from mainly unaltered zircon domains. One concordant analysis from an anomalously high U, altered domain indicates rapakivi age (ca. 1.55 Ga).
4. BSE-dark, metamict zircon domains give highly discordant age data (n=4) and a reference line intercept age of ca. 1.60 Ga. However, because of the multiphase geological history in the area, the metamict, highly discordant data points do not indicate any exact age.

From sample KY-4/04, a total of 21 zircon domains were dated using SIMS (fig. 4.44b). One analysis was rejected because of high common lead content (tab. 4.5). Most of the dated zircon domains are undoubtedly inherited and show mainly high Th/U. The inherited zircons are as follows:

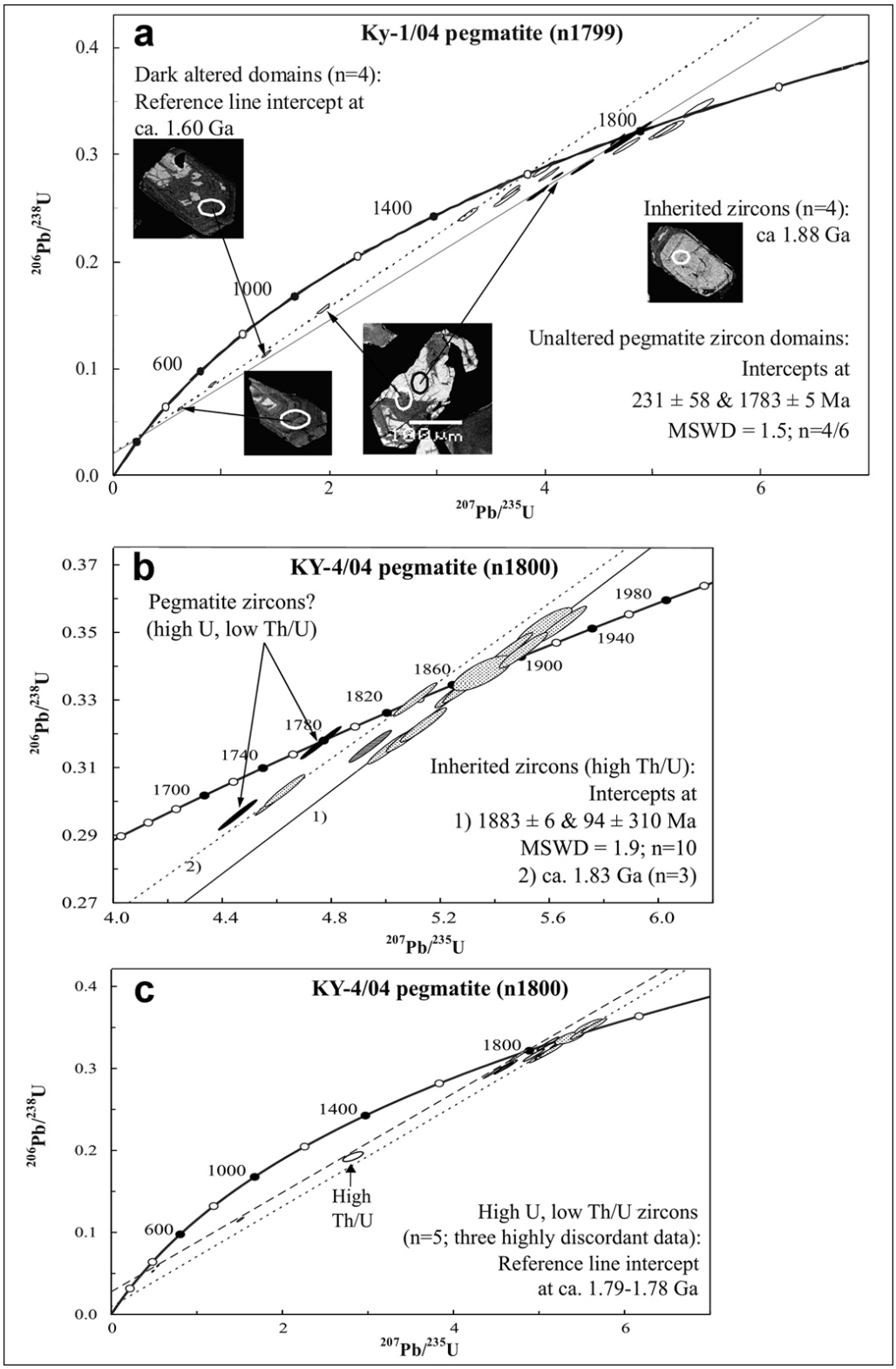

Fig. 4.44. Concordia plots of ion microprobe zircon U-Pb isotopic data for pegmatite samples **a)** KY-1/04 and **b-c)** KY-4/04. Modified from original plots by I. Mänttäri.

1. Ten form a discordia line with an upper intercept age of 1883±6 Ma (coeval with the obtained magmatic ages for the gneisses).
2. Three have an age ca. 1.83 Ga and two of these have quite low Th/U.
3. One plots between the aforementioned age groups.
4. One analysis is highly discordant.

The rest of the data (n=5) include three highly discordant, one concordant, and one slightly discordant analysis from high U and low Th/U pegmatitic zircons (fig. 4.44c). Two of these, analysed on mainly unaltered domains of zircons (one concordant and the other slightly discordant) have ages of ca. 1.78-1.79 Ga. The three analyses on dark, BSE altered domains show extremely discordant age data. All these data plot roughly on a same ca. 1.79 Ga reference line. However, the upper intercept age is practically determined by the concordant (12a) data point.

As a summary, the ion microprobe U-Pb data from both pegmatite samples clearly show a ca. 1.88 Ga inherited zircon population. An age of 1.78-1.79 Ga can be suggested for the pegmatite dykes, and is also therefore the suggested maximum age for the brittle pseudotachylytes. The pegmatite high U-low Th/U zircons were susceptible for later disturbances of their U-Pb system, probably caused by the effect of rapakivi intrusion. The closest rapakivi intrusions are the Åland rapakivi, ca. 20 km NW of the sampling area (fig. 4.3), and the smaller Kökar rapakivi, ca. 15 km SSW of the sampling area.

Pseudotachylyte $^{40}Ar/^{39}Ar$ age

An average of the best steps from the pseudotachylyte sample KY-4/02 yields an age of 1583 ± 5 Ma (fig. 4.45a). This coincides approximately with the intrusion of the rapakivi granites in the area (e.g. Vaasjoki 1977: 1576±10 Ma). The sample To-MLN-1 from Torsholma gives an average age of 1556 ± 6 Ma (fig. 4.45b), which is in relatively good agreement with sample KY-4/02. However, the pseudotachylytes contain tiny relict mineral fragments (fig. 4.38h), and it can therefore be assumed that relict mineral grains are present and may contribute with a large amount of radiogenic argon. Consequently, it is possible that the obtained age reflects the cooling through the closure temperature of K-feldspar (approximately 160 ºC; Zeitler 1987), rather than the true age of the pseudotachylyte. On the other hand, possible excess argon may have contributed to the results and the obtained age may therefore be too old. Pseudotachylite melts however generally have temperatures of 800-1300 ºC, and therefore the melts may have contained enough heat to degas the inherited argon system in the pseudotachylites, especially if the pseudotachylytes formed at relatively low pressures (Cosca et al. 2005). Also the rapakivi intrusions close to the study area may have affected the system. Unfortunately, little is known about the exact temperature at which the pseudotachylyte formed, and this fact makes it more difficult to determine whether the true age of the pseudotachylyte is younger or older than the obtained age. However, assuming that the high frictional temperatures of a pseudotachylite-forming event would degas the inherited argon in the pseudo-tachylite, the obtained age can be interpreted as a minimum age for

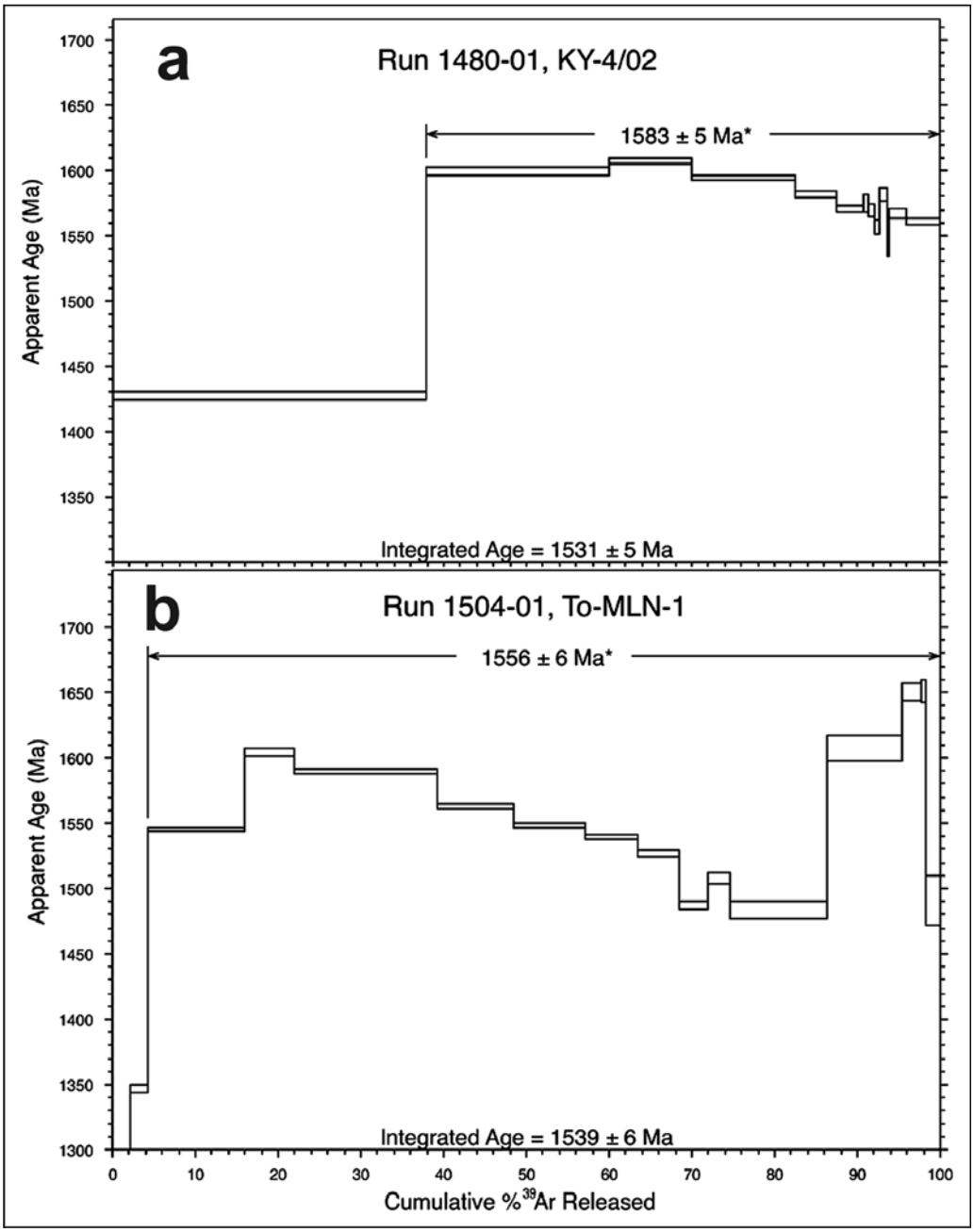

Fig. 4.45. $^{40}Ar/^{39}Ar$ step-heating spectra for pseudotachylite samples **a)** KY-4/02 and **b)** To-MLN-1. Modified from an original plot by T. Hermansson and L. Page.

---

the pseudotachylite, although it is obvious that this conclusion should be taken with caution. As a summary, the age of the pseudotachylite-forming event is within this study bracketed between 1.58 and 1.78 Ga.

4.5.4 SUMMARY AND DISCUSSION

Summary of the obtained ages is presented in table 4.4.

The magmatic protolith ages obtained for the gneissose and mylonitic rocks are around 1880-1890 Ma, and the zircons from the unmylonitised granodiorite (KY-7/03) are marginally older with an age of 1895±4 Ma. The obtained magmatic ages do not deviate from those published from elsewhere in SW Finland (e.g. Ehlers et al. 2004; Väisänen et al. 2002). If the bright, rounded, smoothly zoned, unfractured ca. 1.89 Ga zircons exclusively found in the ultramylonite sample KY-8/04 resulted from recrystallisation of inherited zircon, also co-magmatic deformation may have taken place since a core domain of one of these zircons yields an inherited age of ca. 1.92 Ga. However, the age results do not give enough evidence to make any conclusions of the presence of a co-magmatic deformation phase.

The post-intrusion deformation events were detected from the granodiorite gneiss and the wide mylonite zircons. These thin zircon domains yield metamorphic ages of ca. 1.85 Ga and 1.83 Ga, respectively. The youngest, ca. 1.79-1.80 Ga deformation phase was not observed in the analysed zircons.

The U-Pb titanite ages from the mylonites, tonalite gneiss and the semidiscordant metadiabase dyke form three separate age groups, each of which is interpreted to represent a separate ductile deformational phase (fig. 4.43). In samples with two titanite populations, the clearly differing appearances and petrographic associations of the titanites confirm that there has been a pause in the ductile deformation between 1.85 and 1.83 as well as between 1.83 Ga and 1.79 Ga. The metamorphic ages of 1.85 and 1.83 Ga were also observed in zircons. The break in deformation between 1.83 and 1.79 Ga is supported by observations by e.g. Väisänen et al. (2000), who report a 1815 ± 2 Ma undeformed monzodiorite (interpreted as post-collisional) from Turku region. In addition, the 1.79 Ga titanites in the semidiscordant metadiabase dyke (KY-1/03A) and the protomylonite (KY-2/03B) also have an association with the latest deformation fabrics in thin section, indicating a separate deformation phase at this time - for sample KY-2/03, the obtained age is also interpreted to be the age of the protomylonitic deformation. On the other hand, the age of the ultramylonitic deformation (sample KY-8/04) remains uncertain, as the metamorphic ages obtained for the ultramylonite sample are interpreted to reflect earlier deformation phases. In the light of the results it is probable that the rocks entered the amphibolite-greenschist facies transition after ca. 1.79 Ga due to continuing and, possibly, accelerating uplift and exhumation so that the crust was relatively rigid at the time of the pegmatite intrusions 1.78-1.79 Ga ago. It is noteworthy that Väisänen et al. (2000) concluded that the uplift and exhumation within the LSGM in Turku region (ca. 70 km NE of the area of this study) ceased already by ca. 1.80 Ga..

Pseudotachylytes cut the ca. 1.78-1.79 Ga pegmatite dykes. On the other hand, the pseudotachylyte samples yield a minimum $^{40}Ar/^{39}Ar$ age of 1.58 Ga, although as discussed above, the obtained age should be taken with some caution and in any case may not represent the formation of the pseudotachylite itself. The age of the pseudo-

tachylytes nevertheless within this study bracketed between ca. 1.79 Ga and 1.58 Ga.

Previous studies indicate that the earliest deformation phase (D_1) in southern Finland usually precedes the intrusion of the 1.89-1.88 Ga granitoids (e.g. Ehlers et al. 1993). The following D_2 deformation phase that refolded the D1 structures along E-W trending fold axes occurred at ca. 1.87 Ga according to Skyttä et al. (2006) and Väisänen et al. (2002). During subsequent D_3 and D_4 phases much of the deformation already partitioned into ductile crustal-scale shear zones within the Svecofennian domain (e.g. Kärki et al. 1993). In southern Finland, D_3 occurred ca. 1.82-1.83 Ga ago, during which the transpressional stress field rotated from an early N-S direction to a late NW-SE compression (Levin et al. 2005). D_4 deformation phase in southwestern Finland is commonly referred to have taken place at ca. 1.80 Ga, although this is a tentative age interpreted from the association of some shear zones with ca. 1.80 Ga postorogenic intrusions (Branigan 1987). Steep D_4 strike-slip shear zones in southern Finland are also described by e.g. Väisänen & Hölttä (1999). They report N-S to NE-SW shear structures in Turku region where deformation initiated close to the brittle-ductile transition (during D4). These zones were later reactivated within the brittle regime, producing pseudotachylytes.

Structures formed due to the regional deformation phases D_1-D_2 are not readily observable within the shear zone. One 1.92 Ga inherited zircon core was found, suggesting a presence of older Palaeoproterozoic crust. The ductile deformation phase I (ca. 1.85 Ga) within the SJSZ corresponds most closely to the regional deformation phase D_2. This age may represent the last regional deformation phase before the deformation partitioned into the shear zone, because metamorphic zircon ages younger than 1860 Ma or metamorphic (titanite) ages falling into SJSZ phase II (ca. 1.83 Ga) have not been reported in the proximity of the study area outside the shear zone itself (Ehlers et al. 2004). On the other hand, ca. 1.79 Ga (SJSZ phase III) magmatic and metamorphic events seem quite common also south of the shear zone (e.g. Ehlers et al. 2004, Suominen 1991). The SJSZ phases II and III nevertheless probably reflect the regional D_3 and D_4, respectively. In the light of the data, the following scenario for the evolution of the ductile shearing within the SJSZ is suggested. The rocks were emplaced around 1.88-1.89 Ga, and the first subsequent deformation phase (phase I) occurred around 1.85 Ga. Also Hermansson et al. (2007) describe an early-Svecofennian regional deformation phase at amphibolite facies conditions around 1.85 Ga in Forsmark region, south-central Sweden, NW of the area of this study. A second, more intensive deformation phase II occurred at ~1.83-1.82 Ga (D_3) by which the shear zone was already well developed, although some deformation probably still occurred outside the SJSZ. The age data combined with field studies indicate that the bulk of the large-scale folding and the mineral lineations at the SW margin of the shear zone developed latest at this stage. It is also interpreted that the recorded 'peak' metamorphic conditions of ca. 680°C and 7 kbar (Torvela and Annersten 2005; chapter

4.6) were reached at this time. Also the vertical movement of SW-side up (chapter 4.2) is interpreted to have commenced at this stage, but probably continued during the last ductile phase as well. After phase II there was another break in deformation as indicated by the age data as well as the high-T static recrystallisation textures of the gneisses. The last ductile phase took place at 1.80-1.79 Ga during phase III (regional D_4) in retrograde but still relatively high-T conditions (Torvela and Annersten 2005), and at least the protomylonites were formed latest at this time. The undeformed pegmatites intruded the already relatively rigid crust 1.78-1.79 Ga ago, i.e. soon after phase III (late- to post-D_4).

The results suggest that the rocks cooled rapidly around or soon after 1.79 Ga due to uplift of the rocks into increasingly lower-T conditions. The deformation may have continued for an unknown period of time, or occurred as a separate phase some time after 1.79 Ga, within the semi-ductile regime producing the finer-grained mylonites and ultramylonites, although it is also probable that some fine-grained mylonitisation occurred already during the dominantly gneissose phases II and III due to rheological differences between rock types (sample E-2/03). In this context, it is interesting to note that Welin et al. (1983) interpreted the largely undeformed Mosshaga pluton (NW of the island of Sottunga) to have intruded into relatively high crustal levels (1-2 kbar) because the pluton cooled rapidly enough to show whole rock Rb-Sr ages relatively close to the U-Pb zircon ages (1742±34 Ma and 1788±11 Ma, respectively). Furthermore, Hermansson et al. (2006) report $^{40}Ar/^{39}Ar$ data from Forsmark area in south-central Sweden that indicate cooling of rocks below 500ºC and 300ºC between 1834-1793 Ma and 1704-1635 Ma, respectively, so that the brittle regime was probably reached before ca 1700 Ma. Moreover, Väisänen (2002) concludes that the crustal uplift in Turku area was most intense around 1.80 Ga. The data obtained during this study support the notion of rapid cooling and exhumation of the rocks from relatively high-T conditions into high crustal levels soon after ca. 1.79 Ga. The last, brittle activity period along the shear zone is recorded by the pseudotachylytes, the age of which remains unknown but is probably between 1.78-1.58 Ga.

4.5.5 CONCLUSIONS

The results of this study suggest that the crustal-scale deformation and shearing along the South Finland shear zone, and possibly also along other Palaeoproterozoic shear zones in southern Finland, was not restricted to the D3 and D4 regional deformation phases, but probably commenced earlier than 1.83 Ga. The obtained U-Pb isotopic data indicate the onset of the ductile deformation within the study area at about 1.85 Ga. Evidence of a second, clearly separate, more intensive deformation phase around 1.83 Ga exists. A third reactivation of the shear zone within the ductile regime occurred ca 1.79 Ga. The maximum age of the main mylonitic deformation is ca. 1.79 Ga based on the ages obtained from the ductilely deformed diabase dyke and the wide mylonite zone. The geochronologic, petrographic and mineralogical differences between the various mylonite types suggest that

the mylonitization was probably a long-lived process that continued for an unknown period after 1.79 Ga, and locally possibly even before that (sample E-2/03 in table 2). The SJSZ was therefore active and reactivated at least three times within the ductile regime between 1.85 – 1.79 Ga, and at least once between 1.78-1.58 Ga during the brittle pseudotachylite-forming phase. The results indicate that the crust cooled rapidly around and soon after 1.79 Ga, probably due to uplift and exhumation, bringing the rocks into increasingly semi-ductile and, subsequently, brittle regimes.

4.6 GEOTHERMOBAROMETRY

The physical conditions during the formation of two different deformation systems (gneissose and mylonitic) within the SJSZ were estimated by means of standard geothermobarometric calculations. Seven rock samples in the Åland archipelago were studied and selected for analysis (fig. 4.46). Geothermobarometric methods were applied on the analysed rock samples in order to estimate the metamorphic P-T conditions (for method descriptions, see chapter 3.1.2). The analyses were carried out in cooperation with Hans Annersten from Uppsala University and Bo Johanson from the Geological Survey of Finland. Many of the geothermometric results presented in this chapter are also published in Torvela & Annersten (2005).

4.6.1 FIELD RELATIONSHIPS, PETROGRAPHY AND MINERAL CHEMISTRY

As discussed in chapter 4.2.1, the rock types can roughly be divided into three types: the ductilely deformed striped gneisses belonging to the earliest shearing phase(s); the ductile to semi-ductile mylonites, belonging to a somewhat younger deformation phase; and the pseudotachylytes, representing the last, brittle movements along the zone. The gneisses cover most of the area, while the mylonites are present as narrow, mostly as cm-scale but occasionally as up to 30-40 m wide zones.

Aluminous minerals such as staurolites and Al_2SiO_5 polymorphs have not been found in the rocks. Even garnets are rare in all rock types; only few narrow garnet-bearing gneiss layers have been identified (Hellsö, Storskär (Kyrkogårdsö), Husö). Where garnets do occur, especially on Hellsö, they occasionnally show some retrograde alteration to biotite and, more rarely, chlorite at the rims and within the fractures of the garnets. However, even unaltered garnets are common. In contrast to the other gneiss types, the biotite in the garnet-bearing gneisses is commonly red-brown in colour indicating a higher Ti-content than in the samples without garnet, while epidote, hornblende and titanite are largely absent. Instead, occasional white mica is present as very small grains.

Seven samples were selected for electron microprobe analysis (fig. 4.46). Four of the samples were collected from ductile gneisses, two samples are from the wide mylonite zone on Kyrkogårdsö (one protomylonite and one ultramylonite), and the seventh sample was taken from a garnet-bearing tonalitic mylonite on the island of Storskär. Of the four gneissose samples, one is a semidiscordant metadiabase dyke within the main shear zone (Kyrkogårdsö) that intruded the surrounding gneisses at a relatively late stage and that was subsequently sheared together with the gneisses. Two samples are from garnet-bearing granodioritic gneisses, while the fourth is a tonalitic gneiss from within the main SJSZ.

The garnet-bearing gneissose samples were collected from outside the main SJSZ from the medium-grained, granodioritic gneisses of Hellsö (K-5/02 and K-3/03; figs. 4.46, 4.26d). *Sample K-5/02* from Hellsö consists of plagioclase, quartz, red-

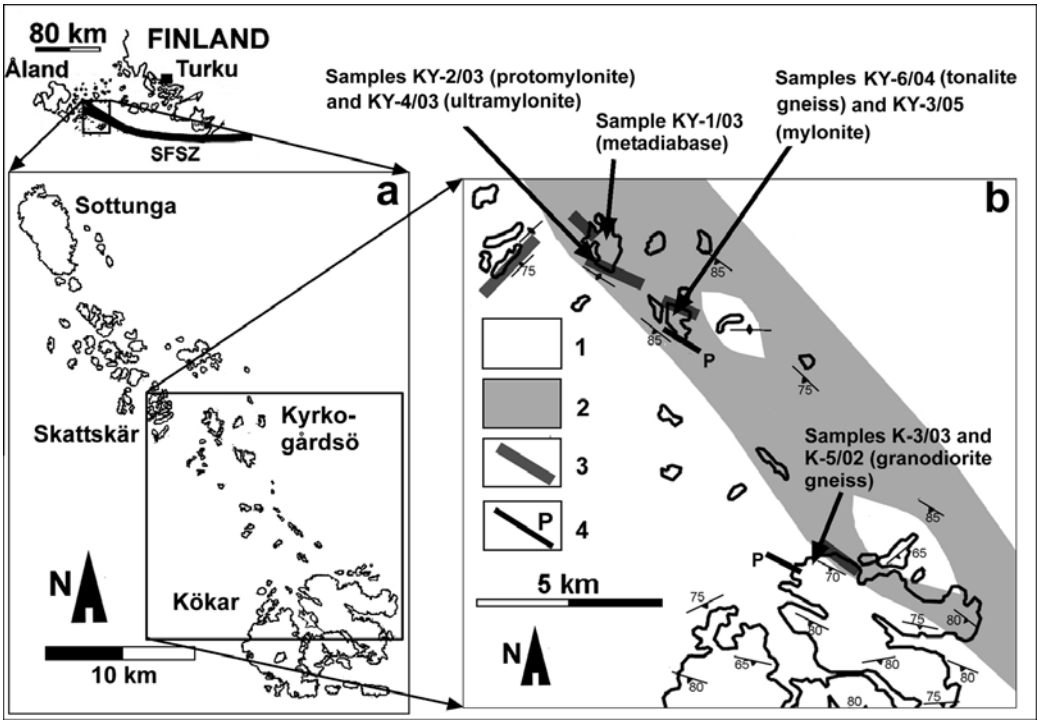

Fig. 4.46. a) Study area in Åland archipelago. **b)** Sampling locations for the electron microprobe analyses. Key: **1)** Medium-grained, granitic to tonalitic gneisses with local dioritic and gabbroic lenses; **2)** Main shear zone; **3)** Prominent mylonite zones; **4)** Pseudotachylytes.

brown biotite with minor local chloritisation, and unchloritised garnet, with accessory zircon and opaques. The texture is that of a recovered rock with relatively straight grain boundaries and strain-free grains, implying that the temperature remained relatively high after the peak of the deformation so that static recrystallisation processes were enabled (chapter 4.3.1; Evans et al. 2001, Kruhl 2001). This in turn implies that stable mineral reactions were favoured so that equilibrium may have been reached. The garnets in the sample are porphyroblasts, pre- to syn-tectonic with irregular inclusion patterns, grown over the earlier mineral assemblages during metamorphism (fig. 4.26d). The foliation defined by the orientated biotite grains is deflected around the porphyroblasts. In sample K-5/02 the garnets are Fe-rich with minor amounts of Ca, Mn and Mg (tab. 4.8). Microprobe analyses show the garnets to be relatively homogeneous, although there are some occasional variations in geochemistry and local impurities of feldspar and mica within the grains. Some retrograde manganese zoning at the rims can be observed (fig. 4.47a). The more homogeneous part of the garnet core is therefore interpreted to represent the peak metamorphism conditions. The plagioclase cores in sample K-5/02 are constantly more Na-rich and Ca-poor than the grain rims (tab. 4.8). This implies that since the rocks are poor in Ca, the albitic component in plagioclase has increased simultaneously with garnet growth,

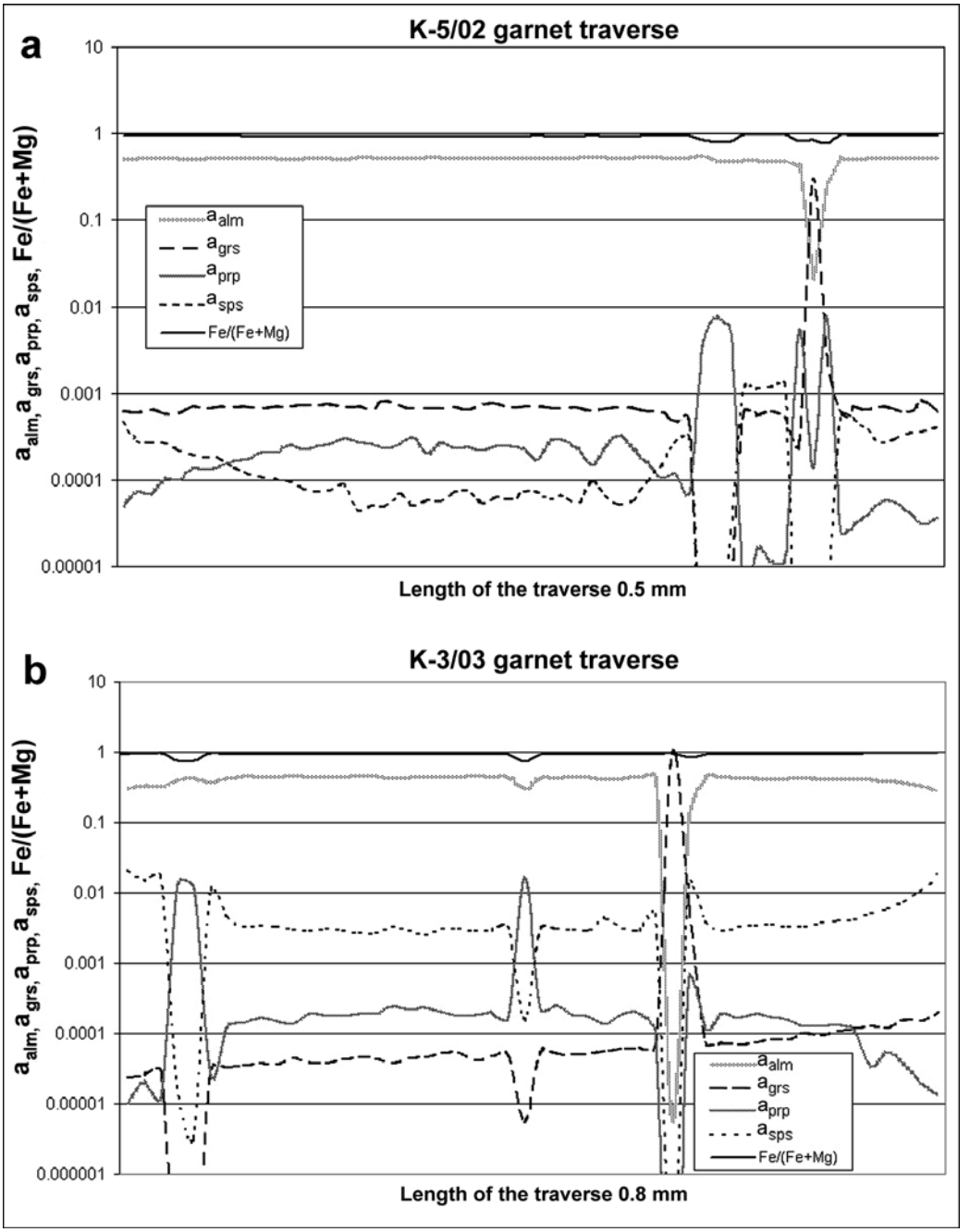

Fig. 4.47. Examples of garnet traverses in the analysed samples; sample points plotted against almandine, grossular, pyrope and spessartine activities and the Fe-number. See text for discussion **a)** Sample K-5/02, **b)** sample K-3/03.

i.e. during progressive metamorphism (Spear 1995). During retrogression, the plagioclase rims were enriched in Ca as a result of lower-T equilibrium mineral reactions, while the grain cores have not been thoroughly equilibrated to retrograde conditions. The plagioclase cores in this sample

have therefore been interpreted to represent the minimum peak metamorphic conditions of deformation.

Sample K-3/03 has a mineral composition rather similar to the sample K-5/02. However, the sample K-3/03 has experienced a more extensive retrograde alteration. The plagioclases in this sample evidence of this as they are thoroughly sericitised, sometimes with a partial rim of muscovite as a retrograde phase, and the cores show a Ca-content equal to or in some cases even higher than the grain rims. The plagioclases can therefore not be considered to have maintained their peak metamorphic geochemistries. Also the biotite is slightly more retrogressed to chlorite than in sample K-5/02. The garnets in this sample are slightly poorer in Fe and Ca being instead richer in Mn than the garnets in the sample K-5/02. The garnets frequently show minor chlorite alteration along the grain rims and cracks. The garnet traverse analyses show minor retrograde Mn-alteration, localised along the porphyroblast rims (fig. 4.47b).

The third gneissose *sample KY-6/04* was collected from the Kyrkogårdsö area within the main shear zone (fig. 4.46). The rock has a tonalitic composition, containing plagioclase, hornblende, quartz, biotite and abundant accessory apatite, titanite and opaques (figs. 4.48a, 4.38b). Minor epidote is present, usually as a narrow rim around the opaque (ilmenite/ilmeno-rutile?) grains, but no chloritisation can be observed in thin section. The gneiss is intensely sheared with quartz ribbons and elongated hornblende grains. The Ca- and Fe-rich hornblende is poor in Ti and Na.

Sample KY-1/03 (metadiabase) was collected from western Kyrkogårdsö (fig. 4.46). It consists of plagioclase, biotite and amphibole, with abundant titanite and opaques (figs. 4.48b, 4.38c). The rock is unchloritised, intensely sheared but not mylonitic, the foliation being defined by the biotite grains as well as the amphibole and titanite that often show somewhat oblong form and are arranged along the foliation plane. Again, the amphibole is Ti-poor, Fe-rich hornblende with minor Na that does not to show significant geochemical zoning (tab. 4.8). Neither the plagioclase is zoned with respect to Ca and Na.

Three of the seven samples are mylonites, two of which were collected from a ca. 30 m wide, intensely sheared zone on the island of Kyrkogårdsö (fig. 4.46). The zone is dominated by mylonites and ultramylonites with streaks of somewhat less deformed protomylonites in between. Sample KY-2/03 is from an intensely sheared, tonalitic protomylonite, while sample KY-4/03 represents an amphibole-bearing ultramylonite. The third mylonite sample KY-3/05 is a mylonite with ca. 50% fine-grained mica-rich matrix, collected from island of Storskär (fig. 4.46).

Sample KY-2/03 (protomylonite) consists of Ti-poor, Fe-rich hornblende, plagioclase, biotite and quartz with accessory titanite, zircon and opaques (figs. 4.28c and g). Some very fine-grained chlorite has formed in the thin shear bands observable in thin section, but chloritisation processes are not

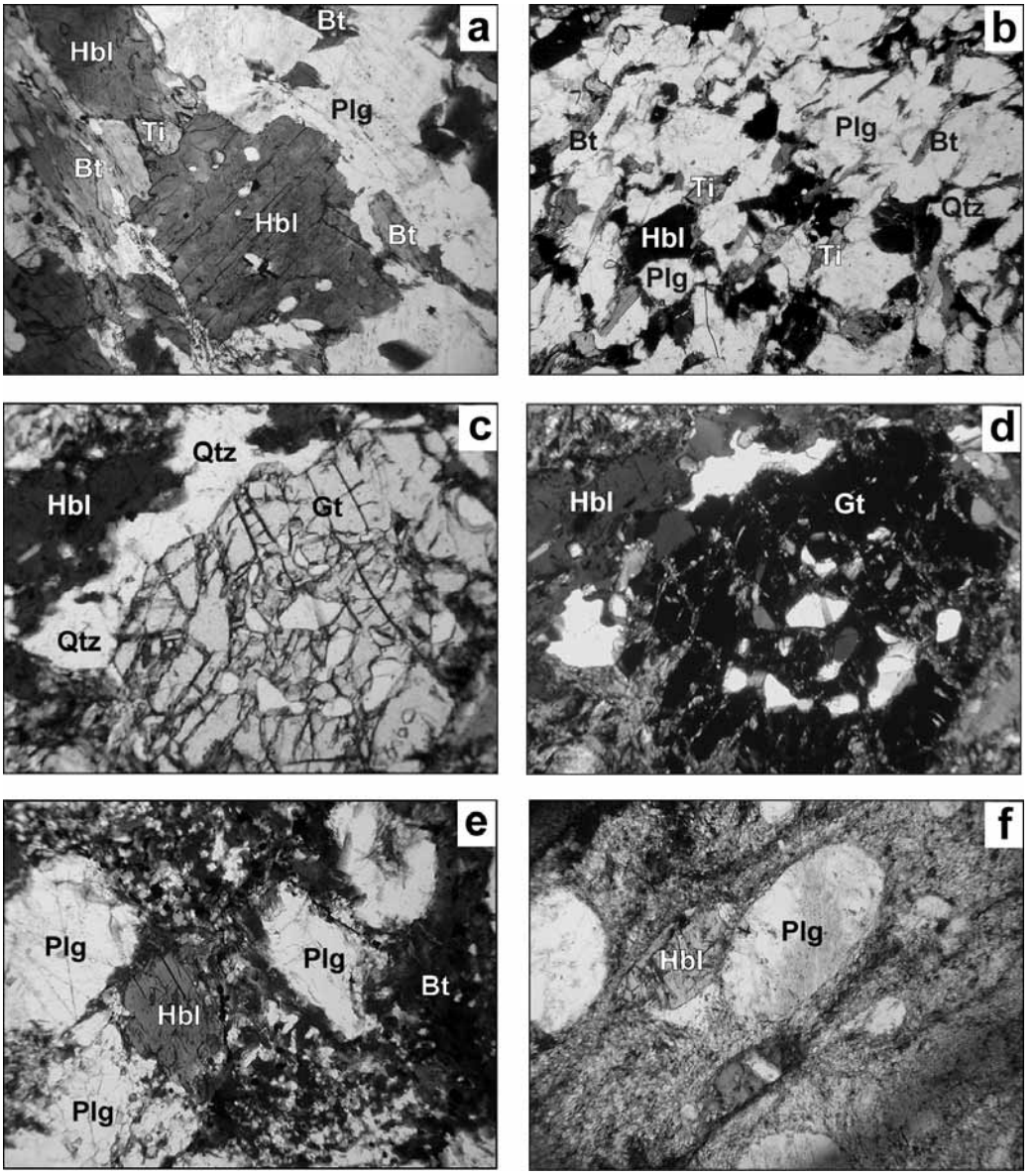

Fig. 4.48. Petrography of the samples analysed for PT-calculations. See text for discussion. Key: Ti = titanite, Hbl = hornblende, Plg = plagioclase, Gt = garnet, Bt = biotite, Qtz = quartz, PPL = plain-polarized light, CPL = cross-polarized light. **a)** Sample KY-6/04, tonalitic gneiss, Storskär. Width of the view 1.8 mm, PPL. **b)** Sample KY-1/03, semidiscordant metadiabase dyke, Kyrkogårdsö. Width of the view 1.8 mm, PPL. **c, d)** Sample KY-3/05, garnet-bearing mylonite, Storskär. The garnet is unaltered, growing over the earlier gneissose fabric. In d), the fabric of the dynamically crystallised quartz ribbon (*centre right toward upper centre*) is visible. Width of the view 1.0 mm, PPL (c), CPL (d). **e)** Sample KY-4/03, tonalitic ultramylonite. Width of the view 1.5 mm, PPL.

extensive. The hornblende shows minor zoning, the grain cores showing slightly higher contents of Al, Na and Ti than the grain rims, the cores instead being somewhat depleted in Si and Mg. The hornblende in this sample is poorer in Fe than the metadiabase sample KY-1/03,

probably reflecting the overall Si-richer composition of the rock. Also the plagioclase shows some zoning (tab. 4.8), the core of the plagioclase being more Ca-rich and Na-poor than the rim. Since the rock does not contain garnet like sample K-5/02, the plagioclase was not depleted in Ca during progressive metamorphism (Spear 1995), and the compositional zoning is therefore the opposite in this sample with respect to Na and Ca, compared to the garnet-bearing K-5/02. The composition zoning in this sample is therefore probably a reflection of the cooling of the rock and thereof resulting change in plagioclase composition. The quartz frequently forms small subgrains with irregular boundaries (SGR and GBM recrystallisation; chapter 4.3.1) and displays some undulose extinction, suggesting that the deformation continued at least some time after the metamorphic peak. The mineralogy and the petrography of this protomylonitic sample suggest that the retrograde mineral alteration processes ceased in relatively high-grade conditions, implying that the temperature decreased relatively rapidly after the conditions recorded in the rock, or that the rock had become too depleted of fluids to allow further hydration and recovery during retrogression. The rim geochemistries in this sample were interpreted to represent the approximate metamorphic temperature conditions during the last ductile deformation phase that affected this rock, i.e. the conditions of the protomylonite formation. The core chemistries possibly reflect the temperature conditions during an earlier deformation phase.

Sample KY-3/05 (mylonite) consists of hornblende, plagioclase, biotite, quartz, garnet, opaques (ilmenite/ilmenorutile), with minor titanite and epidote (fig. 4.48c-e). No chloritisation can be observed in thin section. The few larger remnant lenses that retain the earlier gneissose fabric show strain-free, polygonal 'foam-structure', indicating static recrystallisation and recovery at relatively high-T conditions (chapter 4.3.1), while the mylonitised quartz shows abundant dynamic SGR and GBM recrystallisation (fig. 4.48d). The mylonite matrix consists dominantly of biotite, quartz/plagioclase and opaques with minor hornblende 'microclasts'; indeed, the hornblende porphyroclasts are commonly extensively altered to biotite so that in many places only small hornblende grains remain in a biotite-rich groundmass (fig. 4.48e).

S*ample KY-4/03* (ultramylonite) shows a matrix that is partly of a greenschist facies assemblage with very fine-grained quartz/plagioclase, biotite and opaques with minor chlorite, epidote and calcite. Rounded porphyroclasts of plagioclase, hornblende and small titanite have been preserved in the extremely deformed matrix (fig. 4.48f). Despite the presence of chlorite, biotite is not generally very intensely chloritised, most of the biotite retaining its red-brown colour, implying that the retrograde processes did not advance to a great extent. The retrogressive chlorite alteration that does exist is concentrated to the matrix, while the hornblende porphyroclast rims are unaltered apart from local biotite alteration. It is therefore unclear whether the matrix mineral assemblage described above

Table 4.8. Electron microprobe spot analysis: Representative geochemical data from Kökar (Hellsö) and Kyrkogårsö. Complete analysis results available from the author.

Sample #		K-5/02								K-3/03				
Mineral		Gt	Gt	Bt	Bt	Plg	Plg	Plg	Plg	Gt	Gt	Bt	Bt	Plg
Core/rim; interpretation		C; peak	R adj Bt; retrogr.			C; peak	C; peak	R; retrogr.	R; retrogr.	C; peak	R; retrogr.			C
Oxides wt.%	SiO_2	37.05	36.74	35.12	35.12	56.16	56.59	55.60	55.38	36.69	36.89	34.36	34.36	58.36
	TiO_2	0.02	0.00	1.86	2.26	0.00	0.00	0.00	0.00	0.00	0.02	2.03	2.35	0.00
	Al_2O_3	20.51	20.67	15.49	16.70	27.26	27.31	26.85	27.60	21.16	20.84	17.12	16.75	25.48
	Cr_2O_3	0.00	0.01	0.00	0.08	0.04	0.00	0.00	0.00	0.04	0.00	0.05	0.13	0.00
	FeO	33.76	33.93	22.58	22.21	0.00	0.01	0.01	0.04	31.83	29.53	23.14	22.91	0.03
	MnO	1.78	2.64	0.04	0.00	0.00	0.00	0.01	0.00	5.90	9.13	0.29	0.30	0.00
	MgO	3.14	2.42	9.38	9.66	0.04	0.00	0.00	0.04	3.23	1.51	7.69	8.23	0.00
	CaO	4.01	3.82	0.00	0.01	9.92	9.63	10.18	10.46	1.40	2.73	0.00	0.02	8.21
	Na_2O	0.00	0.00	0.17	0.18	6.30	6.08	5.37	5.55	0.11	0.00	0.11	0.07	6.90
	K_2O	0.00	0.00	8.99	8.98	0.07	0.06	0.06	0.05	0.01	0.00	9.22	8.88	0.14
	SUM	100.26	100.24	93.62	95.20	99.79	99.67	98.07	99.12	100.37	100.64	94.00	94.00	99.11
Oxygens		12	12	22	22	8	8	8	8	12	12	22	22	8
Cations	Si	2.9818	2.9715	5.5500	5.4354	2.5325	2.5474	2.5441	2.5133	2.9574	2.9860	5.4326	5.4204	2.6323
	Ti	0.0015	0.0001	0.2210	0.2626	0.0000	0.0000	0.0000	0.0000	0.0001	0.0009	0.2412	0.2792	0.0000
	Al (tot.)	1.9456	1.9710	2.8854	3.0466	1.4490	1.4489	1.4483	1.4764	2.0100	1.9881	3.1900	3.1142	1.3547
	Al_{IV}[1]			0.4356	0.4823							0.6230	0.5349	
	Cr	0.0000	0.0008	0.0000	0.0096	0.0014	0.0000	0.0000	0.0000	0.0027	0.0000	0.0060	0.0158	0.0000
	Fe	2.2721	2.2953	2.9848	2.8750	0.0001	0.0004	0.0003	0.0015	2.1454	1.9988	3.0608	3.0232	0.0011
	Mn	0.1214	0.1809	0.0046	0.0000	0.0000	0.0000	0.0002	0.0000	0.4027	0.6259	0.0392	0.0396	0.0000
	Mg	0.3763	0.2918	2.2090	2.2290	0.0024	0.0000	0.0000	0.0028	0.3880	0.1826	1.8112	1.9356	0.0000
	Ca	0.3455	0.3313	0.0000	0.0014	0.4794	0.4644	0.4989	0.5087	0.1208	0.2366	0.0006	0.0030	0.3969
	Na	0.0000	0.0000	0.0508	0.0544	0.5511	0.5308	0.4761	0.4882	0.0169	0.0000	0.0326	0.0212	0.6032
	K	0.0000	0.0000	1.8118	1.7740	0.0040	0.0036	0.0037	0.0031	0.0008	0.0000	1.8604	1.7882	0.0078
	Mg/(Mg+Fe)	0.142	0.113	0.425	0.437					0.153	0.084	0.372	0.390	
Mole fractions	X_{Fe}	0.729	0.741							0.702	0.657			
	X_{Mn}	0.039	0.058							0.132	0.206			
	X_{Mg}	0.121	0.094							0.127	0.060			
	X_{Ca}	0.111	0.110			0.463	0.465	0.510	0.509	0.040	0.078			0.394
	X_{Na}					0.533	0.531	0.486	0.488					0.599
	X_K					0.004	0.004	0.004	0.003					0.001
Activities[2]	a_{Gros}	0.0014	0.0012							0.0001	0.0005			
	a_{An}					0.2481	0.2495	0.2905	0.2895					0.1912
	a_{AlIV_Bt}			0.0740	0.0820							0.1086	0.0927	

Table 4.8. *(Continued)*

Sample #		K-3/03	KY-6/04				KY-1/03				KY-2/03			
Mineral		Plg	Hbl	Hbl	Plg	Plg	Hbl	Hbl	Plg	Plg	Hbl	Hbl	Plg	Plg
Core/rim; interpretation		R	R	R	R	R	C	R	R	R	C; peak	R; retrogr.	C; peak	R; retrogr.
Oxides wt.%	SiO_2	60.10	42.89	43.37	56.61	57.66	39.49	39.20	57.23	57.02	41.25	44.08	56.83	59.55
	TiO_2	0.01	0.63	0.51	0.00	0.00	1.14	1.11	0.00	0.00	1.10	0.47	0.00	0.00
	Al_2O_3	25.04	10.90	11.66	25.90	26.38	11.74	12.30	25.88	25.67	10.08	9.28	26.10	24.25
	Cr_2O_3	0.00	0.00	0.00	0.00	0.00	0.02	0.02	0.02	0.00	0.00	0.01	0.06	0.00
	FeO	0.00	18.02	18.36	0.08	0.26	23.36	22.48	0.12	0.10	18.95	18.98	0.01	0.17
	MnO	0.02	0.35	0.22	0.00	0.00	0.58	0.51	0.00	0.00	0.37	0.30	0.00	0.02
	MgO	0.01	9.24	8.85	0.00	0.00	6.61	6.47	0.02	0.00	9.15	9.94	0.03	0.00
	CaO	7.10	11.33	11.85	8.02	8.31	11.46	11.65	8.56	8.48	11.79	11.81	8.90	6.45
	Na_2O	7.41	0.95	1.00	6.66	6.79	1.04	1.10	6.85	6.71	1.10	0.71	6.09	8.12
	K_2O	0.17	0.76	0.71	0.04	0.05	1.66	1.60	0.10	0.13	1.01	0.62	0.08	0.07
	SUM	99.86	95.08	96.53	97.31	99.45	97.11	96.43	98.77	98.11	94.80	96.19	98.09	98.64
Oxygens		8	22	22	8	8	22	22	8	8	22	22	8	8
Cations	Si	2.6800	6.3459	6.3204	2.6004	2.5957	5.9624	5.9361	2.5979	2.6041	6.2102	6.4665	2.5918	2.6920
	Ti	0.0002	0.0701	0.0554	0.0000	0.0000	0.1297	0.1262	0.0000	0.0000	0.1246	0.0522	0.0000	0.0000
	Al (tot.)	1.3158	1.9014	2.0023	1.4025	1.3999	2.0894	2.1952	1.3845	1.3815	1.7890	1.6041	1.4033	1.2923
	Cr	0.0000	0.0000	0.0000	0.0000	0.0000	0.0024	0.0023	0.0008	0.0000	0.0000	0.0007	0.0020	0.0000
	Fe	0.0000	2.2299	2.2375	0.0032	0.0100	2.9498	2.8472	0.0044	0.0039	2.3862	2.3292	0.0003	0.0062
	Mn	0.0009	0.0434	0.0273	0.0000	0.0000	0.0737	0.0659	0.0000	0.0000	0.0472	0.0374	0.0000	0.0009
	Mg	0.0005	2.0383	1.9225	0.0000	0.0000	1.4882	1.4599	0.0013	0.0000	2.0536	2.1740	0.0018	0.0000
	Ca	0.3391	1.7964	1.8506	0.3946	0.4010	1.8546	1.8901	0.4163	0.4148	1.9025	1.8563	0.4349	0.3123
	Na	0.6405	0.2723	0.2817	0.5929	0.5924	0.3042	0.3239	0.6025	0.5940	0.3211	0.2008	0.5385	0.7119
	K	0.0099	0.1436	0.1323	0.0023	0.0028	0.3197	0.3082	0.0060	0.0077	0.1936	0.1160	0.0048	0.0042
	Mg/(Mg+Fe)		0.478	0.462			0.335	0.339						
Mole fractions	X_{Fe}										0.856	0.902		
	X_{Mn}										0.144	0.098		
	X_{Mg}													
	X_{Ca}	0.343			0.399	0.403			0.406	0.408			0.445	0.304
	X_{Na}	0.647	0.123	0.124	0.599	0.595	0.123	0.128	0.588	0.584			0.551	0.692
	X_K	0.002			0.000	0.000			0.001	0.001			0.001	0.001
Activities	a_{Gros}													
	a_{An}	0.1545												
	a_{AlIV_Bt}													

Table 4.8. *(Continued)*

Sample #		KY-3/05								KY-4/03			
Mineral		Bt	Bt	Bt	Gt	Gt	Gt	Plg	Plg	Hbl	Hbl	Plg	Plg
Core/rim; interpretation		R	R	R	R	R	R	R	R	C; peak	R; retrogr.	C; peak	R; retrogr.
Oxides wt.%	SiO_2	35.96	36.17	35.56	37.71	37.40	37.72	55.02	55.30	49.17	50.43	57.92	57.78
	TiO_2	1.61	1.58	1.89	0.00	0.04	0.00	0.00	0.01	0.25	0.17	0.00	0.00
	Al_2O_3	16.51	16.58	16.12	20.74	20.77	20.91	28.60	28.50	6.76	5.52	25.26	24.53
	Cr_2O_3	0.02	0.00	0.02	0.00	0.00	0.01	0.00	0.01	0.00	0.06	0.02	0.00
	FeO	21.72	21.48	21.53	26.59	27.00	26.73	0.12	0.12	14.38	13.10	0.19	0.13
	MnO	0.30	0.28	0.39	5.70	5.74	5.57	0.00	0.06	0.34	0.29	0.01	0.00
	MgO	9.00	9.06	8.80	2.47	2.53	2.53	0.00	0.00	13.59	14.78	0.00	0.04
	CaO	0.19	0.31	0.07	6.48	6.53	6.48	10.90	10.76	12.29	12.33	7.80	7.89
	Na_2O	0.05	0.08	0.02	0.00	0.00	0.00	5.42	5.45	0.74	0.51	7.26	7.03
	K_2O	8.84	8.56	9.06	0.00	0.02	0.00	0.06	0.05	0.45	0.32	0.14	0.08
	SUM	94.18	94.11	93.46	99.70	100.03	99.95	100.12	100.27	97.96	97.49	98.59	97.48
Oxygens		22	22	22	12	12	12	8	8	22	22	8	8
Cations	Si	5.6004	5.6189	5.5952	3.0213	2.9962	3.0131	2.4774	2.4853	6.8722	7.0188	2.6303	2.6502
	Ti	0.1882	0.1850	0.2237	0.0000	0.0021	0.0000	0.0000	0.0002	0.0261	0.0175	0.0000	0.0000
	Al	3.0300	3.0365	2.9899	1.9587	1.9607	1.9694	1.5176	1.5096	1.1131	0.9051	1.3519	1.3260
	Al_{IV}	0.6306	0.6556	0.5853									
	Cr	0.0021	0.0000	0.0023	0.0000	0.0000	0.0006	0.0000	0.0003	0.0002	0.0065	0.0007	0.0000
	Fe	2.8292	2.7905	2.8337	1.7814	1.8090	1.7857	0.0047	0.0045	1.6808	1.5248	0.0071	0.0051
	Mn	0.0391	0.0371	0.0515	0.3865	0.3894	0.3768	0.0000	0.0023	0.0404	0.0336	0.0003	0.0000
	Mg	2.0888	2.0980	2.0631	0.2954	0.3026	0.3011	0.0000	0.0000	2.8311	3.0655	0.0000	0.0029
	Ca	0.0317	0.0514	0.0126	0.5561	0.5604	0.5551	0.5259	0.5183	1.8411	1.8386	0.3797	0.3879
	Na	0.0153	0.0236	0.0070	0.0000	0.0000	0.0000	0.4730	0.4749	0.2000	0.1374	0.6391	0.6248
	K	1.7563	1.6975	1.8192	0.0000	0.0017	0.0005	0.0037	0.0030	0.0801	0.0575	0.0079	0.0046
	Mg/(Mg+Fe)	0.425	0.429	0.421	0.142	0.143	0.144						
Mole fractions	X_{Fe}				0.590	0.591	0.592			0.902	0.930		
	X_{Mn}				0.128	0.127	0.125			0.098	0.070		
	X_{Mg}				0.098	0.099	0.100						
	X_{Ca}				0.184	0.183	0.184	0.525	0.520			0.370	0.381
	X_{Na}							0.472	0.477			0.622	0.614
	X_K							0.001	0.001			0.001	0.001
Activities	a_{Gros}				0.0062	0.0061	0.0062						
	a_{An}							0.3048	0.3006				
	a_{AlIV_Bt}	0.1100	0.1140	0.1026									

[1] Calculated from Al(tot.) with MinPet software [2] Required activities for GBPQ (Wu et al. 2004): $a_{Gros} > 3\%$, $a_{An} > 17\%$, $a_{AlIV\_Bt} > 3\%$.

developed coevally with the mylonitic deformation, or if it was a result of a post-deformation alteration. At any rate, the mineralogy suggests relatively high, lower amphibolite to transitional amphibolite-greenschist facies temperatures during the mylonite-forming event; however not higher than ca. 500-550ºC, but probably not much lower than ca. 450ºC. There is minor geochemical zoning present in the porphyroclasts, especially hornblende, and it is the last preserved record of the changing metamorphic conditions prior to the mylonitisation (tab. 4.8). Therefore, the rim geochemistries in the mylonite sample represent the maximum mylonitisation conditions.

The main petrographic and mineralogical features of the samples that were analysed within the scope of this study are summarised in table 4.9.

4.6.2 GEOTHERMOBAROMETRY – RESULTS AND INTERPRETATIONS

A summary of the results of the geothermobarometric calculations is presented in table 4.9.

For the two garnet-bearing granodioritic gneisses collected from Hellsö, the temperatures calculated by the Gt-Bt method from the garnet and biotite grain cores vary from 635ºC in the sample K-5/02 to 670ºC in the sample K-3/03 (tab. 4.9, fig. 4.49). These temperatures can be considered equal within the uncertainty of the method (±50ºC; Bhattacharya et al. 1992), and give the minimum peak temperature for gneissose deformation. The grain rims record somewhat lower, retrogressive Gt-Bt temperatures of 580ºC and 505ºC for samples K-5/02 and K-3/03, respectively. Not unexpectedly, the more retrogressively altered sample K-3/03 gives significantly lower rim temperatures than sample K-5/02. The rim temperatures of sample K-5/02 are only marginally lower than the core temperature with respect to the uncertainty of the method.

The third gneissose sample, i.e. the tonalitic gneiss (KY-6/04) from within the main shear zone gives Hbl-Plg rim temperatures of 655-695ºC (fig. 4.50a). Interestingly, the obtained temperature, although calculated for Hbl-Plg grain *rim* contact regions, is comparable to the Gt-Bt *core* temperatures in the Hellsö granodioritic gneisses. The reason for this phenomenon may be that the system Hbl-Plg in the rocks is more resistant to lower-T changes than the system Gt-Bt, thus better retaining the higher-T mineral compositions compared to the system Gt-Bt that may have been more easily reset during retrograde metamorphism. Another explanation may be that the tonalitic gneiss within the main shear zone underwent a separate deformation phase at relatively high-T conditions that reset earlier, lower-T equilibrium chemistries. The tonalitic gneiss sample KY-6/04 has been dated (chapter 4.5), the results implying a deformation phase at ca. 1.82 Ga. However, since younger deformation phases than this have been dated within the study area (chapter 4.5), it is more likely that the reason for the high rim temperatures in the system Hbl-Plg are due to a higher resistance of the system to lower-T equilibrium reactions compared to the Gt-Bt system of the granodioritic gneisses.

Table 4.9. Sample descriptions and a summary of the results of the PT-calculations.

Sample #	Rock type	Petrographic and geochemical observations	Method(s)	Average P (kbar)/grain cores	Average P (kbar)/grain rims	Average T(°C)/grain cores	Average T(°C)/grain rims
K-5/02 Hellsö	Gt-bearing granodiori-tic gneiss	Plg-Qtz-Kfs-Bt-Gt[1] assemblage. No chloritization. Garnets: some alteration along the rims, minor retrograde zoning. Plagioclase: locally sericitised grains, some retrograde zoning of grains.	Gt-Bt[2], GBPQ[3]	6.4	5.3	635	580
K-3/03 Hellsö	Gt-bearing granodiori-tic gneiss	Qtz-Kfs-Plg-Bt-Gt-Chl assemblage. Garnets: somewhat altered to biotite and/or chlorite, some geochemical alteration along the rims, no zoning. Plagioclase: grains commonly sericitised, chemically equilibrated to retrograde conditions, no zoning.	Gt-Bt, GBPQ	4.8	5.6	670	500
KY-6/04 Storskär	Tonalitic gneiss	Plg-Hbl-Qtz-Bt-Ti-Opq (ilm) assemblage. No chloritization or sericite alteration. Hornblende: Ca- and Fe-rich, poor in Ti and Na.	Hbl-Plg[4]	-	-	-	675
KY-1/03 Kyrko-gårdsö	Metadia-base (gneiss)	Plg-Bt-Hbl-Ti-Opq (Ilm) assemblage. No chloritization. Hornblende: Ti- and Na-poor, Ca- and Fe-rich, weak zoning. Plagioclase: no zoning.	Hbl-Plg	-	-	805	760
KY-2/03 Kyrko-gårdsö	Tonalitic protomylo-nite	Hbl-Bt-Plg-Qtz-Ti-Chl-Epi-Opq (Ilm) assemblage. Hornblende: commonly altered to biotite along grain margins, geochemical zoning with retrograde effects along rims. Plagioclase: grains only very locally sericitised, clear retrograde geochemical effects along the rims, zoning of grains (Ca-rich cores).	Hbl-Plg	-	-	770	715
KY-3/05 Kyrko-gårdsö	Gt-bearing tonalitic mylonite	Hbl-Plg-Bt-Qtz-Gt-Opq (Ilm), Ti, Epi assemblage. No chloritization.	Gt-Bt, Hbl-Plg, GBPQ	-	7.1	-	610; 695
KY-4/03 Kyrko-gårdsö	Tonalitic ultramylo-nite	Plg-Hbl-Bt-Qtz-Epi-Chl-Calc assemblage. Partly altered plagioclase and hornblende porphyroclasts in a very fine-grained plg-bt-epi matrix. Quartz best visible in ribbons. Calcite in places as an alteration product. Hornblende: geochemical zoning with retrograde effects along rims. Plagioclase: clasts locally sericitised, grains equilibrated to retrograde conditions, no constant zoning. Matrix: no signs of recovery and annealing after the mylonitization.	Hbl-Plg	-	-	670	630

[1] Key: Plg = plagioclase, Qtz = quartz, Kfs = K-feldspar, Bt = biotite, Gt = garnet, Chl = chlorite, Hbl = hornblende, Ti = titanite, Opq = opaques, Ilm = ilmenite, Epi = epidote, Calc = calcite

[2] The uncertainty of the Gt – Bt geothermometer is ± 50ºC (Bhattacharya et al. 1992)

[3] Uncertainty of the GBPQ geobarometer is ± 1.2 kbar (Wu et al. 2004)

[4] The uncertainty of the Hbl-Plg geothermometer is ±35-40ºC (Holland & Blundy 1994)

The last gneissose sample, the metadiabase (KY-1/03), gives average core and rim Hbl-Plg temperatures of 805ºC and 760ºC, respectively (Fig. 4.50b). The higher core temperature probably reflects the crystallisation and cooling of the original intrusion, while the rim temperature is interpreted to indicate the temperature of the last deformation phase that significantly affected the rock. However, the rim temperature is only marginally lower than the core temperature, reflecting the absence of significant geochemical zoning in the analysed grains. This sample has been dated (chapter 4.5), the results suggesting a magmatic age of ca. 1.83 Ga and a metamorphic age of ca. 1.79 Ga. It is therefore possible that the metamorphic conditions of the 1.79 Ga deformation event were not sufficiently high in order to allow 'resetting' of the Hbl-Plg system; thus the lack of zoning in the grains.

GBPQ geobarometry (Wu et al. 2004) could in theory be applied for two of the gneissose samples; that is, the garnet-bearing samples K-5/02 and K-3/03. The mineral activity conditions for GBPQ geobarometry are met in sample K-5/02 except for the a_{Gros} in garnet, which is slightly low and therefore gives cause for some uncertainty regarding the barometric calculations. In sample K-3/03

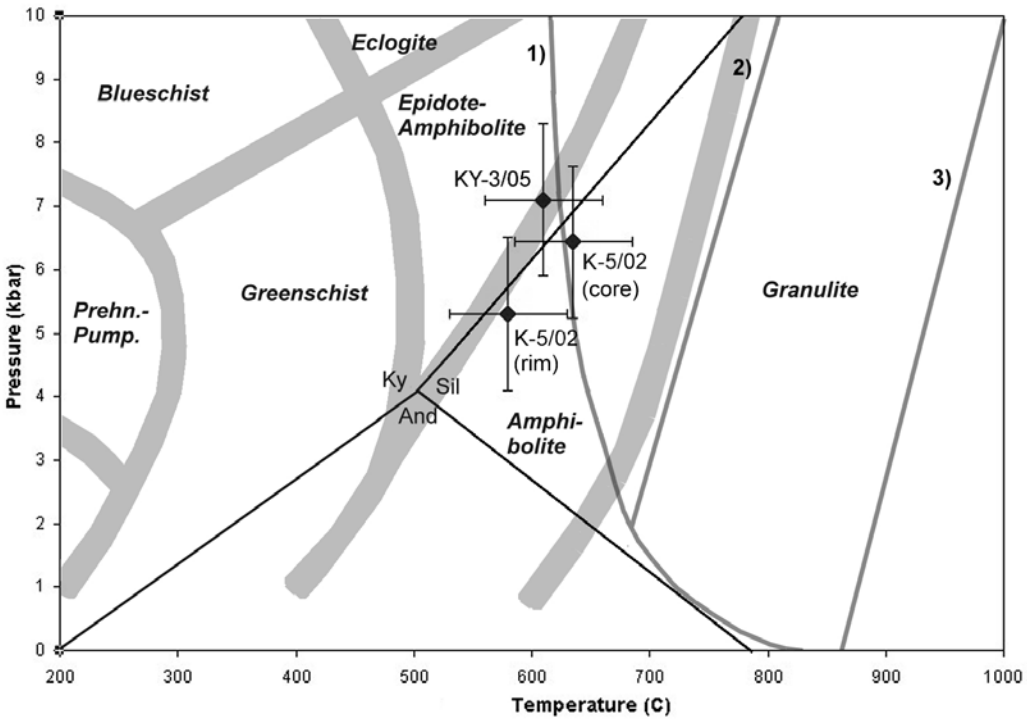

Fig. 4.49. Results of the geothermobarometric calculations of the garnet-bearing samples (Gt-Bt and GBPQ methods; Hellsö and Storskär) compared to the Al_2SiO_5 phase diagram (Holdaway 1971; Ky = kyanite, Sil = sillimanite, And = andalusite), metamorphic facies (in italics; Spear 1995) of and the liquidi of pelitic rocks **1)** H_2O saturated, **2)** with 5% H_2O, and **3)** with 2% H_2O (Spear 1995). The transition zones of the metamorphic facies (shaded) are in reality wider (Spear 1995). Sample K-3/03 is not plotted due to the uncertainties described in the text.

on the other hand, the Ca-content of both the plagioclase and garnet was too low to allow the requirements for grossular and anorthite activities to be met. This leads to significant uncertainties, which together with the extensive retrograde alteration of the sample are reflected in the results for this sample. The geobarometric results for sample K-3/03 can in other words not be regarded as reliable and are ignored due to the extensive retrograde alteration and the severe deviation from the mineral activity limits recommended for the GBPQ geobarometer (Wu et al. 2004). It should be noted however, that the Gt-Bt geothermometry is not affected by grossular activities, so the temperature calculations for sample K-3/03 should nevertheless be accurate. The geobarometric calculations of the more reliable average grain core compositions in the granodioritic sample K-5/02 indicate a pressure of 6.0-6.7 kbar (average 6.4 kbar), while the grain rims record a lower (retrograde) pressure of 5.1-5.4 (av. 5.3 kbar; tab. 4.9, fig. 4.49).

The protomylonitic tonalite gneiss (sample KY-2/03) gives grain core Hbl-Plg temperatures of approximately 770ºC, while the rim temperatures are clearly lower with 715ºC (tab. 4.9, fig. 4.50c). The core temperature possibly reflects the cooling path of the magmatic intrusion. The rim temperature is within the uncertainty of the method equal with the rim temperature of the tonalitic gneiss sample KY-6/04, and only marginally lower than the rim temperature of the metadiabase sample KY-1/03. The mylonite (KY-3/05) shows Gt-Bt rim temperatures between 595-620ºC, the average temperature being 610ºC (tab. 4.9, fig. 4.49). This is in the same range than both the rim and the core temperatures for the garnet-bearing granodioritic gneiss sample K-5/02. The Hbl-Plg thermometer gives a higher temperature of 695ºC for the grain rims in this sample (tab. 4.9, fig. 4.50d). For this mylonite sample, the obtained GBPQ rim pressures varied from 6.4 to 7.6 kbar, with an average pressure of 7.1 kbar (fig. 4.49), which is within the uncertainty of the method ($\pm$1.2 kbar; Wu et al. 2004) the same as the core pressures of the gneissose sample K-5/02. Also in this sample, the grossular activity is slightly low, giving some cause to uncertainty. It is necessary to explain why the rim pressures in the mylonitic sample are be the same or higher than the core pressures for the gneissose sample. One likely explanation may be offered by the fact that the original rims of the mylonite porphyroclasts may have been partly destroyed during mylonitisation, so that the obtained pressures (and temperatures) for the mylonite reflect an earlier deformation phase before the mylonitisation. This is supported by the obtained Gt-Bt temperature estimation that lies close to both the core and the rim temperatures of sample K-5/02.

In the ultramylonite sample (KY-4/03), the hornblende and plagioclase porphyroclasts seem to be slightly zoned, giving average core Hbl-Plg

Fig. 4.50. Results of the Hbl-Plg geothermometric calculations for the gneissose and mylonitic samples of the SJSZ. Note that the reference pressure cannot be used as a geobarometric indicator (see text).

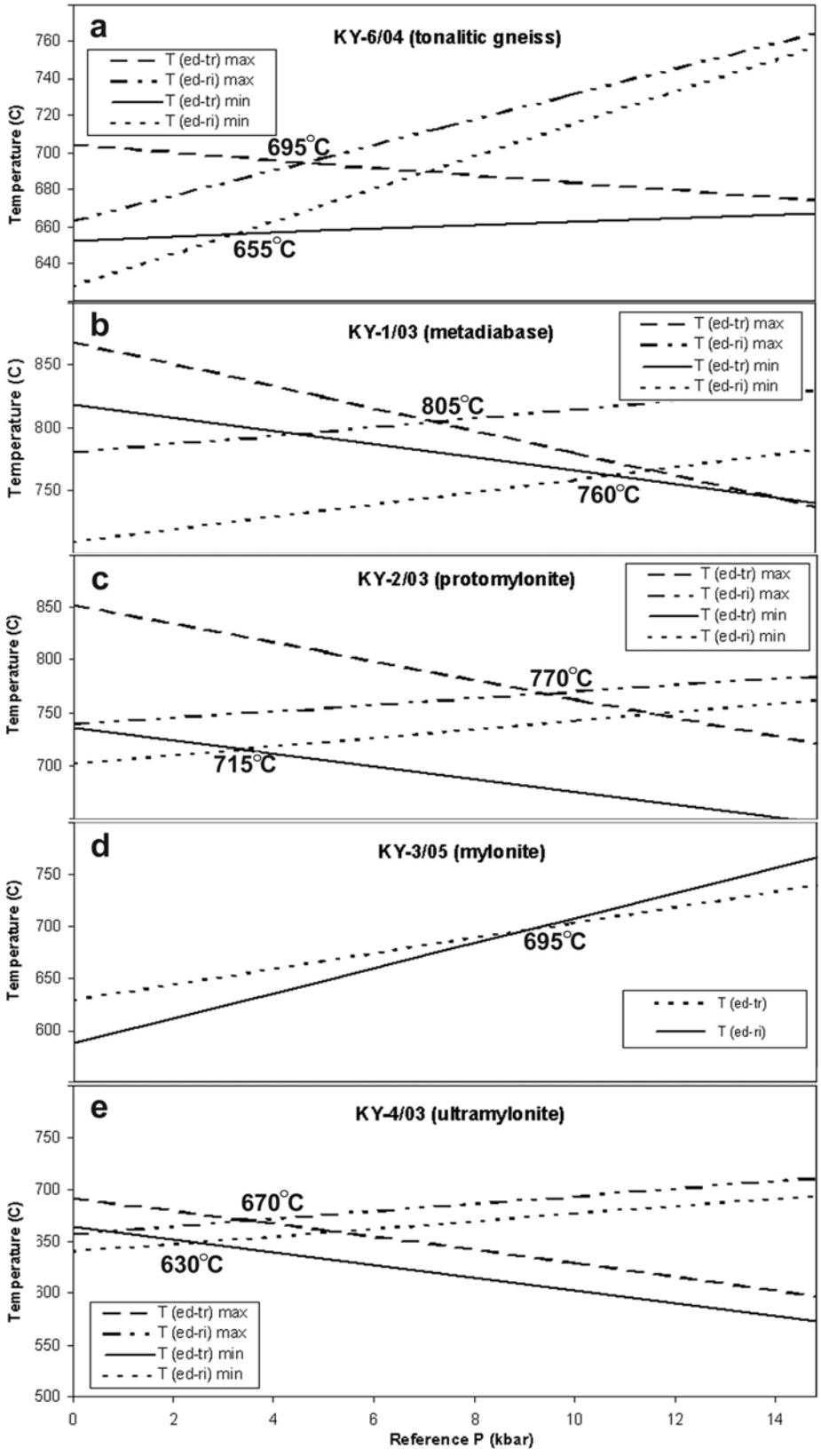
a
KY-6/04 (tonalitic gneiss)
T (ed-tr) max
T (ed-ri) max
T (ed-tr) min
T (ed-ri) min
695°C
655°C
Temperature (C)
b
KY-1/03 (metadiabase)
805°C
760°C
c
KY-2/03 (protomylonite)
770°C
715°C
d
KY-3/05 (mylonite)
695°C
T (ed-tr)
T (ed-ri)
e
KY-4/03 (ultramylonite)
670°C
630°C
Reference P (kbar)

temperatures of 670ºC and rim temperatures of 630ºC (fig. 4.50e). The rim temperatures can be considered equal with the Gt-Bt temperatures of the coarse mylonite sample KY-3/05. The porphyroclasts seem to have undergone little retrograde equilibration, although as mentioned earlier, the ultramylonite matrix contains early greenschist facies mineral assemblages. The temperature was not sufficiently high after the mylonitisation to allow any observable static recrystallisation of the mylonitised fabric around the clasts. The rim temperature of the clasts is therefore here interpreted as the maximum mylonitisation temperature. However, the ultra-mylonites were probably formed at lower temperatures than the 630ºC recorded by the porphyroclast rims since the original clast rims can be expected to have been destroyed during the mylonitic shearing. The geothermometry combined with the sample mineralogy and petrography nevertheless suggests that the mylonites are in fact relatively high-T mylonites (lower amphibolite facies to transitional amphibolite-greenschist facies temperatures).

It should be noted that although the Hbl-Plg method is somewhat pressure-dependent and pressures are used as reference when performing the calculations, the use of the intersection of the two thermometers (fig. 4.50) as a pressure indicator should be avoided (Holland & Blundy 1994).

4.6.3 CONCLUSIONS

The temperature and pressure calculations based on the mineral geochemistry of the analysed samples give results that are somewhat difficult to interpret. The obtained temperatures range from over 800ºC to around 500ºC, reflecting the cooling of the rocks from the crystallisation temperatures toward the transitional greenschist-amphibolite facies conditions. The middle- to higher amphibolite facies temperatures (600-700ºC) are most common (>70% of all calculated temperatures), suggesting partly that most of the ductile deformation and metamorphism may have occurred within that temperature regime, partly that the cooling of the rocks through the middle amphibolite facies temperatures was slow (fig. 4.51). On the other hand, the temperature distribution may be biased due to the fact that many of the middle amphibolite facies temperatures were calculated from mylonites, where the lower-T rims of the porphyroclasts may have been destroyed during mylonitisation. Therefore, temperatures between 500-600ºC may well be equally common within the area, although not frequently observed in this study.

The calculated metamorphic pressures range from ‘peak’ pressures of 6.4-7.1 kbar to retrograde pressures of 5.3 kbar. The slightly low grossular activities in the analysed samples cause some uncertainty to the results, but nevertheless give an indication that the metamorphic peak pressures within the study area are somewhat higher than normally observed for comparable temperatures in SW Finland (within the high-T low-P LSGM; e.g. Väisänen & Hölttä 1999).

Based on the geochemical core-rim relationships within individual grains and the petrographic observations described above, the main transpressive ductile shearing of the

granodioritic and tonalitic rocks within the study area is therefore here interpreted to have taken place at 600-700ºC and 6.4-7.1 kbar. The calculated temperatures are in accordance with the limited migmatisation within the study area, i.e. the liquidus conditions of the rocks were not generally reached during any of the deformation phases. The obtained pressures should be taken with some caution due to the restrictions described above. As mentioned, the pressures are higher than previously reported for southern Finland north of the shear zone at similar temperatures. E.g. Väisänen & Hölttä 1999 calculated temperatures and pressures of migmatisation in different locations in the Turku area to ca. 600-720ºC and 3.2-4.7 kbar. Metamorphism at higher pressures of up to 6.3-6.7 kbar was also observed, the associated temperatures however being significantly higher (up to 800-825ºC). The higher pressure indication obtained from the SJSZ possibly reflects the overall kinematics of the shear zone with a relative vertical movement of the south-side up, resulting in the present

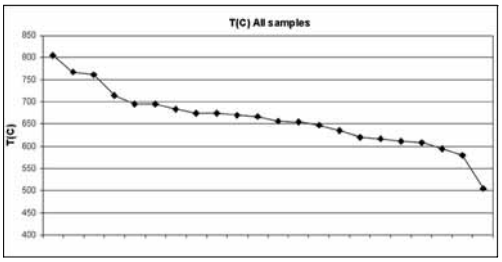

Fig. 4.51. Over 70% of all the obtained average temperatures are between 600-700ºC (see text for further discussion)

level of exposure of the rocks being of a deeper crustal level than the level of exposure to the north of the shear zone. Another possible explanation is a thickening of the crust in the area of the present SJSZ during and/or at late stages of the Svecofennian orogeny.

The results of the temperature calculations of the mylonitic samples tell little of the temperature conditions of the actual mylonite-forming event. The measurements however contribute to the reconstruction of the overall cooling path of the rocks, and support the notion that the mylonitisation was a relatively high-T event.

5 CONCLUSIONS AND SUMMARY

5.1 THE STRUCTURES AND DEFORMATION HISTORY OF THE STUDY AREA – A SUMMARY

The Sottunga-Jurmo shear zone (SJSZ) formed as a result of a partitioning of the regional Svecofennian deformation after the intrusion of the ca. 1.88 Ga igneous granitic, granodioritic and tonalitic rocks and associated mafic lenses. Structurally, the main shear zone is defined by a steeply dipping, NW-SE striking foliation pattern that anastomoses around meter-scale to up to several kilometres (Sottunga) wide, less deformed lenses.

The structural relationship between the rocks south of the main shear zone and the rocks within the shear zone is rather complex, but it appears that the approximately E-W striking, steeply dipping foliations south of the shear zone are refolded and, locally, overturned along steeply to gently toward SE plunging fold axes as the main shear zone is approached. The refolding produced metre- to kilometre-scale F_3 margin folds against the southern margin of the SJSZ (fig. 4.9). The areas where felsic rocks dominate (Kökar and Hellsö) show higher tendency to lateral flow along the shear zone, producing margin folds with gently dipping fold axes and minor shear zones parallel to the main SJSZ. The more mafic rocks (Finnö, Sottunga) behaved in a more competent manner, the resulting overall structural pattern consisting of F_3 margin folds with steep fold axis, and shear zones conjugate to the main SJSZ. In both cases, the folding was probably induced by large-scale partitioning of the deformation into pure shear (folds) and simple shear (minor and major shear zones) components, so that the deformation partitioning was successively enhanced toward the late- and post-orogenic stages. The structural relationships, especially the presence of conical and sheath folds in the NW parts of the study area, further imply a significant vertical kinematic component, so that the block SW of the SJSZ was uplifted in relation to the rocks NE of the shear zone, i.e. the rocks SW of the SJSZ were thrusted up and toward NW along the shear zone.

The structural transition from the shear zone into the LSGM north of the shear zone is more difficult to observe than the southwestern transition, as it is mostly covered by water; also, the transition, where possibly observable, is outside the area of this study. However, based on the geological and geophysical maps, the transition between the SJSZ and the LSGM appears to be much more abrupt than the transition southwards.

The microstructural studies indicate that at least the last two ductile deformation phases (D_3-D_4) mainly took place in relatively high-T conditions of around 600ºC to up to 700ºC. Relatively few indications exist of dynamic deformation and retrograde alteration processes in temperatures below ca. 550ºC, suggesting that the temperature dropped fast after the rocks reached the amphibolite-greenschist facies transition. It may be further concluded that even the mylonites, possibly also the ultramylonites, are high-T mylonites formed at lower amphibolite facies conditions well within the

ductile regime. The petrography and observed mineral assemblages further imply that the rocks cooled slowly through upper and middle amphibolite facies in oxidised, water-rich conditions. After the last ductile, high-T deformation phase (main D_4), there may have been a short period of static recrystallisation and recovery within relatively high-T regime (500-600ºC), after which the temperature dropped sufficiently fast not to allow extensive retrogressive, greenschist facies mineral reactions. On the other hand, some deformation along the shear zone may have occurred below ca. 500ºC (late- to post-D_4) as some feldspars within the main SJSZ gneisses show dynamic microstructures that commonly form in temperatures of 400-500ºC.

The geothermobarometric calculations support the results from the microstructural studies and indicate minimum 'peak' (D_3) metamorphic conditions of 670-720ºC and 6.4-7.1 kbar (corresponds to a crustal depth of ca. 22-25 km). The retrograde temperatures and pressures (D_4) range between 500-630ºC and 5.3 kbar, respectively. Bulk of the calculated temperatures lie between 600-700ºC, possibly reflecting a slow cooling of the rocks through upper and middle amphibolite facies. The obtained pressures are higher than commonly observed in rocks in southern Finland (within the LSGM) in similar temperatures, confirming that the geological history of the area of this study differs from that of the LSGM. The higher pressures may reflect a thicker crust within the study area compared to the LSGM, and/or a deeper exposed section of the crust. In any case, it is obvious that the high heat flow that caused the extensive ca. 1.83 Ga migmatisation within the LSGM did not affect the study area in a manner sufficient to cause large-scale partial melting – the lack of migmatisation is tentatively allocated to the higher pressures observed within the study area. On the other hand, e.g. Kukkonen & Lauri (2006) and Stålfors & Ehlers (2005) suggest a model for the migmatisation where partial melts from a depth of ca. 30-50 km truncated the upper crust as subhorizontal sheets; if the area of this study represents a deeper crustal section than the LSGM, the absence of migmatites and layers of anatectic granites may in the light of their model be simply explained by erosion processes. Stacking of crustal 'slices' in the area may be supported by the presence of the occasional supracrustal(?) layers rich in Ca-minerals (diopside, garnet, calcite), which may represent remnants of sedimentary material that was transported into deeper crustal levels due to stacking. However, the possible stacking must have occurred after the rocks within the study area were formed. The crustal stacking model that has been postulated by e.g. Ehlers et al. (1993) and Kukkonen & Lauri (2006) would be consistent with the slow cooling of the rocks from 700 to 600ºC as the resulting crustal thickening would preserve the heat longer. The possible stacking could at some extent have occurred already during D_2 (ca. 1.85 Ga), but certainly during D_3 and early to main D_4 (ca.1.83 and 1.79 Ga, respectively).

The obtained retrograde temperatures and pressures probably do not for the most part reflect the last deformation phases, as it seems that

especially the system Hbl-Plg was not generally susceptible for equilibrium reactions in temperatures below ca. 675-700ºC. The lowest Hbl-Plg temperature obtained was 630ºC from an ultramylonite, which is clearly too high for ultramylonitic deformation in water-rich conditions, even if the strain rates were very high. The best indications of the cooling path are therefore given by the Gt-Bt thermometer, which records a lowest retrograde temperature of ca. 500ºC. However, temperatures below 600ºC are relatively rare even in the system Gt-Bt, which supports the notion of a slow cooling through amphibolite facies conditions, and rapid cooling from ca. 500-600ºC onwards.

The age determinations confirm the prolonged deformation history of

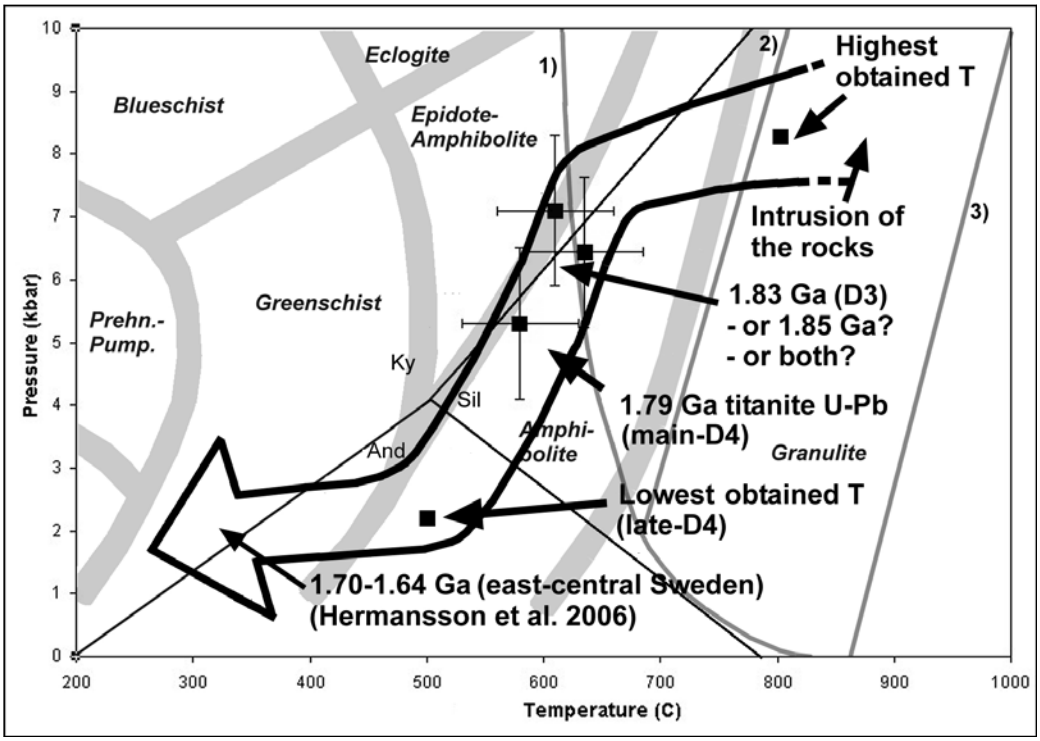

Fig. 5.1. An approximate P-T-t path for the rocks within the study area based on the results of the structural observations, petrography, geothermobarometry and age determinations. Also presented are the Al_2SiO_5 phase diagram (Holdaway 1971; Ky = kyanite, Sil = sillimanite, And = andalusite) and metamorphic facies (in italics; Spear 1995) as well as the liquidi of pelitic rocks **1)** H_2O saturated, **2)** with 5% H_2O, and **3)** with 2% H_2O (Spear 1995). The transition zones of the metamorphic facies (shaded) are in reality wider (Spear 1995). The highest obtained temperature (805ºC) is from a metadiabase dyke (magmatic age ca. 1.83 Ga), but it corresponds relatively well to the highest temperatures (ca. 770ºC) calculated for mineral cores of some tonalitic gneisses and protomylonites. The pressure at the time of the intrusion of the rocks is an estimate, but the geothermobarometric results imply rapid cooling to around 700ºC, after which the cooling was slow between 600-700ºC (see text). The lowest temperature (500ºC), interpreted to represent the late-D_4 stage, is calculated for a garnet-bearing gneiss on Hellsö; the sample displays some retrograde chloritisation of biotite and garnet, which is generally rarely observed within the study area; the associated lowest pressure is taken from Welin et al. (1983) who interpreted the ca. 1.79 Ga Mosshaga pluton having intruded within a pressure regime of ca. 1-2 kbar.

the area, during which the shear zone was reactivated on at least three separate occasions (1.83 Ga, 1.80-1.79 Ga and during cataclastic to pseudotachylitic deformation between 1.78-1.58 Ga), In addition, the first recorded deformation event within the SJSZ occurred at ca. 1.85 Ga, although the structural studies indicate that at this time the deformation was probably more homogeneously distributed throughout the entire study area.

As a summary of the age determinations, the author favours a scenario where the deformation was relatively uniformly distributed during the regional deformation phases D_1 and largely also during D_2 (ca. 1.88 Ga and 1.85 Ga, respectively), although some partitioning of the deformation into the crustal scale SJSZ did occur already ca. 1.85 Ga as this age is not frequently encountered with SW of the main shear zone (Ehlers et al. 2004). At 1.83 Ga (D_3) the shear zone was already well developed, although based on the structural observations deformation and large-scale folding must have continued at this time SW of the shear zone. Plenty of ages around ca. 1.79 Ga exist within the gneisses and protomylonites of the shear zone, but the age has also been observed on Hellsö (Ehlers et al. 2004), indicating that although the bulk of the deformation was partitioned into the SJSZ some deformation and/or metamorphism continued also SW of the main shear zone.

The data and the conclusions presented in this study can be summarized as a P-T-t path (fig. 5.1) and as following main points:

- The SJSZ is an anastomosing, steeply dipping high-strain zone, it shows overall dextral lateral kinematics with a SW-side up vertical component and large-scale deformation partitioning into folds (pure shear component) and shear zones (simple shear component);
- SW of the shear zone, the 1.88 Ga, relatively little deformed rocks, are folded into large-scale margin folds with gently to steeply toward SE plunging fold axes;
- NE of the shear zone lies the LSGM with its overturned, 1.88 Ga rocks that were extensively migmatised at ca. 1.83 Ga;
- The SJSZ represents a major crustal discontinuity, as it separates two crustal blocks (LSGM rocks and 'southern Åland granitoids') that show significant differences in rock types, structures, deformational (age) development and in the metamorphic conditions of deformation;
- The rocks cooled slowly through upper and middle amphibolite facies conditions (600-700ºC, ca. 6.4-7.1 kbar; D_3 and main D_4, possibly even D_2);
- The protomylonites and some of the mylonites were formed within amphibolite facies conditions at ca. 600ºC, and even the ultramylonites latest at late stages of D_4 at ca. 500-550ºC;
- The rocks cooled rapidly after the rocks reached lower amphibolite facies to transitional amphibolite-greenschist facies conditions; some semi-ductile (400-500ºC) deformation along the SJSZ may still have taken place (late- to post-D_4);

- The post-D_4 pseudotachylytes and cataclasites probably formed at relatively deep crustal levels, possibly within greenschist facies conditions, between 1.78-1.58 Ga.

Based on the results presented in this thesis and summarized above, the following geological history for the study area is postulated (fig. 5.2):

1.88 Ga (fig. 5.2a): Intrusion of the rocks with possible synmagmatic, weak deformation (S_1 foliation, possible folding along subhorizontal, E-W fold axes). At this time, the rocks may have been separated of the present LSGM by a strip of mafic crust; Ehlers et al. (1993) and references therein, as well as Korja & Heikkinen (2005) conclude that an extensional basin (fig. 5.2a) existed before or around 1.85 Ga south of the present central Finland granitoid complex, and that some new crust was formed within the basin that subsequently closed around 1.81 Ga. It is also possible that there are two separate 'root zones' within the study area, one being more mafic (Sottunga-Husö areas) than the other (Kyrkogårdsö-Kökar areas; fig. 5.2a).

1.85 Ga (fig. 5.2b): The transpressive motion of the newly formed crust toward N and NNW gives rise to the first recorded deformation phase within the study area (D_2). According to Ehlers et al. (1993) and Ehlers et al. (2004), the extensional basin north of the SJSZ had closed by ca. 1.86 Ga due to horizontal stacking of crustal slabs accompanied by an intrusion of subhorizontal granodioritic sheets. As a result, the 'southern Åland granitoids' SW of the present SJSZ are pressed against the thickened crust north of the study area. At this point, pure shear deformation dominates, although there is probably some strike-slip shearing along the present SJSZ. The small amount of shearing and transpression against the present LSGM is sufficient to produce the asymmetric F_2 folds with steep fold axes.

1.85-1.83 Ga: A break in large-scale deformation.

1.83 Ga (fig. 5.2c): The second recorded deformation phase within the study area (D_3). No large-scale migmatisation occurs, although at the same time north of the study area, the LSGM migmatites are formed. Deformation partitioning becomes significant as the crust slowly cools; the large-scale margin folds form (pure shear dominated deformation), while simultaneously, strike-slip deformation (simple shear dominated deformation) concentrates along the main SJSZ as well as along minor parallel and conjugate shear zones. The attitude of the F_3 margin folds changes from SE toward NW, so that the fold axes become steep toward Skattskär, Finnö and Sottunga. The change in the plunge of the fold axes (and the steepening of the stretching lineations) may possibly be allocated to the rheological differences between the more felsic Kökar-Hellsö areas and the increasingly mafic rock types of the NW parts of the study area, and/or to the possibly deeper crustal level of the NW parts. The strain partitioning may in the NW would therefore have been less pronounced than in the SE and the overall deformation rather accommodated by conjugate, SW-NE striking minor shear zones (e.g. Skattskär; fig. 4.9) and the formation of conical and sheath folds. The more felsic and possibly higher crustal level rocks of

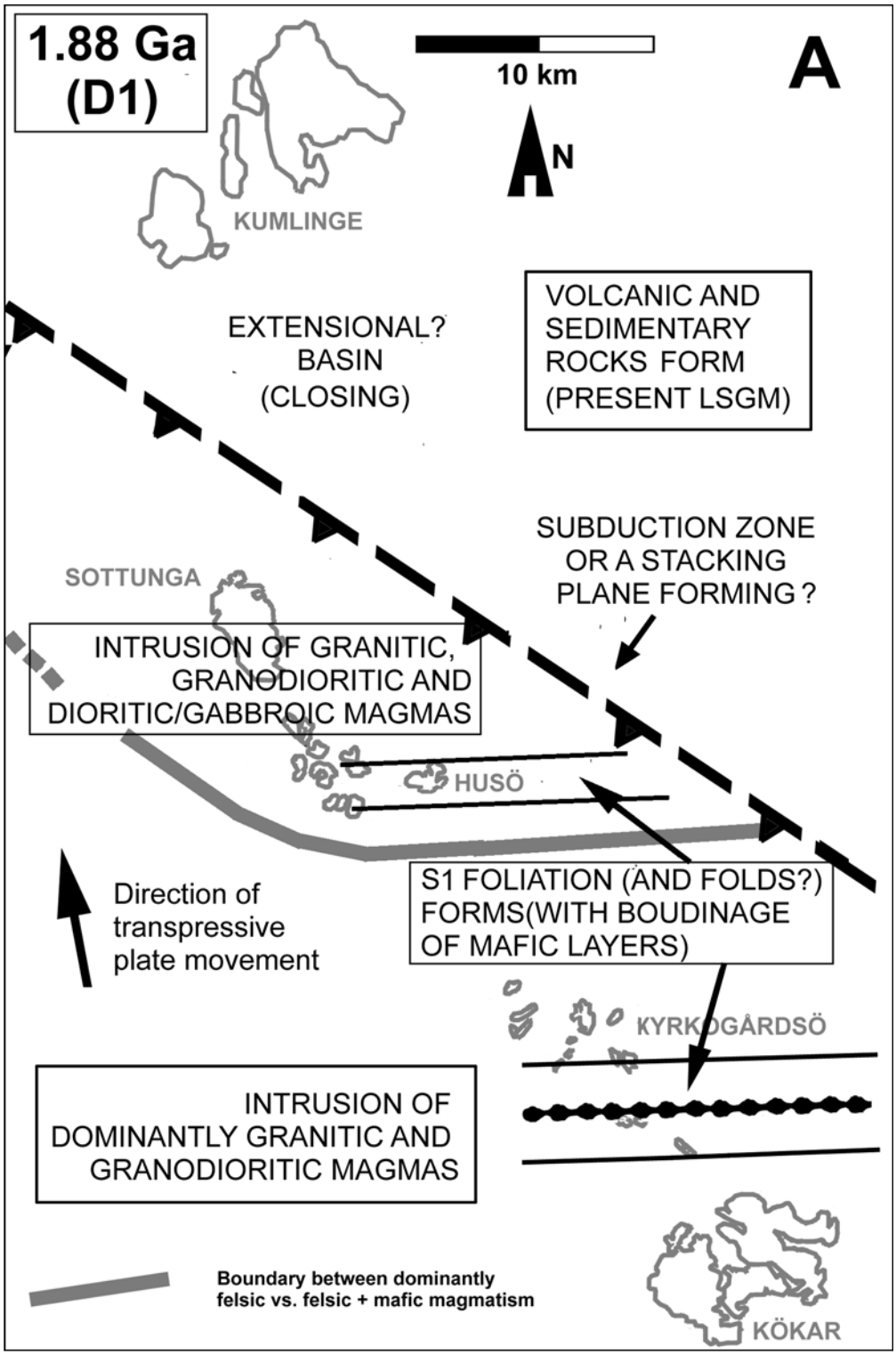

Fig. 5.2. Schematic presentation of the structural and deformational development within and in the immediate vicinity of the study area (see text for more detailed discussion). **a)** Main events at ca. 1.88 Ga: intrusion of magmas into the root zone of a continental (?)island arc (study area),

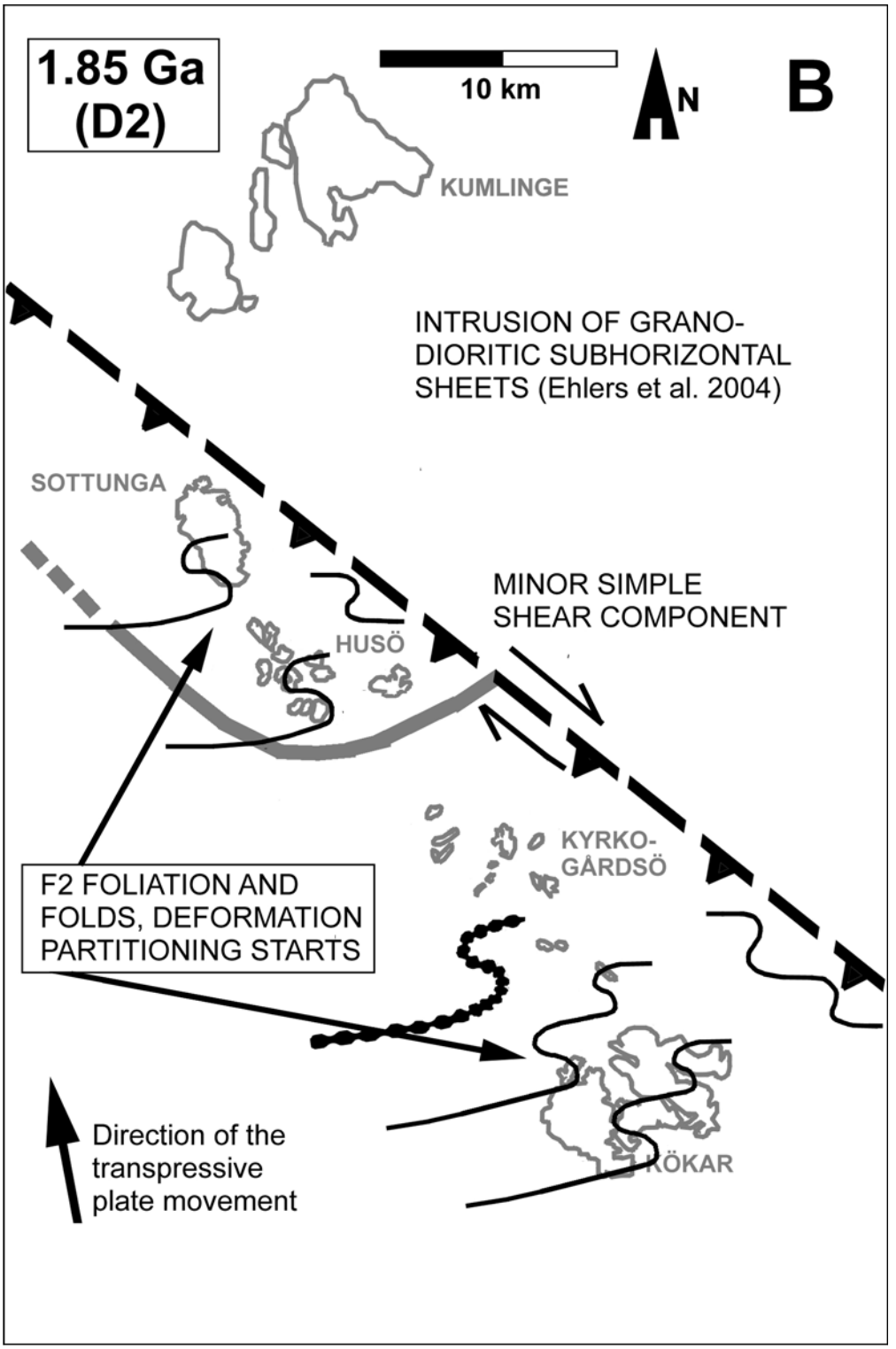

extrusion of volcanics and deposition of sediments into the extensional basin (present LSGM); **b)** Main events at ca. 1.85 Ga: intrusion of granodiorite sheets (present LSGM); F_2 folds form as a result of the initiation of large-scale deformation partitioning into pure shear and simple shear

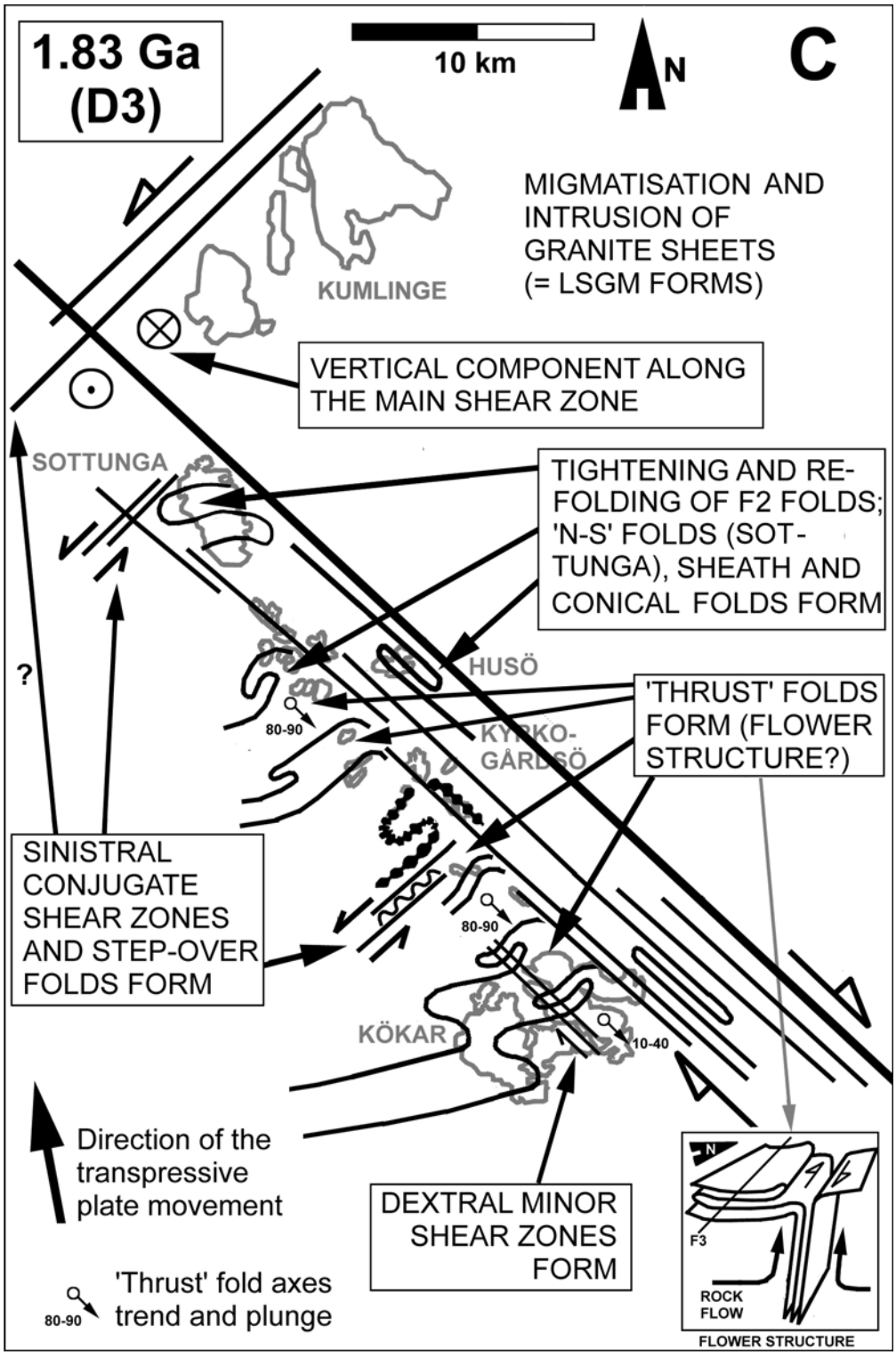

components (study area); **c)** Main events at ca. 1.83 Ga: LSGM forms (extensive migmatisation and granite magmatism); within the study area, as a result of increasing deformation partitioning and introduction of a vertical kinematic component, F_2 folds are refolded and overturned (Hellsö)

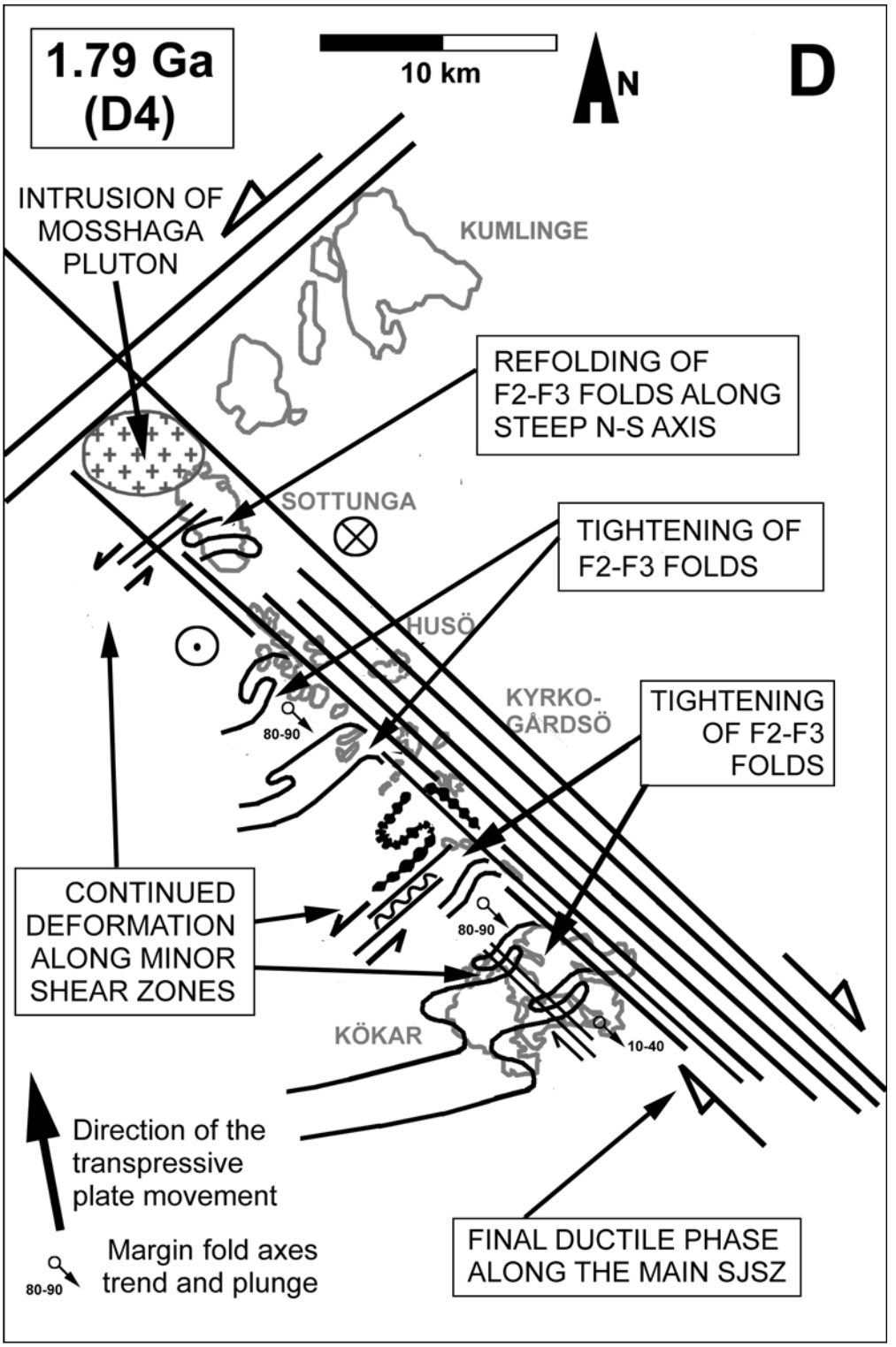

to form large-scale margin folds as well as conical and sheath folds (Finnö, Sottunga), shearing along the main SJSZ is intensified, and minor shear zones form conjugate or parallel to the main shear zone (depending on overall rock rheology and competence); **d)** Main events at ca. 1.79 Ga:

Hellsö seem to have been more susceptible to deformation partitioning and lateral flow that produced folds with gently plunging axes and shear zones parallel to the main SJSZ. The pure shear component affecting the main shear zone may also have produced vertical flow within the shear zone, resulting in a local 'flower structure' that may be partly responsible for the sheath folds within the shear zone and for the F_3 margin folds with shallow fold axes of Hellsö (fig. 5.2c). Assuming that the more felsic Kyrkogårdsö-Kökar area was initially separated from the more mafic Sottunga-Husö block, they are latest at this stage pressed against each other (and against a separate? crustal block NW of the study area) and the vertical kinematic component becomes significant. In summary, the intensified deformation and strain partitioning resulted in an increasingly simple shear dominated deformation along the main SJSZ and the minor parallel and conjugate shear zones, and in a tightening and refolding of the F_2 folds which lead to the formation of the conical and sheath folds and of the large-scale F_3 margin folds. The first protomylonites and mylonites may have been formed at this time due to strain partitioning and/or rheological differences between rock types.

1.83-1.79 Ga: A break in large-scale deformation.

1.79 Ga (fig. 5.2d): The main phase of the third dated ductile deformation phase (D_4). Deformation partitioning is increasingly enhanced and the dynamic deformation is dominantly concentrated into minor and major high-strain zones (shear zones), although some continued tightening of the large-scale folds is possible. On Sottunga, late, very gentle folds with steeply toward S-SSE plunging fold axes refold the earlier folds and sheath folds. D_4 may have continued for an unknown period of time after 1.79 Ga, at which time the rocks still probably remained within a relatively high-T regime (lower amphibolite facies to transitional amphibolite-greenschist facies conditions). Most of the protomylonites and mylonites were formed around or soon after 1.79 Ga, and also the ultramylonites probably formed during late-D_4 or very soon afterwards in relatively high-T conditions. 1.79-1.78 Ga pegmatites intrude the warm but relatively rigid crust.

Post-1.79 Ga (late- and post-D_4): A short period of static recrystallisation and recovery in lower amphibolite facies conditions with very limited retrograde mineral reactions (chloritisation), after which the rocks cooled rapidly due to uplift and exhumation of the rocks. Possibly some dynamic, semi-ductile gneissose and ultramylonitic deformation, accommodating the last movements of the cooling crust within the ductile and semiductile regimes.

1.79-1.58 Ga: A reactivation of the study area within the semi-brittle

---

deformation partitioning within the study area continues to increase, minor tightening of existing fold structures, although the deformation is dominantly concentrated to the major and minor shear zones where protomylonites and mylonites form (possibly also ultramylonites during late-D_4); pegmatites, granites and possibly also diorites intrude the warm but already relatively rigid crust (e.g. Storskär pegmatites, Mosshaga granite pluton and related granite dykes on Sottunga, Husö undeformed diorite intrusion).

regime, evidenced by rare cataclasites and pseudotachylytes.

5.2 PROBLEMS AND UNCERTAINTIES

The geological history of the study area is complicated, as can be expected from an area that has undergone a prolonged history of magmatism, deformation and tectonic reactivation. The interpretation of the structures, geothermobarometry and the age determinations is therefore far from straightforward. However, as the results of the several different studies presented in this thesis complete and support each other, the uncertainties imposed on any individual method are decreased. The most important uncertainties and/or problems related to each separate study are presented within each individual chapter; regardless, some problems should again be briefly mentioned here.

Concerning geobarometry, the mineral activities for the GBPQ method in the analysed samples are not entirely satisfactory. In samples K-5/02 and KY-3/05, the a_{Gros} in garnet is slightly low and therefore gives cause for some uncertainty, and the obtained pressures should therefore be taken with some caution. In sample K-3/03 on the other hand, the Ca-contents of both the plagioclase and garnet are too low to allow the requirements for grossular and anorthite activities to be met, and the geobarometric results from this sample are therefore completely ignored. Despite the uncertainties, the author considers the results from the two more reliable samples nevertheless a good indication for the metamorphic pressure as both samples, collected from different locations, gave similar pressure indications.

The interpretation of microstructures and their formation evolve continuously, and although the latest reference was used to interpret the microstructures it can be expected that some changes will be introduced in future to this relatively new field of study. However, the microstructural interpretations and observations correspond well to observations and results obtained by other methods, and are therefore considered to reflect the last stages of the deformational history relatively accurately.

The most significant questions that this thesis has been unable to provide an exact answer for are probably the age of the ultramylonite- and pseudotachylyte-forming events, and the relation of the study area to other crustal-scale shear zones in southern Fennoscandia. Although a general time frame for the mylonitic and pseudotachylitic events can be established, more accurate knowledge of the styles, age and distribution of the late- and post-D_4 deformation along the SJSZ (and SFSZ) might shed some light to the late- and post-Svecofennian development of the crust in SW Finland. The structural, temporal and deformational relationship between the SJSZ and other Svecofennian shear zones is another important problem that, when solved, would tell us much about the development of the Svecofennian crust and of orogenic processes in general.

ACKNOWLEDGEMENTS

Carl Ehlers, who functioned as a supervisor for this thesis, is heartily thanked for his help and support. Håkan Sjöström is gratefully acknowledged for functioning as the opponent, and Aulis Kärki and Karin Högdahl are warmly thanked for reviewing the manuscript for this thesis.

People at the Department of Geology and mineralogy at Åbo Akademi University are thanked for help and support at various stages of the work, especially Sören Fröjdö, Juha Kauhanen, Fredrik Strandman, Alf Lindroos and Elin Siggberg are acknowledged. Krister Sundblad from the University of Turku is thanked for supervising my ore geology studies. Irmeli Mänttäri and Bo Johanson from the Geological survey of Finland as well as Tobias Hermansson and Laurence Page from the University of Lund are sincerely acknowledged for their contributions. Also, I'm indebted to Hans Annersten, Hannu Huhma, an unknown reviewer to the paper Torvela et al. (accepted), Tuula Hokkanen, Hans Harryson, Alvar Soesoo, Chris Talbot, Leo Kriegsman, Martin Whitehouse, Lev Ilyinsky, Bodil Kajrup, Denis Gapais, Pentti Hölttä, Stefan Bergman, and many others for paper reviews, help with the sample preparations and analyses, and for fruitful discussions. Last but not least, thanks to Peter who's always been there.

Funding for this thesis was received (in chronological order) from Finska Vetenskaps-Societeten (Sohlbergs Delegation), Ella ja Georg Ehrnroothin Säätiö, Nordenskiöld-Samfundet i Finland rf., Suomalainen Konkordia-liitto, Finnish Academy of Science and Letters (Vilho, Yrjö and Kalle Väisälä fund), Stiftelsens för Åbo Akademi Forskningsinstitut, Åbo Akademis Jubileumsfond 1968, Finnish National Graduate School in Geology, Waldemar von Frenckells Stiftelse, Emil Aaltosen säätiö, Naisten Tiedesäätiö. All are sincerely thanked for their contribution.

REFERENCES

All, T., Puura, V. & Vaher, R 2004. Orogenic structures of the Precambrian basement of Estonia as revealed from the integrated modelling of the crust. Proceedings of the Estonian Academy of Sciences, Geology 53/3, 165-189.

Allen, A. R. 1979. Mechanism of frictional fusion in fault zones. Journal of Structural Geology 1, 231-243.

Andersen, T. B. & Austrheim, H. 2006. Fossil earthquakes recorded by pseudotachylytes in mantle peridotite from the Alpine subduction complex of Corsica. Earth and Planetary Science Letters 242, 58-72.

Berger, A. & Stünitz, H. 1996. Deformation mechanisms and reaction of hornblende: examples from the Bergell tonalite (Central Alps). Tectonophysics 257, 149-174.

Bergman, S. & Sjöström, H. 1994. The Storsjön-Edsbyn Deformation Zone, central Sweden. Research report of a project entitled: The tectonometamorphic history of a major shear zone in central Sweden – integrated geological-geophysical study. Institute of Earth Sciences, Uppsala.

Best, M. G. & Christiansen, E. H. 2001. Igneous Petrology. Blackwell Science. 458 p.

Bhattacharya, A., Raith, M., Langen, R. and Sen, S. K., 1992. Non-ideal mixing in the phlogopite-annite binary: Constraints from experimental data on Mg-Fe partitioning and a reformulation of the biotite-garnet geothermometer. Contributions to Mineralogy and Petrology 111, 87-93.

Bigi, S. 2006. An example of inversion in a brittle shear zone. Journal of Structural Geology 28, 431-443.

Bodnar, R. J. 2003. Introduction to fluid inclusions. In: Samson, I., Anderson, A. & Marshall, D. 2003 (Eds.). Fluid Inclusions – Analysis and Interpretation. Mineralogical Association of Canada, Short Course Series Volume 32, 374 p.

Bowen, N. L. 1940. Progressive metamorphism of siliceous limestone and dolomite. Journal of Geology 48, 225-274.

Branigan, N. P. 1987. The role of shearing in the Proterozoic development of the Åland archipelago, S.W. Finland. Bulletin of the Geological Society of Finland 59, 117-128.

Broska, I., Harlovb, D., Tropperc, P. & Simand, P. 2007. Formation of magmatic titanite and titanite–ilmenite phase relations during granite alteration in the Tribeč Mountains, Western Carpathians, Slovakia. Lithos 95, 58-71.

Cagnard, F., Durrieu, N., Gapais, D., Brun, J.-P., & Ehlers, C. 2006. Crustal thickening and lateral flow during compression of hot lithospheres, with particular reference to Precambrian times. Terra Nova 18, 72-78.

Chester, F. M. & Logan, J. M. 1987. Composite planar fabric of gouge from the Punchbowl Fault, California. Journal of Structural Geology 9, 621-634.

Claesson, S., Huhma, H., Kinny, P.D. & Williams, I.S. 1993. Svecofennian detrital zircon ages - implications for the Precambrian evolution of the Baltic Shield. Precambrian Research 64, 109-130.

Cosca, M. A., Caby, R. & Bussy, F. 2005. Geochemistry and $^{40}Ar/^{39}Ar$ geochronology of pseudotachylyte associated with UHP whiteschists from the Dora Maira massif, Italy. Tectonophysics 402, 93-110.

Culshaw, N., Purves, M., Reynolds, P. & Stott, G. 2006. Post-collisional upper crustal faulting and deep crustal flow in the eastern Wabigoon subprovince of the Superior Province, Ontario: Evidence from structural and $40^{Ar}/39^{Ar}$ data from the Humboldt Bay High Strain Zone. Precambrian Research 145, 272-288.

Davidson, C., Davis, K. J., Bailey, C.M., Tape, C.H., Singleton, J. & Singer, B. 2003. Age, origin, and significance of brittle faulting and pseudotachylyte along the Coast shear zone, Prince Rupert, British Columbia. Geology 31, no. 1, 43-46.

Deer, W. A., Howie, R. A. & Zussman, J. 1992. An Introduction to the Rock-Forming Minerals. Longman Scientific & Technical, 696 p.

Dewey, J. F., Holdsworth, R. E. & Strachan, R. A. 1998. Transpression and transtension zones. In: Holdsworth, R. E., Strachan, R. A. & Dewey, J. F. (eds.) 1998. Continental Transpressional and Transtensional Tectonics. Geological Society, London, Special Publications 135, 1-14.

Diamond, L. W. 2003. Systematics of H_2O inclusions. In: Samson, I., Anderson, A. & Marshall, D. 2003 (Eds.). Fluid Inclusions – Analysis and Interpretation. Mineralogical Association of Canada, Short Course Series Volume 32, 374 p.

Dickin, A. P. 1997. Radiogenic Isotope Geology. Cambridge University Press. 490 p.

DiToro, G. & Pennacchioni, G. 2004. Superheated friction-induced melts in zoned pseudotachylytes within the Adamello tonalites (Italian Southern Alps). Journal of Structural Geology 26, 1783-1801.

Ehlers, C. 1976. Homogenous deformation in Precambrian supracrustal rocks of Kumlinge area, southwest Finland. Precambrian Research 3, 481-504.

Ehlers, C. & Ehlers, M. 1977. Shearing and multiple intrusion in the diabases of Åland archipelago, S.W. Finland. Geological Survey of Finland, Bulletin 289, 31 p.

Ehlers, C. & Lindroos, A. 1990. Low-angle ductile shears in the early Proterozoic rock of SW Finland. Geologiska Föreningen i Stockholms Förhadlingar 112, 177-178.

Ehlers, C., Lindroos, A. & Selonen, O. 1993. The late Svecofennian granite-migmatite zone of southern Finland – a belt of transpressive deformation and granite emplacement. Precambrian Research 64, 295-309.

Ehlers, C., Skiöld, T. & Vaasjoki, M. 2004. Timing of Svecofennian crustal growth and collisional tectonics in Åland, SW Finland. Bulleting of the Geological Society of Finland 76, 63-91.

Eichelberger, J. C., Izbekov, P. E. & Browne, B. L. 2006. Bulk chemical trends at arc volcanoes are not liquid lines of descent. Lithos 87, 135-154.

Eklund, O., Konopelko, D., Rutanen, H., Fröjdö, S. & Shebanov, A. D. 1998. 1.8 Ga Svecofennian post-collisional magmatism in the Fennoscandian shield. Lithos 45, 87-108.

Eklund, O. & Shebanov, A. 2005. Prolonged postcollisional shoshonitic magmatism in the southern Svecofennian domain – a case study of the Åva granite-lamprophyre ring complex. Lithos 80, 229-247.

Eklund, O., Shebanov, A., Fröjdö, S., Yli-Kyyny, K. & Andersson, U-B. 1996. A flow-foliated ignimbrite related to the Åland rapakivi granite in SW Finland. Terra Nova 6, 548-557.

Eskola, P. 1915. On the relation between the chemical and mineralogical composition in the metamorphic rocks of the Orijarvi region. Bulletin de la Commission Géologique de Finlande 44, 109-145.

Etheridge, M. A. 1983. Differential stress magnitudes during regional deformation and metamorphism: upper bound imposed by tensile fracturing. Geology 11, 231-234.

Evans, B. W. 1990. Phase relations in epidote-blueschists. Lithos, v. 25, p. 3–23.

Evans, B., Renner, J. & Hirth, G. 2001. A few remarks on the kinetics of static grain growth in rocks. International Journal of Earth Sciences 90, 88-103.

Faure, G. 1986. Principles of Isotope Geology. John Wiley & Sons. 589 p.

Ferry, J. M. & Spear, F. S. 1978. Experimental calibration of partitioning Fe and Mg between biotite and garnet. Contributions to Mineralogy and Petrology 66, 113-117.

Frost, B. R., Chamberlain, K. R. & Schumacher, J. C. 2001. Sphene (titanite): phase relations and role as a geochronometer. Chemical Geology 172, 131-148.

Gaál, G. & Gorbatschev, R. 1987. An outline of the Precambrian evolution of the Baltic Shield. In: Gaál, G. & Gorbatschev, R. (Eds.) 1987. Precambrian Geology and Evolution of the Central Baltic Shield. Precambrian Research 35, 15-52.

Ganne, J., Betts, P. G., Weinberg, R. & Noble, M. 2005. Structural complexity in the Curnamona Province (South Australia): Polyphase strain partitioning and reactivation. Precambrian Research 143, 50-74.

Gapais, D. 1989. Shear structures within deformed granites: mechanical and thermal indications. Geology 17, 1144-1147.

Geyh, M.A. & Schleicher, H. 1990. Absolute Age Determination: Physical and Chemical Dating Methods and Their Application. Springer-Verlag, 503 p.

Grocott, J. 1981. Fracture geometry of pseudotachylyte generation zones: a study of shear fractures formed during seismic events. Journal of Structural Geology 3, 169-178.

Guermani, A. & Pennacchioni, G. 1998. Brittle precursors of plastic deformation in a granite: an example fraom the Mont Blanc Massif (Helvetic, western Alps). Journal of Structural Geology 20, 135-148.

Hermansson, T., Söderlund, P., Stephens, M. B. & Page, L. 2006. Timing of ductile deformation and cooling history in the Svecokarelian orogen, south-central Sweden. In: Peltonen, P. & Pasanen, A., 2006. The 27th Nordic Geological Winter Meeting, Abstract Volume. Bulletin of the Geological Society of Finland, Special Issue I, p. 49.

Hermansson, T. Stephens, M. B., Corfu, F., Andersson, J. & Page, L. 2007. Penetrative ductile deformation and amphibolite-facies metamorphism prior to 1851 Ma in the western part of the Svecofennian orogen, Fennoscandian shield. Precambrian Research 153, 29-45.

Högdahl, K. 2000. Late-orogenic, ductile shear zones and protolith ages in the Svecofennian Domain, central Sweden. Meddelanden från Stockholms Universitets Institution för Geologi och Geokemi, No. 309. Dissertation.

Högdahl, K. & Sjöström, H., 2001. Evidence for 1.82 Ga transpressive shearing in a 1.85 Ga granitoid in central Sweden: implications for the regional evolution. Precambrian Research 105, 37-56.

Holdaway, M. J. 1971. Stability of andalusite and the aluminium silicate phase diagram. American Journal of Science 271, 97-131.

Holland, T. & Blundy, J. 1994. Non-ideal interactions in calcic amphiboles and their bearing on amphibole-plagioclase thermometry. Contributions to Mineralogy and Petrology 116, 433-447.

Hölttä, P. & Klein, V. 1991. PT-development of granulite facies rocks in Southern Estonia. Geological Survey of Finland, Special Paper 12, 97-131.

Hubbard, F. & Branigan, N. 1987. Late Svecofennian magmatism and tectonism, Åland, southwest Finland. In: Gaál, G. & Gorbatschev, R. (Eds.) 1987. Precambrian Geology and Evolution of the Central Baltic Shield. Precambrian Research 35, 241-256.

Huhma, H. 1986. Sm-Nd, U-Pb and Pb-Pb isotopic evidence for the origin of the Early Proterozoic Svecokarelian crust in Finland. Geological Survey of Finland, Bulletin 337, 48 s.

Imon, R., Okudaira, T. & Fujimoto, A. 2002. Dissolution and precipitation processes in the deformed amphibolites: an example from the ductile shear zone of the Ryoke metamorphic belt, SW Japan. Journal of Metamorphic Geology 20, 297-308.

Jensen, L. S. 1976. A New Cation Plot for Classifying Subalcalic Volcanic Rocks. Ontario Division of Mines, Misc. Publ. 66, 22 p.

Kähkönen, Y., Huhma, H. & Aro, K. 1989. U-Pb zircon ages and Rb-Sr whole-rock isotope studies of early Palaeoproterozoic volcanic and plutonic rocks, near Tampere, southern Finland. Precambrian Research 45, 27-43.

Kähkönen, Y. 1998. Svekofenniset liuskealueet – merestä peruskallioksi. In: Lehtinen, M., Nurmi, P. & Rämö, T. (Eds.) 1998. 3000 vuosimiljoonaa – Suomen kallioperä. Geological Society of Finland. 375 p.

Kaneko, Y. & Miyano, T. 2004. Recalibration of mutually consistent garnet-biotite and garnet-cordierite geothermometers. Lithos 73, 255-269.

Kärki, A., Laajoki, K. & Luukas, J., 1993. Major Palaeoproterozoic shear zones of the central Fennoscandian shield. Precambrian Research 64, 207-223.

Koistinen, T., Stephens, M. B., Bogatchev, V., Nordgulen, Ø., Wennerström, M. & Korhonen, J. 2001. Geological map of the Fennoscandian shield, scale 1:2 000 000. Geological Surveys of Finland, Norway and Sweden and the North-West Department of Natural Resources of Russia.

Kontinen, A. 1987. An early Proterozoic ophiolite – the Jormua mafic-ultramafic complex, northeastern Finland. In: Gaál, G. & Gorbatschev, R. (Eds.) 1987. Precambrian Geology and Evolution of the Central Baltic Shield. Precambrian Research 35, 313-341.

Korja, A. & Heikkinen, P. 2005. The accretionary Svecofennian orogen – insight from the BABEL profiles. Precambrian Research 136, 241-268.

Korhonen, J. V., Aaro, S., All, T., Nevanlinna, H., Skilbrei, J. R., Säävuori, H., Vaher, R., Zhdanova, L. & Koistinen, T. (comp.) 2002. Magnetic anomaly map of the Fennoscandian Shield 1 : 2 000 000: DGRF-65 anomaly of total field. The Geological Surveys of Finland, Norway and Sweden and the Ministry of Natural resources of the Russian Federation.

Korsman, K., Koistinen, T., Kohonen, J., Wennerström, M., Ekdahl, E., Honkamo, M., Idman, H. & Pekkala, Y. (Eds.), 1997. Bedrock Map of Finland 1:1000000. Geological Survey of Finland.

Kousa, J., Marttila, E. & Vaasjoki, M. 1994. Petrology, geochemistry and dating of Palaeoproterozoic metavolcanic rocks in the Pyhäjärvi area, central Finland. Geological Survey of Finland, Special Paper 19, 7-27.

Krogh, T.E., 1982. Improved accuracy of U-Pb zircon ages by the creation of more concordant systems using an air abrasion technique, Geochimica et Cosmochimica Acta 46, 637-649.

Krogh, T.E., 1973. A low-contamination method for hydrothermal decomposition of U and Pb for isotopic age determinations. Geochim. Cosmochim. Acta, 37, 485-494.

Kruhl, J. H. 2001. Crystallographic control on the development of foam textures in quartz, plagioclase and analogue material. In: Dresen, G. & Handy, M. (eds).

Deformation mechanisms, rheology and microstructures. International Journal of Earth Sciences 90, 104-117.

Kruhl, J. H. 1996. Prism- and basal-plane parallel subgrain boundaries in quartz; a microstructural geothermobarometer. Journal of Metamorphic Geology 14, 581-589.

Kukkonen, I. T. & Lauri, L. S. 2006. Modelling the thermal evolution of a Precambrian orogen: high heat production migmatitic granites of southern Finland. In: Kukkonen, I. T., Eklund, O., Korja, A., Korja, T., Pesonen, L. J. & Poutanen, M. 2006 (eds.). Lithosphere 2006 – fourth symposium on the structure, composition and evolution of the lithosphere in Finland. Programme and extended abstracts. 233 p.

Kurhila, M., Vaasjoki, M., Mänttäri, I., Rämö, T. & Nironen, M. 2005. U-Pb ages and Nd isotope characteristics of lateorogenic, migmatizing microcline granites in southwestern Finland. Bulletin of the Geological Society of Finland 77, 105-128.

Lahtinen, R. 1996. Geochemistry of Palaeoproterozoic supracrustal and plutonic rocks in the Tampere-Hämeenlinna area. Geological Survey of Finland, Bulletin 389, 113 p.

Lahtinen, R. & Huhma, H. 1997. Isotopic and geochemical constraints on the evolution of the 1.93-1.79 Ga Svecofennian crust and mantle in Finland. Precambrian Research 82, 13-34.

Laird, J. 1980. Phase equilibria in mafic schist from Vermont. Journal of Petrology 21, 1-37.

LeBas, M. J., LeMaitre, R. W., Streckeisen, A. & Zanettin, B. 1986. A chemical classification of volcanic rocks based on the total alkali silica diagram. Journal of Petrology 27, 745-750.

Levin, T., Engström, J., Lindroos, A., Baltybaev, S. & Levchenkov, O. 2005. Late-Svecofennian transpressive deformation in SW Finland – evidence from late-stage D_3 structures. Geologiska Föreningen i Stockholms Förhadlingar 127, 129-137.

Lin, A., 1994. Glassy pseudotachylyte veins from the Fuyun fault zone, northwest China. Journal of Structural Geology 16, 71-84.

Lin, A. & Shimamoto, T. 1998. Selective melting processes as inferred from experimentally generated pseudotachylytes. Journal of Asian Earth Science 16, 533-545.

Lindroos, A., Romer, R. L., Ehlers, C. & Alviola, R. 1996. Late-orogenic Svecofennian deformation in SW Finland constrained by pegmatite ages. Terra Nova 8, 567-574.

Liou, J. G., Kuniyoshi, S. & Ito, K. 1974. Experimental studies of the pure phase relation between greenschist and amphibolite in a basaltic system. American Journal of Science 274, 613-632.

Ludwig, K.R. 2003. Isoplot/Ex 3. A geochronological toolkit for Microsoft Excel. Berkeley Geochronology Center. Special publication No. 4.

Ludwig, K.R. 1991. PbDat 1.21 for MS-dos: A computer program for IBM-PC Compatibles for processing raw Pb-U-Th isotope data. Version 1.07.

Magloughlin, J. F. & Spray, J. G. 1992. Frictional melting processes and products in geological materials: introduction and discussion. Tectonophysics 204, 197-204.

Mainprice, D., Bouchez, J. L., Blumenfeld, P. & Tubia, J. M. 1986. Dominant c-slip in naturally deformed quartz: implications for dramatic plastic softening at high temperature. Geology 14, 819-822.

Maniar, P. D. & Piccoli, P. M. 1989. Tectonic discrimination of granitoids. Geological Society of America Bulletin 101, 635–643.

McCulloch, M. T. & Bennett, V. C. 1994. Progressive growth of the Earth's continental crust and depleted mantle: geochemical constraints. Geochimica et Cosmochimica Acta 58, 4717-4738.

McNulty, B. A. 1995. Pseudotachylyte generated in the semi-brittle and brittle regimes, Bench Canyon shear zone, central Sierra Nevada. Journal of Structural Geology 17, 1507-1521.

Merrihue, C. & Turner, G. 1966. Potassium-argon dating by activation with fast neutrons. Journal of Geophysical Research 71, 2852-2857.

Mohr, O. 1882. Ueber die Darstellung des Spannungszustandes und des Deformationszustandes eines Körperelementes und über die Anwendung derselben in der Festigkeitslehre. Civilingenieur 28, 113–156.

Moody, J. B., Meyer, D. & Jenkins, J. E. 1982. Experimental characterization of the greenschist/amphibolite boundary in mafic systems. American Journal of Science 283, 48-92).

Nironen, M. 1997. The Svecofennian orogen: a tectonic model. Precambrian Research 86, 21-44.

Nironen, M., Elliott, B. A. & Rämö, O. T. 2000. 1.88-1.87 Ga post-kinematic intrusions of the Central Finland Granitoid Complex: a shift from C-type to A-type magmatism during lithospheric convergence. Lithos 53, 37-58.

O'Hara, K. D. 2001. A pseudotachylyte geothermometer. Journal of Structural Geology 23, 1345-1357.

Park, A. F. 1985. Accretion tectonism in the Proterozoic Svecokarelides of the Baltic shield. Geology 13, 725-729.

Park, R. G. 1997. Foundations of Structural Geology. Chapman & Hall. 202 p.

Passchier, C. W. & Trouw, R. A. J. 2005. Microtectonics. Springer-Verlag. 366 p.

Patchett, J. & Kouvo, O. 1986. Origin of continental crust of 1.9-1.7 Ga age: Nd isotopes and U-Pb zircon ages in the Svecokarelian terrain of South Finland. Contribution to Mineralogy and Petrology 92, 1-12.

Pearce, J. 1996. Sources and settings of granitic rocks. Episodes 19, No. 4, 120-125.

Pearce, J. A. 1976. Statistical analyses of major element patterns in basalts. Journal of Petrology 17, 15-43.

Peltonen, P. 1995. Petrogenesis of ultramafic rocks in the Vammala Nickel Belt: Implications for crustal evolution of the early Proterozoic Svecofennian arc terrane. Lithos 34, 253-274.

Pennacchioni, G. & Cesare, B. 1997. Ductile-brittle transition in pre-Alpine amphibolite facies mylonites during evolution from water-present to water-deficient conditions (Mont Mary nappe, Italian Western Alps). Journal of Metamorphic Geology 15, 777-791.

Ploegsma, M. 1991. A pilot Rb-Sr dating of the Suomusjärvi ultramylonite: evidence for major post-Svecofennian deformation in SW Finland. Bulletin of the Geological Society of Finland 63, 3-13.

Pouchou, J.L. & Pichoir, F. 1986. Basic expression of "PAP" computation for quantitative EPMA. In: Brown, J.D. & Packwood, R.H. (eds.) 11 th international Congress on X - ray Optics and Microanalysis (ICXOM), 249 - 253.

Pryer, L. L. 1993. Microstructures in feldspars from a major crustal thrust zone: the Grenville Front, Ontario, Canada. Journal of Structural Geology 15, 21-36.

Pryer, L. L & Robin, P. Y. F. 1995. Retrograde metamorphic reactions in deforming granites and the origin of flame perthite. Journal of Metamorphic Geology 14, 645-658.

Puura, V., Hints, R., Huhma, H., Klein, V., Konsa, M., Kuldkepp, R., Mänttäri, I, & Soesoo, A. 2004. Svecofennian metamorphic zones in the basement of Estonia. Proceedings of the Estonian Academy of Sciences, Geology 53/3, 190-209.

Rämö. O.T., Vaasjoki, M., Mänttäri, I., Elliott, B.A. & Nironen, M. 2001. Petrogenesis of the post-kinematic magmatism of the Central Finland Granitoid Complex I; radiogenic isotope constraints and implications for crustal evolution. Journal of Petrology 42, 1971-1993.

Raymond, L. A. 1995. Petrology: the Study of Igneous, Sedimentary and Metamorphic Rocks. Wm. C. Brown Publishers. 742 p.

Reinikainen, J. 2001. Petrogenesis of Palaeoproterozoic marbles in the Svecofennian Domain, Finland. Geological Survey of Finland. Report of Investigations 154. 84 p.

Renne, P. R., Swisher, C. C., Deino, A.L., Karner, D. B., Owens, T. L., DePaolo, D. J., 1998. Intercalibration of standards, absolute ages and uncertainties in $^{40}Ar/^{39}Ar$ dating. Chemical Geology 145, 183-188.

Resor, P. G., Chamberlain, K. R., Frost, C.D., Snoke, A. W. & Frost, B. R. 1996. Direct dating of deformation: U-Pb age of syndeformational sphene growth in the Proterozoic Laramie Peak shear zone. Geology 24, 623-626.

Riedel, W. 1929. Zur Mechanik geologischer Brucherscheinungen. Zentralblatt für Mineralogie, Geologie und Paläontologie 1929B, 354-368.

Rutland, R. W. R., Kero, L., Nilsson, G. & Stølen, R. K. 2001. Nature of major tectonic discontinuity in the Svecofennian province of northern Sweden. Precambrian Research 112, 211-237.

Rutter, E. H. 1986. On the nomenclature of mode of failure transitions in rocks. Tectonophysics 122, 381-387.

Sanderson. D. J. & Marchini, W. R. D. 1984. Transpression. Journal of Structural Geology 11, 1021-1027.

Sederholm, J. J. 1890. Från Ålands rapakivins västra gräns. Geologiska Föreningen i Stockholms Förhadlingar Blad 12, 460-470.

Selonen, O. & Ehlers, C. 1998. Structural observations on the Uusikaupunki trondhjemite sheet, SW Finland. Geologiska Föreningen i Stockholms Förhadlingar 120, 379-382.

Shebanov, A. D. & Eklund, O. 1997. Interaction between acid and basite magmas in the Hammarudda complex, SW Finland: P-T conditions obtained by mineralogical thermometry and barometry. Petrology 5, 141-166.

Sibson, R. H. 1973. Interactions between temperature and pore fluid pressure during earthquake faulting – a mechanism for partial or total stress relief. Nature 243, 66-68.

Sjöström, H. & Bergman, S. 1998. Svecofennian Metamorphic and Tectonic Evolution of East Central Sweden. Research report of a project entitled: Svekofennisk metamorf och tektonisk utveckling i östra mellansverige. Research report, Geological Survey of Sweden. 42 p.

Skyttä, P., Väisänen, M., Mänttäri, I., 2006. Preservation of Palaeoproterozoic early Svecofennian structures in the Orijärvi area, SW Finland – Evidence for polyphase strain partitioning. Precambrian Research 150 (3-4), 153-172.

Soesoo, A., Puura, V., Kirs, J., Petersell, V., Niin, M. & All, T. 2004. Outlines of the Precambrian basement of Estonia. Proceedings of the Estonian Academy of Sciences, Geology 53/3, 149-164.

Spear, F. S. 1995. Metamorphic Phase Equilibria and Pressure-Temperature-Time Paths. Mineralogical Society of America. 789 p.

Spray, J. G. 1995. Pseudotachylyte controversy: fact or friction? Geology 23, 1119-1122.

Spray, J. G., Kelley, S. P. & Reimold, W. U. 1995. Laser probe $^{40}Ar/^{39}Ar$ dating of coesite- and stishovite-bearing pseudotachylytes and the age of the Vredefort impact event. Meteoritics 30, 335-343.

Stacey, J.S. & Kramers, J.D. 1975. Approximation of terrestrial lead isotope evolution by a two-stage model. Earth and Planetary Science Letters, 26, 207-221.

Stålfors, T., Ehlers. C. 2005. Emplacement mechanisms of late-orogenic granites: structural and geochemical evidence from southern Finland. International Journal of Earth Sciences 95 (4), 557-568.

Stipp, M., Stünitz, H., Heilbonner, R. & Schmid, S. M. 2002. the eastern Tonale fault zone: a “natural laboratory” for crystal plastic deformation of quartz over a temperature range from 250 to 700ºC. Journal of Structural Geology 24, 1861-1884.

Sun, S.-s. 1980. Lead isotopic study of young volcanic rocks from mid-ocean ridges, oceanic ridges and island arcs. Philosophical Transactions of the Royal Society of London A297, 409-445.

Sun, S.-s. & McDonough, W. F. 1989. Chemical and isotopic systematics of oceanic basalts: implications for mantle compositions and processes. In: Saunders, A. D. & Norry, M. J., Magmatism in the Ocean Basins. Geological Society, Special Publication 42, 313-345.

Scholz, C. H. 1988. The brittle-plastic transition and the depth of seismic faulting. Geologische Rundschau 77, 319-328.

Sundblad, K. 1991. Svecofennian lead isotopic provinces in the Baltic Shield. In: Pagel, M. & Leroy, J. L. (Eds.) Source, Transport and Deposition of Metals. Balkema, Rotterdam, 355-358.

Suominen, V. 1972. Om sambandet mellan småstrukturer och store veckning på Skattskär, Sottunga, Åland. Licentiatavhandling (dissertation), Åbo Akademi University, Dept. of geology and mineralogy. 91 p.

Suominen, V. 1991. The chronostratigraphy of southwester Finland with special reference to Postjotnian and Subjotnian diabases. Geological Survey of Finland Bulletin 356, 100 p.

Talbot, C. J. 1998. Can field data constrain rock viscosities? Journal of Structural Geology 21, 949-957.

Talbot, C. J. & Sokoutis, D. 1992. The importance of incompetence. Geology 20, 951-953.

Taylor, S. R. & McLennan, S. M. 1985. The Continental Crust: Its Composition and Evolution. Blackwell, Oxford, 312 p.

Torvela, T., Annersten, H. 2005. PT-conditions of deformation within the Palaeoproterozoic South Finland shear zone: some geothermobarometric results. Bulletin of the Geological Society of Finland 77, 151-164.

Torvela, T., Mänttäri, I. & Hermansson, T. (accepted). Timing of deformation phases within the South Finland shear zone, SW Finland. Precambrian Research.

Tullis, J. T., Snoke, A. W. & Todd, V. R. 1982. Significance of petrogenesis of mylonitic rocks. Geology 10, 227-230.

Tullis, J. & Yund, R. A. 1991. Diffusion creep in feldspar aggregates: experimental evidence. Journal of Structural Geology 13, 987-1000.

Tullis, J. & Yund, R. A. 1987. Transition from cataclastic flow to dislocation creep of feldspar: mechanisms and microstructures. Geology 15, 606-609.

Turner, F. J. 1981. Metamorphic Petrology. McGraw-Hill, New York. 512 p.

Vaasjoki, M. 1994. Valijärven hapan vulkaniitti: minimi Hämeen liuskejakson iäksi. Summary: Radiometric age of meta-andesite at Valijärvi, Häme schist zone, southern Finland. Geologi 46, 91-92.

Vaasjoki, M., 1977. Rapakivi granites and other post orogenic rocks in Finland; their age and lead isotope composition of certain associated galena mineralisations. Geological Survey of Finland, Bulletin 294, 1-64.

Vaasjoki, M. & Sakko, M. 1988. The evolution of the Raahe-Ladoga zone in Finland: isotopic constraints. Geological survey of Finland, Bulletin 343, 7-32.

Väisänen, M. 2002. Tectonic Evolution of the Palaeoproterozoic Svecofennian Orogen in Southwestern Finland. Dissertation, Annales Universitatis Turkuensis, AII, 154. 143 p.

Väisänen, M. & Hölttä, P. 1999. Structural and metamorphic evolution of the Turku migmatite complex, southwestern Finland. Bulletin of the Geological Society of Finland 71, Part 1, 177-218.

Väisänen, M. & Mänttäri, I. 2002. 1.90-1.88 Ga arc and back-arc basin in the Orijärvi area, SW Finland. Bulletin of the Geological Society of Finland 74, 185-214.

Väisänen, M., Mänttäri, I. & Hölttä, P. 2002. Svecofennian magmatic and metamorphic evolution in southwestern Finland as revealed by U-Pb zircon SIMS geochronology. Precambrian Research 116, 111-127.

Väisänen, M., Mänttäri, I., Kriegsman, L. M. & Hölttä, P., 2000. Tectonic setting of post-collisional magmatism in the Palaeoproterozoic Svecofennian Orogen, SW Finland. Lithos 54, 63-81.

Di Vincenzo, G., Rocchi, S., Rossetti, F. & Storti, F. 2004. ^{40}Ar–^{39}Ar dating of pseudotachylytes: the effect of clast-hosted extraneous argon in Cenozoic fault-generated friction melts from the West Antarctic Rift System. Earth and Planetary Science Letters 223, 349-364.

Wang, C. & Ludman, A. 2004. Deformation conditions, kinematics, and displacement history of shallow crustal ductile shearing in the Norumbega fault system in the Northern Appalachians, eastern Maine. Tectonophysics 384, 129-148 .

Welin, E., Vaasjoki, M. & Suominen, V. 1983. Age differences between Rb-Sr whole rock and U-Pb zircon ages of syn- and postorogenic Svecokarelian granitoids in Sottunga, SW Finland. Lithos 16, 297-305.

Welin, E., Christansson, K. & Kähr, H.-M. 1993. Isotopic investigations of metasedimentary and igneous rocks in the Palaeoproterozoic Bothnian Basin, central Sweden. Geologiska Föreningen i Stockholms Förhadlingar 115, 282-285.

Wetherill, G. W. 1956. Discordant uranium-lead ages. Transactions, American Geophysical Union 37, 320-327.

White, S. H., Burrows, S. E., Carreras, J., Shaw, N. D. & Humphreys, F. J. 1980. On mylonites in ductile shear zones. Journal of Structural Geology 2. 175-187.

Whitehouse, M.J., Kamber. B.S., 2005. Assigning dates to thin gneissic veins in high-grade metamorphic terranes: a cautionary tale from Akilia, southwest Greenland. Journal of Petrology 46, 291-318.

Whitehouse, M.J., Kamber, B. & Moorbath, S. 1999. Age significance of U-Th-Pb zircon data from early Archaean rocks of west Greenland – a reassessment based on combined ion-microprobe and imaging studies. Chemical Geology, 160, 201-224.

Wiedenbeck, M., Allé, P., Corfu, F., Griffin, W.L., Meier, M., Oberli, F., von Quadt, A., Roddick, J.C., & Spiegeln, W. 1995. Three natural zircon standards for U-Th-Pb, Lu-Hf, trace element and REE analysis. Geostandards Newsletter, 19, 1-23.

Winchester, J. A. & Floyd, P. A. 1977. Geochemical discrimination of different magma series and their differentiation products using immobile elements. Chemical Geology 20, 325-343.

Wu, C.-M., Zhang, J. & Ren, L.-D. 2004. Empirical Garnet-Biotite-Plagioclase-Quartz (GBPQ) Geobarometry in Medium- to High-Grade Metapelites. Journal of Petrology 45, number 9, 1907-1921.

Xirouchakis, D., Lindsley, D. H. & Frost, R. 2001. Assemblages with titanite ($CaTiSiO_4$), Ca-Mg-Fe olivine and pyroxenes, Fe-Mg-Ti oxides, and quartz: Part II, Application. American Mineralogist 86, 254-264.

Yardley, B. W. D. 1996. An Introduction to Metamorphic Petrology. Longman Earth Science Series. 264 p.

Yoder, H. S., Jr., & Tilley, C. E. 1962. Origin of basalt magmas: An experimental study of natural and synthetic rock systems. Journal of Petrology 3(3):342-532.

Zeitler, P.K. 1987. Argon diffusion in partially outgassed alkali feldspar: insights from $^{40}Ar/^{39}Ar$ analysis. Chemical Geology, 65, 167–181.

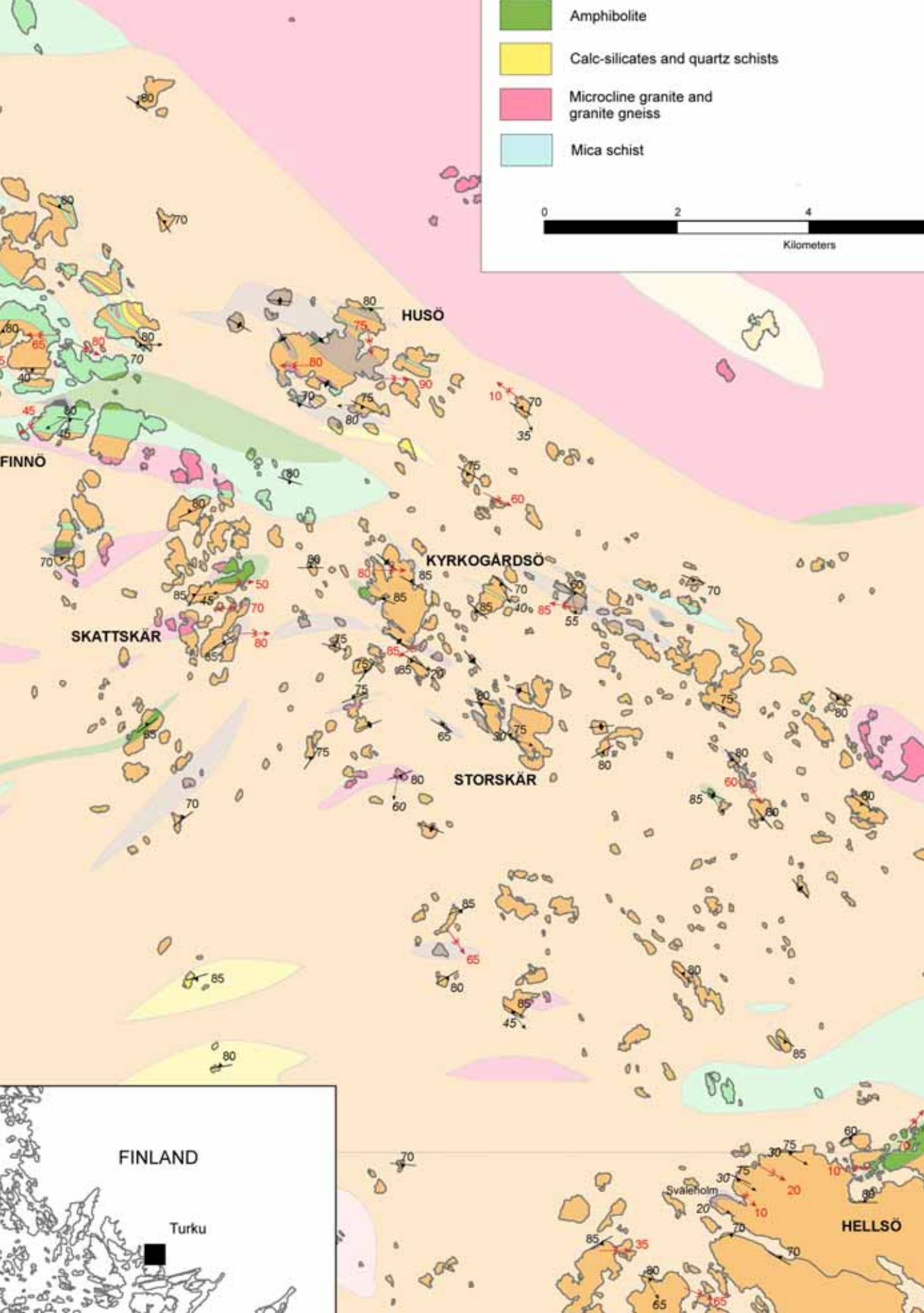
Amphibolite
Calc-silicates and quartz schists
Microcline granite and granite gneiss
Mica schist
0
2
4
Kilometers
HUSÖ
FINNÖ
KYRKOGÅRDSÖ
SKATTSKÄR
STORSKÄR
HELLSÖ
Svaleholm
FINLAND
Turku

ACTA ACADEMIAE ABOENSIS, SER. B

Mathematica et physica

Mathematics, science, engineering

Vol. 63 (2003)

1 **Gustafsson, Jan**: The effect of pH and electrolyte concentration on the dispersion properties of titanium dioxide. 54 pp.

Vol. 64 (2004)

1 **Mylläri, Tatiana**: Studies in the theory of random forests. 88 pp.

Vol. 65 (2005)

1 **Meriluoto, Jussi and Codd, Geoffrey A.** (editors): TOXIC : cyanobacterial monitoring and cyanotoxin analysis. 149 pp.
2 **Glader, Christer**: Constructive methods for rational interpolation and uniform approximation on the unit disc. 99 pp.
3 **Carlsson, Niclas**: Markov chains on metric spaces : invariant measures and asymptotic behaviour. 28 pp.
4 **Saarela, K-E., Harju, L., Lill, J-O., Heselius, S-J., Rajander, J., Lindroos, A.**: Quantitative elemental analysis of dry-ashed bark and wood samples of birch, spruce and pine from south-western Finland using PIXE. 27 pp.

Vol. 66 (2006)

1 **Koissi-Kouassi, Marie-Claire**: Modeling mortality rates : improvements, uncertainties and effects on life annuities. 39 pp.
2 **Palmberg, Niklas**: Analytic function spaces : properties of operators and duality. 38 pp.

Vol. 67 (2007)

1 **Torvela, Taija**: The Sottunga-Jurmo shear zone : structure and deformation history of a crustal-scale ductile shear zone in SW Finland. 187 pp.

Åbo Akademis förlag – Åbo Akademi University Press
Biskopsgatan 13, FI-20500 ÅBO, Finland
Tel. +358 2 215 3292, fax +358 2 215 4490
Distribution: Oy Tibo-Trading Ab
PB 33, FI-21601 PARGAS, Finland
Tel. +358 2 454 9200, fax + 358 2 448 9220